Pd Model Catalysts: Effects of Aging Environment, Aging Duration and Interrupting Aging with Brief Air Pulses on Lean Pd Redispersion

Jason Aaron Lupescu

A dissertation submitted in partial fulfillment
of the requirements for the degree of
Doctor of Philosophy
(Chemical Engineering)
in the University of Michigan
2016

Doctoral Committee:

Professor Johannes W. Schwank, Chair
Adjunct Professor Galen B. Fischer
Adjunct Professor George W. Graham
Associate Professor Emmanuelle Marquis
Robert W. McCabe, National Science Foundation
Professor Robert M. Ziff

Table of Contents

List of Tables vii

List of Figures ix

Chapter

1. Introduction
   - 1.1. The Basics of Automotive Catalysts 1
   - 1.2. Existing Literature on Pd Redispersion 5
   - 1.3. Objectives of this Research 9
   - 1.4. Sequence of this Research 10
   - 1.5. Potential Impact of Research 13
   - 1.6. References 13

2. Methods
   - 2.1. Rationale for Selection of Experimental Methods 16
   - 2.2. Preparation of Model TWC Samples 18
   - 2.3. Procedures for TWC Aging and Regeneration 19
   - 2.4. Procedures for Sample Characterization
     - 2.4.1. X-ray Fluorescence Spectroscopy 22
     - 2.4.2. N_2 Physisorption 24
     - 2.4.3. X-ray Photoelectron Spectroscopy 25
     - 2.4.4. Diffuse Reflectance Infrared Fourier Transform Spectroscopy 27
     - 2.4.5. X-ray Diffraction 28
   - 2.5. Procedures for Pd Particle Size Characterizations

2.5.1. H_2 Chemisorption 29
2.5.2. X-ray Diffraction 31
2.5.3. Electron Microscopy 32
2.6. Procedures for Catalyst Activity Tests
2.6.1. Flow Reactor 34
2.6.2. Oxygen Storage Capacity Measurement 35
2.6.3. Water-Gas Shift Measurement 37
2.6.4. CO Light-off Measurement 38
2.6.5. Kinetic Measurements 39
2.6.6. Pd Oxidation Rate Measurement 42
2.7. Vehicle TWC Emission and Temperature Evaluation 44
2.8. Accuracy of the Methods
2.8.1. Error Estimation 45
2.8.2. Electron Microscopy Pd Size 46
2.8.3. XRD Pd Peak Fit 49
2.8.4. Chemisorption Pd Size 51
2.8.5. XPS Surface Concentration 53
2.8.6. Kinetic Rate Measurements 54
2.9. References 55

3. Pd Model Catalysts: Effect of Aging Environment and Lean Redispersion 58
3.1. Introduction 60
3.2. Experimental
3.2.1. Preparation of Model TWC Samples 62
3.2.2. Model TWC Sample Aging and Lean Treatment Procedures 62
3.2.3. Catalyst Characterization Techniques 63
3.2.4. Catalyst Activity Measurements 65
3.2.5. Vehicle TWC Emission and Temperature Evaluation 66
3.3. Results

3.3.1. Sample Composition Characterization and Aging Comparison 67
3.3.2. Surface Area and Pore Volume Characterization 68
3.3.3. Pd Particle Size Characterizations 70
3.3.3.1. XRD Pattern Phase Identification 71
3.3.3.2. Average Pd Size Estimation Comparison with H_2 Chemisorption and XRD 72
3.3.3.3. STEM Image 73
3.3.4. XPS Surface Characterization 78
3.3.5. Catalytic Activity Tests 81
3.3.6. Examination for Totally Encapsulated Palladium Particles on Ceria-Zirconia 88
3.3.7. Investigation of the Model for Redispersed Palladium Particles on Ceria-Zirconia 90
3.3.8. Comparision of Lean Pd Redispersion to Vehicle Exhaust Conditions 91
3.4. Discussion
3.4.1. Oxidation of the system, collapse of SMSI effect 93
3.4.2. Redispersion of Pd 96
3.5. Conclusions 99
3.6. Acknowledgements 100
3.7. References 101

4. Pd Model Catalysts: Effect of Aging Duration on Lean Redispersion 104
4.1. Introduction 106
4.2. Experimental
4.2.1. Preparation of Model TWC Samples 108
4.2.2. TWC Aging Procedures 108
4.2.3. TWC Preconditioning 109
4.2.4. TWC Characterization Techniques 109
4.2.5. High Temperature X-Ray Diffraction (HTXRD) 111

4.2.6. Thermogravimetric Analysis (TGA) 112
4.2.7. TWC Activity Measurements 112
4.3. Results
4.3.1. Catalyst Aging and Pd Redispersion Zone 113
4.3.2. Surface Area and Pore Volume Characterization 115
4.3.3. XRD Pattern Phase Identification 116
4.3.4. Average Pd Size Comparison 118
4.3.5. XPS Surface Characterization 120
4.3.6. Infrared measurements 123
4.3.7. Catalytic Activity 125
4.3.8. PdO Formation Observed by HTXRD 127
4.3.9. PdO Formation Observed by TGA 132
4.3.10. Effect of Additional Brief Lean Treatments 133
4.4. Discussion
4.4.1. Aging environment 134
4.4.2. Aging duration 135
4.4.3. Support effects 136
4.5. Conclusions 137
4.6. Acknowledgements 138
4.7. References 138

5. Pd Model Catalysts: Effect of Air Pulse Length during Redox Aging Cycle and Lean Redispersion Effects 141
5.1. Introduction 143
5.2. Experimental
5.2.1. Preparation of Model TWC Samples 145
5.2.2. Model TWC Sample Aging and Lean Treatment Procedures 145
5.2.3. Catalyst Characterization Techniques 146
5.2.4. Catalyst Activity Measurements 149
5.3. Results

5.3.1. Support Phase Identification 150
5.3.2. Catalyst Characterization 151
5.3.3. XPS Surface Characterization 154
5.3.4. Infra-red measurements 156
5.3.5. Catalyst Activity Tests 160
5.4. Discussion 163
5.5. Conclusions 168
5.6. Acknowledgements 168
5.7. References 168

6. Conclusions and Future Work 171
6.1. Concluding Remarks 171
6.2. Potential Future Work
6.2.1. Higher Catalyst Aging Temperature 175
6.2.2. Post Aging Lean Treatment Effects 179
6.2.3. Redox Aging Environment Length 182
6.2.4. Redox Aging Environment Lambda 183
6.2.5. Adlineation site length 185
6.3. References 186

List of Tables

Table		
2-1.	Statistical analysis of electron microscopy results	47
2-2.	Statistical analysis of XRD peak fit results	50
2-3.	Chemisorption discrepancies caused by different adsorptive gases	52
2-4.	Statistical analysis of chemisorption results	53
2-5.	Statistical analysis of XPS surface concentration results	54
2-6.	Error propagation of kinetic rate results at 400°C	55
3-1.	Characterization of fresh sample elemental oxide compositions by XRF	67
3-2.	Characterization of fresh and aged catalyst samples	69
3-3.	Comparison of Pd particle diameter measured with STEM to other methods	78
3-4.	XPS surface elemental composition: atomic percent (at%)	79
3-5.	Pd/CZO and Pd/Al kinetic parameters measured with OSC and WGS tests	88
3-6.	Comparison of TOF parameters to literature	88
4-1.	Support surface area and Pd size characterization of Pd/CZO samples	116
4-2.	Comparison of Pd size characterization methods on Pd/CZO samples	119
4-3.	Atomic surface concentrations of fresh and aged Pd/CZO	123

	samples by XPS	
4-4.	IR bands on CZO and Pd	124
4-5.	Avrami model rate constant and exponent for measured PdO formation	130
5-1.	Catalyst Samples and Characterization Results	152
5-2.	Atomic surface concentrations of fresh and aged samples by XPS	156
5-3.	Probable locations of IR bands from literature	157
5-4.	Summarized catalyst activity tests	165
6-1.	Support surface area and Pd size characterization of Pd/CZO samples	177
6-2.	Characterization of redox aged and regenerated catalyst samples	184

List of Figures

Figure		
1-1.	Generalized Reactions over an Automotive TWC (from Ref. 9)	3
1-2.	Illustration of hypotheses: a) first, b) third, and c) fourth	11
2-1.	Powder Aging Reactor Schematic	21
2-2.	X-ray Fluorescence Spectrometer Schematic	23
2-3.	Solution for the BET equation	25
2-4.	X-ray Diffractometer Schematic	29
2-5.	Flow reactor schematic and example of an OSC Test	35
2-6.	Water Gas Shift Reaction Mechanisms (from Ref. 38)	38
2-7.	CO Oxidation and WGS Rates at 515K for Pd/Ceria (from Ref. 38)	40
2-8.	JEOL 3100R05 STEM images of Pd/CZO samples	48
3-1.	Palladium oxide thermal stability from reference [16]	68
3-2.	Pd supported samples X-ray Diffraction patterns	72
3-3.	Pd/Al samples imaged with HAADF STEM	75
3-4.	Pd particle size histograms based on STEM Images of Pd/Al samples	76
3-5.	XPS surface analysis of fresh and redox aged samples	81
3-6.	Generated CO2 over Pd/Al samples during OSC test	83
3-7.	CO conversion to CO2 over Pd/Al samples during WGS test	83
3-8.	Generated CO2 over Pd/CZO samples during OSC test	84
3-9.	CO conversion to CO2 over Pd/CZO samples during WGS test	84

3-10.	Generated CO2 over Pd/TWC samples during OSC test	84
3-11.	CO conversion to CO2 over Pd/TWC samples during WGS test	84
3-12.	Arrhenius plot of OSC test turnover frequency	87
3-13.	Arrhenius plot of WGS test turnover frequency	87
3-14.	Examination of XRD pattern for encapsulation or decoration of Pd by CZO	89
3-15.	Characterization of Pd/CZO after separate dry lean treatment schemes	91
3-16.	Environment of a catalytic converter on the US06 drive cycle	92
3-17.	Proposed Pd redispersion mechanism on Al and CZO supports	94
4-1.	Bulk Palladium Oxide thermal stability using a published equation from reference [26]	115
4-2.	XRD pattern results	117
4-3.	XPS Surface Analysis of Pd 3d	121
4-4.	XPS Surface Analysis of Ce 3d	122
4-5.	IR spectra during CO exposure to clean samples at 22°C	125
4-6.	OSC test on Pd/CZO samples CO2 yield as a function of age	126
4-7.	WGS test on Pd/CZO samples CO2 yield as a function of age	126
4-8.	HTXRD data acquisition scans with Pd[111] on CZO	128
4-9.	Measured and fit PdO formation rates in air at low temperature	130
4-10.	Arrhenius model fit of PdO formation rates in air at low temperature	131
4-11.	TGA results on Pd/CZO redox aged 700°C/16h + 700°C/2h air	133
4-12.	Effect of additional dry lean treatments	134
5-1.	Redox aging cycle and air pulse length	146
5-2.	XRD Patterns of Pd model catalyst samples	151
5-3.	XPS Patterns of Pd model catalyst samples	155
5-4.	IR spectra of “as-is” fresh samples in N_2-only or with 1%O_2	158
5-5.	IR spectra during CO exposure onto clean samples at 22°C	159
5-6.	IR spectra in N_2 after 2h CO exposure at 22°C	160

5-7.	Catalyst activity tests on Pd/CZO samples	161
5-8.	Catalyst activity tests on Pd/Al samples	162
5-9.	CO light-off catalyst activity tests	163
6-1.	XRD Patterns of Pd/CZO catalysts	176
6-2.	Catalyst activity tests on Pd/CZO samples	178
6-3.	Catalytic activity test TOF on Pd/CZO samples	180
6-4.	DRIFTS pattern of CO adsorption onto cleaned samples for 2 hours at 22°C	182
6-5.	Illustration of O_2 concentrations used for both aging environments relative to bulk PdO decomposition line	184

Chapter 1 - Introduction

1.1 The Basics of Automotive Catalysts

Since the government regulations introduced by the Clean Air Act of the 1970s, gasoline automobile emission control has relied on catalytic converters to abate combustion byproducts under the reaction parameter constraints of a vehicle exhaust system. The modern catalytic converter is called a Three-Way Catalyst (TWC) since it is designed to simultaneously oxidize and reduce three regulated pollutant categories of Carbon Monoxide (CO), Nitrogen Oxides (NOx) and Hydrocarbons (HC) in unison with engine controls for exhaust oxygen management. TWCs operate in harsh environments with temperatures that can exceed 1000°C, constant cycling between oxidizing and reducing exhaust gas conditions, and with continual exposure to steam, carbon dioxide, and oil- and fuel-derived poisons. Increasingly strict government regulations force TWCs to perform at warmed-up efficiencies in excess of 99% in the federal test procedure over a full useful lifetime (FUL) of 15 years and/or 150,000 miles for California and Green State emissions compliance. Research into catalysts typically includes evaluation after low-mileage or “degreened” aging, then exposure to severe rapid aging protocols until a simulated FUL condition, and re-evaluation to demonstrate an acceptable level of performance [1, 2, 3, 4, 5, 6, 7, 8]. While this “heat and beat” approach provides initial- and final-state activity (and scarce characterization) data, little is known about the detailed mechanisms by which TWCs age.

The design of the fresh catalytic converter must include excessive quantities of expensive and strategic noble metals and rare earth oxides to ensure the residual activity at FUL is adequate to abate engine emissions. The current state of monolith

coated TWC technology contains a noble metal catalyst (Pt, Pd and/or Rh) impregnated onto a complex support material composed of alumina (Al_2O_3) for high surface area and oxygen storage capacity (OSC) promoters including ceria (CeO_2) and zirconia (ZrO_2), and rare earth oxide stabilizers such as lanthana (La_2O_3) and yttria (Y_2O_3) [9]. The ceria in automotive TWC technologies is usually stabilized with rare earth oxides since it is otherwise not durable at simulated FUL conditions. For example, model catalysts of Pd-ceria demonstrated a loss in activity after cyclic H_2/O_2 aging at a mild degreened aging condition of only 500°C for 5 hours [10] or at 400°C during a steady-state CO/steam exposure for 2 hours [11]. Ceria can be mixed with zirconia and demonstrates superior oxidation and reduction properties over pure ceria after a severe aging condition of 1050°C [5]. The oxidation and reduction of ceria and ceria-zirconia mixed oxides (CZO) depend on the oxygen migration ability of the material [12, 13, 14, 15, 16]. The oxidation of combustion pollutants over automotive TWC formulations under exhaust oxygen deficient conditions depends on the extent of contact between the noble metal particle and the oxygen storage material.

While much effort has gone into formulating exhaust catalysts durable to FUL conditions, relatively little attention has been paid to controlling the aging environment on the vehicle, and techniques currently in use to protect the catalyst act counter to increasing demands for higher fuel economy. This work specifically aims at developing a fundamental understanding of the dynamic changes occurring in automotive exhaust three-way catalyst (TWC) oxygen storage components, and their functions associated with noble metals under various aging conditions imposed by new types of driving modes characteristic of emerging powertrain technologies such as hybrid vehicles and down-sized, turbocharged engines. Hybrid vehicles will shut the engine down after warm-up at low driver torque demand, which creates a fuel-lean environment for the TWC. Downsized turbocharged engines under high driver torque demand may over fuel the engine to cool the exhaust temperature and prevent damage to the downstream components, but this creates a fuel-rich environment for the TWC. The impacts of fuel-rich, fuel-lean, and oscillating net stoichiometric feed streams are all important and changing in modern vehicles from those of only five years ago. With the understanding of how these factors change, manufacturers may be encouraged to implement control

strategies that could lead to in-situ regeneration of catalysts under appropriate conditions on the vehicle.

Exhaust gas oxygen is controlled during stoichiometric engine operation using sensors around the first TWC to achieve simultaneous oxidation (for HC and CO) and reduction reactions (for oxides of nitrogen). Cyclical air/fuel fluctuations caused by feedback control between the on-board computer and the exhaust gas oxygen sensors generate brief perturbations of fuel-rich and fuel-lean exhaust products about stoichiometric engine operation [17]. OSC materials in TWC washcoats provide oxygen to the catalyst during fuel-rich perturbations (deficient oxygen) for HC and CO oxidation; then they are replenished during fuel-lean perturbations (excess oxygen) and effectively dampen the inlet air/fuel fluctuations. There are vast ranges of reduction and oxidation chemical reactions that can occur over a TWC and the key reactions are generalized below in Figure 1-1 reprinted from a review by Kašpar [9]. The oxidation reactions dominate during the fuel-lean perturbations while the reduction, water gas shift (WGS) and steam reforming reactions dominate during the fuel-rich perturbations.

Oxidation	$2CO + O_2 \rightarrow 2CO_2$
	$HC + O_2 \rightarrow CO_2 + H_2O$[a]
Reduction/three-way	$2CO + 2NO \rightarrow 2CO_2 + N_2$
	$HC + NO \rightarrow CO_2 + H_2O + N_2$[a]
	$2H_2 + 2NO \rightarrow 2H_2O + N_2$
WGS	$CO + H_2O \rightarrow CO_2 + H_2$
Steam reforming	$HC + H_2O \rightarrow CO_2 + H_2$[a]

[a] Unbalanced reaction.

Figure 1-1: Generalized Reactions over an Automotive TWC (from Ref. 9)

The decreased efficiency of the TWC to perform the reactions in Figure 1-1 can be linked to deactivation. Useful life and high temperature TWC deactivation modes have been reviewed elsewhere [9, 18] and the main deterioration modes for current monolith-based TWC technologies include noble metal sintering [19, 20], poisoning by fuel and oil additives [21], loss of surface area and OSC component sintering. OSC component sintering can be further divided into loss of contact between the noble metal

and OSC components [3, 10, 11], and encapsulation of the noble metal by the OSC components [7, 10]. However, there is still a lack of fundamental understanding of the atomic scale mechanisms that lead to TWC deactivation. The noble metal sintering is believed to be by agglomeration through simple particle migration and coalescence or Ostwald Ripening. However, it was concluded that no inference about sintering mechanism could be determined by microscopy using the particle distribution method of Pt and Pd particles on alumina support [19]. Ostwald Ripening involves the growth of larger particles by atoms drawn from smaller particles. Small metal particles are thermodynamically less stable than larger particles since atoms on the surface of a particle are energetically less stable than the interior atoms already well ordered and packed. In addition, the relative contribution of noble metal particle encapsulation toward the TWC deactivation is not well understood [6, 7, 9, 22, 23].

TWC deactivation is largely irreversible. Automakers can limit the amount of poisons deposited on the catalyst only through engine designs to burn less oil. Deliberate engine control events are used to remove the few reversibly adsorbed poisons like sulfur from fuel combustion [9, 17, 24]. Engine controls are also refined to limit combustion event misfires that can remove TWC surface area or melt the substrate. Full useful life thermal sintering of noble metals and supports is a result of where the TWC is positioned in the vehicle exhaust system in order to warm-up in time to meet tailpipe emissions standards. Ceria-based OSC components are claimed to assist the noble metal in the oxidation, WGS and steam reforming reactions [9, 15, 25]. The deterioration of OSC has been linked to high temperature induced growth of ceria crystals,38 decrease in surface area and loss of contact with the metal that limits ceria reducibility [26]. However, a Pd/CZO model catalyst subjected to redox cyclic aging at 1173 K (900°C) for 5 hours, a lean treatment during cool down, then a reduction at 573K (300°C) for 1 hour had higher CO oxidation activity (lower T_{50} light-off temperature) and higher O_2 uptake versus another Pd/CZO model catalyst subjected to the same redox cyclic aging environment maintained during the cool down [2]. Pd particle size measurement by H_2 and CO chemisorption showed little if any difference in the two cool down procedures as the sub 1% Pd dispersion values were near the detection limit [2]. It is this type of active intervention with lean treatment to reverse

TWC deactivation that requires further evaluation with probe reactions designed to assess the metal-support interface and multiple Pd particle size measurement methods.

1.2 Existing Literature on Pd Redispersion

The first notable work on Pd dispersion improvement by environmental means appeared in 1981, and was performed by Chen and Ruckenstein on Pd crystallites in a size range of 3-35 nm deposited upon an Al_2O_3 thin film while filming under an electron microscope in 1 atm oxygen [27, 28]. At 350°C within 2 hours they observed that Pd crystallites formed pits and became porous during the transformation into PdO. However, at 1 hour the PdO crystallites below 15 nm could not maintain their leading circular edge due to the lower interfacial tension than in the metallic state and the surface tension gradient caused the oxide to wet the surface and the particles spread about the alumina film. At 500°C, all Pd crystallites wet the surface and spread about, and these mobile particles ruptured over the support surface to form smaller PdO particles. At 750°C, the spreading was less extensive and at 920°C the oxide decomposed and the Pd particles sintered. While the Pd oxide particles were found to easily move about a smooth thin film surface, investigation of Pd redispersion about a high surface area support material of automotive relevance followed soon thereafter. In 1985, Lieske and Völter reported a study on 0.6wt% Pd impregnated onto γ-Al_2O_3 powder with temperature programmed reduction to determine Pd oxidation state and oxygen adsorption to estimate Pd dispersion [29]. With these techniques they observed that Pd needed to be in the Pd^{2+} oxidation state before appreciable increases to Pd dispersion would occur and proposed that redispersion may be through a two-dimensional PdO surface complex with the alumina. They also confirmed the earlier observations from Chen and Ruckenstein that the temperature when Pd particles began to oxidize to PdO was related to the Pd particle size. Once PdO had formed, PdO redispersion appeared to happen within the temperature range up to the oxide decomposition temperature. Meanwhile, Peuckert studied bulk Pd crystals in 0.1-1 MPa oxygen gas over a temperature range of 300K to 920K [30]. He developed an equation

for PdO decomposition as a function of both oxygen concentration and temperature. This independent yet complimentary work by Peuckert effectively approximates the temperature below which PdO can redisperse in various automotive exhaust air/fuel compositions.

About 10 years later, other automotive oxide supports were investigated for Pd oxidation and provided new insights into their potential for Pd redispersion. Farrauto *et al.* carried out a thermal gravimetric analysis of Pd oxidation in air with Pd supported on several oxides [31]. They determined that there is a hysteresis between the temperature of PdO decomposition to Pd and re-formation of Pd to PdO. The relative magnitude of the temperature difference in the hysteresis was a function of the support material with the temperature window of Al_2O_3 and ZrO_2 being the largest (over 200°C) while reducible oxides TiO_2 and CeO_2 being the smallest (80°C and 45°C, respectively). Farrauto *et al.* used high temperature X-ray diffraction (HTXRD) to acquire a pattern of 8wt% Pd/Al_2O_3 then measured the Pd peak width and used the Scherrer equation to determine the average Pd particle size. They observed that above the decomposition temperature at 900°C in air, Pd particles sintered to 36-40 nm and then as the sample was cooled down, some particles reformed PdO and redispersed into 20-30 nm particles. However, they only reported Pd size results with HTXRD on Al_2O_3. Meanwhile, Rodriguez *et al.* studied Pd on oxide thin films with controlled atmosphere electron microscopy while heating in 0.2 Torr oxygen [32]. They confirmed the Pd to PdO observations of Chen and Ruckenstein on Al_2O_3 for the temperature range of 350°C to 800°C. As Rodriguez *et al.* extended the study to temperatures above 800°C, they found that PdO particles formed thin-flat needle-like structures where pits formed on the Al_2O_3 surface demonstrating an interaction between the materials. Pd platelets measuring 60 nm shrank and changed when cooled from 900°C in O_2 to room temperature into hexagonal shaped $Pd\text{-}PdO\text{-}Al_2O_3$ crystallites measuring 15 nm. They also observed at 890°C that PdO was more stable on a thin film of ZrO_2 than on Al_2O_3, which they argued was due to a stronger interaction with the support material. They attributed these observations to the differences in the optical dielectric constant of the metal-oxide systems ($Pd\text{-}ZrO_2$ at 4.75 and 2.9 for $Pd\text{-}Al_2O_3$). In addition, the literature they cited correlated the higher optical dielectric constant and electronic polarization for

the metal and support to increasing wetting and spreading characteristics. Datye *et al*. reported a study on a 5wt%Pd/Al_2O_3 sample heated in air with thermal gravimetric analysis, x-ray photoelectron spectroscopy and electron microscopy [33]. They observed that at 850°C the reduction of PdO to Pd proceeds by small domains of Pd metal forming on the surface of PdO leading to polycrystalline particles that are easy to reoxidize upon cooling in air. However, samples heated to 925°C were completely reduced to Pd metal as perfect single crystals and would not so easily reoxidize when cooled in air. The difference in sample reoxidation during cooling in air was proposed as a lack of PdO nucleation sites on the perfect Pd crystals. They also observed that the process of Pd transformation into PdO alone did not cause Pd to redisperse on undoped alumina on quenched sample portions taken during heating in air to 1000°C then cooled in air to room temperature. However, this observation does not contradict the earlier observations by Farrauto of Pd redispersion on Al_2O_3 as Datye specifically took Pd up to 1000°C where it is very stable then cooled it rapidly through the PdO formation hysteresis temperature to a much lower temperature where the kinetics of PdO formation were much slower. This prevented PdO nucleation. Datye's 2000 paper [33] highlights the importance of keeping Pd catalysts at or below the temperature where a metastable polycrystalline phase coexists with PdO, so that an oxidizing environment can promote rapid reformation of PdO and enable Pd redispersion.

The observations by Farrauto and Rodriguez generated new interest into whether other support materials would enable Pd to redisperse better than on Al_2O_3. In 2004, Hickey et al. reported a study on 0.64wt% Pd on CZO powder and 0.51wt% Pd on Al_2O_3 with CO oxidation, CO-OSC, and CO and H_2 chemisorption tests [2]. They subjected the model catalysts to either an oxidizing environment (lean aged) or a cycling of reducing and oxidizing environments (redox aged) at 900°C and showed much less deterioration with the lean aged sample with respect to the light-off temperature for CO oxidation and the apparent Pd dispersion. The redox aged Pd/CZO sample was later exposed to oxygen at high temperature and cooled down. Further testing and characterization showed a lower light-off temperature for CO and increased O_2 uptake compared to the sample that had not been exposed to oxygen. While chemisorption results were not reported to confirm a higher Pd dispersion via high

temperature oxidizing treatment, this was the first work to investigate the Pd redispersion phenomena on a CZO support similar to the OSC material used in automotive catalytic converters. A few years later, studies emerged on nanoscale PdO formation and redispersion as a function of time at constant temperature. Newton *et al.* reported a study on cycling 5% CO or 5% NO with and without a 5:1 ratio of O_2:NO, all at 400°C, with a catalyst of 1% Pd on 10wt% CZO-Al_2O_3 [34]. Using coordination numbers derived from energy-dispersive extended X-ray adsorption fine-structure spectroscopy, they observed that the reduction pulse created 75 nm Pd hemispheres that then shrank to 47 nm or flattened into discs within the first two seconds of the oxidation pulse, coinciding with the timeframe of the Pd to PdO transition. Their work suggests that if the Pd oxidation rate can be measured, then perhaps the Pd redispersion rate can be estimated. Newton *et al*. showed that 2-10 seconds is enough time to redisperse Pd particles on CZO-Al_2O_3 during CO/NO cycling at 400°C, but it is unclear if such a short air exposure time is also sufficient to first reverse any existing strong metal support interaction effects and then redisperse Pd on laboratory-aged catalysts after simulated automotive exhaust conditions. Recently, Peterson et al. used scanning transmission electron microscopy, operando X-ray absorption spectroscopy, and CO oxidation up to 300°C to study Pd on La_2O_3-Al_2O_3 and undoped Al_2O_3 [35]. They showed that supported Pd clusters treated at 700°C in air or with 1% O_2 formed Pd particles with near atomic dispersion that were stable on La_2O_3-Al_2O_3 when held at 70°C, but not on undoped Al_2O_3. However, these atomically dispersed Pd particles were sintered as the CO oxidation test progressed to 300°C and the next run showed a decrease in performance on both supports. The catalysts could be reactivated with another treatment in air at 700°C. In addition, microscopy and density functional theory work by Johns *et al*. showed that bulk PdO is very stable at 800°C in air and would not emit atoms into the vapor phase (as by Ostwald ripening) [36]. Kang *et al*. aged Pd catalysts at 600°C in 3-21% O_2 and showed that higher oxygen concentrations can lead to a lower extent of Pd particle sintering [37]. The literature review conducted by Johns and Kang enabled them to link properties such as the roughly three orders of magnitude lower vapor pressure and 50% lower surface tension of PdO versus Pd metal as the reason behind the stability of the oxide. Their argument was that after the bulk oxide

forms, the atomic Pd emission becomes more difficult, while PdO mobility and eventual fracture into smaller particles are enhanced. Therefore, the improved sintering resistance of PdO versus Pd under oxidizing conditions relates to differences in their thermodynamic and physical properties.

1.3 Objectives of this Research

TWCs deactivate as a function of time, temperature and gas environment. One of the main deactivation modes is the loss of CO activity due to degradation of OSC. OSC involves transfer of oxygen from a CZO support phase to the active precious metal sites. Emerging powertrain technologies can cause new environments for TWCs such as extended fuel-lean excursions brought about by hybrid vehicles engine-off modes and extended fuel-rich excursions brought about by exhaust component protection modes on down-sized, turbocharged engines such as Ford's Ecoboost technology. Each mode can have their own effects on the catalyst particles and the supporting materials beyond the traditional near-stoichiometric lean-rich oscillations. With the understanding of how these components change with aging environments, manufacturers may be encouraged to use new TWC materials capable of regeneration or implement engine control strategies that could enable in-situ regeneration of catalysts under appropriate conditions on the vehicle. At each stage of aging the degree to which loss of interaction (and corresponding loss of catalyst activity) can be regenerated will be investigated. Palladium (Pd) is the primary precious metal component of current TWCs and the metal most responsible for promoting OSC via ceria-based supporting phases. Thus, the scope of the TWC studies will be limited to Pd model catalysts and its effective utilization. Special attention will be paid to aging-induced changes in the metal-support interface and the role of species adsorbed along the metal-support interface. Pairing the results from a WGS reaction with those from CO oxidation [38, 39] or an OSC measurement [12, 15] are approaches that only a few researchers have taken to probe the extent of CO oxidation and CeO_2 reduction with TWC aging.

The research objectives of this study are 1) measure the relative deactivation of

a matrix of model TWC catalysts, 2) correlate the OSC to water-gas shift (WGS) reaction kinetics, 3) identify the most severe aging modes, and 4) explore ways to inhibit or even counteract the aging process by utilizing lean/rich switching strategies with optimized timing, temperature, and air/fuel composition control. The final objective of this research will be to find answers to these objectives and have those results published into the open literature. A sequence of hypotheses listed in the following section will be based on these research objectives and addressed in each paper and chapter.

1.4 Sequence of this Research

After a brief overview of the methods used (Chapter 2), Chapter 3 examines three different aging environments simulating aspects of the traditional near-stoichiometric lean-rich oscillations on Pd model catalysts and the effects each have on the potential to redisperse Pd with post-aging air treatments at 550°C or 700°C [40]. While the previous work on Pd redispersion used dry air treatments to shrink Pd particles, these dispersion claims were often made with data from just one characterization technique: Rodriguez as well as Chen and Ruckenstein used only electron microscopy [27, 28, 32], Faurrauto used just XRD pattern Pd peak broadening measurements [31], while Hickey disclosed only CO light-off temperatures [2], and Lieske used only oxygen adsorption [29]. Hickey reported chemisorption results for all samples except for the one after the oxidizing treatment [2]. Electron microscopy, XRD and chemisorption each have limitations examining automotive TWCs based on the support materials, size of Pd particles and interactions between the metal and support. Chapter 2 will further describe the benefits and challenges of each technique and how a synthesis of multiple techniques is a more reliable approach. Two hypotheses were formed and tested with probe reactions, such as WGS and OSC measurements, coupled with a battery of physical and chemical characterization methods all for an improved understanding of aging environment induced catalyst deterioration. The first hypothesis was that different aging protocols under varying oscillating air/fuel ratios lead

to very different catalyst structures and performance characteristics. Model catalysts were exposed to reduction, oxidation, or cycling of both (redox) compositions at a fixed temperature and at a fixed aging duration in a flow reactor as illustrated in Figure 1-2a. Unpublished work at Ford identified a catalyst regeneration phenomenon, wherein catalysts that have been aggressively aged on accelerated dynamometer aging cycles for up to 200 hours (simulating FUL) have been partially regenerated under various short term driving cycles on the vehicle or under specific "stabilization" or "recovery" protocols tacked onto the end of the accelerated dyno aging. However, lean catalyst regeneration is currently a "hit or miss" proposition and appears dependent on catalyst preparation or treatment conditions [41]. The key to this course of research was whether the extent of lean Pd redispersion by dry air at 550°C or 700°C was significant on model support materials after a 700°C redox aging treatment for 16 hours. The second hypothesis was that oxygen transfer depends on the contact line between the support and the perimeter precious metal particles (so-called adlineation sites). This allowed important insights into the effect of varying aging protocols with different time-temperature trajectories and reactive environments on these interface sites. The rate of oxygen transfer was measured under steady-state WGS flow reactor conditions or at the leading edge of the CO_2 peak in the OSC test, and provided a very sensitive probe of the concentration and characteristics of adlineation sites between the metal and support. The keys to this research were: 1) observe differences in how the support is reoxidized between OSC and WGS for the different aging environments, 2) correlate these OSC and WGS results to the Pd size and dispersion results to make associated structure-activity relationships.

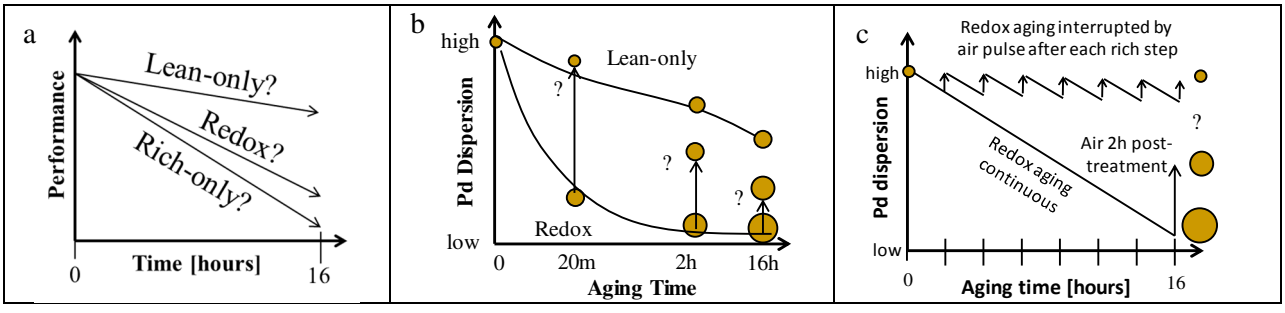

Figure 1-2: Illustration of hypotheses: a) first, b) third, and c) fourth

Chapter 4 examines three different aging durations while reusing similar aging environments from the first paper and the effects each have on the potential to redisperse Pd with post-aging air treatments at 550°C or 700°C [42]. A third hypothesis was formed and tested, which was that larger Pd particles are more difficult to reoxidize and redisperse. While oxidized Pd is the prerequisite for Pd redispersion, support collapse and metal-support interaction may limit PdO mobility and particle rupture. Model catalysts were exposed to a fixed redox composition at a fixed temperature and at gradual aging step durations in a flow reactor as illustrated in Figure 1-2b. Probe reactions and several characterization methods tested this hypothesis and carefully walked a trajectory of catalyst deterioration. Conventional methods of x-ray diffraction and thermogravimetric analysis measured the Pd oxidation rate to estimate the Pd redispersion rate, compared to the more time intensive synchrotron work of Newton *et al*. [34]. The key to this course of research was whether the extent of lean Pd redispersion diminished at each aging duration interval, and to find the Pd size required to achieve rapid PdO formation and significant Pd redispersion.

Chapter 5 examines the changes to Pd dispersion and catalyst activity for samples aged with increasing air pulse duration after the rich step on the redox cycle. The first few hypotheses were tested with samples that were exposed to post-aging treatments of air for 2 hours to restore lost Pd dispersion. However in this plan, a brief lean treatment was used based upon realistic ≈10 second engine fuel shut off events during typical automotive operation to interrupt the deterioration during the redox aging cycle as illustrated in Figure 1-2c. Chapter 4 describes our findings that during a 10 second fuel cut, samples with average Pd size of 8.8nm allowed only 55% Pd oxidation (and redispersion) while samples with average Pd size of 13nm allowed only 37% Pd oxidation. Therefore, this plan periodically interrupted short durations of redox aging with air pulses on the lean step to keep the Pd size small. A fourth hypothesis is that any Pd redispersion gains achieved during the air treatment can be quickly undone by the following rich step of the redox aging cycle. Probe reactions and several characterization methods tested this hypothesis and carefully walked a trajectory of catalyst recovery. The key to this course of research was determining the air pulse length required so that the lean Pd redispersion treatment was as significant when

applied to interrupt short redox aging spans as compared to a two hour post-aging treatment after the 16h continuous redox aging cycle.

1.5 Potential Impact of Research

This research will have the broader impact of aiding the design of future TWC technologies, while also improving the performance and durability of related automotive exhaust catalyst technologies typically rapid aged near 700°C, such as lean NOx traps and hydrocarbon adsorber-catalysts. The results will assist in developing methods to track (or infer) the aging process on the vehicle and either avoid severe aging modes or actively intervene at various points to preserve or regenerate the catalyst, rather than accepting deterioration over time. This project should also have potential for better utilizing existing on-board diagnostic algorithms that currently are limited to identifying failed converter systems. Potentially, these systems can be used in a prognostic mode to provide an early indication of catalyst systems that are showing signs of excessive deactivation, and modifying the engine operation to delay or reverse those trends.

1.6 References

[1] D. Fernandes, A, Neto, M. Cardoso, F. Zotin, "Commercial automotive catalysts: Chemical, structural and catalytic evaluation, before and after aging", *Catal. Today* 133–135 (2008) 574–581

[2] N. Hickey, P. Fornasiero, R. Di Monte, J. Kašpar, J. R. González-Velasco, M. A. Gutiérrez-Ortiz, M. P. González-Marcos, J. M. Gatica, S. Bernal, “Reactivation of aged model Pd/Ce0.68Zr0.32O2 three-way catalyst by high temperature oxidising treatment”, *Chem. Comm*. 1 (2004) 196-197

[3] A. Iglesias-Juez, A. Martínez-Arias, M. Fernández-García, "Metal–promoter interface in Pd/(Ce,Zr)Ox/Al_2O_3 catalysts: effect of thermal aging", *J. Catal.* 221 (2004) 148–161

[4] C. Bozo, F. Gaillard, N. Guilhaume, "Characterization of ceria–zirconia solid solutions after hydrothermal ageing", *Appl. Catal. A: Gen.* 220 (2001) 69–77

[5] J. Cuif, S. Deutsch, M. Marczi, H. Jen, G. Graham, W. Chung, R. McCabe, "High Temperature Stability of Ceria-Zirconia Supported Pd Model Catalysts", *SAE Technical Paper Series*, 980668 (1998)

[6] J. Jiang, X. Pan, G. Graham, R. McCabe, J. Schwank, "Microstructure of a Pd/ceria–zirconia catalyst after high-temperature aging", *Catal. Lett.* 53 (1998) 37–42

[7] G. Graham, H. Jen, W. Chun, R. McCabe, "Encapsulation of Pd particles by ceria–zirconia mixed oxides", *Catal. Lett.* 44 (1997) 185-187

[8] X. Wu, L. Xu, D. Weng, "The thermal stability and catalytic performance of Ce-Zr promoted Rh-Pd/g-Al_2O_3 automotive catalysts", *Appl. Surf. Sci.* 221 (2004) 375–383

[9] J. Kašpar, P. Fornasiero, N. Hickey, "Automotive catalytic converters: current status and some perspectives", *Catal. Today* 77 (2003) 419–449
[10] B. Wang, D. Weng, X. Wu, J. Fan, " Influence of H_2/O_2 redox treatments at different temperatures on Pd-CeO_2 catalyst: Structure and oxygen storage capacity", *Catal. Today* 153 (2010) 111–117
[11] X. Wang, R. Gorte, J. Wagner, "Deactivation Mechanisms for Pd/Ceria during the Water–Gas Shift Reaction", *J. Catal.* 212 (2002) 225–230
[12] Z. Han, J. Wang, H. Yan, M. Shen, J. Wang, W. Wang, M. Yang, "Performance of dynamic oxygen storage capacity, water–gas shift and steam reforming reactions over Pd-only three-way catalysts", *Catal. Today* 158 (2010) 481–489
[13] H. Vidal, J. Kašpar, M. Pijolat, G. Colon, S. Bernal, A. Cordón, V. Perrichon, F. Fally, "Redox behavior of CeO_2–ZrO_2 mixed oxides II. Influence of redox treatments on low surface area catalysts", *Appl. Catal. B: Environ.* 30 (2001) 75–85
[14] E. Mamontov, T. Egami, R. Brezny, M. Koranne, S. Tyagi, "Lattice Defects and Oxygen Storage Capacity of Nanocrystalline Ceria and Ceria-Zirconia", *J. Phys. Chem. B*, 104 (2000) 11110-11116
[15] T. Bunluesin, R. Gorte, G. Graham, "Studies of the water-gas-shift reaction on ceria-supported Pt, Pd, and Rh: implications for oxygen-storage properties", *Appl. Catal. B: Environ.* 15 (1998) 107–l 14
[16] R. Gorte, " Ceria in Catalysis: From Automotive Applications to the Water–Gas Shift Reaction", *AIChE J.,* 56 (2010) 1126-1135
[17] M. Shelef, R. McCabe, "Twenty-five years after introduction of automotive catalysts: what next?", *Catal. Today* 62 (2000) 35–50
[18] C. Bartholomew, "Mechanisms of catalyst deactivation", *Applied Catalysis A: General* 212 (2001) 17–60
[19] A. Datye, Q. Xu, K. Kharas, J. McCarty, "Particle size distributions in heterogeneous catalysts: What do they tell us about the sintering mechanism?", *Catal. Today* 111 (2006) 59–67
[20] R. Goeke, A. Datye, "Model oxide supports for studies of catalyst sintering at elevated temperatures", *Top. Catal.* 46 (2007) 3-9
[21] L. Martín, J. Arranz, O. Prieto, R. Trujillano, M. Holgado, M. Galán, V. Rives, "Simulation three-way catalyst ageing Analysis of two conventional catalyst", *Appl. Catal. B: Environ.* 44 (2003) 41–52
[22] G. Graham, A. Shigapov, "Revised Model of Strain in Ceria-Zirconia Encapsulated Precious-Metal Particles", *Catal. Lett.*, 81 (2002) 253-258
[23] G. Graham, A. O'Neill, A. Chen, "Pd encapsulation in automotive exhaust-gas catalysts", *Appl. Catal. A: Gen.* 252 (2003) 437–445
[24] F. Arosioa, S. Colussib, G. Groppia, A. Trovarelli, "Regeneration of S-poisoned Pd/Al_2O_3 and Pd/CeO_2/Al_2O_3 catalysts for the combustion of methane", *Top. Catal.* 42–43 (2007) 405-408
[25] J. Barbier Jr., D. Duprez, "Steam effects in three-way catalysis", *Appl. Catal. B: Environ.* 4 (1994) 105-140
[26] M. Zhao, M. Shen, J. Wang, W. Wang, "Influence of Pd Morphology and Support Surface Area on Redox Ability of Pd/$Ce_{0.67}Zr_{0.33}O_2$ under CO-He Pulse and Transient CO-O_2 Measurements", *Ind. Eng. Chem. Res.* 46 (2007) 7883-7890
[27] J.J. Chen, E. Ruckenstein, "Role of Interfacial Phenomena in the Behavior of Alumina-Supported Palladium Crystallites in Oxygen", *J. Phys. Chem*. 85 (1981) 1606-1612
[28] E. Ruckenstein, J.J. Chen, "Wetting Phenomena during Alternating Heating in O_2 and H_2 of Supported Metal Crystallites", *J. Coll. Interface Sci*. 86 (1982) 1-11
[29] H. Lieske, J. Völter, "Pd Redispersion by Spreading of PdO in O2 Treated Pd/Al_2O_3", *J. Phys. Chem*. 89 (1985) 1841-1842
[30] M. Peuckert, "XPS Study on Surface and Bulk Palladium Oxide, Its Thermal Stability, and a Comparison with Other Noble Metal Oxides", *J. Phys. Chem*. 89 (1985) 2481-2486
[31] R.J. Farrauto, J.K. Lampert, M.C. Hobson, E.M. Waterman, "Thermal decomposition and reformation of PdO catalysts; support effects" *Appl. Catal. B: Environ*. 6 (1995) 263-270
[32] N.M. Rodriguez, S.G. Oh, R.A. Dalla-Betta, R.T.K. Baker, "In-situ Electron Microscopy Studies of Palladium Supported on Al_2O_3, SiO_2, and ZrO_2 in Oxygen", *J. Catal*., 157 (1995) 676-686
[33] A.K. Datye, J. Bravo, T.R. Nelson, P. Atanasova, M. Lyubovsky, L. Pfefferle, "Catalyst microstructure and methane oxidation reactivity during the Pd-PdO transformation on alumina supports", *Appl. Catal. A: Gen*. 198 (2000) 179–196

[34] M.A. Newton, C. Belver-Coldeira, A. Martínez-Arias, M. Fernández-García, ""Oxidationless" Promotion of Rapid Palladium Redispersion by Oxygen during Redox CO/(NO+O2) Cycling", *Angew. Chem. Int. Ed*. 46 (2007) 8629-8631
[35] E.T. Peterson, A.T. DeLaRiva, S. Lin, R.S. Johnson, H. Guo, J.T. Miller, J.H. Kwak, C.H.F. Peden, B. Kiefer, L.F. Allard, F.H. Ribeiro, A.K. Datye, "Low-temperature carbon monoxide oxidation catalysed by regenerable atomically dispersed palladium on alumina", *Nat. Comm*. 5 (2014) 4885
[36] T.R. Johns, R.S. Goeke, V. Ashbacher, P.C. Thüne, J.W. Niemantsverdriet, B. Kiefer, C.H. Kim, M.P. Balogh, A.K. Datye, "Relating adatom emission to improved durability of Pt–Pd diesel oxidation catalysts", *J. Catal*. 328 (2015) 151-164
[37] S.B. Kang, S.J. Han, S.B. Nam, I.S. Nam, B.K. Cho, C.H. Kim, S.H. Oh, "Effect of Aging Atmosphere on Thermal Sintering of Modern Commercial TWCs", *Top. Catal*. 56 (2013) 298–305
[38] T. Bunluesin, R. Gorte, G. Graham, "CO oxidation for the characterization of reducibility in oxygen storage components of three-way automotive catalysts ", *Appl. Catal. B: Environ.* 14 (1997) 105-115
[39] M. Al-Harbi, W. Epling, A. Yezerets, N. Currier, H. Chen, H. Hess, "The Effects of Thermal Degradation on the Performance of a NO_X Storage/Reduction Catalyst", *SAE Technical Paper Series* 2009-01-0631(2009)
[40] J.A. Lupescu, J.W. Schwank, K.A. Dahlberg, C.Y. Seo, G.B. Fisher, S.L. Peczonczyk, K. Rhodes, M.J. Jagner, L.P. Haack, "Pd Model Catalysts: Effect of Aging Environment and Lean Redispersion", *Appl. Catal. B: Environ*. 183 (2016) 343–360
[41] X. Chen, Y. Cheng, C.Y. Seo, J.W. Schwank, R.W. McCabe, "Aging, re-dispersion, and catalytic oxidation characteristics of model Pd/Al_2O_3 automotive three-way catalysts", *Appl. Catal. B: Environ.* 163 (2015) 499–509
[42] J.A. Lupescu, J.W. Schwank, G.B. Fisher, X. Chen, S.L. Peczonczyk, A.R. Drews, "Pd Model Catalysts: Effect of Aging Duration and Lean Redispersion", *Appl. Catal. B: Environ*. 185 (2016) 189–202

Chapter 2 - Methods

2.1 Rationale for Selection of Experimental Methods

The model catalysts will be subjected to an iterative characterization protocol at various stages of aging and regeneration in order to establish aging-structure-activity relationships. The experimental conditions selected were not those typically used in catalyst research "heat and beat" literature. Typical rapid aging conditions on a dynamometer use inlet temperatures in excess of 1000°C with wide air/fuel fluctuations to produce deterioration that simulates 150,000 miles in mere hours as higher temperatures are used to compress the catalyst deterioration time scale along an Arrhenius relationship. Therefore the results of this study cannot be successfully incorporated into a dynamometer aging environment at 1000°C, but could influence operation under real-world in-use conditions at highway speeds where 700°C is well within the range of operating temperatures. Vehicle emission and temperature data were necessary to confirm the conditions selected were typical of vehicle operating conditions and fuel cut duration. The Pd particle size will need to be known to relate the activity in terms of reaction rate (turnover frequency) and to quantify the extent of Pd redispersion in air. This requires evaluation of a TWC to characterize the Pd particle size in concert with probe reactions to assess the metal-support interface and measure residual catalyst activity, support surface area changes and PdO formation rate. While the Pd model catalysts were provided by a generous supplier with specification sheets regarding their preparation, characterization studies were conducted for confirmation. Established catalyst characterization methods were used including x-ray fluorescence (XRF) for semi-quantification of bulk elemental composition, x-ray diffraction (XRD) for

bulk material phase identification and N_2 physisorption for surface area measurement. The latter two methods are also useful for indicating the deterioration of a sample with aging by comparison to the fresh results.

There is no one technique that can derive the true Pd size on automotive catalyst supports, so a synthesis of multiple, yet limited techniques, were used so that a consistent interpretation could be made. The bulk average Pd particle size will be measured indirectly with H_2 chemisorption and XRD pattern peak fits, and directly with Scanning Transmission Electron Microscopy (STEM) images. Some difficulties in obtaining Pd particle size measurements are as follows: 1) the XRD pattern peaks of small, fresh Pd particles will be too broad and obscured by the support material peaks, 2) the amount of H_2 chemisorbed onto large, aged Pd particles may be too small to be detected apart from the H_2 weakly adsorbed on the support material and 3) Pd and CZO are too similar in atomic mass to achieve a good contrast with STEM to view an unobstructed Pd particle perimeter. Discrepancies with the results of Pd size and dispersion between chemisorption and other characterization techniques may suggest a strong metal support interaction (SMSI), which involves reducible oxides in the support migrating, interacting with and decorating the Pd surface during reducing conditions [1, 2, 3, 4]. CO adsorption onto the surface of supported Pd catalysts during acquisition of infrared spectra has shown capability to identify the accessible Pd facets [5, 6] and provide evidence of reducible oxide coverage of Pd via SMSI [2]. X-ray photoelectron spectroscopy (XPS) can also be used to measure the surface of a catalyst to gather indirect evidence for coverage of the Pd metal by Ce in the support material [7]. Here, we characterize these changes and identify the most severe deactivation modes so that they can be avoided through engine control methods.

It has proven very difficult to find ways to measure the impact of both metal agglomeration and changes in the metal-support interaction through the life of a catalyst. Catalyst activity test results can be confounded by OSC components, as a bifunctional mechanism exists for oxidation due to mobile oxygen that can be drawn out of the support material or gas phase oxygen that can be in the feed stream. Therefore activity tests must be selected to evaluate one functional mechanism while minimizing

the contribution of the other. The use of the WGS and OSC probe reactions meets this requirement as CO oxidation is from oxygen drawn from the support material since gas-phase oxygen is not present in the CO containing feed stream. CO light-off can be used to confirm Pd dispersion results since the 50% oxidation temperature is mostly a function of exposed metal active sites to the gas phase ($CO + O_2$) for a given support material.

The Pd to PdO phase transition was shown by Newton *et al*. to coincide with or followed within seconds by Pd redispersion [8]. If the Pd oxidation rate can be measured, then the Pd redispersion rate can be estimated and used as part of an engine control strategy to optimize the redispersion process. However, Datye *et al*. claimed no Pd redispersion was observed due just to PdO formation after the PdO on alumina had been thermally decomposed to Pd at 900°C and then cooled to room temperature in air [9]. This discrepancy observed by Datye was likely due to the wide temperature hysteresis observed by Faurrauto *et al*. delaying PdO formation [10] until a much lower temperature was reached corresponding to a slower kinetic rate and limited redispersion. PdO decomposition and reformation temperature is often measured with thermogravimetric analysis (TGA) sensitive enough to detect weight fluctuations of a few milligrams. Crystalline phase transitions can also be measured by high temperature XRD with a sample environmental chamber. Both methods will be used to measure PdO formation rates as the Pd/CZO samples will need to be in different initial states: pre-oxidized to avoid support oxygen uptake with TGA and pre-reduced to provide crystalline Pd metal peaks for XRD.

2.2 Preparation of Model TWC Samples

The current state of this Three-Way Catalyst (TWC) converter washcoat technology contains noble metals (Pt, Pd and/or Rh) impregnated onto a complex support material composed of alumina (Al_2O_3) for a high surface area, mixed oxides of ceria and zirconia (CZO) for oxygen storage capacity (OSC) promotion required to continue oxidation reactions during environments deficient in gas phase oxygen, and

rare earth oxides such as lanthana (La_2O_3) to stabilize the alumina surface area against high temperature hydrothermal conditions. Pd is the most common noble metal used on catalytic converters for emissions control of gasoline fuel stoichiometric emissions. Therefore model catalysts of 1.5wt%Pd on relevant support materials of 4wt%La_2O_3-doped γ-Al_2O_3 (Pd/Al) and Pd/ceria-zirconia (Pd/CZO) were selected for this study and were generously prepared at a Ford OEM supplier laboratory by incipient-wetness impregnation of the supports with a palladium solution free from chlorides. These catalysts were calcined at 500°C for 4 hours in an oven with air to fix the metals upon the support materials. One Pd-based model TWC (Pd/TWC) was made from a one-to-one mixture by weight of the fresh Pd/Al and Pd/CZO model powder catalysts as an attempt to simulate a fully formulated automotive TWC. Two additional samples were acquired for comparison, a 1.6wt% Pd on TH 100/150 γ-Al_2O_3 without La_2O_3 from Sasol (Pd/A) was prepared for and described in another work [11] and uncatalyzed $Ce_{0.5}Zr_{0.5}O_2$ (CZO) powder from Solvay (Rhodia). All powders were sieved to obtain particles between 40-60 mesh (250-420 microns) for catalyst samples.

2.3 Procedures for TWC Aging and Regeneration

The initial work on different aging environments leading to different catalyst characteristics was tested with air-fuel aging conditions adopted from prior work with quartz boat powder aging in a flow reactor [12]. Automotive engine operation performs lean/rich switches at a frequency near 1Hz, but adopting that frequency for our work, the full extreme of each redox pulse may not be sufficiently experienced by the entire depth of powder in the quartz boat. At 10 minutes in pulse length, the entire bed of powder was sufficiently exposed to rich and lean environments on each step. A measurement of exhaust gas oxygen concentration commonly used in automotive emissions research is the lambda value, λ or the measured air/fuel ratio normalized to stoichiometric gasoline air/fuel combustion of 14.52.

Equation 1: Lambda, λ = [measured air/fuel ratio] / [14.52]

The initial air-fuel aging gas compositions were: 1) a lean-only composition of 0.5% O_2, 10% H_2O and N_2, 2) a rich-only composition of 0.75% CO, 0.25% H_2, 10% H_2O and N_2, and 3) redox conditions where the lean-only and rich-only feeds were alternated in 10 minute step pulses. The inlet aging gas composition air/fuel fluctuations were measured with a UEGO sensor at $\lambda = 0.97$ for rich-only and $\lambda = 1.03$ for lean-only. The remaining work was tested with a tighter air-fuel modulation to represent operating conditions of an automotive close-coupled catalytic converter. The tight air-fuel aging gas compositions were: 1) a lean-only composition of 0.1% O_2, 10% H_2O and N_2, 2) a rich-only composition of 0.15% CO, 0.05% H_2, 10% H_2O and N_2, and 3) redox conditions where the lean-only and rich-only feeds were alternated in 10 minute step pulses. These air/fuel fluctuations were measured with a UEGO sensor to a $\lambda = 0.992$ for rich-only and $\lambda = 1.008$ for lean-only.

Catalyst aging environments were established in a continuous flow reactor shown in Figure 2-1 at 700°C for 16 hours to represent the conditions of an automotive TWC, similar to an in-use drive cycle at the engine-out location or a high temperature durability dynamometer cycle at the underbody location. The gas feed was controlled with a Matheson dynablender and flow controllers to 3 L/min. Most of the stainless steel tubing was wrapped with heating tape (red lines) and maintained at 150ºC to prevent condensation of water. The resulting gas space velocity through the sample was 25000 hr^{-1}. Solenoids were placed before and after the reaction chamber to direct the gases either to the sample or to the bypass line. Flow leaving the downstream solenoid was evenly split off to two sets of analyzer benches. One stream was diluted with 2 L/min of nitrogen, mixed in a 4ft long x ¾ inch OD heated tube and sent to an MKS Fourier Transform Infra-Red (FTIR) analyzer. The other stream was diluted with 11 L/min of nitrogen, mixed in a 4ft long x 5/8 inch OD tube and a sample was pumped to the FID/O_2 gas analyzer bench with the rest going to vent. Instrument signals from the various analyzers were acquired at a 1 Hz rate. The CO gas stream was scrubbed of iron carbonyls with a 20 inch long ¾ inch diameter column of zeolite 5A beads of 4-8 mesh size heated to 350°C. A stacked solenoid set was configured with one gas stream of CO (gas A) or O_2/N_2 (gas B) injected into the reactor feed gas stream while the other gas was vented with a pressure restriction to provide a square injection pulse

during switching. Another identical stacked solenoid set was downstream of the first set with gas A as the aging gas composition and gas B was dry air. A round bottomed quartz boat measured 100 mm long, 17 mm wide and 5mm tall was loaded with 1.50 g of catalyst powder and placed inside a 19 mm ID quartz reaction tube in the heating zone of the surrounding oven with a 1/16 inch diameter thermocouple placed over the boat in the aging gas stream and a 1/32 inch diameter thermocouple bent into the boat with the tip buried in the powder. After loading the boat into the reactor tube, the samples were heated in nitrogen to 700°C as measured by the powder thermocouple, and then the desired aging environment was introduced for 16 hours. The cycle was ended on the rich step for the redox cycle. The redox and rich-only aged samples were each divided into 0.50 g portions and two portions were reserved for one of two levels of lean Pd redispersion treatments at 550°C or 700°C for 2 hours made of dry air or 21% O_2 in helium. Compressed air at 700°C was applied to the catalyst substituting for a portion (x) of the 10 minute lean pulse for 1/6, 1, 2 or 10 minutes (simulated fuel cuts). A schematic of the redox aging is shown in Figure 2-1 with the typical 10 minute pulse cycling over 20 minutes and an optional air pulse beginning at the end of the rich pulse in each cycle. A 1/6 minute fuel cut is similar in length to an actual engine fuel cut when a vehicle slows down from highway speed. Longer fuel cuts in the range of 1 minute and all the way up to 10 minutes (a complete replacement of the lean step for air) were performed in order to investigate the minimum length required to redisperse the Pd or remove the SMSI effects on each support.

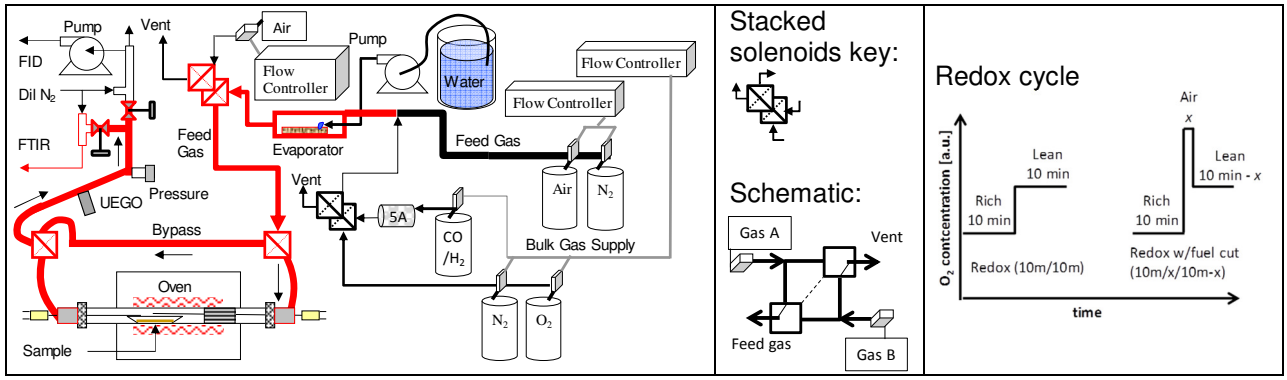

Figure 2-1: Powder Aging Reactor Schematic

After catalyst aging or lean redispersion treatments, the samples were cooled

down to 350°C in nitrogen. Once stabilized for 10 minutes, the sample was exposed to 0.75% CO, 0.25% H_2 in N_2 for 1 hour. This environment provided a mild reduction of the sample, which was below what is reported in the literature to sinter Pd [13], so that Pd would be in the metallic state and at the size caused by the aging environment.

2.4 Procedures for Sample Characterization

2.4.1 X-ray Fluorescence Spectroscopy

The bulk elemental compositions of the fresh model catalyst samples were confirmed by X-ray Fluorescence (XRF) spectroscopy. XRF involves the bombardment of a sample by a broad spectrum of X-rays. An inner shell electron of an atom in the material can be ejected when it is struck by an incident X-ray photon with energy greater than the electron's binding energy. Fluorescence occurs when an outer shell electron transitions to fill the inner shell vacancy and the surplus energy is released in the form of an X-ray photon. The energy of the emitted X-ray photon will be equal to the difference between inner shell and outer shell electron energy levels, and thus is characteristic of the element. The various wavelengths of X-rays emitted from the sample are separated using crystals and applying Bragg's law as shown below in Equation 2 [14].

Equation 2: $\lambda = 2d \sin\theta$

In wavelength dispersive X-ray spectroscopy (WDS), Bragg's Law can be interpreted as XRF crystals with known interplanar spacing, d, are used to determine the wavelengths λ of X-rays being emitted by the sample through the rotated crystal angle, θ, as shown in Figure 2-2 below. The X-ray tube is the source of incident X-rays that irradiate the sample, causing the atoms in the sample to emit characteristic X-rays. X-ray tubes contain a tungsten filament (cathode) and metal target (anode). When the X-ray tube is energized, a current is run through the filament and a high voltage is applied to the target. This causes electrons emitted by the filament to accelerate and strike the target. Energy lost by the electrons impacting the metal target

produces a broad spectrum of X-rays called bremsstrahlung. A fraction of the electrons hitting the target also produces the emission of X-rays characteristic of the target metal. The most common X-ray tube target metals used for XRF are Rh, Au, Mo and Cr. The characteristic X-ray spectrum of Rh interferes with quantification of Pd and Rh that are common to three-way catalyst samples, so a Cr target X-ray tube was used instead. Crystals are placed between the sample and the detectors. For full-spectrum scan, each crystal is rotated with a very small step size producing a plot of X-ray intensity versus wavelength. For faster quantitative analysis the crystal is rotated to the known 2θ position for each element of interest and held there for sufficient time to determine the count rate. Further, the correlation between the concentration of an element in a sample and the intensity of characteristic X-ray emissions can be used for quantification.

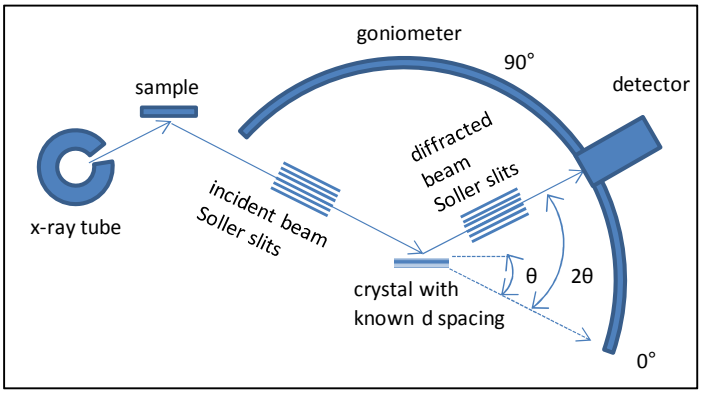

Figure 2-2: X-ray Fluorescence Spectrometer Schematic

All the XRF work of sample preparation, equipment operation and data analysis was performed by Mark Jagner at Ford Motor Company. The equipment used was a PANalytical PW2400 WDS XRF Spectrometer equipped with a Cr target X-ray tube as the excitation source. X-ray tube power of 60 kV/40 mA was used for wavelengths shorter than 2 Å, and 40 kV/60 mA for wavelengths longer than 2Å. A 200 µm Al tube filter was used for the portion of the spectrum in the vicinity of the Cr K lines. Qualitative and semi-quantitative XRF analyses were conducted using the UniQuant5 program. UniQuant5 is a fundamental parameters quantitative analysis program that uses intrinsic sensitivity factors derived from high purity single-element and single-compound reference materials. Pd was quantified using the Lα1 X-ray line which gave

better results than the Kα1 X-ray line using UniQuant5 for these samples. The estimated relative error for Pd quantification is expected to be in the range of +/- 10% to +/- 20%, although the accuracy has not been verified with known reference materials prepared in the same manner. Specimens were prepared by placing approximately 700 mg samples of each powder on top of 4.5 g of boric acid in aluminum caps and compacting them into 31 mm diameter pellets using a hydraulic press.

2.4.2 N_2 Physisorption

Surface area analysis was determined by N_2 physisorption onto the clean surface of the catalyst samples. The origins of this technique go back to Langmuir theory for gas adsorption onto a solid. The key assumptions are: infinite layers at saturation, one site per molecule, physical adsorption only - no interactions in the gas layer or with the surface, Arrhenius law for molecule desorption and similarities to each adsorbed gas layer. The Brunauer-Emmett-Teller (BET) method was used to calculate surface area in m^2/g of sample [15]. Equation 3 below is the classis BET equation where the parameters are: P = equilibrium pressure of N_2, P_o = saturation pressure of N_2, v = adsorbed N_2 volume, v_m = volume of monolayer, E_1 = heat of adsorption of N_2 at the sample surface and to E_L = heat of adsorption of N_2 on N_2, R = universal gas constant and T = N_2 adsorption temperature. Equation 4 is for the total BET surface area where the parameters are: N_{Avg} = Avogadro's number, A_{CS} = N_2 cross sectional area, v_m = volume of monolayer, m_s = mass of sample and V_m = molar volume of N_2. Equation 3 is solved by acquiring the adsorbed N_2 volume across the adsorption pressure ranges of N_2, then plotting the data as in Figure 2-3 below to find the slope m and intercept b, which are needed to solve v_m in equation 3.

Equation 3:

$$\frac{1}{v\cdot\left(\left(P_o/P\right)-1\right)}=\frac{c-1}{v_m\cdot c}\left(\frac{P}{P_o}\right)+\frac{1}{v_m\cdot c}$$

$$c=\exp\left(\frac{E_1-E_L}{RT}\right)$$

Equation 4:

$$\mathrm{BET}=\frac{(N_{Avg}\cdot A_{CS}\cdot v_m)}{(m_s\cdot V_m)}$$

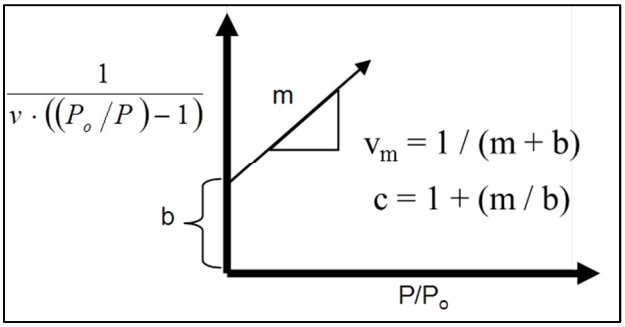

Figure 2-3: Solution for the BET equation

The BET specific surface area, pore volume, and pore size distribution were determined with a Micromeritics ASAP2420 instrument. Samples were placed in a pyrex container of known weight and were heated and evacuated of all deposited surface gas with a vacuum pump. The sample container with sample was weighted again to determine the clean sample mass. The sample container was later immersed in a liquid N_2 bath at 77K while N_2 gas is deposited onto the sample surface by control of the partial pressure. A 48-point adsorption and 33-point desorption isotherm plot was generated across a range of 0.1-0.9 P/P_0 to generate a plot of adsorbed N_2 volume versus pressure P/P_0 ratio.

2.4.3 X-ray Photoelectron Spectroscopy

The surface elemental compositions of the fresh model catalysts were evaluated by X-ray Photoelectron Spectroscopy (XPS). XPS involves the bombardment of a sample by a high speed electron source under ultra-high vacuum while measuring the x-rays, kinetic energy and number of electrons that escape from the top 0 to 10 nm of the sample. Since the incident or source x-ray photon energy (hv) is known, and the kinetic energies (E_K) of the emitted electrons are measured, the electron binding energy (E_B) of each emitted electron can be determined by the Equation 5 below for XPS based on work by Ernest Rutherford in 1914 [16].

Equation 5: $E_B = hv - E_K - \Phi_{CF}$, where Φ_{CF} is an instrument correction factor

The electron binding energy, or ionization energy, is the energy required to remove the most loosely bound electron from its orbital. The elements present in the

sample produce a characteristic set of peaks corresponding to the configuration of their orbital electrons (i.e., 3p, 3d). The signal intensity (I), or number of detected electrons, can be divided by an atomic sensitivity factor (F) specific to that element to get the atomic concentration of that element on the sample surface. For a material with n components, the atomic fraction of an element (A) can be estimated using the following equation below:

Equation 6: $A\ [\text{atom \%}] = (I_A/F_A) / \Sigma(I_n/F_n)$.

All the XPS work of sample preparation, equipment operation and data analysis was performed by Sabrina Peczonczyk at Ford Motor Company. Elemental composition and chemical state information were determined using a Kratos AXIS 165 Electron Spectrometer. The base pressure of the spectrometer was 2×10^{-9} Torr. Photoelectrons were generated using a monochromatic Al Kα (1486.6 eV) X-ray excitation source operated at 12 kV, 20 mA (240 W), and collected using hybrid mode magnification. Pass energies of 80 eV or 20 eV were used to collect survey or high resolution spectra, respectively. All spectra were acquired using charge neutralization with an electron flood source. Elemental quantification of the high resolution spectra was accomplished using CASAXPS software Version 2.3.16, using routines based on Scofield photoionization cross-section values. A Shirley type background was used to fit all high resolution spectra. For Pd on alumina support the high resolution Pd 3d spectra was fit with a doublet using 60% Gaussian and 40% Lorentzian line shapes with an area ratio of 0.667, a full width at half-maximum (FWHM) constrained within 0.6-2.8, and a peak separation of 5.2 eV. For Pd on CZO support the minor Pd 3d peaks are sandwiched between the substantially larger Zr 3p core level peaks. In order to deconvolute the Pd 3d peaks from the spectral envelope, the Zr 3p fit was first determined from a CZO standard using 60% Gaussian and 40% Lorentzian line shapes with an area ratio of 0.5, a FWHM constrained between 0.6-2.8, and a peak separation of 13.4 eV. The remaining area under the envelope was then fit by adding Pd 3d peaks using the fitting parameters described above for Pd on alumina. This semi-quantitative analysis technique has an estimated error for elemental quantification is expected to be in the range of +/- 10%. Binding energies were referenced to the aliphatic C 1s peak at

284.6 eV [16]. Samples were received in the reduced state, exposed to room air, pressed into a pellet and then mounted onto sticky double sided pressure sensitive adhesive tape.

2.4.4 Diffuse Reflectance Infrared Fourier Transform Spectroscopy

Diffuse Reflectance Infrared Fourier Transform Spectroscopy (DRIFTS) is a technique that involves directing infrared light onto the surface of a powder sample, then that light is reflected and diffused at different directions, and collected by the use of a mirror into a spectrometer. The infrared light energy is only sufficient to excite molecular movement between vibrational states of the surface molecules. The vibrations of the entire molecule produce a characteristic spectrum that can be used to identify bending and stretching of functional groups. This technique has been around for decades and vibrational spectra peaks characteristic to CO adsorption onto ceria, single Pd crystals and supported Pd particles are well studied [17, 18, 19, 20]. Unknown molecules on the sample surface can be qualitatively identified by the functional groups found in the infrared spectra compared against literature values of known gas phase adsorbants on known materials. Known molecules adsorbed onto a known powder sample surface can be used to identify accessible active metal sites as well as spectator species that do not disappear from the surface during reaction conditions. CO in the gas phase exhibits spectra peaks starting at 2050 cm^{-1} through 2200 cm^{-1}. CO generally adsorbs with the carbon end attached to the metal adsorption site. Exchange of electrons between CO and the metal forms a strong bond and polarizes the molecule, shifting the spectra frequency lower. CO-Pd bond peaks are near a frequency of 1800-2000cm^{-1}.

DRIFTS was conducted with a Nicolet 6700 FTIR spectrometer with Auxiliary Experiment Module including a praying mantis cell to facilitate gas exchange to and heating of the sample. Fine powder catalyst samples recovered from the XRD analysis were poured into the praying mantis sample cup onto a supporting screen. Clean samples were prepared as follows: 1) 25% H_2 in nitrogen fed to the sample for 16 hours at 400°C, 2) switched to 1% O_2 in nitrogen carrier gas to burn off saturated carbonate

and formate surface species for an hour, 3) switched off O_2 and heated the sample cell to 600°C for one hour in nitrogen-only to decompose surface PdO, 4) sample was cooled to 22°C and stabilized over one hour. The IR spectra were collected with 64 scans at a resolution of 2 cm^{-1} in repeating loops every two minutes. A clean sample background was acquired first under flowing nitrogen then 1% CO was added to saturate the surface through two hours.

2.4.5 X-ray Diffraction

Support phase identification was measured with X-ray diffraction (XRD) pattern analysis. XRD involves the bombardment of a crystalline sample by a focused X-ray source, while measuring the diffracted beams off of the sample at various angles relative to the incident beam angle. Atoms in the crystal alter the path length of incident X-rays leading to a difference in phase. The diffracted beam in an ordered crystal is composed of a large number of scattered rays that are in-phase with each other and reinforce one another to increase the wave intensity or amplitude and produce strong peaks. The diffracted beam in an amorphous material made of atoms arranged randomly causes scattering in all directions and produce weak peaks. If a monochromatic X-ray source beam has a known wavelength λ, the number of wavelengths in the path difference between rays scattered by adjacent planes is n, the measured crystals have planes spaced at a characteristic distance d' apart, and the incident angle of the X-ray on the crystal is θ, just first order reflections are considered and spaced at a distance of 1/n from the previous spacing to set d = d'/n, then Equation 2 can also be used for XRD sample analysis [14]. Bragg's Law can be interpreted as at certain measured angles θ for a known wavelength λ, the plane spacing d of an unknown sample crystal may be measured as shown in Figure 2-4 below. The sample position is initialized at θ=0°, which is at the same angle as the incident X-rays, then rotates through the angles on the goniometer, producing a plot of X-ray intensity versus angles, 2θ, of the rotating sample relative to the detector. The measured plot can then be compared to characteristic intensity peaks at 2θ locations for known materials to identify phases present in the unknown sample.

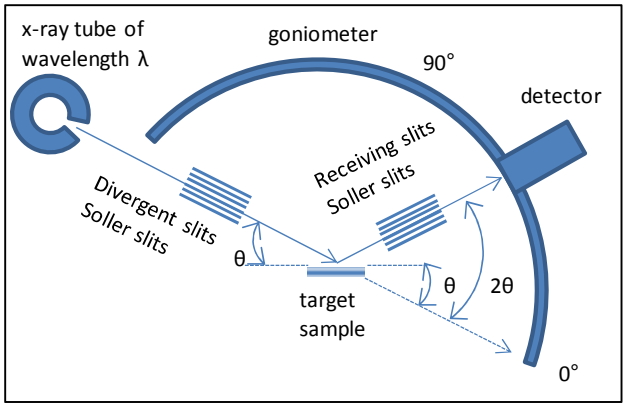

Figure 2-4: X-ray Diffractometer Schematic

The instrument used for phase identification and measurement of mean Pd crystalline length was a Rigaku Miniflex II diffractometer with CuKα X-Ray radiation source set at 30 kV and 15 mA. A catalyst sample mass of 0.1 g was wet-milled with a mortar and pestle in ethanol then pipetted onto a quartz slide and allowed to dry. Scans were performed with a step size of 0.005°2θ at a scan speed of 1°2θ/min.

2.5 Procedures for Pd Particle Size Characterizations

2.5.1 H_2 Chemisorption

Bulk average Pd particle diameter and dispersion was primarily determined by H_2 chemisorption. This technique is based on injecting a known quantity of H_2 adsorptive gas at a fixed temperature to the clean surface of a sample and onto the exposed active metal surface. The results generate a Langmuir isotherm with increasing H_2 pressure on the x-axis and adsorbed H_2 quantity as the y-axis. A strong chemical bond between H_2 and the active metal (chemisorption) only occurs on the first layer of deposited H_2 in direct contact with the active metal, while the remaining adsorbed H_2 will form weak bonds (physisorption) on inert support materials not of interest. At the fixed isotherm temperature under vacuum, the strong bonds are generally irreversible, while the weak bonds are reversible. An evacuation at 35°C will remove the physisorbed H_2 while raising the temperature to 350°C will remove the chemisorbed H_2. The difference in chemisorbed and physisorbed H_2 quantity in the first isotherm test can be distinguished

by running a second isotherm test after an evacuation as the chemisorbed H_2 would still be in direct contact with the active metal and lower the total adsorbed H_2 quantity during the second test. Subtracting the different adsorbed H_2 isotherm between the two tests yields the chemisorbed H_2 quantity isotherm. The plateau of the chemisorbed H_2 quantity isotherm can be extrapolated back to the y-axis to yield the monolayer coverage, V_s [L]. The hydrogen adsorption stoichiometry, *f*, used the well-established value of 1 [21], for one adsorbed H atom per every one surface Pd atom. After the sample is degassed and reduced, the total sample weight can be measured, m_{cat} [g]. Equation 7 was used to determine the bulk average dispersion of the Pd particles, D_{Pd} [%], then equation 8 can be used to find the bulk average Pd metal size, d [nm], which is described further by Baylet et al. assuming spherical Pd particles [22]

Equation 7: D_{Pd} [%] = 100 x $\left[\frac{(V_S \times f)}{(X_{Pd} \times m_{cat} \times 22.414\ L/mole)}\right]$ x M_{Pd}

Equation 8: d [nm] = (6 x 10^5) * (M_{Pd}) / (ρ_{Pd}* S_{Pd} * D_{Pd} [%])

where m_{Pd} is the palladium atomic mass of Pd at 106.42 g/mol, X_{Pd} is the known weight percent of Pd on the sample, the palladium density, ρ_{Pd} is 12 g/cm^3, and the palladium metal molar surface area assuming an equidistribution of the low index faces, S_{Pd} is 47,780 m^2/mol.

A Micromeritics ASAP2020 instrument with a static volumetric chemisorption method with two isotherms was used to perform H_2 chemisorption. The quartz j-tube side that held the catalyst sample measured 12.8 mm (½ inch) OD and 10.5 mm ID, while the other side was 6.4 mm (¼ inch) OD and 2.4 mm ID. A catalyst sample mass of 300 mg was loaded between 6 mm redistributing layers of quartz wool above the widening neck of the ½ inch OD j-tube. The bed height for each catalyst support was 4 mm for the Pd/CZO and 6 mm for Pd/Al. The sample was degassed in N_2 at 500°C then cooled down under vacuum to 1 microtorr prior to evaluation. The sample was reduced at 350°C in 1 atm H_2, then exposed to vacuum at 1 microtorr and 350°C to remove Pd hydride prior to H_2 chemisorption measurements at 35°C. These conditions were assumed not to sinter Pd particles supported on CZO or La_2O_3-Al_2O_3, since 400°C

in 1 atm H_2 is known not to sinter Pd particles supported on SiO_2 or Al_2O_3 [21]. Consecutive 5-point adsorption isotherm plots were generated across a range of 140 mmHg to 280mmHg. The differential results of adsorbed H_2 mmol/g versus pressure were used to separate physisorbed H_2 on the support from chemisorbed H_2 on the Pd metal.

2.5.2 X-ray Diffraction

Post-process curve fitting of the XRD pattern was performed with the Rigaku PDXL software program. A LaB6 calibration standard corrected the instrument broadening on the measured Bragg angle and peak width. The Pd peak location was isolated in the XRD pattern at 40°2θ for Pd/CZO and Pd/TWC samples, and 82°2θ for Pd/Al and Pd/A samples. The Pd peak shape was fit with a split pseudo Voigt normalized line profile and the background pattern was refined. The software used equation 9 below, known as the Scherrer equation, for estimating mean Pd crystalline length (L) from measured XRD pattern peak breadth (B) found at Bragg angle θ [23]. For this work, the CuKα X-Ray radiation source wavelength (λ) was 1.5406Å, the shape factor (K) used was 0.89 for spherical crystallites and the peak integral method was used to determine peak breadth.

Equation 9: $L = (K \lambda) / (B \cos \theta)$

Pd particles crystallite length within the size range in the literature of 2-33 nm is often synonymous with Pd particle size, as other works presented electron microscopy and chemisorption for confirmation [24, 25, 26, 27, 28]. Note that crystallite length can be smaller than particle size if large particles are made of agglomerated crystals of if any poorly crystalline regions exist in the particle.

The Pd dispersion results derived by XRD line broadening represents the ideal case where the entire volume of bulk Pd crystallites are exposed and located on top of the support material. A metal dispersion value using the Pd size from XRD measurement has meaning only if the Pd particles were not covered by support material. It is therefore useful to check XRD Pd size against that measured by H_2

chemisorption when suspecting coverage of Pd by a reducible oxide in the support material. Equation 8 used for H_2 chemisorption can be rewritten as equation 10 below to solve for dispersion and use the bulk average crystalline length, L [nm], from XRD analysis, as an estimate for the average Pd particle diameter.

Equation 10: D_{Pd} [%] = (6 x 10^5) * (M_{Pd}) / (ρ_{Pd}* S_{Pd} * L)

2.5.3 Electron Microscopy

The scanning transmission electron microscope (STEM) technique involves use of a focused electron beam targeting a thin sample mounted on a carbon grid under ultra-high vacuum. The electron source has a wavelength less than 0.3 nm and is used for illumination rather than visible light used in optical microscopes that has a wavelength of 400-700 nm. The smaller wavelength of the electrons enables them to either 1) pass between the sample atoms and transmit through or 2) interact with the target sample atoms and scatter. A transmitted signal is generated as the electrons pass through the sample atoms that is magnified and focused onto a camera for image capture. The camera image contrast is due to the adsorption of electrons by the sample material, which is affected by the material thickness and elemental composition. A scattered signal is generated by electrons scattered weakly or strongly based on the strength of the elastic interactions between the incident electron beam and the target sample. The electrons that are scattered and deflected more than 1° away from the electron beam path are counted with an annular collector, while the rest are considered part of the focused electron beam transmission that proceeds towards the camera. The high angle annular dark field (HAADF) detector composition contrast avoids structure sensitive effects and is directly related to the atomic number of the elements, which is known as the z-contrast [29]. The heavy atom planes that scatter electrons are directly imaged as bright areas while lighter atom planes that transmit electrons are directly imaged as dark areas. Planes that are evenly spaced scatter at the same angle and provide constructive interference as with XRD. The camera and annular detector data are acquired simultaneously allowing direct correlation between the camera image and scattered signals. Alternatively, a bright field image is the inverse of a dark field image.

Pd particle size measurements were performed by Kevin Dahlberg and Chang Yup Seo using HAADF imaging with a JEOL 2010F Probe-Corrected Analytical Electron Microscope set at 200 kV. The microscope was equipped with a zirconated tungsten [100] thermal field emission tip filament and operated at 1.5x10-7 torr vacuum with 200kV accelerating voltage. The JEOL HAADF detector had a probe size of 0.5 nm and camera length of 12 cm. This instrument has a resolution of 0.1 nm. Samples for imaging were prepared by dispersing 10mg of catalyst sample powder in 2 mL of ethanol followed by ultrasonification for one hour to make a suspension. The catalyst was mounted onto a 200-mesh carbon coated copper grid by applying one or two drops of the ethanol suspension onto the grid and then dried. The STEM image processing was carried out with Image J software. The scale bar on the uploaded Image J file was used to calibrate the image for pixels/nm. After calibration, the Freehand Area Selection tool was used to draw boundaries around bright edges of each palladium particle. Area of the particle within the boundary was calculated by Image J software. The diameter was calculated with an assumption that each palladium particle was a sphere.

The sizes of metal particles are frequently compared to values obtained by multiple characterization methods. STEM images of metal particles with diameter, d_i, and the number of particles of a particular diameter, n_i, can be simply reported as a numerical average in equation 11. However, the metal particle diameter evaluated by chemisorption is calculated by surface area analysis and XRD by volume weighted particle length. The STEM image particle data can be calculated as a surface-averaged diameter to compare against H_2 chemisorption results using equation 12 and a volume-averaged diameter to compare against XRD results using equation 13 [27].

Equation 11:	Equation 12:	Equation 13:
Number-Average	Surface-Average	Volume-Average
$d_n = \Sigma n_i d_i / \Sigma n_i$	$d_s = \Sigma n_i d_i^3 / \Sigma n_i d_i^2$	$d_v = \Sigma n_i d_i^4 / \Sigma n_i d_i^3$

Equation 14 was used to solve for Pd dispersion with the appropriate STEM image particle diameter found in the equations above.

Equation 14: D_{Pd} [%] = (6 x 10^5) * (M_{Pd}) / (ρ_{Pd}* S_{Pd} * d [nm])

2.6 Procedures for Catalyst Activity Tests

2.6.1 Flow Reactor

A flow reactor was used to enable measurement of CO_2 formed by selected probe reaction tests on a characterized catalyst sample. The ASAP2020 quartz j-tube, quartz spacer tube, quartz wool and powder sample used in the H_2 chemisorption test described above in section 2.5.1 was fit onto this flow reactor as shown in Figure 2-5. Matheson dynablenders and flow controllers managed the gas flow through the system. A pyrex water bubbler was used to supply a stable stream of water vapor by saturating the room temperature bulk gas stream. A solenoid set could be triggered to bypass the bulk gas around the water bubbler. The parts downstream of the water bubbler were stainless steel and wrapped in heat tape maintained at 150°C to limit condensation. Two o-ring adapter fittings were attached on one end to the ¼ and ½ inch OD j-tube ends and the other ends were connected to two corresponding bulkhead fittings that in turn were suspended by a fixed bracket attached above the oven that held up the j-tube at a fixed location inside the oven. The CO gas stream was fed through a column of gamma alumina pellets heated at 350°C to remove iron carbonyls before connecting to the microvalve. The bulk gas feed was sent to the top of a ¼ inch cross fitting. The sides of the cross fitting were adapters for 1/16 inch pipes from microvalves connected to the CO/Ar or O_2/Ar feeds. Each 1/16 inch pipe ran through the ¼ inch adapter fitting and was bent down to inject the gas co-currently into the bulk gas feed. At the bottom of the cross fitting was a solenoid set to bypass the j-tube. Two K-type 1/32-inch diameter thermocouples were placed 16 mm before and 13 mm after the sample bed. A Hiden HPR20 quadrupole electron ionization mass spectrometer, pressure sensor and Horiba lambda sensor were used to sample the gas stream downstream of the j-tube. The HPR20 SEM detector measured five mass values with a 2 Hz sampling rate at an inlet sampling pressure of 1E-5 torr. Two separate measurement configurations were used for OSC and WGS experiments, and each required two corrections. First,

the double excitation Argon mass 20 value was scanned, which is 11% of the total Argon level, rather than the typical mass 40 to get the measured Argon value below the SEM detector limit of 1E-6 torr. Second, there was a CO and CO_2 mass overlap of 11.4%, so that amount of the CO_2 value was subtracted from the CO value during data processing. Multiple OSC and WGS tests were run to determine whether the results drifted with changes to the sample caused by exposure to the gas stream at 400°C. At least three OSC and WGS measurements were run on all samples. The last run was usually selected for comparison to the other sample aging conditions.

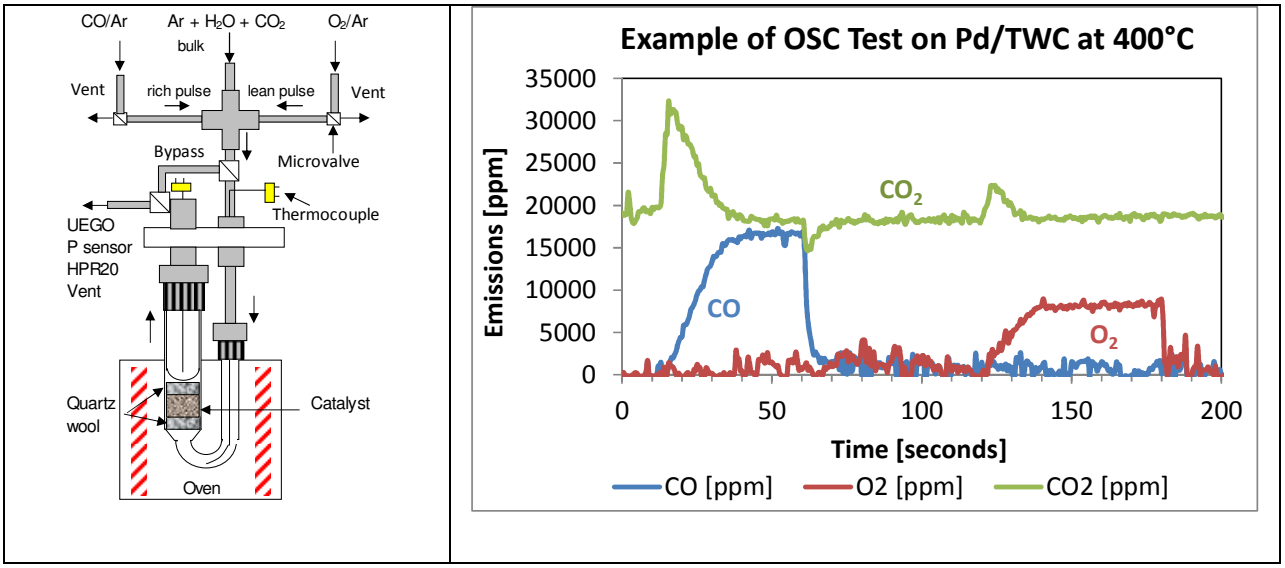

Figure 2-5: Flow reactor schematic and example of an OSC Test

Gasoline engines operate about stoichiometry so the catalyst OSC state is partly depleted. Therefore, all activity measurements began with the samples in a reduced state. The sample was exposed to 9% H_2 in Argon at 300°C for 30 minutes flowing at 0.22 L/min to remove the surface oxygen. The sample was then cooled down in Argon to room temperature.

2.6.2 Oxygen Storage Capacity Measurement

The OSC measurement involves alternating step pulses of gas phase reactant (CO) to an oxidized catalyst sample to generate CO_2 later followed by support regeneration (O_2) over a catalyst sample. The CO_2 yield in micromoles is then

quantified at fixed temperatures per catalyst mass. The CO pulse oxidation mechanism pathway generally proceeds with reactions 1, 4 and 5 below, while the O_2 pulse regeneration pathway includes reactions 2, 3 and 6 below [30].

1. $CO + site \leftrightarrow CO_{ad}$ (equilibrium)
2. $O_2 + site \rightarrow O_{2,ad}$ (rate limiting)
3. $O_{2,ad} + site \rightarrow 2O_{ad}$ (fast)
4. $O_{ad} + CO_{ad} \rightarrow CO_2 + 2\ sites$ (fast)
5. $2CeO_2 \rightarrow O_{ad} + Ce_2O_3$
6. $Ce_2O_3 + ½O_2 \rightarrow CeO_2$
7. $Ce_2O_3 + H_2O \rightarrow CeO_2 + H_2$

For catalysts without OSC materials (i.e., Pd/Al_2O_3), CO oxidation is generally accepted to proceed along reactions 1-4 in excess CO (ignoring metal oxides) where the reaction rate is limited by the strong adsorption of CO and lack of sites on the metal for oxygen to adsorb. For catalysts with OSC materials (i.e., Pd/CZO), a free site on the metal for oxygen adsorption is not the limiting step as oxygen can migrate from the support to the metal interface for oxidation according to the proposed reaction 5. The support lattice oxygen is replenished mostly by exhaust gas oxygen in fuel-lean exhaust according to reaction 6 or by water disassociation in fuel-rich exhaust according to reaction 7. However, oxygen transport mechanisms in automotive TWC technologies are not completely understood, and ceria reduction by H_2 and CO along with OSC regeneration by H_2O and CO_2 suggest that reactions 4, 5 and 7 may be equilibrium relations rather than simply kinetically controlled [31]. Because of the complexity of these issues it is most practical to consider model TWC samples in our study to deconvolute the reactions and deactivation mechanisms.

The catalyst OSC metric was defined by Yao as the amount of oxygen uptake at equilibrium for the reaction conditions used [32]. An OSC model based on CO uptake was developed by Holmgren et al. for Pt/ceria catalysts that included the total surface area of the catalyst and the perimeter of the metal particles as key parameters, which was found to contribute equally to the total measured OSC data at 400°C using regression analysis [17]. Nibbelke *et al*. conducted an OSC experiment with a Pt-Rh TWC catalyst and achieved a good model fit of the CO oxidation results by identifying the initial reaction path as gas phase CO undergoing a surface reaction with pre-

adsorbed oxygen on the catalyst metal site to form CO_2, which is related to the size of the catalyst metal particles [33]. Therefore the determination of the OSC reaction rate as a function of temperature can be calculated based on the initial rise of the CO_2 production from the pulse of CO as in reaction 4 [34].

OSC measurements were carried out by the conventional pulse method of alternating one minute lean or rich, each separated by a one minute purge as shown in Figure 2-5. The purge pulse was just the constant bulk carrier gas of CO_2 and Argon at 975 mL/min while microvalves added a square step pulse of CO or O_2 into the carrier gas at 25 mL/min. The bulk flow with lean pulse was 1% O_2, 2% CO_2 and balance Ar. The bulk flow with rich pulse was 2% CO, 2% CO_2 and balance Ar. The gas mixture was initially established at equilibrium over the catalyst sample at 50°C. At least five CO pulses were measured at a fixed oven temperature before increasing the heating set point to the next 50°C increment, to a maximum set point of 400°C.

2.6.3 Water-Gas Shift Measurement

The OSC and WGS catalyst activity tests share the CO oxidation mechanism where adsorbed CO reacts with oxygen from the support or metal surface. The difference between OSC and CO light-off versus WGS is the support reoxidation step (i.e., directly via O_2 for OSC and via H_2O for WGS). The WGS reaction on an inert alumina support with Pd is simply: $CO + H_2O \rightarrow CO_2 + H_2$. However, Ceria-based OSC components provide oxygen to metal sites and promote two reaction mechanisms for $CO \rightarrow CO_2$ as shown in Figure 2-6 reprinted from an article by Kalamaras *et al*. [35]. The WGS reduction and oxidation (redox) mechanism pathway (route A in Figure 2-6) generally proceeds with the reaction mechanisms below along the metal-support interface:

8. $CO + site \leftrightarrow CO_{ad}$ (equilibrium)
9. $2CeO_2 \rightarrow O_{ad} + Ce_2O_3$
10. $O_{ad} + CO_{ad} \rightarrow CO_2 + 2$ sites
11. $Ce_2O_3 + H_2O \rightarrow CeO_2 + H_2$

Reaction 8 involves just one site, so the WGS reaction is considered insensitive to catalyst structure. Reaction 10 occurs at the metal-support interface, so the WGS reaction is considered sensitive to interfacial area, which is related to the size of the catalyst metal particles. The WGS associative formate mechanism pathway (route C in Figure 2-6) generally proceeds with reaction intermediates along the metal-support interface suggesting that the reaction mechanisms 8-11 are incomplete. Attempts to determine reaction kinetics with Fourier-Transform Infrared (FTIR) spectroscopy were unable to determine the role of the reaction intermediates [36]. The deterioration of the WGS reaction rate has been shown to have a linear relationship with the decline of metal surface area, which is measured by the catalyst metal dispersion [37]. The determination of the WGS reaction rate as a function of temperature can be calculated based on the CO conversion efficiency to CO_2 [38]. Running the WGS experiment with less than excess water can generate unwanted side reactions such as methane and carbon formation [39].

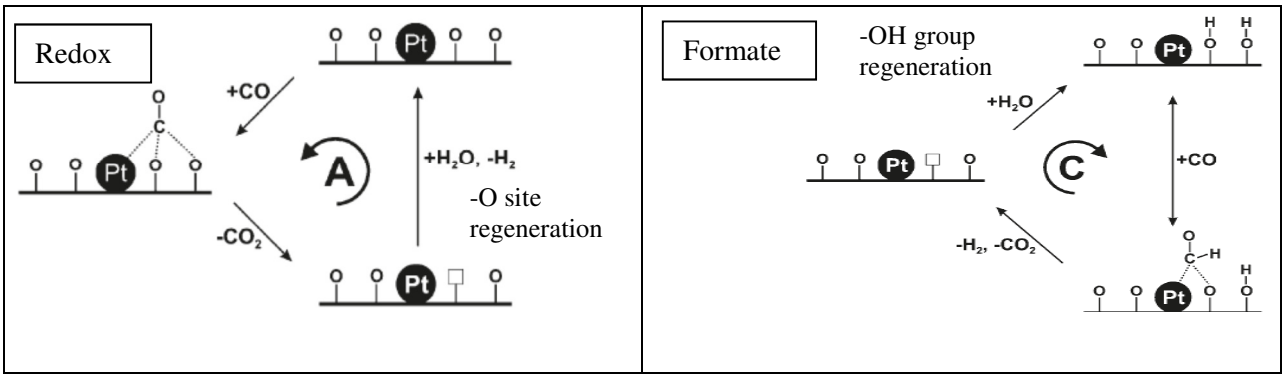

Figure 2-6: Water Gas Shift Reaction Mechanisms (from Ref. 35)

WGS measurements were carried out with a constant feed of bulk carrier gas made up of 2% CO, 2% CO_2, 2.5% H_2O and Argon at a total flow of 1 L/min. The bulk stream of argon and CO_2 were fed through the water bubbler at 22°C to saturate the bulk gas and later downstream the CO was injected at the microvalve. The gas mixture was initially established at equilibrium over the catalyst sample at room temperature. The oven heating ramp was then triggered at 10°C/min to 400°C.

2.6.4 CO Light-off Measurement

The CO light-off test had similarities to the prior two catalyst activity measurements. The flow composition was based on the OSC measurement, but both CO and O_2 were continuously injected while the argon was adjusted so the total flow rate remained 1 L/m. The same WGS oven ramp program was used to heat the catalyst sample. The parameter of interest was the inlet temperature where 50% of the inlet CO was oxidized into CO_2 (T_{50} CO). CO oxidation with gas phase O_2 scales with Pd dispersion. However, support oxygen mobility in CZO confounds the T_{50} CO results with gas phase oxygen. Therefore this test will be used simply to confirm SMSI suspicions in the Pd size and dispersion measurements.

The CO light-off gas mixture was initially established at equilibrium over the catalyst sample at 30°C as 2% CO, 2% CO_2, 1% O_2 and balance Ar. A special step was required for Pd/CZO samples to prevent light-off at 30°C driven primarily by support reoxidation with gas phase oxygen since the catalysts were initially reduced; CO was not introduced until the temperature rise from reoxidized CZO was cooled back down to room temperature. The measured outlet CO level after stabilization at 30°C was used as the fully unconverted baseline. Later the oven heating ramp was triggered at 10°C/min to 400°C.

2.6.5 Kinetic Measurements

Work by Bunluesin *et al*. measured CO oxidation and WGS reaction rates at a temperature of 515K (242°C) as a function of CO partial pressure as shown in Figure 2-7 [40]. In their work, CO oxidation had a zero order reaction rate with respect to CO for ceria support degreened at 570K (297°C), but a negative rate with respect to CO is observed for ceria support severely aged at 1670K (1397°C), while the WGS reaction had a zero order rate with respect to CO for both catalysts, but the WGS rate was much lower for the more severely aged catalyst. Other work showed a strong link in WGS CO oxidation and OSC when evaluated at 200°C, but those similarities diminished when evaluated at 300°C, and all together disappeared when evaluated at 400°C and higher [41]. Therefore our less severely aged catalysts coupled with the low reaction

temperatures of 400°C and below may create a special operating window where the CO oxidation is sufficiently kinetically limited so that oxygen transport from the ceria support to the Pd metal drives both the CO oxidation and WGS reaction at nearly equal rates. Automotive manufacturers typically use signals from the oxygen sensors to help determine the deterioration of the catalytic converters by measuring the OSC [42]. Similarly this work may enable an on-board determination using oxygen sensors of the catalyst deterioration with the WGS reaction as others have done with a diesel NOx adsorber catalyst [43].

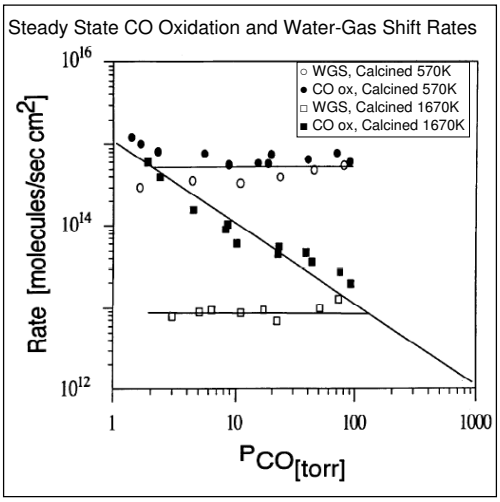

Figure 2-7: CO Oxidation and WGS Rates at 515K for Pd/Ceria (from Ref. 40)

The calculations used for the production of CO_2 for the catalyst activity measurements are listed below as equations 15 and 16. CO_2 production can be measured directly by the mass spectrometer in units of partial pressure (i.e, torr). Partial pressure of CO_2 can be added with the other measured gas species to determine the total pressure and enable a relative concentration calculation for each gas species. Equation 15 shows micromoles of CO_2 per gram of catalyst can be calculated for the OSC experiment by subtracting the average CO_2 level during the CO pulse from the average background CO_2 level for 20 seconds before and after the CO pulse, then multiplying that difference by the CO pulse length (1 minute) and gas flow rate (1 L/min), then dividing by the gas constant (22.414 L/mole) and the mass of catalyst powder used. Equation 16 shows conversion of CO to CO_2 during the oven ramp of the WGS and CO light-off experiments can be calculated by taking the current

CO_2 level subtracted by the minimum CO_2 level as a background, then taking that difference and dividing it by the stabilized unconverted CO outlet gas level at room temperature.

Equation 15:
$$CO_2 \text{ Yield [µ-moles/g]} = \frac{10^{-6} * (\text{average } CO_2\ [\%] - \text{background } CO_2\ [\%]) * (\text{CO pulse length [m]}) * (\text{gas flow rate [L/m]})}{(22.414 \text{ L/mole} * \text{mass of catalyst sample [g]})}$$

Equation 16:
$$CO_2 \text{ Yield [\%]} = \frac{(\text{current } CO_2\ [\%] - \text{background } CO_2\ [\%])}{(\text{CO at room temperature [\%]})}$$

A comparison of Palladium on both supports was performed by normalizing the reaction rate to the accessible metal surface atoms. The CO_2 production rate for the WGS measurement was calculated using equation 17 below from Han *et al*. where for a given temperature the turnover frequency (TOF) is the product of the following: the conversion of CO to CO_2 (X), the number of inlet CO molecules per second (dN_{CO}/dt) and the number of exposed Pd surface atoms (N_S^{Pd}) [38]. The CO_2 production rate for the OSC measurement was calculated using a method from Hori *et al*. where the initial CO_2 generation peak edge was integrated during the CO pulse [34]. This method from Hori *et al*. for OSC requires a modification to equation 17, which is shown below as equation 18. The event marker for t_0=0 was just before the CO_2 peak rise and the value of t_1 was at the maximum of the CO_2 peak or four seconds later.

Equation 17: WGS TOF [1/s] = $$\left[\left(\frac{X}{100}\right) \times \left(\frac{dN_{CO}}{dt}\right)\right] \times \left(\frac{1}{N_S^{Pd}}\right)$$

Equation 18: OSC TOF [1/s] = $$\left[\frac{\int_{t_0}^{t_1} N_{CO_2}\, dt}{(t_1 - t_0)}\right] \times \left(\frac{1}{N_S^{Pd}}\right)$$

$N_S^{Pd} = m_{cat}\, X_{Pd}\, D_{Pd}\, N_A/M_{Pd}$

N_{CO} = Inlet molecules of CO per second

N_{CO_2} = Molecules of CO_2 formed]

m_{cat} = Mass of catalyst [g]

X_{Pd} = Pd loading weight fraction

D_{Pd} = Pd dispersion by H_2 chemisorption

N_A = Avogadro's number

M_{Pd} = Pd molecular mass

2.6.6 Pd Oxidation Rate Measurement

The high temperature XRD technique is based on the typical XRD technique described above in section 2.4.5, but adds: an environmental chamber to exchange gases across the sample, a heating strip to acquire above ambient temperature patterns and a fixed position 120 degrees angled detector. The added capability to measure across 120 degrees 2θ simultaneously enables fast pattern acquisition to detect environmental and temperature changes. However, because of the large width of the beam (~1mm) and the limited positional resolution of the detector (0.3 mm), the instrumental resolution (~0.36°) is poor compared to conventional focusing diffractometers. Long scan times are therefore required to achieve a balance with good resolution. At sufficiently high temperatures, the growth of Pd particles becomes too fast for the HTXRD measurement acquisition time. To enable this approach, an accurate kinetic model of the time dependence of the growth of PdO fraction appearance during the HTXRD experiment is used based on the Avrami-Erofe'ev model [44, 45].

HTXRD was measured using a Bueler HDK furnace attachment mounted to a Scintag X1 diffractometer equipped with a low divergence (0.03°) beam of Cu-Kα radiation produced using an Osmic collimating optic. Data were collected using an Inel 120° position sensitive detector with a 250 mm radius. X-Ray source settings were 45 kV and 40 mA. Scans were performed with an interval of 0.015°2θ. Samples were prepared by wet-milling 20 mg of powder in ethanol and pipetting it onto a 1 mm thick, 10 mm square silicon carbide single crystal slide and allowing it to dry. The slide was then placed onto the primary heating strip that includes a Pt thermocouple welded to its underside for feedback temperature control. Calibration of the sample temperature was verified to be within +/-5°C by comparing the observed melting transition in its HTXRD pattern to the known melting point of high purity aluminum. Gas flow into the furnace

chamber was controlled with MKS mass-flow controllers at a total flow rate of 1 L/min. The internal volume of the furnace chamber was about 1.5 L.

Oxidation experiments were conducted after an initial *in-situ* 1 hour reduction in 250 sccm of 5% H_2 in balance N_2 at 300°C. Prior to each experiment, the chamber was purged with pure N_2 for 5 minutes and the heating strip temperature was adjusted to the temperature of interest. HTXRD data were recorded with one scan during the purge to obtain the initial Pd [111] peak size and the feed gas was switched to dry air simultaneously with the beginning of an acquisition of repeated scans. The PdO phase fraction was calculated as one minus the quotient of the current integrated Pd peak area at time *t* divided by the initial Pd peak area at time zero. Temperatures used to collect HTXRD data began at 200°C and went up in 50°C steps eventually to 350°C where over 70 data points could still be collected during the slow transition of Pd to PdO.

The Avrami-Erofe'ev model is shown below as equation 19 and relates the growth of an emerging phase fraction α at time t, rate constant k, and growth factor exponent n. By plotting the phase fraction against time on a log-log scaling, k and n can be easily extracted using the linearized Avrami-Erofe'ev model in equation 20. An Arrhenius relationship is shown as equation 21 or the linearized Arrhenius relationship in equation 22 where the activation energy E_a and constant A are determined by fitting the rate constants k at the temperatures of each measurement. E_a and A can then be used in the Arrhenius relationship to extrapolate the rate constant k at a higher temperature than was measured by using equation 21. Finally, equation 19 can be used with the extrapolated k and an average n value (from the lower temperature results) to plot an estimated PdO phase fraction as a function of time at that higher temperature.

Equation 19: $\alpha = 1 - \exp(-kt)^n$

Equation 20: $\ln(\ln[1/(1-\alpha)]) = n * \ln(k) + n * \ln(t)$

Equation 21: $k = A * \exp(-E_a/RT)$

Equation 22: $\ln(k) = (-E_a/R)*(1/T) + \ln(A)$

Thermogravimetric analysis (TGA) was used to verify the HTXRD work. TGA involves precise measurement of a catalyzed sample mass change during a fixed sample environment either isothermally as a function of time or as a function of increasing temperature up to 1000°C. The weight change sensitivity is generally 0.01 mg. A Curie point temperature calibration using nickel (placed in the sample pan) confirmed the actual sample temperature is within +/- 2°C of the oven set value. PdO decomposition and Pd reoxidation was measured in a TA Q500 instrument. About 77 mg of Pd/CZO sample was placed on the sample pan. The sample was preconditioned by holding at 400°C in an environment of 10% O_2 and balance N_2 at 100 mL/min for 180-240 minutes for complete oxidation, then switching off O_2 and holding in N_2 for 60-120 minutes at 100 mL/min and heating to 700°C at a 5°C/min ramp rate to decompose PdO. The oven temperature was then adjusted to one of two desired measurement temperatures, 350°C or 700°C, and held for 30 minutes before switching on the 10% O_2 to begin Pd oxidation at 1L/m.

2.7 Vehicle TWC Emission and Temperature Evaluation

The Ford Motor Company vehicle emission research laboratory (VERL) test cell facility consisted of a 48 inch single roll dynamometer, a constant volume sampler (CVS), a three-probe modal emission sampler, a remote mix tee (RMT) dilution system and a data acquisition unit for electronic signals. A 2009MY 2.0L Ford Focus Test vehicle with gasoline fuel was secured to the cell floor while only the front tires were in contact with the exposed dynamometer roll surface that simulated road conditions. The vehicle was operated using the federal test procedure FTP-75 as a warm-up then followed immediately by the federal US06 or Supplemental Federal Test Procedure (SFTP). Tailpipe emissions were measured using Horiba MEXA 9000 analyzers at a 1 Hz data collection rate and the spindt method was used to determine the engine exhaust lambda equivalence ratio, or the actual air/fuel ratio divided by the stoichiometric air/fuel ratio, from the exhaust emissions and fuel parameters [46]. K-type thermocouples were installed through-out the exhaust system including one in the

catalytic converter bed location, which was 1 inch downstream of the first brick front face.

2.8 Accuracy of the Methods

2.8.1 Error Estimation

When comparing results of two different samples, it is necessary to know whether the calculated difference is statistically significant due to changes in the sample characteristics or because of sampling variation or error introduced by a combination of the particular sample, equipment accuracy, number of measurements and sampling method. A confidence interval contains a set of plausible values for a sampling statistic, such as a mean, and equals a theoretical probability point of normally distributed data at critical point α with n-1 degrees of freedom ($t_{\alpha/2,n-1}$), times the standard deviation of the sample data set (s), divided by the square root of the number of counted particles (n) according to equation 23 [47]. A standard deviation describes the calculated difference of the sampling distribution from the calculated sample mean and by itself can be a useful measure of scatter in the data set apart from the sample mean. Therefore, if the same sampling method was performed on future samples with the same instrument to compute a result and an interval estimate about each sample mean, we would expect the true sample mean to fall within the confidence interval estimate a certain percentage of the time, equal to 100%*(1-α). Statistically significant differences between results of a mean with a confidence interval can be done by comparing one mean of normally distributed data and examining if it is outside the confidence interval around another mean of normally distributed data.

Equation 23: Confidence Interval, CI = $\frac{(t_{\alpha/2,n-1})(s)}{\sqrt{n}}$

s = standard deviation = $\sqrt{\frac{\sum(x-\mu)^2}{n-1}}$

μ = sample mean = $(\sum x)/n$

x = measured value

n = number of values measured

When multiple sources of error are identified and can be reasonably estimated, a propagation of error can be estimated from the square root of the sum of the squared error terms as previously performed by Lee [48]. For example, a propagation of error in measured kinetic reaction rate (*ΔTOF/TOF*) based on equations 17 or 18 would be:

Equation 24: $$\left(\frac{\Delta TOF}{TOF}\right)^2 = \left(\frac{\Delta X}{X}\right)^2 + \left(\frac{\Delta N_{CO}}{N_{CO}}\right)^2 + \left(\frac{\Delta m_{cat}}{m_{cat}}\right)^2 + \left(\frac{\Delta D_{Pd}}{D_{Pd}}\right)^2$$

For all terms except the error in measured conversion efficiency (*ΔX/X*), Lee used the following 3σ error estimates for precision manufactured instruments and equipment [48]:

$\left(\frac{\Delta N_{CO}}{N_{CO}}\right)$ = 0.01 (precision flow controllers)

$\left(\frac{\Delta m_{cat}}{m_{cat}}\right)$ = 0.01 (precision digital scale)

$\left(\frac{\Delta D_{Pd}}{D_{Pd}}\right)$ = 0.01 (precision chemisorption)

2.8.2 Electron Microscopy Pd Size

The role of electron microscopy in our work was to verify average Pd dispersion and size measurements with the other methods of chemisorption and XRD, and whether the lean treatments reduced the mean particle size. Chemisorption and XRD can only provide average particle size results, while microscopy can provide particle size distribution (PSD). Based on the PSD, an average particle size can be calculated (equation 11) and compared against the other two methods (equations 12-13). The aged sample particle size distributions, with about 200 counted particles each, demonstrated bell shapes or normal distributions [1]. However, the fresh particle size distribution was not normal due to the long tail of large particles, so a statistical analysis with equation 23 was applicable for just the aged catalysts [1]. Table 2-1 below is a statistical analysis on counted particles of Pd/Al samples. The standard deviation was

4-8 nm for these samples. The confidence interval for a desired confidence level of 95% was about 4-7% of the samples mean Pd size. An increase in counted particles to 1000 changes the inverse t-distribution at 95% probability ($t_{0.025,n-1}$) from 1.6524 at n = 204 to just 1.6464 at n = 1000, resulting in just a 0.4% change in the confidence interval. Therefore one would only need to acquire more particle size data if the claims of significant difference were not yet true at a desired level of confidence.

Table 2-1: Statistical analysis of electron microscopy results

Statistical Metric	Fresh	Redox aged	Redox aged + 550°C/2h air	Redox aged + 700°C/2h air
Mean, μ	6.0	16.0	14.6	11.6
Count, n	274	248	174	204
$\sqrt{n}$	17	16	13	14
Standard deviation, s	5	8	6	4
Probability point of t distribution, $t_{\alpha/2,n-1}$	1.6505	1.6510	1.6537	1.6524
95% Confidence Interval on the mean, CI	0.4	0.8	0.8	0.5

HAADF-STEM provides excellent z-contrast for Pd/Al samples since Pd (z=46) and Al (z=13) are very different. However, little z-contrast exists between Pd particles and support materials containing Ce (z=58) [4] or Zr (z=40). Kai Sun, a UofM microscope expert, attempted to acquire HRTEM images of the model Pd/CZO samples using a JEOL 3100R05 Double Cs-Corrected Analytical Electron Microscope to obtain direct evidence of a Ce covering on Pd. Dark field images were acquired at an accelerating voltage of 300 kV, using a tungsten cold field emission tip. This instrument has a resolution of 0.055nm point-to-point, and is therefore one of the most powerful electron microscopes currently available. However, even with this powerful instrument, we were unable to discern further information about the samples. Figure 2-8 shows the poor z-contrast of the Pd/CZO samples. In addition, a carbon sphere quickly formed about the area of interest as the electron beam excited the carbonaceous species on the fresh Pd/CZO surface, which confound efforts for elemental mapping by parallel spectroscopy techniques such as X-ray Energy Dispersive Spectroscopy (XEDS) or Electron Energy Loss Spectroscopy (EELS). The carbon was removed by use of a

heated sample stage at 400°C for 2 hours. After removal of carbon (that is conductive and can prevent sample charging) and cooling to 100°C, sample charging induced image artifacts (i.e., lattice vibration) that made it impossible to reach the required resolution where atomic spacing may identify oxides or metals.

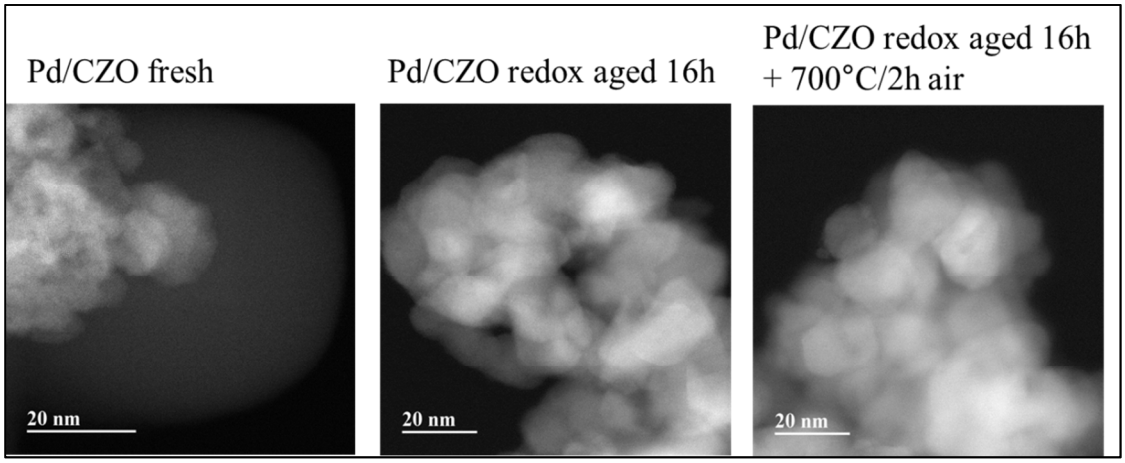

Figure 2-8: JEOL 3100R05 STEM images of Pd/CZO samples

Besides the possibility of beam induced changes in particle size, other sources of error with microscopy in the Pd size measurement include the dopants present in the support material, convention for handling agglomerates, image pixel resolution used for the fit, and the assumption of spherical particles. The difference in atomic mass for the reduced 1.5wt%Pd (z=46) metal and Al (z=13) in the 4wt% La_2O_3-Al_2O_3 support material was sufficient to compare bright versus dull particles and accurately determine boundary lines in the dark field image. We considered all bright areas in the STEM dark field images to be Pd and not La_2O_3 in spite of the larger atomic weight of La (z = 56). This assumption is not without precedent as previous work by Fujisaki *et al*. with high resolution transmission electron spectroscopy included images of γ-Al_2O_3 and La_2O_3 doped γ-Al_2O_3 powders that revealed no discernable difference in z contrast in the bright field image as La was too highly dispersed within the γ-Al_2O_3 matrix [49]. In our dark field images [1], bright Pd shapes that appeared to be made of multiple circular particles, or agglomerates, were ignored for particle counting rather than estimating boundaries of individual particles. This convention for handling agglomerates produces little error as it would be similar to adding a few more particles to the existing count near

200 particles (the typical sampling error of n counted particles out of z total particles in the population diminishes with an increasing number of counted particles as with equation 23). If we assume that a pixel on the particle boundary has at least 50% Pd in it, then the error in the Pd size measurement will scale with the number of boundary pixels relative to interior pixels. The error will mostly affect small particles, but will be minimized with high resolution images. The calibration used for the image was 1.678 pixels per nm, or a pixel diameter of 0.596 nm. This pixel diameter is approximately equal to the 0.5 nm 95% confidence interval or about 4-7% of the samples mean Pd size from Table 2-1. The Pd particle orientation is assumed to be random relative to the electron beam and normally distributed. As our 2D images appear mostly circular [1], we have little evidence that the assumption of spherical particles is incorrect. The particle size was determined by pixel area calculation then the diameter was calculated using the surface area equation for a circle. Therefore the result represents an average diameter for an irregularly shaped particle so this spherical assumption error may be on the order of the pixel fit error.

2.8.3 XRD Pd Peak Fit

The Pd size results for Pd/Al and Pd/CZO samples are listed in Table 2-2 below. The standard deviation listed is error from the goodness of fit using a split pseudo-Voigt peak profile on the measured XRD pattern, which is considered to be a normal probability distribution. Scans were performed with a step size of 0.005°2θ, or about 200 scans per degree 2θ. To approximate the length of the pattern subject to the peak fit, the full width at half maximum (FWHM) height was used in units of degrees 2θ. Therefore the estimated data points used in the split pseudo-Voigt peak fit was at least FWHM times 200. Recalling equation 23, the inverse t-distribution at 95% probability ($t_{0.01,n-1}$) for 74 points is about 1.99 and 170 points is about 1.97. For most samples the estimated Pd particle size had a standard deviation near 3 nm, similar to the standard deviation of the microscopy results. The confidence interval for a desired confidence level of 95% was 3-7% of the samples mean Pd size, similar to microscopy.

Table 2-2: Statistical analysis of XRD peak fit results					
Sample	**Pd Size, d [nm]**	**Standard deviation, *s* [nm]**	**FWHM [deg 2θ]**	**Scans used in the fit, *n***	**Confidence interval 95% [nm]**
Pd/CZO 700C/16h rich	11.5	2.6	0.75	150	0.42
Pd/CZO 700C/16h rich + 550C/2h air	10.7	2.3	0.73	146	0.38
Pd/CZO 700C/16h redox	19.8	3.8	0.40	80	0.85
Pd/CZO 700C/16h redox + 550C/2h air	20.4	3.9	0.40	80	0.87
Pd/CZO 700C/16h redox + 700C/2h air	24.4	7.2	0.37	74	1.67
Pd/Al fresh	14.0	3.0	0.85	170	0.45
Pd/Al 700C/16h redox	16.2	2.9	0.76	152	0.46
Pd/Al 700C/16h redox + 550C/2h air	15.1	2.7	0.80	160	0.42
Pd/Al 700C/16h redox + 700C/2h air	14.4	2.7	0.80	160	0.42

Besides the possibility of lattice strain and stress, other sources of error with XRD Pd size measurement include the convention for selecting Pd peaks to fit amid the support peaks, a low number of scans per degree 2θ, low scan time, insufficient sample on a slide, a low metal load on the sample and small metal particles that may go undetected. Pd peaks were selected that were away from support peaks to enable accurate Pd peak fitting and avoid errors associated with background refinement. The current scan rate and step size provided 200 scans per degree 2θ for the peak fit. Further improvements in accuracy are possible, but limited. Much like the small 0.4% improvement in the confidence interval for microscopy going from 200 counted particles to 1000, the associated increase in confidence would be similarly small with a slower scan rate or smaller step size to achieve 1000 scans per degree 2θ for the peak fit. The signal to noise ratio is defined as the signal average divided by the standard deviation of the background, and a value of at least 5 is considered sufficient for distinguishing features from the background. At 0.1g of sample powder applied per slide, the Pd [111] signal to noise ratio was 5 for 700°C/16h redox aged Pd/CZO. More powder could be used since the 700°C/2h air treated 700°C/16h redox aged Pd/CZO sample had a Pd [111] signal to noise ratio of 4 and the largest confidence interval in Table 2-2. It is difficult to evaluate the Pd crystallite size from XRD peak broadening if the sample metal loading is small (≤ 1 wt%) [24], which causes a low signal to noise ratio. In addition, very small Pd crystallites (< 6 nm) have excessively broad peaks that would

not be completely detectable apart from the support diffraction pattern, since the width of the X-ray diffraction peak is inversely related to the crystallite length. If a portion of the Pd particle size distribution is too small to be detected (< 6 nm), then the large particles that are detectable will contribute to an overestimation of the bulk Pd size.

2.8.4 Chemisorption Pd Size

The H_2 chemisorption technique also has limitations. Reducible oxide from the support material can decorate and block H_2 access to the metal surface and affect the results of this technique [50, 51]. H_2 spill-over is a known problem for the classic H_2-O_2 pulse titration technique, but is a negligible issue for the double isotherm adsorption technique and difference method used by the Micromeritics ASAP 2020 apparatus as spill-over H_2 adsorption will compete with H_2 adsorbed anyway on the support (Al_2O_3 and/or CZO). Pd hydride formation is actually more of a concern, but works by Benson et al. [52] and Ragaini et al. [53] go through the proper conditions to avoid Pd hydride formation (temperature and pressure) affecting the irreversibly adsorbed chemisorption results. A similarly configured back-sorption procedure is used by the Micromeritics ASAP 2020 apparatus that was used in our work.

For consistency across all Pd/CZO and Pd/Al samples, H_2 was used as the adsorptive gas since CO formed stable carbonate species on Pd/CZO giving an overestimate of irreversibly adsorbed adsorptive gas [54]. The data shown in Table 2-3 below contains chemisorption results acquired with the Micromeritics ASAP 2020 apparatus for two adsorptive gases, H_2 and CO. As the results show, CO chemisorption on CZO supports results in overestimation of metal dispersion and cannot be used for the Pd/CZO catalysts, especially for high CeO_2 CZO catalysts. Chemisorption on the 0.5wt% Pt/Al_2O_3 reference material supplied by Micromeritics was claimed to result in a dispersion of 34.1% +/- 5% by difference method, without specification of the adsorptive gas used. Our results were 28% with H_2 and 40% for CO. This discrepancy between H_2 and CO chemisorption may be due to 1) interference with surface carbon that can reduce adsorption of H_2 more so than for CO [55], and 2) formation of a metal-$(CO)_x$ binary carbonyls that are unstable on Pd yet stable on Pt and would result in non-unity

CO adsorption stoichiometry [56, 57]. Since there were also problems with CO adsorption on CZO support shown in Table 2-3, we elected to use only H_2 adsorptive gas on all samples for consistency. A round robin sample exchange was conducted with Pd/Al samples at the University of Michigan and Ford Research; both with H_2 adsorptive gas. The fresh Pd/Al sample was found to have a dispersion of 9.1% at UofM and 8.4% at Ford. The redox aged Pd/Al sample was found to have a dispersion of 1.1% at UofM and 0.7% at Ford. This comparison gave us confidence that the H_2 chemisorption results were reliable.

Table 2-3: Chemisorption discrepancies caused by different adsorptive gases

Model TWC Samples	Adsorptive gas	Dispersion	Size [nm]
1.4wt% Pd/$Ce_{0.75}Zr_{0.25}O_2$ fresh	H_2	12%	9.7
	CO	132%	0.8
1.5wt% Pd/$Ce_{0.5}Zr_{0.5}O_2$ fresh	H_2	22%	4.9
	CO	49%	2.3
1.5wt% Pd/La-Al_2O_3 fresh	H_2	9.1%	12
	CO	12%	9.2
0.5wt% Pt/Al_2O_3 Micromeritics reference material (= 34.1% +/- 5% by difference)	H_2	28%	4.0
	CO	40%	2.8

The data shown in Table 2-4 below contains chemisorption results acquired with the Micromeritics ASAP 2020 apparatus for the fresh Pd/CZO and Pd/Al samples, assuming normally distributed data. H_2 chemisorption tests were always run before catalyst activity testing and then after the final catalyst activity test to check for changes since those tests ran up to 400°C. A third evaluation was run with a new tube, sample powder and quartz wool to evaluate differences in sample packing. The results of these tests show a standard deviation of 0.3 nm for Pd/CZO and 0.9 nm for Pd/Al. Therefore the Pd size did not appear to change as a result of running the catalyst activity tests or packing samples differently. However, since only three tests were run on these samples, the confidence interval was up to 2.3 nm and about 15% of the samples mean Pd size. The standard deviation divided by the mean ($\Delta D_{Pd}/D_{Pd}$) was near 6%, which was above the 3σ error estimate of 1% from equation 24.

Table 2-4: Statistical analysis of chemisorption results		
Statistical Metric	**Fresh Pd/CZO**	**Fresh Pd/Al**
Pd size mean, μ	5.2	13.4
Count, n	3	3
$\sqrt{n}$	1.7	1.7
Standard deviation, s	0.3	0.9
($\Delta D_{Pd}/D_{Pd}$)	5.8%	6.7%
Probability point of t distribution, $t_{\alpha/2,n-1}$	4.30	4.30
95% Confidence Interval on the mean, CI	0.7	2.3

Besides the possibility of an H_2 adsorption stoichiometry on Pd different than two, other sources of error with H_2 chemisorption Pd size measurement include insufficiently cleaned Pd surfaces following the 10^{-6} torr evacuation at 350°C, measured sample weight, low adsorptive gas purity and system leaks. Work by Aben studied the temperature required to clean H_2 from a Pd surface during evacuation to 10^{-6} torr prior to the H_2 adsorption isotherm measurement, which revealed ~0% residual H_2 when evacuated at 580°C, 3% H_2 at 400°C and 11% H_2 at 300°C [21]. Assuming an exponential decay fit for Aben's data, a 350°C evacuation may leave about 6% residual H_2 on the Pd surface, which is close to our $\Delta D_{Pd}/D_{Pd}$ value in Table 2-4. The Denver Instruments precision scale model TR-403 used in our work registered values in milligrams and is regularly calibrated on an annual basis. Since each sample weight was about 300 mg, the error from sample weight may be near the $\Delta D_{Pd}/D_{Pd}$ 3σ error estimate of 1% from equation 24. The gas cylinder from Airgas was Ultra High Purity Hydrogen 5.0 Grade with 99.999% purity (supplier claim of 1 ppm O_2 and 2 ppm H_2O and 0.5 ppm THC), so the error attributed to it would be well below 1%. The observed leak rate from successfully analyzed samples was 0 μmHg/s; so any error attributed to it would be negligible.

2.8.5 XPS Surface Concentration

The data shown in Table 2-5 below contains XPS elemental composition results acquired with the Kratos AXIS 165 Electron Spectrometer for fresh and redox aged

Pd/Al samples assuming normally distributed data. Five pressed pellets were made from each sample and then evaluated. The atomic surface concentration results show a standard deviation of 0.04-0.06% for Pd and La. The 95% confidence interval on the Pd mean for each sample was 29% of the fresh mean and 41% of the aged mean. The 95% confidence interval on the La mean for each sample was 23% of the fresh or aged mean. The surface concentration of Pd did not change from fresh to aged, as 0.20% +/- 0.06% was not statistically different than 0.19% +/- 0.08%. The surface concentration of La increased from fresh to aged, as 0.24% +/- 0.05% was statistically different than 0.33% +/- 0.07%.

Table 2-5: Statistical analysis of XPS surface concentration results				
Statistical Metric	**Pd Fresh Pd/Al**	**Pd Aged Pd/Al**	**La Fresh Pd/Al**	**La Aged Pd/Al**
Composition mean, μ	0.20%	0.19%	0.24%	0.33%
Count, n	5	5	5	5
$\sqrt{n}$	2.24	2.24	2.24	2.24
Standard deviation, s	0.05%	0.06%	0.04%	0.06%
Probability point of t distribution, $t_{\alpha/2,n-1}$	2.13	2.13	2.13	2.13
95% Confidence Interval on the mean, CI	0.06%	0.08%	0.05%	0.07%

2.8.6 Kinetic Rate Measurements

Equation 24 can be used to estimate the error associated with the kinetic rate measurements. Table 2-6 shows the analysis for error propagation of the kinetic rates results at 400°C. A mean value and standard deviation were calculated for each sample using the repeat results for WGS CO_2 yield or the initial CO_2 peak area formed during seven CO pulses during the OSC test. The error in the conversion efficiency ($\Delta X/X$) was the standard deviation (s) divided by the mean (μ). The ($\Delta D_{Pd}/D_{Pd}$) was found to be close to 6% from Table 2-4. The 3σ estimates for the other parameters in equation 24 can be used to yield the propagated error ($\Delta TOF/TOF$). For the WGS kinetic data, the error was about 2% for the kinetic measurement of either sample. For the OSC kinetic data, the error was about 6% for the Pd/CZO samples and 7% for the Pd/Al samples.

Table 2-6: Error propagation of kinetic rate results at 400°C				
Statistical Metric	**Fresh Pd/CZO WGS**	**Fresh Pd/Al WGS**	**Fresh Pd/CZO OSC**	**Fresh Pd/Al OSC**
WGS CO_2 yield mean, μ	71.6%	10.5%	-	-
OSC initial CO_2 yield mean, μ [µ-mol/s]	-	-	6.76	2.83
Count, n	5	3	7	7
Standard deviation, s	0.96%	0.11%	0.09	0.12
$(\Delta X/X)$ =	1.3%	1.1%	1.3%	4.1%
$(\Delta TOF/TOF)$ =	6.3%	6.3%	6.3%	7.4%

2.9 References

[1] J.A. Lupescu, J.W. Schwank, K.A. Dahlberg, C.Y. Seo, G.B. Fisher, S.L. Peczonczyk, K. Rhodes, M.J. Jagner, L.P. Haack, "Pd Model Catalysts: Effect of Aging Environment and Lean Redispersion", *Appl. Catal. B: Environ.* 183 (2016) 343–360

[2] A. Badri, C. Binet, J.-C. Lavalley, "Metal-support interaction in Pd/CeO_2 catalysis Part 2. – Ceria textural effects", *J. Chem. Soc. Farad. Trans.* 92(9) (1996) 1603-1608

[3] H.P. Sun, X.P. Pan, G.W. Graham, H.-W. Jen, R.W. McCabe, S. Thevuthasan, C.H.F. Peden, "Partial encapsulation of Pd particles by reduced ceria-zirconia", *Appl. Phys. Lett*. 87 (2005) 201915

[4] L. Kępiński, M. Wolcyrz, "Microstructure of Pd/CeO_2 catalyst: Effect of high temperature reduction in hydrogen", *Appl. Catal. A: Gen.* 150 (1997) 197-220

[5] T.P. Bebee, J.T. Yeates, "Spectroscopic Detection of (111) Facets on Supported Pd Crystallites: Site Blocking by Ethyldyne on Pd/Al_2O_3", *Surf. Sci. Lett*. 173 (1986) L606-L612

[6] R.F. Hicks, A.T. Bell, "Effects of Metal-Support Interactions on the Hydrogenation of CO over Pd/SiO_2 and Pd/La_2O_3", *J. Catal*. 90 (1984) 205-220

[7] M. Alexandrou, R.M. Nix, "The growth, structure and stability of ceria overlayers on Pd(111)", *Surf. Sci*. 321 (1994) 47-57

[8] M.A. Newton, C. Belver-Coldeira, A. Martínez-Arias, M. Fernández-García, ""Oxidationless" Promotion of Rapid Palladium Redispersion by Oxygen during Redox $CO/(NO+O_2)$ Cycling", *Angew. Chem. Int. Ed.* 46 (2007) 8629-8631

[9] A.K. Datye, J. Bravo, T.R. Nelson, P. Atanasova, M. Lyubovsky, L. Pfefferle, "Catalyst microstructure and methane oxidation reactivity during the Pd-PdO transformation on alumina supports", *Appl. Catal. A: Gen.* 198 (2000) 179–196

[10] R. J. Farrauto, J. K. Lampert, M. C. Hobson, E. M. Waterman, "Thermal decomposition and reformation of PdO catalysts; support effects" *Appl. Catal. B: Environ.* 6 (1995) 263-270

[11] X. Chen, Y. Cheng, C.Y. Seo, J.W. Schwank, R.W. McCabe, "Aging, re-dispersion, and catalytic oxidation characteristics of model Pd/Al_2O_3 automotive three-way catalysts", *Appl. Catal. B: Environ*. 163 (2015) 499–509

[12] J.C. Jiang, X.Q. Pan, G.W. Graham, R.W. McCabe, J. Schwank, "Microstructure of a Pd/ceria–zirconia catalyst after high-temperature aging", *Catal. Lett*. 53 (1998) 37–42

[13] M.A. Aramendia, V. Borau, C. Jiménez, J.M. Marinas, A. Moreno, "Comparative measurements of the dispersion of Pd catalyst on SiO_2-$AlPO_4$ support using TEM and H_2 chemisorption", *Coll. Surf. A: Physicochem. Engin. Aspec.* 106 (1996) 161-165

[14] B.D. Cullity, Elements of X-Ray Diffraction – Second Edition, Addison-Wesley, Philippines, 1978

[15] S. Brunauer, P.H. Emmett, E. Teller, “Adsorption of Gases in Multimolecular Layers” *J. Am. Chem. Soc.* 60(2) (1938) 309–319
[16] D. Briggs, M.P. Seah, Practical Surface Sci. Analysis by Auger and X-ray Photoelectron Spectroscopy, John Wiley & Sons, New York, 1984
[17] A. Holmgren, B. Anderson, D. Duprez, “Interactions of CO with Pt/ceria catalysts”, *Appl. Catal. B: Environ*. 22 (1999) 215–230
[18] G.N. Vayssilov, M. Mihaylov, P. St. Petkov, K.I. Hadjiivanov, K.M. Neyman, “Reassignment of the Vibrational Spectra of Carbonates, Formates, and Related Surface Species on Ceria: A Combined Density Functional and Infrared Spectroscopy Investigation”, *J. Phys. Chem. C* 115 (2011) 23435–23454
[19] N.B. Colthup, “Spectra-Structure Correlations in the Infra-Red Region”, *J. Optic. Soc. Amer.* 40 (1950) 397- 400
[20] F.M. Hoffmann, “Infrared Reflection-Absorption Spectroscopy of Adsorbed Molecules”, *Surf. Sci. Rep.* 3 (1983) 107-192
[21] P.C. Aben, “Palladium Areas in Supported Catalysts - Determination of Palladium Surface Areas in Supported Catalysts by Means of Hydrogen Chemisorption”, *J. Catal*. 10 (1968) 224-229
[22] A. Baylet, S. Royer, P. Marécot, J. Tatibouët, D. Duprez,”Effect of Pd precursor salt on the activity and stability of Pd-doped hexaaluminate catalysts for the CH_4 catalytic combustion”, *Appl. Catal. B: Environ.* 81 (2008) 88–96
[23] A.L., Patterson, “The Scherrer Formula for X-Ray Particle Size Determination”, *Phys. Rev*. 56 (1939) 978-982
[24] J.K. Plischke, M.A. Vannice, “Effect of Pretreatment on the Adsorption Properties of Silver Crystallites”, *Appl. Catal*. 42 (1988) 255-283
[25] R.T.K Baker, E.B. Prestridge, G.B. McVicker, “The Interaction of Palladium with Alumina and Titanium Oxide Supports” *J. Catal*. 89 (1984) 422-432
[26] F.M. Dautzenberg, H.B.M. Wolters, “State of Dispersion of Platinum in Alumina-Supported Catalysts” *J. Catal.* 51 (1978) 26-39
[27] C.R. Adams, H.A. Benesi, R.M. Curtis, R.G. Meisenheimer, “Particle Size Determination of Supported Catalytic Metals: Platinum on Silica Gel”, *J. Catal*. 1 (1962) 336-344
[28] G. Prelazzi, M. Cerboni, G. Leofanti, “Comparison of H_2 Adsorption, O_2 Adsorption, H_2 Titration, and O_2 Titration on Supported Palladium Catalysts”, *J. Catal*.181 (1999) 73-79
[29] S.J. Penneycook, L.A. Boatner, “Chemically sensitive structure-imaging with a scanning transmission electron microscope”, *Nature* 336 (1988) 565-567
[30] R. Gorte, " Ceria in Catalysis: From Automotive Applications to the Water–Gas Shift Reaction", *AIChE J.,* 56 (2010) 1126-1135
[31] R. Möller, M. Votsmeier, C. Onder, L. Guzzella, J. Gieshoff, "Is oxygen storage in three-way catalysts an equilibrium controlled process?", *Appl. Cataly. B: Environ.* 91 (2009) 30–38
[32] H. Yao, Y. Yao, "Ceria in Automotive Exhaust Catalysts I. Oxygen Storage", *J. Catal.* 86 (1984) 254-265
[33] R. Nibbelke, A. Nievergeld, J. Hoebink, G. Marin, “Development of a transient kinetic model for the CO oxidation by O_2 over a Pt/Rh/CeO2/γ-Al_2O_3 three-way catalyst”, *Appl. Catal. B: Environ.* 19 (1998) 245-259
[34] C. Hori, A. Brenner, S. Ng, K. Rahmoeller, D. Belton, “Studies of the oxygen release reaction in the platinum-cria-zirconia system”, *Catal. Today* 50 (1999) 299-308
[35] C. Kalamaras, I. Gonzalez, R. Navarro, J. Fierro, A. Efstathiou, "Effects of Reaction Temperature and Support Composition on the Mechanism of Water Gas Shift Reaction over Supported-Pt Catalysts", *J. Phys. Chem. C* 115 (2011) 11595–11610
[36] A. Phatak, N. Koryabkina, S. Rai, J. Ratts, W. Ruettinger, R. Farrauto, G. Blau, W. Delgass, F. Ribeiro, "Kinetics of the water–gas shift reaction on Pt catalysts supported on alumina and ceria", *Catal. Today* 123 (2007) 224–234
[37] X. Wang, R. Gorte, J. Wagner, "Deactivation Mechanisms for Pd/Ceria during the Water–Gas Shift Reaction", *J. Catal.* 212 (2002) 225–230
[38] Z.Han, J. Wang, H. Yan, J. Fan, "Performance of dynamic oxygen storage capacity, water–gas shift and steam reforming reactions over Pd-only three-way catalysts", *Catal. Today* 158 (2010) 481–489

[39] E. Xue, M. O'Keeffe, J. Ross, "Water-gas shift conversion using a feed with a low steam to carbon monoxide ratio and containing sulphur", *Catal. Today* 30 (1996) 107-118
[40] T. Bunluesin, R. Gorte, G. Graham, "Studies of the water-gas-shift reaction on ceria-supported Pt, Pd, and Rh: implications for oxygen-storage properties", *Appl. Catal. B: Environ.* 15 (1998) 107–l 14
[41] M. Al-Harbi, W. Epling, A. Yezerets, N. Currier, H. Chen, H. Hess, "The Effects of Thermal Degradation on the Performance of a NO_X Storage/Reduction Catalyst", *SAE Technical Paper Series* 2009-01-0631(2009)
[42] J. Kašpar, P. Fornasiero, N. Hickey, "Automotive catalytic converters: current status and some perspectives", *Catal. Today* 77 (2003) 419–449
[43] A. Yezerets, S. Popuri, N. Currier, W. Epling, P. Millington, D. Lafyatis, "Method for on-board diagnostics of diesel engine NOx adsorber catalysts", US Patent US7628063 B2 (2009)
[44] M. Avrami, "Kinetics of Phase Change. I General Theory", *J. Chem. Phys*. 7 (1939) 1103-1112
[45] M. Avrami, "Kinetics of Phase Change. II Transformation-Time Relations for Random Distribution of Nuclei", *J. Chem. Phys*. 8 (1940) 212-224
[46] D. Bresenham, J. Reisel, K. Neusen, "Spindt Air-Fuel Ratio Method Generalization for Oxygenated Fuels", SAE [Special Publication] SP (1998), SP-1381(Emissions in 2-Stroke and Small 4-Stroke Engines), 219-238
[47] A.J. Hayter, Probability and Statistics for Engineers and Scientists, PWS Publishing Co., Boston, MA, 1996
[48] J.Y. Lee, "Metal Support Interactions in Supported Monometallic and Dimetallic Ruthenium and Gold Catalysts", PhD Thesis, University of Michigan, 1985
[49] S. Fujisaki, M.H. Zahir, Y.H. Ikuhara, Y. Iwamoto, K. Kuroda, "Nanostructural Characterization of Hydrothermally Stable γ-Alumina-Based Composite Materials by Transmission Electron Microscopy", *Adv. Mater. Res*., 26-28 (2007) 1109-1112
[50] R.F. Hicks, Q.-J. Yen, A.T. Bell, "Effects of Metal-Support Interactions on the Chemisorption of H_2 and CO on Pd/SiO_2 and Pd/La_2O_3", *J. Catal*. 89 (1984) 498-510
[51] J.S. Rieck, A.T. Bell, "Studies of the Interactions of H_2 and CO with Pd/SiO_2 Promoted with La_2O_3, CeO_2, Pr_6O_{11}, Nd_2O_3, and Sm_2O_3", *J. Catal*. 99 (1986) 278-292
[52] J.E. Benson, H.S. Hwang, M. Boudart, "Hydrogen-Oxygen Titration Method for the Measurement of Supported Palladium Surface Areas", *J. Catal* 30 (1973) 146-153
[53] V. Ragaini, R. Giannantonio, P. Magni, L. Lucarelli, G. Leofanti, "Dispersion Measurement by the Single Introduction Method Coupled with the Back-Sorption Procedure: A Chemisorption and TPD Study of the Different Chemisorbed Hydrogen Species II. Pd on Alumina", *J. Catal.* 146 (1994) 116-125
[54] T. Takeguchi, S. Manabe, R. Kikuchi, K. Eguchi, T. Kanazawa, S. Matsumoto, W. Ueda, "Determination of dispersion of precious metals on CeO_2-containing supports", *Appl. Catal. A: Gen*. 293 (2005) 91–96
[55] N. Krishnankuty, A.M. Vannice "The Effect of Pretreatment on Pd/C catalysts – 1. Adsorption and Absorption Properties" *J. Catal*. 155 (1995) 312-326
[56] E.P. Kündig, D. McIntosh, M. Moskovits, G. A. Ozin, "Binary Carbonyls of Platinum, Pt(CO), (Where n = 1-4). A Comparative Study of the Chemical and Physical Properties of M(CO), (Where M = Ni, Pd, or Pt; n = 1-4)", *J. Am. Chem. Soc*. 95 (1973) 7234-7241
[57] K. Chakarova, M. Mihaylov, K. Hadjiivanov, "Polycarbonyl species in Pt/H–ZSM-5: FTIR spectroscopic study of 12CO–13CO co-adsorption", *Catal. Commun*. 6 (2005) 466–471

Chapter 3 - Pd Model Catalysts: Effect of Aging Environment and Lean Redispersion

Jason A. Lupescu[1,2,*], Johannes W. Schwank[1], Kevin A. Dahlberg[1], Chang Yup Seo[1], Galen B. Fisher[1], Sabrina L. Peczonczyk[2], Kevin Rhodes[2], Mark J. Jagner[2] and Larry P. Haack[2]

[1]University of Michigan, Ann Arbor, MI 48109 USA

[2]Ford Motor Company, Dearborn, MI 48124 USA

First published in: Applied Catalysis B: Environmental 183 (2016) 343–360

http://dx.doi.org/10.1016/j.apcatb.2015.10.018

Abstract

The performance of automotive three-way catalysts (TWC) deteriorates with time, temperature and aging environment. Engine control methods are needed to minimize the extent of catalyst deactivation and provide an environment capable of partially redispersing noble metal catalyst particles. In this study, Palladium-based model

powder catalysts on ceria-zirconia or alumina supports were exposed to three different exhaust compositions, lean-only, rich-only and redox, each at 700°C for 16 hours. Catalyst activity was determined by CO oxidation with the Water Gas Shift (WGS) reaction and Oxygen Storage Capacity (OSC) measurements to probe the contact between the noble metal and support at a given state of catalyst deterioration. Lean catalyst treatments at 550°C and 700°C were applied to determine the effect on measured Pd size and catalyst activity. The lean-only gas environment was above the PdO decomposition condition, yet showed slightly deteriorated catalyst activity from the fresh state. The rich-only and redox gas environments significantly deteriorated catalytic activity through a combination of metal oxidation state effects and support/additive interactions, both with various degrees of reversibility depending on lean treatment time and temperature. The insight gained from this work could be used to develop engine control and aftertreatment design strategies to track (or infer) the aging process on the vehicle, avoid severe aging modes and actively intervene at various points to regenerate the catalyst.

3.1 Introduction

Automotive manufacturers are required to modify an increasing fraction of their annual production fleet towards meeting extremely low tailpipe emission standards. The catalytic converter together with engine controls for exhaust oxygen management were developed to simultaneously oxidize and reduce three regulated combustion pollutants of Carbon Monoxide (CO), Nitrogen Oxides (NOx) and Hydrocarbons (HC) [1, 2, 3]. The current state of this Three-Way Catalyst (TWC) converter washcoat technology contains noble metals (Pt, Pd and/or Rh) impregnated onto a complex support material composed of alumina (Al_2O_3) for high surface area, mixed oxides of ceria and zirconia (CZO) for oxygen storage capacity (OSC) promotion, and rare earth oxides such as lanthana (La_2O_3) to stabilize the alumina surface area. The harsh exhaust gas environment causes the vast initial amount of noble metal to end up buried inside large metal agglomerates and lost to gas-phase reactions [4, 5, 6]. Characterization studies of full useful life aged automotive TWCs revealed that dispersion of noble metals was only about 1-5% [7, 8]. The catalytic converter suppliers must include excessive quantities of expensive noble metals and rare earth oxides to ensure the residual activity after full useful life aging (150,000 miles) is adequate to abate engine emissions. Automotive manufacturers need capable engine controls that avoid or limit the exhaust environments that cause severe TWC deactivation and permit exhaust environments that facilitate restoration of TWC dispersion and function.

Although TWC deactivation is largely irreversible, the catalyst environment can cause a dramatic change in activity and metal dispersion. Hickey *et al.* and Kang *et al*. subjected Pd model catalysts to either an oxidizing environment (lean aged) or a cycling of reducing and oxidizing environments (redox aged) at 900°C and showed much less deterioration with the lean aged sample with respect to the temperature required for CO oxidation and the apparent Pd dispersion [9]. Chen *et al.* aged a series of Pd model catalysts at fixed temperatures in either an oxidizing or reducing environment and showed higher metal dispersion with the samples aged in the oxidizing environment at 850°C and below [10]. In both works, the samples that were not aged in the oxidizing environment were later exposed to oxygen at high temperature and cooled down;

further testing and characterization showed a lower temperature for 50% inlet CO conversion and increased Pd dispersion or O_2 uptake compared to the sample that was not exposed to oxygen [9, 10]. The cause of this Pd dispersion improvement is linked to earlier observations of PdO migration during heating of Pd/Al_2O_3 catalysts in oxygen and filming them under an electron microscope, where Pd changed to PdO above 325°C then wet and spread over the support between 350°C to 800°C, and finally mobile particles ruptured over the support surface [11, 12, 13]. Lieske *et al.* observed that the initial temperature when Pd particles oxidize to PdO was related to the Pd particle size and hence the severity of the catalyst aging [14]. The upper temperature of Pd redispersion was found coincide with PdO decomposition [11, 12], which was determined to be a function of the support material and gas phase oxygen concentration [15, 16, 17]. While oxidized Pd is the prerequisite for Pd redispersion, support collapse and metal-support interaction may limit PdO mobility and particle rupture.

The goals of this investigation were to determine how supported model Pd catalyst characteristics were affected by prolonged exposure to oxidizing and/or reducing exhaust gas environments, and identify opportunities to limit or reverse TWC deactivation that correlate with conditions achievable on a vehicle. The oxygen storage capacity (OSC) and water-gas shift (WGS) tests were included since the oxidation of CO gives insight into activity of the exposed Pd particle surface and contact between the Pd particle and support at a given state of deterioration. Determining the Pd particle size is a challenge because of the various aging mechanisms caused by automotive engine exhaust, the inability of any one characterization technique to give a clear picture of accessible Pd surface sites and the complexity of the materials used in TWC washcoat technology [18, 19, 20]. We found that the Pd model catalysts were deteriorated most by a redox and constant reducing environment versus exposure to a constant oxidizing environment, but these redox aged catalysts showed improvement in Pd dispersion and catalyst activity test performance after a 700°C dry air treatment.

3.2 Experimental

3.2.1 Preparation of Model TWC Samples

Pd-based model powder catalysts of 1.5wt% Pd on La_2O_3-doped γ-Al_2O_3 (Pd/Al) and Pd/ceria-zirconia (Pd/CZO) were prepared at an OEM supplier laboratory by incipient-wetness impregnation of the supports with a palladium solution free from chlorides. After drying, these catalysts were calcined at 500°C for 4 hours in air to fix the metals on the support materials. A mixture was made of the fresh Pd/Al and Pd/CZO model powder catalysts on an equal mass basis to simulate an automotive Pd-based TWC washcoat (Pd/TWC). Two additional samples were acquired for comparison, a 1.6wt% Pd on TH 100/150 γ-Al_2O_3 without La_2O_3 from Sasol (Pd/A) was described in another work [10] and uncatalyzed $Ce_{0.5}Zr_{0.5}O_2$ (CZO) powder from Solvay. All powders were sieved to obtain particles between 40-60 mesh (250-420 microns).

3.2.2 Model TWC Sample Aging and Lean Treatment Procedures

Catalyst aging environments were established in a continuous flow reactor at 700°C for 16 hours to simulate in-use drive cycle conditions at the engine-out location. Three aging gas compositions were introduced at a flow rate of 3 L/m: lean-only (0.5% O_2, 10% H_2O and N_2), rich-only (0.75% CO, 0.25% H_2, 10% H_2O and N_2), and redox conditions (alternated 10 minute step pulses of lean then rich). Automotive engine operation performs lean/rich switches at a frequency near 1Hz, but adopting that frequency for our work, the full extreme of each redox pulse may not be sufficiently experienced by the entire depth of powder in the boat. Our conditions were adopted from prior work with quartz boat powder aging in a flow reactor [21]. At 10 minutes in pulse length, the entire bed of powder was sufficiently exposed to rich and lean environments on each step.

The CO gas stream was scrubbed of iron carbonyls before introduction to the reactor. A 1.50 g portion of catalyst powder was loaded in a quartz boat and placed inside a 19 mm ID quartz reaction tube in the heating zone of the surrounding oven. A thermocouple was placed over the boat in the aging gas stream and a second

thermocouple was bent into the boat with the tip buried in the powder. A few samples were given lean treatments at 550°C or 700°C for two hours in 21% O_2/He or zero air to redisperse the sintered Pd particles. Gasoline engines typically operate close to the fuel/air stoichiometric ratio so the automotive catalyst OSC state is generally partly depleted. The catalyst samples in this work were characterized and evaluated in the reduced state by exposing them to a flow of 9% H_2 in argon at 300°C for 30 minutes prior to cooling in argon to room temperature.

3.2.3 Catalyst Characterization Techniques

The Pd/Al and Pd/CZO catalysts bulk composition was confirmed by X-ray Fluorescence (XRF) while the support phase identification was performed with X-ray diffraction (XRD) pattern analysis. The elemental composition was determined using a Philips PW2400 XRF Spectrometer and UniQuant5 software. A catalyst sample mass of 0.7 g on top of 4.5 g of boric acid in aluminum caps were compacted into pellets with a hydraulic press. Pd was quantified using the Lα1 X-ray line. Support phase identification was performed with a Rigaku Miniflex II diffractometer with Cu Kα X-Ray (λ = 1.5406Å) radiation source set at 30 kV and 15 mA. A catalyst sample mass of 0.1 g was wet-milled with a mortar and pestle in ethanol then dripped onto an off-axis cut silicon crystal sample substrate and dried. Scans were performed with a step size of 0.005°2θ at a scan speed of 1°2θ/min from 5°2θ to 90°2θ.

The surface characteristics of the catalysts were determined by N_2 physisorption and X-ray photoelectron spectroscopy (XPS). The BET specific surface area and BJH pore volume (for pores between 17-300Å) were determined with a Micromeritics ASAP2420 instrument using N_2 adsorption at 77K. A 48-point adsorption and 33-point desorption isotherm plot was generated across a range of 0.1-0.9 P/P_0. Elemental composition and chemical state information were determined with a Kratos AXIS 165 Electron Spectrometer using a monochromatic Al Kα (1486.6 eV) X-ray excitation source operated at 12 kV, 20 mA (240 W). Each sample was pressed into a pellet and then mounted onto sticky double sided pressure sensitive adhesive tape. Data was collected using pass energies of 80 eV or 20 eV to collect survey or high resolution

spectra, respectively. All spectra were acquired using charge neutralization with an electron flood source. Elemental quantification of the high resolution spectra was accomplished using CASAXPS software Version 2.3.16, using routines based on Scofield photoionization cross-section values. A Shirley type background was used to fit all high resolution spectra. For Pd on alumina support the high resolution Pd 3d spectra was fit with a doublet using 60% Gaussian and 40% Lorentzian line shapes with an area ratio of 0.667, a full width at half-maximum (FWHM) constrained within 0.6-2.8, and a peak separation of 5.2 eV. For Pd on CZO support, the Zr 3p fit was first determined from a CZO standard using 60% Gaussian and 40% Lorentzian line shapes with an area ratio of 0.5, a FWHM constrained between 0.6-2.8, and a peak separation of 13.4 eV. The remaining area under the envelope was then fit by adding Pd 3d peaks using the fitting parameters described above for Pd on alumina. Binding energies were referenced to the aliphatic C 1s peak at 284.6 eV [22].

Pd particle size estimates were performed using three techniques. Post-process curve fitting of the XRD pattern Pd peak for mean Pd crystalline length was performed with the Rigaku PDXL software program. The software calculations used for estimating mean Pd crystalline length from XRD pattern line broadening was based on the Scherrer equation [23]. The shape factor used was 0.89 for spherical crystallites and the peak integral method was used to determine peak breadth. The instrument broadening was corrected with a LaB_6 calibration standard. H_2 chemisorption was performed using a Micromeritics ASAP2020 instrument with a static volumetric adsorption/out-gas/re-adsorption method described by Chen *et al.* [10]. Prior to analysis, each sample was first degassed in N_2 at 500°C, reduced at 350°C in pure H_2, exposed to vacuum at 1 microtorr and finally dosed with H_2 at 35°C for chemisorption measurements using a 5-point isotherm extrapolated to zero pressure. This technique is an improvement upon the classic H_2–O_2 titration method and avoids problems of H_2 spill-over and Pd hydride formation from interfering with the irreversible adsorbed H_2 calculation [24, 25]. The differential results were used to report Pd dispersion and size to exclude physisorbed H_2 on the support. H_2 chemisorption was used for all samples since we found that CO chemisorption significantly overestimated the Pd dispersion on the CZO supports, probably due in part to CO adsorption on CZO forming stable

carbonate species [26]. Scanning transmission electron microscope (STEM) images were collected with a JEOL 2010F instrument using high angle annular dark-field (HAADF) imaging. The microscope was equipped with a zirconated tungsten [100] thermal field emission tip filament and operated at $1.5x10^{-7}$ torr vacuum with 200kV accelerating voltage. The JEOL HAADF detector had a probe size of 0.5 nm and camera length of 12 cm. Samples for imaging were prepared by dispersing 10mg of catalyst sample powder in 2 mL of ethanol followed by ultrasonification for one hour to make a suspension, then dripped onto a 200-mesh carbon coated copper grid and dried. The Pd particle diameter was calculated with Image J software. A JEOL 3100R05 Double Cs-Corrected analytical electron microscope with a resolution of 0.055 nm point-to-point was used to image Pd/CZO samples. However, even with this powerful instrument, we were unable to discern Pd on CZO due to the poor diffraction contrast between Pd and the CZO support. Furthermore, electron beam heating caused rapid growth of carbonaceous overlayers obscuring the image and hindering elemental mapping by energy-dispersive X-ray spectroscopy. After removal of these carbonaceous overlayers in a heated sample stage, charging induced image artifacts made it impossible to reach the required resolution.

3.2.4 Catalyst Activity Measurements

A flow reactor was used to enable measurement of CO_2 formed by probe reaction tests on a characterized catalyst sample. The ASAP2020 quartz j-tube and sample used in the H_2 chemisorption test was fit onto the flow reactor. The j-tube measured 10.5 mm ID and a catalyst sample mass of 0.30 g was loaded between 6 mm redistributing layers of quartz wool. The bed height was 4 mm for the Pd/CZO and 6 mm for Pd/Al samples. Matheson dynablenders and flow controllers managed the gas flow through the system. The gas stream could be triggered to route through a water bubbler and lines were maintained at 150°C to limit condensation. The CO gas stream was scrubbed of iron carbonyls with alumina chips heated at 350°C. Two K-type 1/32-inch diameter thermocouples were placed 16 mm before and 13 mm after the sample bed. A Hiden HPR20 quadrupole electron ionization mass spectrometer with Secondary Electron Multiplier (SEM) detector measured five mass values in torr with a 2

Hz sampling rate at an inlet sampling pressure of 1E-5 torr and required two corrections to normalize the signals from other species into individual concentrations. First, the double excitation argon (Ar) mass 20 value was scanned, which is 11% of the total Ar level, rather than the typical mass 40 to get the measured Ar value below the SEM detector limit of $1x10^{-6}$ torr. Second, there was a CO and CO_2 mass overlap of 11.4%, so that amount of the CO_2 value was subtracted from the CO value. OSC measurements were run by alternating one minute lean or rich pulses, each separated by a one minute purge. The purge pulse was CO_2 and Ar at 975 mL/min while a square step pulse of CO in Ar or O_2 in Ar was added at 25 mL/min. The lean pulse was 1% O_2, 2% CO_2 and balance Ar. The rich pulse was 2% CO, 2% CO_2 and balance Ar. At least five CO pulses were measured in each 50°C increment, starting at 50°C and ending at 400°C. WGS measurements were run with a constant feed of 2% CO, 2% CO_2, 2.5% H_2O and Ar at 1 L/min. The gas mixture was initially established at equilibrium over the catalyst sample at 50°C, then the oven heating ramp was triggered at 10°C/min to 400°C.

3.2.5 Vehicle TWC Emission and Temperature Evaluation

The Ford Motor Company vehicle emission research laboratory (VERL) evaluated a 2009MY 2.0L Ford Focus test vehicle with gasoline fuel. Only the front tires were in contact with the exposed dynamometer roll surface that simulated EPA certification road conditions. The vehicle was operated using the light-duty vehicle FTP-75 (federal test procedure) and US06 Supplemental Federal Test Procedure (SFTP). Tailpipe emissions were measured using Horiba MEXA 9000 analyzers at a 1 Hz data collection rate and the exhaust emissions and fuel parameters were used to calculate the engine exhaust lambda equivalence ratio, or the actual air/fuel ratio divided by the stoichiometric air/fuel ratio, by the Spindt method [27]. K-type thermocouples were installed through-out the exhaust system including one in the catalytic converter bed location, which was 1 inch downstream of the first brick front face.

3.3 Results

3.3.1 Sample Composition Characterization and Aging Comparison

The XRF elemental oxide composition results of the Pd model catalysts are shown in Table 3-1. Concentrations were calculated as oxides (except Pd, which was calculated as an element). Reported values of just the top components are listed in weight percent since minor amounts of other species were also detected in the catalyst sample. The catalysts contained the same amount of Pd metal. The Pd/Al catalyst contained about 94% alumina with about 4 wt% lanthana added for surface area stabilization against steam. The 0.4 wt% Pr_6O_{11} in the aluminum support was considered an impurity of the lanthana. The Pd/CZO catalyst contained primarily ceria and zirconia oxide in a weight ratio of 56/44 and atomic ratio of 50/50. The 0.8 wt% HfO_2 was considered an impurity of zirconia.

Table 3-1: Characterization of fresh sample elemental oxide compositions by XRF

Pd/Al	Pd/CZO
93.7 wt% Al_2O_3	54.7 wt% CeO_2
3.86 wt% La_2O_3	42.4 wt% ZrO_2
1.42 wt% Pd	1.42 wt% Pd
0.40 wt% Pr_6O_{11}	0.80 wt% HfO_2
0.30 wt% SO_3	0.49 wt% Al_2O_3
0.05 wt% CaO	0.10 wt% La_2O_3
0.27 wt% other	0.09 wt% other

The conditions used to age these catalyst samples were compared to the literature. Peuckert developed an equation for the temperature of bulk PdO decomposition as a function of gas phase oxygen concentration [16]. Figure 3-1 shows a plot of that equation for a pressure of 1 atm. Lieske and Völter observed that Pd needed to be oxidized before redispersion would occur [14], so the “Pd Redispersion Zone” shown in Figure 3-1 must extend below the PdO decomposition line. The lean-only and lean redox step at 700°C used just 0.5% O_2, an environment where the catalyst was above the bulk PdO decomposition temperature of about 670°C. Colussi *et al*. ran heating/cooling cycles in 0.5% O_2 and observed a similar 677°C onset

temperature of PdO decomposition when supported on either Al_2O_3 or 10%CeO_2-Al_2O_3, however the PdO reformation temperature began near 600°C on 10%CeO_2-Al_2O_3 and near 500°C on Al_2O_3 [17]. Therefore, once the PdO on our catalysts decomposed into Pd near 670°C during heating in 0.5% O_2 up to 700°C, reoxidation of Pd would not occur until the temperature had dropped below the hysteresis temperature. Consequently, the supported Pd would likely be in the metallic state for all three aging environments. The lower Pd redispersion zone boundary was tested with lean treatments at 550°C or 700°C in dry air, an environment where the supported catalyst was well below the bulk PdO decomposition temperature of about 800°C. These lean treatment conditions were based on work by Chen *et al*. who demonstrated higher Pd dispersion when the lean feed gas stream was dry compared to one containing 10% steam [10].

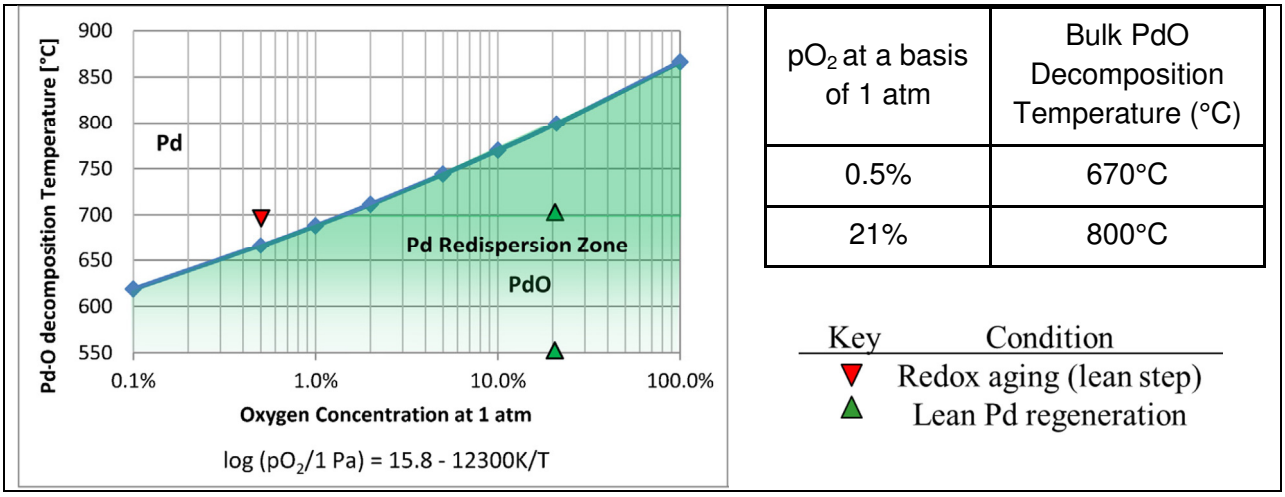

pO_2 at a basis of 1 atm	Bulk PdO Decomposition Temperature (°C)
0.5%	670°C
21%	800°C

Key	Condition
▼	Redox aging (lean step)
▲	Lean Pd regeneration

Figure 3-1: Palladium oxide thermal stability from reference [16]

3.3.2 Surface Area and Pore Volume Characterization

The BET surface area and BJH adsorption pore volume for each sample are listed in Table 3-2, both fresh and after exposure to various aging environments. The fresh Pd/Al sample had a surface area of 209 m^2/g and a pore volume of 0.58 cm^3/g. The 700°C/16 hour lean aged Pd/Al sample showed a decrease of about 20% in surface area and about 7% in pore volume, relative to the fresh Pd/Al sample. All of the aged Pd/Al samples had a surface area within 3% of 160 m^2/g and the pore volume

within 2% of 0.54 cm^3/g, which demonstrated an insensitivity of the alumina to the aging environments. The fresh Pd/CZO sample had a surface area of 91 m^2/g and a pore volume of 0.16 cm^3/g. The 700°C/16 hour lean aged Pd/CZO sample showed a decrease of about 46% in surface area and 6% in pore volume relative to the fresh Pd/CZO sample. The redox aging method was the most severe for the Pd/CZO samples with a 62% surface area loss compared to loss of 55% for rich-only and 46% for lean-only. Unlike alumina, CZO is a reducible support under these conditions and the repeated redox cycling was more degrading to CZO than the constant rich-only environment after 16 hours. The Pd/TWC sample had a surface area and pore volume in between that of the Pd/Al and Pd/CZO samples. The lean treatments of 550°C/2h or 700°C/2h in air showed minor effects on the surface area or pore volume. The fresh Pd/A sample had a surface area of 138 m^2/g and a pore volume of 0.75 cm^3/g. The 700°C/16 redox aged Pd/A sample showed a decrease of about 10% in surface area and no loss of pore volume relative to the fresh Pd/A sample. The fresh Pd/A sample had about 30% lower surface area, but about 20% higher pore volume than the fresh Pd/Al sample. The fresh CZO sample had similar surface area, but over twice the pore volume than the fresh Pd/CZO sample.

Table 3-2: Characterization of fresh and aged catalyst samples							
Sample	Condition	Surface Area [m^2/g]	Pore Volume [cm^3/g]	Pd dispersion [%]		Pd particle size [nm]	
				by H_2[a]	by XRD[b]	by H_2[a]	by XRD[b]
Pd/Al	Fresh	209	0.58	9.1%	7.9%	12	14
	Lean-only 700°C/16h	164	0.54	5.0%	5.9%	22	19
	Rich-only 700°C/16h	158	0.54	1.0%	6.8%	107	16
	+ 550°C/2h air	157	0.53	4.6%	7.5%	24	15
	Redox (10/10) 700°C/16h	164	0.55	0.7%	6.8%	159	16
	+ 550°C/2h air	161	0.54	3.9%	7.3%	28	15
	+ 700°C/2h air	157	0.53	5.7%	7.6%	19	14
Pd/CZO	Fresh	91	0.16	22%	u/d	4.9	u/d
	Lean-only 700°C/16h	49	0.15	15%	u/d	7.3	u/d
	Rich-only 700°C/16h	41	0.15	u/d	10%	u/d	11
	+ 550°C/2h air	41	0.15	0.8%	10%	134	11
	Redox (10/10) 700°C/16h	35	0.15	u/d	5.6%	u/d	20
	+ 550°C/2h air	35	0.15	u/d	5.4%	u/d	20
	+ 700°C/2h air	35	0.15	4.1%	4.5%	27	24
Pd/TWC	Fresh	138	0.34	12%	14%	9.2	7.8
	Redox (10/10) 700°C/16h	94	0.33	u/d	8.7%	u/d	13
	+ 550°C/2h air	97	0.35	2.3%	7.4%	49	15
	+ 700°C/2h air	90	0.33	4.9%	8.2%	23	13
Pd/A	Fresh	138	0.75	10%	11%	11	10
	Redox (10/10) 700°C/16h	124	0.80	5.0%	7.4%	22	15
CZO	Fresh	97	0.46	-	-	-	-

[a] H_2 Chemisorption by difference method, [b] XRD Pd peak fit by Scherrer equation

3.3.3 Pd Particle Size Characterizations

Three techniques were used to assess the changes to the Pd particle size from the fresh to aged state, since each had limitations. The XRD peak analysis provides a quantitative volumetric bulk estimate of the Pd crystallite size, unless the Pd particles are agglomerated crystallites, or a large number of the Pd particles are small (<7 nm) and undetectable apart from the background XRD pattern. H_2 chemisorption provides a quantitative measurement of exposed metal surface, but strong metal-support interactions reduce probe molecule adsorption [18,19] and yield overly large calculated Pd particle sizes. The STEM image was assumed to contain spherical shapes to calculate the Pd particle diameter. Imaging the Pd particles on CZO samples proved

too difficult since electron microscopy provides little contrast between small metallic Pd particles and a CeO_2 support [20].

The bulk Pd metal dispersion (D) is related to the bulk Pd particle size (d_P), assuming spherical shapes, by the following equation used by Baylet *et al*. [28]:

$$D\ [\%] = (6 \times 10^5) * (M_{Pd}) / (\rho_{Pd} * S_{Pd} * d_P\ [nm])$$

With M_{Pd} as the palladium molar weight of 106.4 g/mol, ρ_{Pd} as the palladium density of 12 g/cm^3, S_{Pd} as the molar surface area of palladium assuming an equidistribution of the low index faces of 47,780 m^2/mol for Pd metal.

3.3.3.1 XRD Pattern Phase Identification

The XRD patterns of the fresh, aged and post lean treated samples of Pd/Al are shown in Figure 3-2a and are consistent with gamma alumina support material. The XRD patterns of the fresh, aged and post lean treated samples of Pd/CZO are shown in Figure 3-2b and are consistent with the expected peaks for CZO support. No new support phases were observed during the 700°C aging for either model catalyst. The redox aged Pd/CZO sample had a small peak emerge at 26.4°2θ, which could be the cubic phase of Ce_2O_3 [100] and indicate an aging induced phase separation out of bulk CZO [29, 30, 31], but the accompanying peak of Ce_2O_3 [101] at 30.3°2θ is not in the pattern, so this peak at 26.4°2θ is the K(β) reflection of CZO [111]. The Pd metal peak was observed at 40°2θ only for the redox and rich-only aged Pd/CZO samples. The fresh and lean-only aged CZO samples had Pd particles that were too small to be detected by XRD. The XRD patterns of the combined Pd/TWC sample are shown in Figure 3-2c with every Pd peak at least partially confounded by a support peak. The Pd peak used to obtain line broadening or peak width measurements for particle size determination was 40°2θ [111] on the Pd/CZO and Pd/TWC samples, and 82°2θ [311] on the Pd/Al samples.

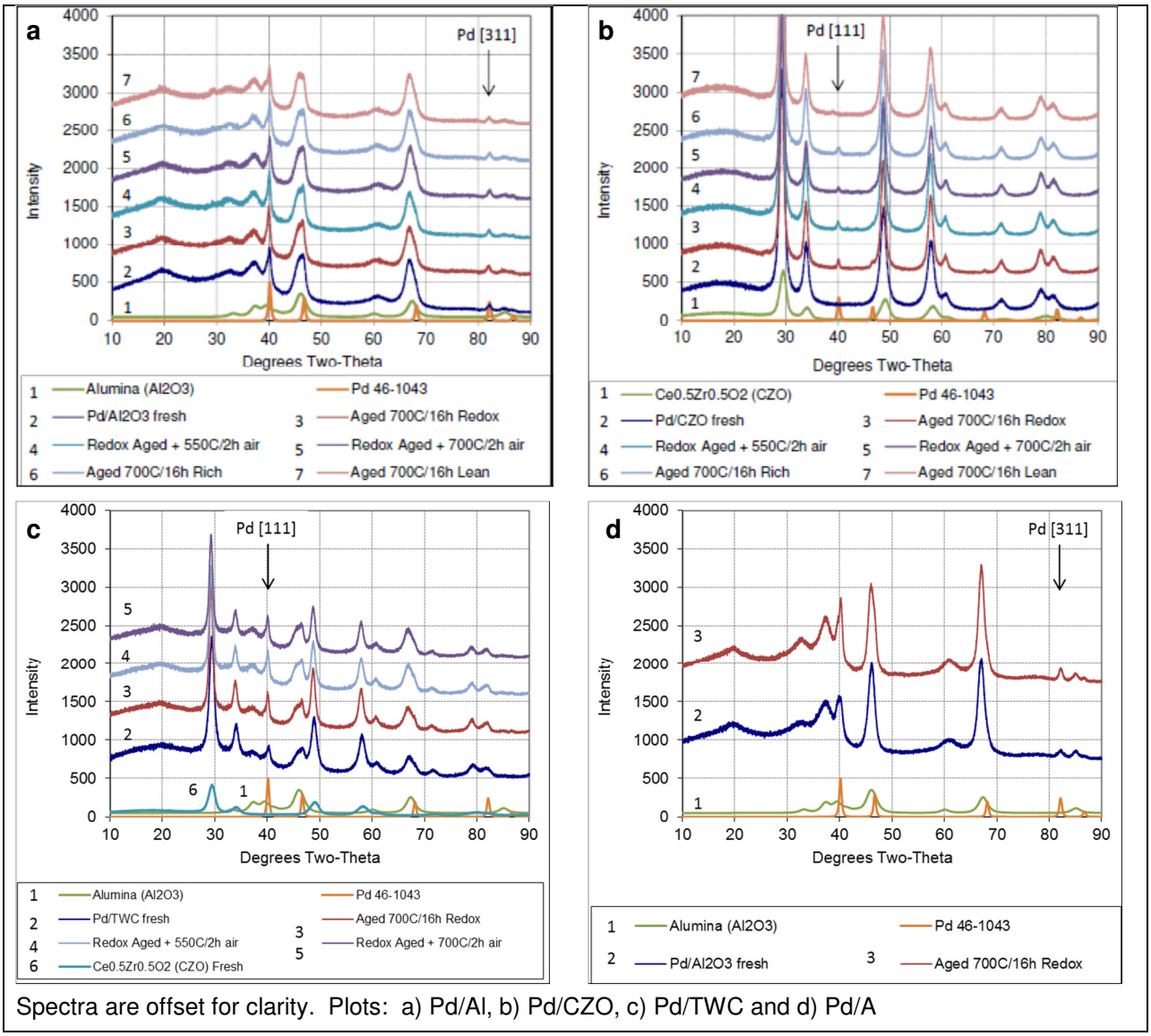

Spectra are offset for clarity. Plots: a) Pd/Al, b) Pd/CZO, c) Pd/TWC and d) Pd/A

Figure 3-2: Pd supported samples X-ray Diffraction patterns

3.3.3.2 Average Pd Size Estimation Comparison with H_2 Chemisorption and XRD

The apparent Pd dispersion and Pd particle size for each sample are listed in Table 3-2. Some conditions resulted in undetectable (u/d) Pd size measurements. The Pd metal sintering severity as measured by XRD was similar for each aging environment on the Pd/Al samples, but had a clear trend with environment on the Pd/CZO samples with redox (20 nm) > rich-only (11 nm) > lean-only (u/d). These Pd/Al size results seem to conflict with the results of Chen *et al*. on Pd/Al_2O_3 or Kang *et al*. on

Pd/TWC that showed much more severe Pd dispersion loss with rich aging than lean aging in the temperature range of 600°C-700°C [10, 32], however their lean aging feed included 3% O_2 or more that maintained the Pd in the oxidized state to prevent sintering while the 0.5% O_2 used in our lean aging feed fell below the Pd-PdO transition conditions shown in Figure 3-1. Large discrepancies in rich-only and redox aged sample Pd dispersion results between H_2 chemisorption and XRD methods in Table 3-2 may indicate that the support material chemically affected the Pd particles, partially encapsulated the Pd particles or decorated the Pd surface, which are all examples of strong metal support interaction (SMSI) [18, 19, 20, 33, 34, 35, 36, 37, 38].

The lean treatment at 550°C or 700°C had different effects on the Pd particle sizes listed in Table 3-2 depending on the support material and aging environment. The lean treatment of 550°C/2h showed minor improvements in Pd dispersion as measured by H_2 chemisorption, but the redox aged Pd/CZO sample stayed undetectable. The Pd size measured by XRD appeared to confirm that the lean treatment of 550°C/2h had a minor reduction for the redox and rich-only aged Pd/Al samples, while showing no change for the Pd/CZO samples. The lean treatment of 700°C/2h on the redox aged Pd/Al sample increased Pd dispersion from 0.7% to 5.7% as measured by H_2 chemisorption, which appeared to be confirmed by XRD with a reduction of 2 nm in the bulk Pd crystallite size. The lean treatment of 700°C/2h on the redox aged Pd/Al sample produced Pd particles that were comparable in size to the lean-only aged Pd/Al sample as measured by H_2 chemisorption. The lean treatment of 700°C/2h on the redox aged Pd/CZO sample increased Pd dispersion from u/d to 4.1% as measured by H_2 chemisorption, but a bulk Pd crystallite size reduction was not confirmed by XRD. With both lean treatments, H_2 chemisorption and XRD Pd peak fitting methods suggest that Pd redispersion occurred on the redox aged Pd/Al samples, while both methods did not agree that Pd redispersion occurred on the Pd/CZO samples. The 700°C lean treatment demonstrated better Pd redispersion results than the 550°C lean treatment.

3.3.3.3 STEM Image

The STEM images for fresh and redox aged Pd/Al samples are shown in Figure

3-3. The Pd particles shown in the dark field are bright and appear to be roughly circular in shape given the 2D image. Figure 3-3a shows the small Pd particles in the fresh condition while Figure 3-3b shows much larger Pd particles after redox aging at 700°C for 16 hours. Figure 3-3c shows the Pd particles size and shape after the lean treatment at 550°C for 2 hours lacked the large crystals compared to before the lean treatment in Figure 3-3b. Figure 3-3d shows the Pd particles size and shape after the lean treatment at 700°C for 2 hours are smaller compared to before the lean treatment in Figure 3-3b. In addition, Figure 3-3d shows Pd particles with "hollow" centers, perhaps due to the presence of a void space at the core, as has been reported elsewhere for Pd metallic particles that were oxidized and then reduced [39, 40, 41]. Other works with high temperature oxidation of Ni and Co metallic particles, suggest that this void formation was caused by a diffusion couple between metal cations and anions where an inward flux of vacancies towards the particle core was required to offset the flux of faster cations towards the particle surface [42, 43]. This process, also known as the nanoscale Kirkendall effect, eventually generates hollow metal particles when the concentration of vacancies at the core is sufficient to coalesce into a single large void [43]. We attempted acquiring HRTEM images to prove direct evidence of a reducible ceria oxide thin film covering on Pd, but were ultimately unsuccessful at discerning Pd from CZO.

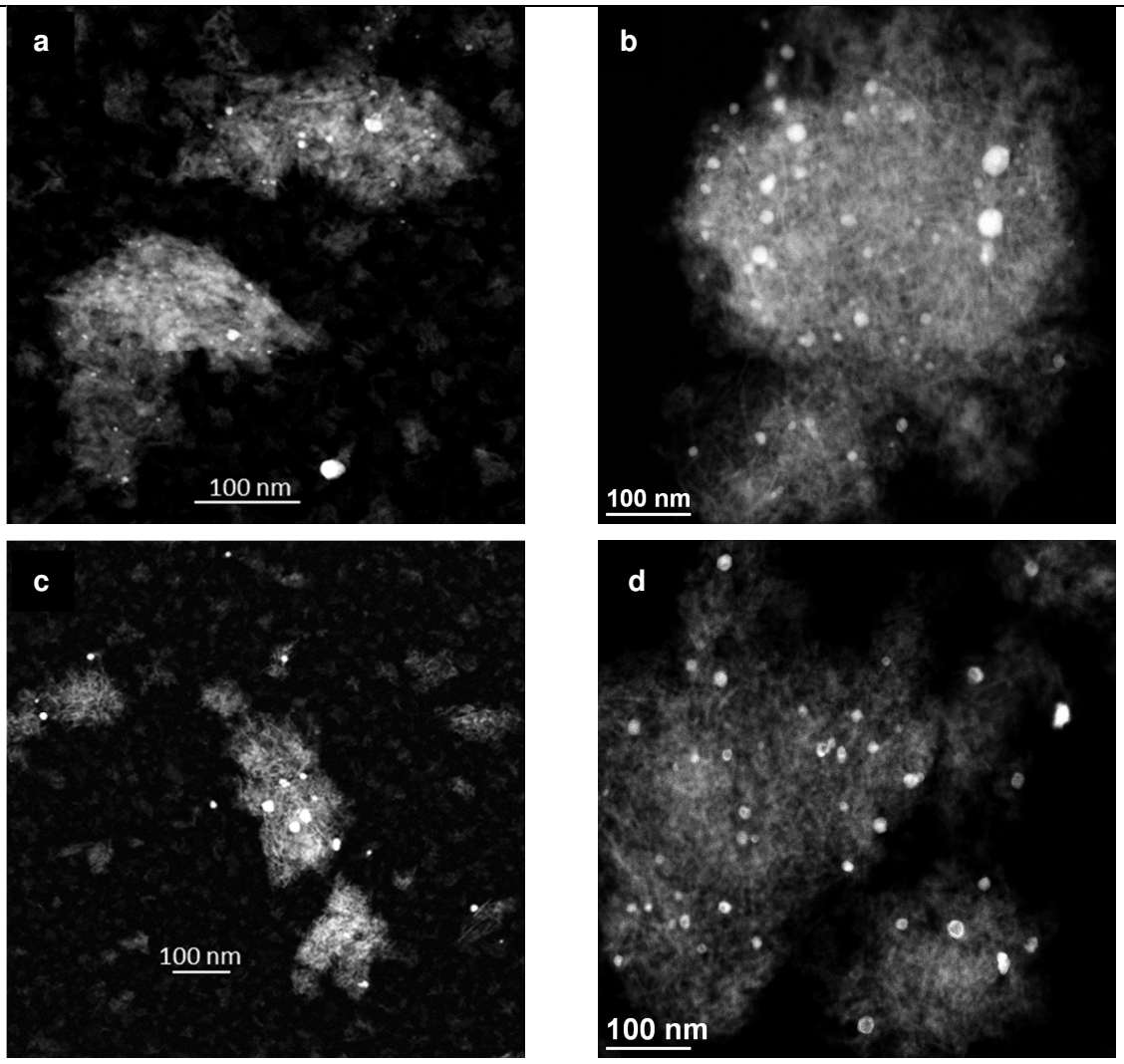

Plots: a) Pd/Al Fresh, b) Redox Aged 700°C/16h, c) Redox Aged + 550°C/2h air and d) Redox Aged + 700°C/2h air

Figure 3-3: Pd/Al samples imaged with HAADF STEM

The counted Pd particles are shown as histograms in Figure 3-4 with the number average Pd particle size with 99% confidence interval on the mean. The histogram x-axis bins are labeled at the maximum value in the bin range. For example 15 nm is the counted particles in the 11-15 nm range. The aged samples particle size distribution (PSD) each followed a bell shaped curve or normal distribution; except for the fresh PSD that had a long tail of large particles. Therefore, a statistical analysis is applicable for the aged catalysts. A confidence interval contains a set of plausible values for a parameter, such as a mean. A confidence interval equals a theoretical probability point

of normally distributed data at critical point α with n-1 degrees of freedom ($t_{\alpha/2,n-1}$), times the standard deviation of the data set (*s*), divided by the square root of the number of counted particles (n): [44].

$$CI = (t_{\alpha/2,n-1})^*(s)/SQRT(n)$$

This evaluation is done by comparing one mean and examining if it is outside the confidence interval around another mean.

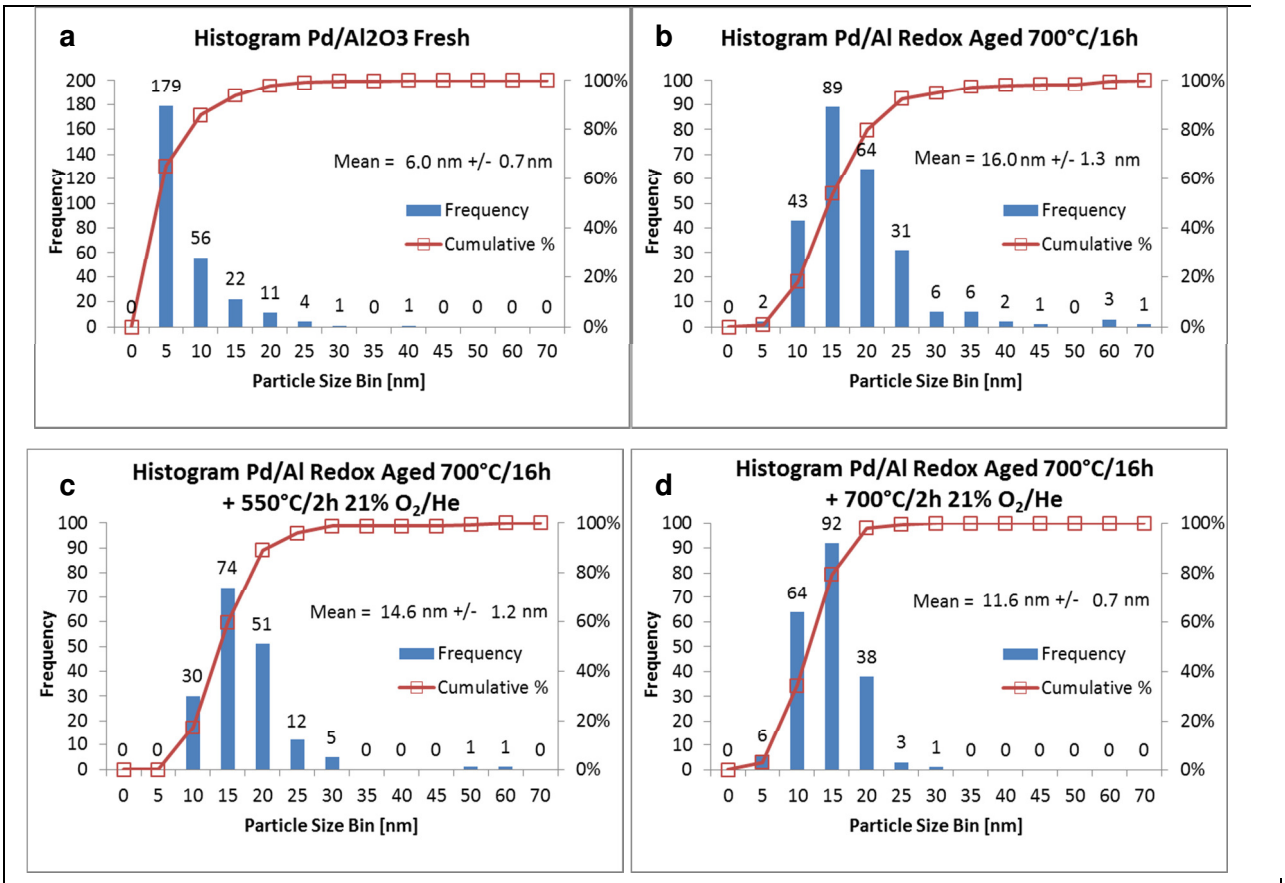

Pd/Al samples Pd size numerical mean shown with 99% confidence interval. Plots: a) Pd/Al Fresh, b) Redox Aged 700°C/16h, c) Redox Aged + 550°C/2h air and d) Redox Aged + 700°C/2h air

Figure 3-4: Pd particle size histograms based on STEM Images of Pd/Al samples

The fresh sample Pd particles in Figure 3-4a had a numerical mean diameter of 6.0 nm +/- 0.7 nm, showing most of the particles in the small range up to 10 nm and a long particle size distribution tail greater than 25 nm. After the 700°C/16h redox aging, the sintered Pd particles in Figure 3-4b had a numerical mean diameter of 16.0 nm +/-

1.3 nm. The redox aged particles had a tail of “small” particles up to 10 nm making up 18% of the cumulative total and a tail of “large” particles greater than 25 nm making up 5% of the cumulative total. The 550°C/2h lean treatment produced a numerical mean of 14.6 nm +/- 1.2 nm; a statistically significant reduction in Pd size of 1.4 nm. The tails of small (up to 10 nm) Pd particles were 17% of the cumulative total, essentially unchanged from before the 550°C/2h lean treatment. The cumulative total of large (>25 nm) Pd particles decreased to 1%, a reduction from 5%. Therefore at 550°C in air, the extent of Pd redispersion did not generate new small particles, but shrank the particles greater than 15 nm, increasing the count of particles measuring 11-15 nm from 36% to 43% of the total. The 700°C/2h lean treatment produced a numerical mean of 11.6 nm +/- 0.7 nm; a reduction in Pd size of 4.4 nm. The tails of small (up to 10 nm) Pd particles were 34% of the cumulative total, up from 18% before the 700°C/2h lean treatment. The cumulative total of large (>25 nm) Pd particles decreased to 0%, a reduction from 5%.

The STEM images of metal particles with diameter, d_i, and the number of particles of a particular diameter, n_i, can be calculated as a surface-averaged diameter to compare against H_2 chemisorption results and a volume-averaged diameter to compare against XRD results as shown by the equations below used by Adams *et al*. [45]:

Number-Average	Surface-Average	Volume-Average
$d_n = \Sigma n_i d_i / \Sigma n_i$	$d_s = \Sigma n_i d_i^3 / \Sigma n_i d_i^2$	$d_v = \Sigma n_i d_i^4 / \Sigma n_i d_i^3$

The resulting STEM number average, surface average and volume average Pd particle size results are shown in Table 3-3 for fresh and redox aged Pd/Al samples. The Pd particle size measurement from surface averaged STEM and H_2 chemisorption were comparable for all samples except the 700°C/16h redox aged sample, likely due to strong metal-support interaction with La_2O_3, which is known to interact with Pd and reduce H_2 adsorption strength [19]. The Pd particle size determined from volume average STEM and XRD were comparable for the fresh and 700°C/2h air treatment

sample, but were at least twice the Pd crystallite length determined from XRD for the other samples, indicating that some Pd particles in Figure 3-3 may have been agglomerates of two or more Pd crystals. The STEM Pd size results listed in Table 3-3 confirm the Pd size reduction results reported in Table 3-2 on the redox aged Pd/Al sample after 700°C/2h air treatment and to a lesser degree the 550°C/2h air treatment.

Table 3-3: Comparison of Pd particle diameter measured with STEM to other methods

Pd/Al Samples	Particles Counted, n	Number-Average, d_n [nm]	Surface-Average, d_s [nm]	H_2 Chemisorption [nm]	Volume-Average, d_v [nm]	XRD [nm]
Fresh	274	6	15	12	22	14
Redox 700°C/16h	248	16	27	159	36	16
+ 550°C/2h air	174	15	22	28	30	15
+ 700°C/2h air	204	12	14	19	15	14

3.3.4 XPS Surface Characterization

The atomic surface concentrations of the top surface layers are shown in Table 3-4. For the Pd/Al and Pd/A samples, the amount of Pd stayed the same for both fresh and redox aged. This consistency of exposed Pd surface from fresh to aged agrees with the XRD measurements in Table 3-2 where the Pd size increased from 14 nm to only 16 nm after redox aging on Pd/Al and from 10 nm to just 15 nm after aging on Pd/A. These Pd sizes are well within the detection depth of the XPS instrument. These XPS results also do not show the dramatic drop in Pd dispersion that the H_2 chemisorption results showed for the redox aged Pd/Al sample. The Pd/Al sample showed that surface La increased by 50% from fresh to aged, yet surface Pd stayed about the same, which does not support the proposed model of reduced La_2O_3 species decorating the Pd particle during reducing aging conditions as proposed by Bell *et al*. [19, 46, 47]. The increase in La_2O_3 while maintaining similar Pd surface concentrations after aging could be explained by: 1) sintering of the alumina surface area leaving more La_2O_3 at the surface, coupled with 2) a phase segregation caused by reducing conditions, which drove more La_2O_3 to the surface that could then interface with the Pd particles. The latter explanation may cause the Pd to exhibit gas phase adsorption characteristics as if supported on La_2O_3 rather than on alumina. For the Pd/CZO catalyst, redox aging

decreased the surface concentration of Pd by half simultaneously with a surface concentration increase in Ce by 30% and Zr by 10%, without a significant increase in oxygen. The XRD measurements in Table 3-2 showed the Pd size increased from less than 7 nm (u/d) to 20 nm after redox aging on Pd/CZO, which was larger than observed on alumina. The loss of half the initial surface Pd atoms from XPS detection coupled with increased surface Ce and Zr atoms was partially due to increased particle size and may also confirm that the reduced support crept up the sides or decorated the Pd surface during redox aging. The increase in surface atoms of Ce was three times the increase in Zr, which is beyond the 50/50 atomic ratio of the support and may be explained by a phase separation of CZO where reducible Ce oxide species decorated the Pd surface leaving behind a support richer in ZrO_2. All samples had some adventitious carbon on the surface due to exposure to air and the CZO support material attracted more than the alumina.

Table 3-4: XPS surface elemental composition: atomic percent (at%)

Sample	C	O	Pd	Ce	Zr	Al	La	Pr
Pd/Al Fresh	13.5	48.5	0.22	-	-	37.6	0.20	0.02
Pd/Al Redox 700°C/16h	11.7	49.9	0.23	-	-	37.8	0.30	0.01
Pd/A Fresh	11.8	48.7	0.24	-	-	39.3	-	-
Pd/A Redox 700°C/16h	12.0	48.1	0.22	-	-	39.6	-	-
Pd/CZO Fresh	28.6	55.4	0.40	4.5	10.9	-	-	-
Pd/CZO Redox 700°C/16h	26.4	55.5	0.21	5.9	12.0	-	-	-

The XPS spectra of the Pd/A and Pd/Al catalyst samples are shown in Figure 3-5, plots a-c. The Pd/Al sample had a Pd $3d_{5/2}$ peak appear at 334.8 eV +/- 0.1 eV for both fresh and aged conditions that corresponds to the metallic state, plus the fresh Pd/Al sample had a shoulder at about 336.5 eV for Pd^{+2} perhaps due to Pd interface sites with the support La_2O_3. These results are comparable to XPS work reported by Zhao *et al*. on fresh, reduced 1.4wt% Pd on La_2O_3-Al_2O_3 support that had the Pd $3d_{5/2}$ peak at 335.2 eV for metallic Pd with a shoulder at 336.5 eV for Pd^{+2} [48]. The Pd/Al sample metallic Pd peak location was shifted below the value reported by Zhao *et al*. by 0.7 eV. The Pd/A sample had a Pd $3d_{5/2}$ peak appear at 334.5 eV +/- 0.1 eV for both fresh and aged conditions that corresponds to the metallic state, but did not show a peak for Pd^{+2}. Pd catalysts exposed to a high temperature reduction in hydrogen have been reported

to show a chemical shift or reduced peak intensity due to reducible oxides in the support [18, 37, 46, 49]. However, the position of the Pd/A sample Pd metal peak is similar to that observed with the Pd/Al sample, in spite of the absence of La_2O_3. The Pd/Al sample La 3d peaks did not show a peak shift or change in intensity from the fresh to aged state.

The XPS spectra of the Pd/CZO catalyst samples are shown in Figure 3-5, plots d-f. The Zr 3p plot of the reference CZO material compared to the Pd/CZO sample shows similar peak position. The Pd 3d peaks were fit inside the shoulders of the Zr 3p peaks. The fresh Pd/CZO sample had two Pd $3d_{5/2}$ peaks, a smaller one at 335.1 eV for Pd metal and a larger one at 336.9 eV for Pd^{+2}. While the fresh catalyst sample was reduced, about half of the fresh Pd was still Pd^{+2}, perhaps due to an abundance of interface sites with finely dispersed Pd and oxygen from CeO_2. These results are comparable to XPS work reported by Zhao *et al*. on fresh, reduced 1.4wt% Pd on $Ce_{0.65}Zr_{0.30}La_{0.05}O_2$ support that had the Pd $3d_{5/2}$ peak at 335.9 eV, although no separate peaks of Pd^0 and Pd^{+2} were fitted [48]. The Pd metal peak location of Pd/CZO was 0.4 eV higher than Pd/Al and 0.6 eV higher than Pd/A. Redox aging of the Pd/CZO catalyst and accompanying coverage of Pd by CZO changed the Pd $3d_{5/2}$ peak location of Pd metal by +0.2 eV, but the Pd^{+2} peak was no longer observed. Alexandrou and Nix deposited CeO_2 on top of a Pd [111] single crystal substrate and observed a positive binding energy shift in the Pd $3d_{5/2}$ peak at 334.5 eV (clean) by about +2 eV with 3.8 mL of CeO_2, which was not reversed upon oxidation [35]. While Alexandrou and Nix ruled out Pd-Ce alloying [35], oxidation of metallic Pd interface sites by deposited CeO_2 may explain their observed positive binding energy shift. Since Figure 3-5e shows minimal Pd peak shift with no Pd^{+2} peak after redox aging, the metallic Pd interface sites with oxygen supplied by CeO_2 were lost after coverage by Ce. The Pd/CZO sample Ce 3d peaks had a slight increase in intensity from the fresh to aged state, but the Ce $3d_{5/2}$ peak at 882.0 eV or the Ce $3d_{5/2}$ peak at 900.4 eV did not show a shift. The other Ce 3d peaks shown were satellite peaks that arose from interactions with the Ce 4f valence electrons after the 3d core electron was emitted. Each core level ($3d_{5/2}$ and $3d_{3/2}$) had 3 satellite peaks associated with it. The $3d_{5/2}$ satellite peaks were at v' = 884.0 eV, v'' =

889.1 eV, and v''' = 897.8 eV. Analogously, the 3d $_{3/2}$ satellite peaks were at u' = 903.2 eV, u'' = 908.1 eV, and u''' = 916.3 eV.

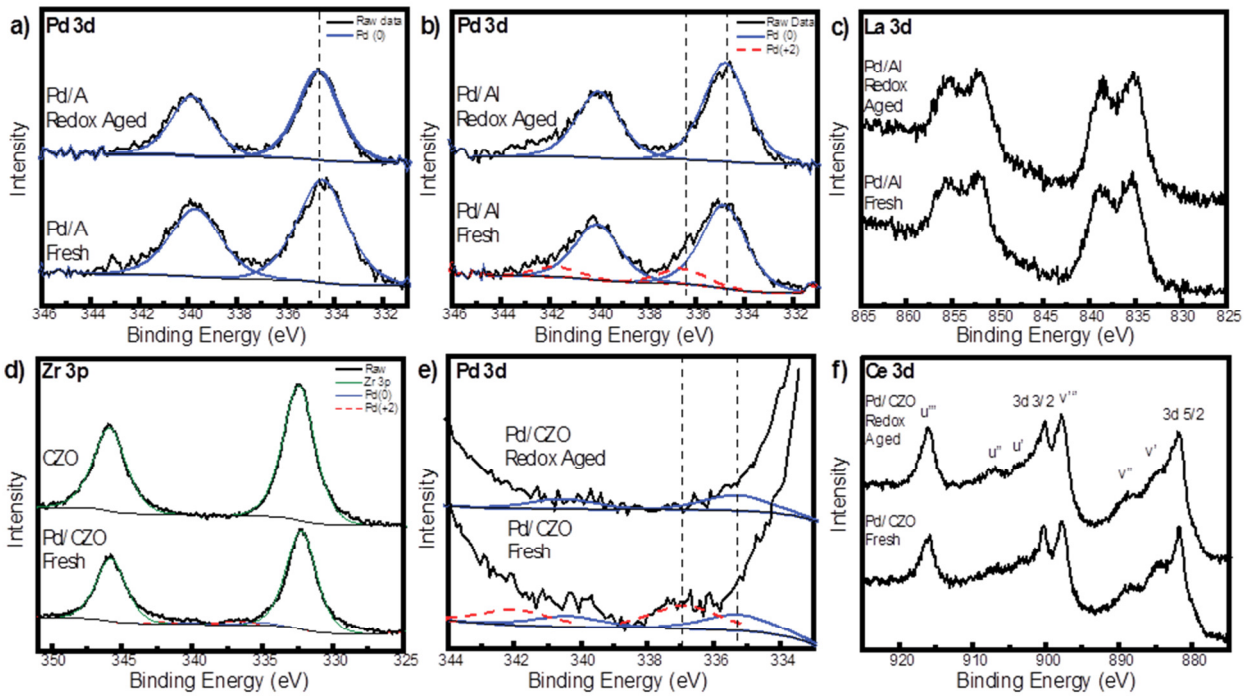

Spectra are offset for clarity. Solid blue lines are representative fits for Pd metal, dashed red lines are representative fits for Pd^{+2}. Vertical dashed black lines indicate Pd peak centers. Plots: a) Pd/A Pd 3d, b) Pd/Al Pd 3d, c) Pd/Al La 3d, d) Pd/CZO Pd 3d + Zr 3p, e) Pd/CZO Pd 3d fits and f) Pd/CZO Ce 3d

Figure 3-5: XPS surface analysis of fresh and redox aged samples

3.3.5 Catalytic Activity Tests

The OSC and WGS tests were selected as probe reactions since these two CO conversion processes share the step of oxidation with potential spillover oxygen from the support. The oxidation of CO gives us insight into the contact between the noble metal and support at a given state of catalyst deterioration. These tests differ from CO oxidation light-off tests (co-feed of gas phase CO + O_2) since reaction with gas phase O_2 will confound metal-support O_2 mobility, and show performance trends essentially aligning with earlier Pd dispersion results and not providing new insight. All catalysts were initially in the reduced state prior to evaluation. CO and CO_2 was measured directly by a mass spectrometer in units of partial pressure (i.e, torr) and converted to concentration. Micromoles of CO_2 per gram of catalyst can be calculated for the OSC

experiment using the following equation where the average CO_2 20 seconds before and after the CO pulse is used as the background:

$$CO_2 \text{ Yield [µ-moles/g]} = \frac{\begin{array}{c}(\text{average } CO_2\ [\%] - \text{background } CO_2\ [\%]) * \\ (\text{CO pulse length [m]}) * (\text{gas flow rate [L/m]})\end{array}}{(22.414 \text{ L/mole} * \text{mass of catalyst sample [g]})}$$

Conversion of CO to CO_2 during the WGS experiment can be calculated using the following equation where the average CO_2 concentration at room temperature is used as a background:

$$CO_2 \text{ Yield [\%]} = \frac{100 * (\text{current } CO_2 - \text{background } CO_2)}{(\text{CO at room temperature})}$$

The catalytic activity of Pd/Al samples measured by generation of CO_2 is shown in Figure 3-6 for the OSC test and the conversion of CO to CO_2 is shown in in Figure 3-7 for the WGS test. The trends observed for aging method severity at 400°C were the same between the WGS and OSC and were as follows: redox > rich-only = lean-only. The amount of CO_2 generated during the OSC test was below 150 µmol CO_2/g and the CO_2 conversion on the WGS test was below 12%. The poor Pd/Al catalyst activity was due to the lack of oxygen mobility in the support material. CO_2 was generated in the lowest quantity over the redox aged sample compared to the other samples, and only significantly above 300°C, likely due to the La_2O_3 interacting with Pd more after redox cycling than with a fixed rich-only environment. Both lean redispersion treatments showed a slight CO_2 generation benefit over the raw redox aged sample up to a comparable performance of the other samples. This suggests that 550°C/2h in air is sufficient to restore the chemical and geometric structure of Pd so that La_2O_3 does not inhibit CO adsorption on Pd/Al samples.

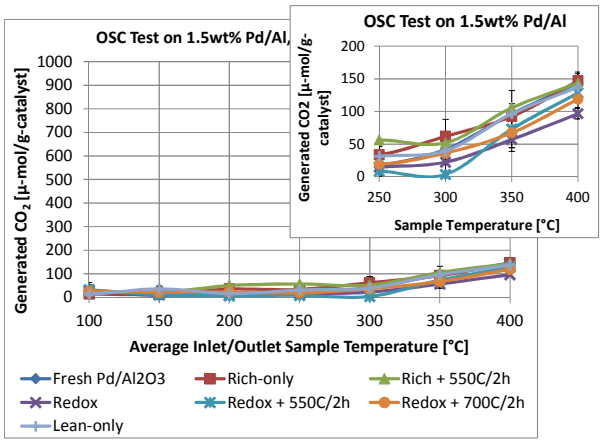

Figure 3-6: Generated CO_2 over Pd/Al samples during OSC test

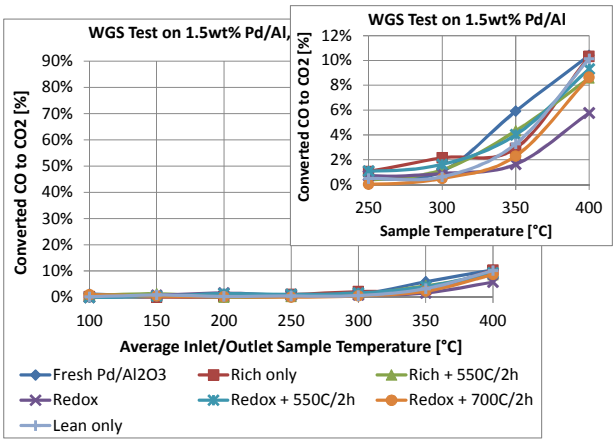

Figure 3-7: CO conversion to CO_2 over Pd/Al samples during WGS test

The catalytic activity of Pd/CZO samples measured by generation of CO_2 is shown in Figure 3-8 for the OSC test and the conversion of CO to CO_2 is shown in Figure 3-9 for the WGS test. The trends observed for aging method severity were the same between the WGS and OSC and were as follows: redox > rich-only >> lean-only. These trends suggests that 1) redox aging brought more reducible oxide over the Pd surface than the fixed rich-only aging, 2) the reducible oxide on the Pd surface limited adsorption of CO for reaction with O_2, and 3) the interface sites between Pd and CZO with oxygen mobility were severely deactivated after redox aging. The 550°C/2h lean redispersion treatment showed a CO_2 generation benefit for the rich-only sample, but the redox sample showed only a slight improvement on the OSC test and no improvement for the WGS test. The 700°C/2h lean redispersion treatment showed a large benefit for the redox aged sample and improved the results to a level comparable with the lean-only aged sample for both tests. The uncatalyzed fresh CZO sample showed OSC activity comparable to the Pd/Al samples, illustrating the contribution of the CZO support towards CO adsorption and CO_2 generation. The uncatalyzed fresh CZO sample showed no WGS activity through 400°C since this sample lacks the metal-support interface sites required for this reaction. The OSC data at 350°C and 400°C showed that the CO_2 conversion of the four most active catalysts were limited due to the complete consumption of CO over the first several seconds.

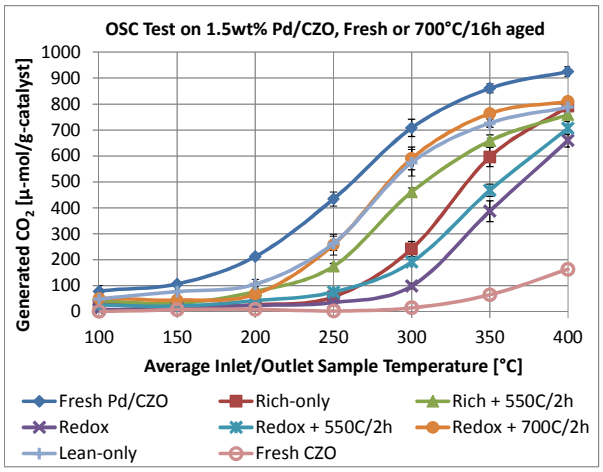

Figure 3-8: Generated CO_2 over Pd/CZO samples during OSC test

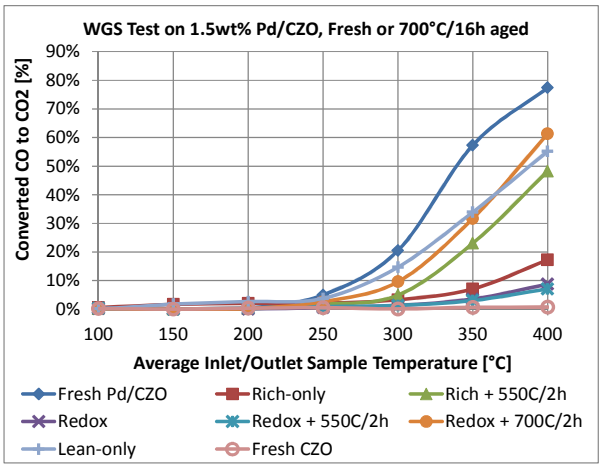

Figure 3-9: CO conversion to CO_2 over Pd/CZO samples during WGS test

The catalytic activity of Pd/TWC samples measured by generation of CO_2 is shown in Figure 3-10 for the OSC test and the conversion of CO to CO_2 is shown in Figure 3-11 for the WGS test. The OSC test results appear to be simply an average of the results achieved with the Pd/CZO and Pd/Al samples. The WGS test results appear to be comparable to the results achieved with the Pd/CZO sample. The 700°C/2h treatment in air showed significant improvement in the OSC and WGS performance over the redox aged sample while the 550°C/2h treatment in air showed perhaps a slight improvement.

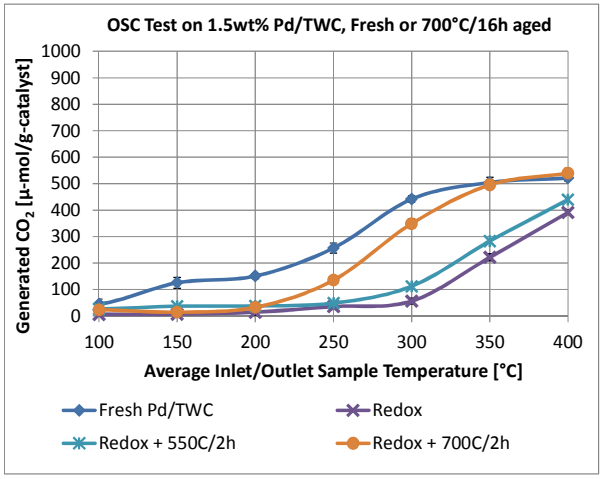

Figure 3-10: Generated CO_2 over Pd/TWC samples during OSC test

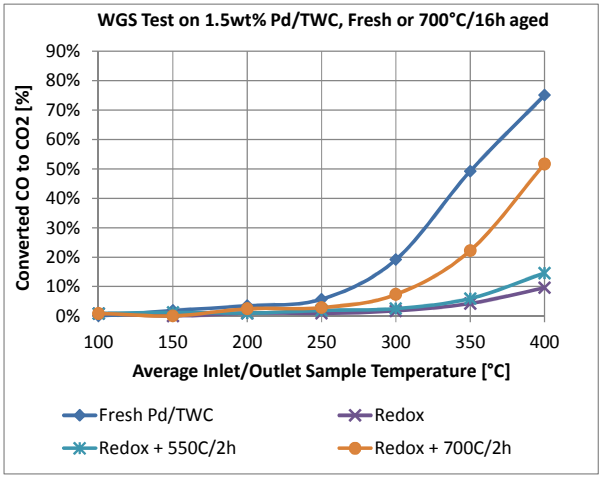

Figure 3-11: CO conversion to CO_2 over Pd/TWC samples during WGS test

The OSC and WGS mechanisms differ in how oxygen is supplied to the Pd. Three samples had undetectable Pd particles by H_2 chemisorption as listed in Table 3-2 that also showed the worst WGS and OSC performance, which suggest that these samples had Pd surfaces that were covered, perhaps by reducible Ce oxide separated from the CZO support. These "Ce-Pd/CZO" samples had WGS performance at 400°C similar to the Pd/Al samples at 6-11% conversion of CO to CO_2, yet significantly lower than the other aged Pd/CZO samples at 47-62% conversion of CO to CO_2. For the Pd/Al and Ce-Pd/CZO samples to have the same WGS CO to CO_2 conversion, the CO and water should still adsorb onto the exposed surface of the Pd and perhaps the reducible Ce oxide decoration sites, but the mechanism for CZO support participation along the Pd-adlineation sites must be deactivated by the reducible Ce oxide decoration of Pd to render it essentially as inert as alumina. The reducible Ce oxide decoration seemed to block the sites necessary for oxygen, fed indirectly via water decomposition, to be fed to the Pd by the bulk CZO support along the adlineation sites. However the Ce-Pd/CZO samples were able to demonstrate OSC roughly 5 times greater than the Pd/Al samples and uncatalyzed CZO, but had much less OSC than the other Pd/CZO samples at 300°C and lower. The CZO near the Pd particle may still supply limited oxygen, fed directly via gas phase adsorption, through the reducible Ce oxide that decorated and partially encapsulated the Pd.

A comparison of Palladium on both supports was performed by normalizing the reaction rate to the accessible metal surface atoms. The CO_2 production rate for the WGS measurement was calculated using an equation from Han *et al*. where for a given temperature the turnover frequency (TOF) is the product of the following: the conversion of CO to CO_2 (X), the number of inlet CO molecules per second (dN_{CO}/dt) and divided by the number of exposed Pd surface atoms (N_S^{Pd}) [50]. The CO_2 production rate for the OSC measurement was calculated using a method from Hori *et al*. where the initial CO_2 generation peak edge was integrated during the CO pulse [51]. The event marker for t_0=0 was just before the CO_2 peak rise and the value of t_1 was at the maximum of the CO_2 peak or four seconds later for t_1=4.

WGS TOF [1/s] = $\left[(X/100)*(dN_{CO}/dt)\right]*\left(1/N_S^{Pd}\right)$

OSC TOF [1/s] = $\left[\int_{t_0}^{t_1} N_{CO_2}\,dt \Big/ (t_1 - t_0)\right]*\left(1/N_S^{Pd}\right)$

$N_S^{Pd} = m_{cat}\, X_{Pd}\, D_{Pd}\, N_A/M_{Pd}$

N_{CO} = Inlet molecules of CO per second

N_{CO_2} = Molecules of CO_2 formed]

m_{cat} = Mass of catalyst [g]

X_{Pd} = Pd loading weight fraction

D_{Pd} = Pd dispersion by H_2 chemisorption

N_A = Avogadro's number

M_{Pd} = Pd molecular mass

The turnover frequencies (TOF) from the catalyst activity tests can be plotted in terms of the Arrhenius equation to determine the activation energy (E_a) and coefficient (A) as:

$\ln(TOF) = (-E_a/R)*(1/T) + \ln(A)$

Figures 12 and 13 show the Arrhenius plots of catalyst activity. The WGS data used to plot the TOF ranged from 250°C to 400°C for both Pd/Al and Pd/CZO. The OSC data used to plot the TOF also ranged from 250°C to 400°C for Pd/Al, but only the data from 100°C to 300°C could be used for Pd/CZO to avoid the temperatures where the leading edge of inlet CO was completely consumed. The H_2 chemisorption technique was used to determine the Pd dispersion, since XRD could not detect a Pd peak for the fresh or lean-only aged samples. The Pd/Al samples each had a TOF that was similar to the others for the WGS and OSC tests; illustrating the contribution of the exposed Pd surface on a support without oxygen mobility. The Pd/CZO samples were each higher in TOF than the Pd/Al samples; the TOF gap illustrates the contribution of the support oxygen mobility and metal-support interface sites. The Pd/CZO samples also showed more separation in the TOF with the 700°C/2h air treated redox aged sample at a higher rate than the other samples for the WGS and OSC tests. An explanation for the higher

apparent rate with the 700°C/2h air treated redox aged sample may be due to a higher participation of support sites near the Pd particles during the WGS and OSC tests. Support sites along the perimeter of the metal are called adlineation sites and on a reducible oxide are known to participate in catalytic activity tests [52]. The TOF equation contains an exposed Pd surface atoms term (N_S^{Pd}) that does not account for adlineation site participation from reducible oxides in the support. The composition of the metal-support interface sites were likely altered by the redox aging environment followed by reducible Ce oxide decomposition from the Pd surface during the 700°C/2h air treatment, enriching the local Pd interface sites with more CeO_2 than the original $Ce_{0.5}Zr_{0.5}O_2$ support of the fresh and lean aged samples. Other work with CZO solid solutions has shown available OSC was increased by over 20% when CeO_2 compositions were adjusted from 50% to 65% [53, 54, 55].

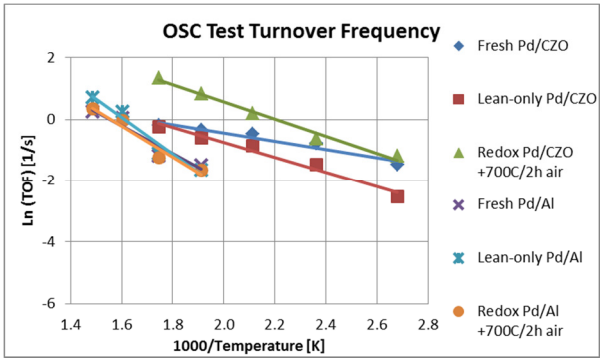

Figure 3-12: Arrhenius plot of OSC test turnover frequency

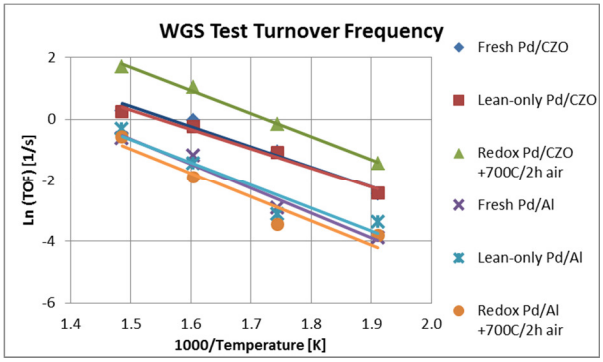

Figure 3-13: Arrhenius plot of WGS test turnover frequency

Table 3-5 lists the apparent E_a and A determined from linear fits of the Arrhenius equation in Figures 12 and 13. The Pd/CZO samples had lower E_a than the Pd/Al samples in the OSC tests, demonstrating the benefit of support oxygen mobility on palladium CO oxidation. Therefore, CO oxidation appears to depend on the total number of metal-support interface sites and support oxygen transfer ability. The fresh samples from Table 3-5 are compared to similar fresh catalysts found in the literature as shown in Table 3-6 [50, 56, 57, 58, 59]. The WGS test in this work produced comparable E_a to the literature. The OSC rate calculation method from Hori *et al.* was used by others with an integration length convention set to one second (t_1=1) to calculate a so called dynamic oxygen storage capacity or rate (DOSC or DOSR) over a

catalyst bed of 10 mm diameter by 1.5 mm long in a gas stream flowing at 300 mL/min [50, 56]. Since they did not disclose an E_a, an Arrhenius equation fit was performed using their DOSC or DOSR test data provided from 200°C-500°C to obtain the results listed in Table 3-6. The OSC test in this work produced a slightly higher E_a than the literature, which may be due to the difference in support ceria content or catalyst bed dimensions.

Table 3-5: Pd/CZO and Pd/Al kinetic parameters measured with OSC and WGS tests

Catalyst Sample	OSC Test		WGS Test	
	E_a (kJ/mol)	A	Ea (kJ/mol)	A
Pd/CZO fresh	11	9.5E+00	55	3.1E+04
Pd/CZO lean-only	20	6.0E+01	53	1.8E+04
Pd/CZO redox + 700C/2h air	23	4.6E+02	63	2.9E+05
Pd/Al fresh	37	1.1E+03	68	1.1E+05
Pd/Al lean-only	49	1.4E+04	62	4.0E+04
Pd/Al redox + 700C/2h air	42	2.6E+03	65	4.5E+04

Table 3-6: Comparison of TOF parameters to literature

Fresh Samples	E_a [kJ/mole]	ln A	Test	Reference
0.5 wt% Pd/$Ce_{0.67}Zr_{0.33}O_2$	28	6	WGS	[50]
1.8 wt% Pd/$Ce_{0.75}Zr_{0.25}O_2$	62	13.4	WGS	[57]
1.0 wt% Pd/$Ce_{0.5}Zr_{0.5}O_2$	49		WGS	[58]
1.5 wt% Pd/$Ce_{0.5}Zr_{0.5}O_2$	55	10	WGS	This work
1.8 wt% Pd/Mg-Al_2O_3	76	13.7	WGS	[57]
2.0 wt% Pd/Al_2O_3	82		WGS	[59]
1.5 wt% Pd/La-Al_2O_3	68	11.6	WGS	This work
0.5 wt% Pd/$Ce_{0.67}Zr_{0.33}O_2$	12	8	OSC	[50]
0.5 wt% Pd/$Ce_{0.7}Zr_{0.3}O_2$	6	8	OSC	[56]
1.5 wt% Pd/$Ce_{0.5}Zr_{0.5}O_2$	20	60	OSC	This work

3.3.6 Examination for Totally Encapsulated Palladium Particles on Ceria-Zirconia

Characterization methods to determine whether aged Pd particles were completely encapsulated by the CZO support have been described in the scientific literature with similar catalysts. One method by Graham *et al*. involved a 2.25wt% Pd/$Ce_{0.5}Zr_{0.5}O_2$ sample that was redox aged 1050°C/12h and later oxidized at 700°C in air for 2 hours where the XRD pattern showed both a strained Pd [111] peak at 40.5°2θ

and the broad PdO [110] peak at 41.9° 2θ, which lead them to claim some Pd metal was inaccessible to the oxidation feed and must be buried by the CZO support as surface area was degraded by 97% [60].

Figure 3-14 shows a similar sequence was applied to the 700°C/16h redox aged Pd/CZO sample in this study. Upon reoxidation at 700°C for 2 hours in step 2, the Pd [111] peak completely disappeared and a broad PdO [110] appeared just above the background. The lack of a clear PdO peak may indicate that the oxide is highly disordered perhaps even amorphous. So while the 700°C/16h redox aging condition caused a thin reducible Ce oxide layer to cover the Pd particles, gas phase oxygen decomposed the reducible Ce oxide and reoxidized the Pd metal.

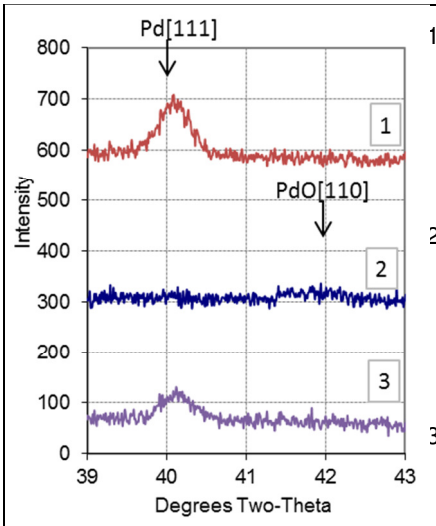

1. Redox aging was ended on rich step. Sample was cooled in N_2 then reduced at 350°C for 0.5h in 1% CO/H_2 balance N_2. Detectable Pd reduced to metal state.
2. Sample was then oxidized at 700°C for 2h in air. Detectable Pd was oxidized to PdO without showing encapsulated Pd metal at 40° 2θ.
3. Sample was then reduced at 350°C for 0.5h in 1% CO/H_2 balance N_2. Detectable Pd reduced to metal state.

Figure 3-14: Examination of XRD pattern for encapsulation or decoration of Pd by CZO

Going from step 1 to step 3 it can be seen that the Pd [111] peak area decreased significantly. As shown previously in Table 3-2 for the effect of the 700°C/2h lean treatment, the XRD pattern Pd [111] peak fit resulted in a Pd size increase from 20 nm to 24 nm with an accompanying decrease in dispersion from 6% to 5%. However, the H_2 chemisorption results in Table 3-2 also showed an increase in Pd dispersion from u/d to 4%. A Pd dispersion increase measured by H_2 chemisorption without a

corresponding decrease in Pd particle size as measured by XRD may be due to the following possibilities: 1) the lost Pd-CZO interface due to aging in a reducing environment (i.e., see Figure 3-5e XPS plot of Pd^{+2} fresh to aged) was reestablished causing a significant portion of the Pd metal to go to PdO under the room temperature conditions, which is hard to observe at 41.9° 2θ apart from the background or 2) PdO particles actively redispersed to form new particles too small for XRD detection so that the peak width was due to just the particles larger than 7 nm.

3.3.7 Investigation of the Model for Redispersed Palladium Particles on Ceria-Zirconia

An alternate lean/rich sequence was developed to gain further insight on the effects of a 700°C lean treatment based on initially exposed Pd metal surface. The two portions of the Pd/CZO redox aged sample were selected with different Pd dispersion values determined by H_2 chemisorption: sample #1 was after the 700°C/2h lean treatment (4.1% dispersed Pd) and sample #2 was in as-is condition (no exposed Pd). Both samples were then exposed to repeated cycles of a brief 700°C reoxidation in dry air for 0.10 hours followed by the typical 350°C reduction in pure H_2 for two hours as part of the automated H_2 chemisorption procedure. An XRD pattern was collected only after each sample reached the final lean/rich cycle.

Figure 3-15 shows the Pd dispersion results by H_2 chemisorption after each lean/rich cycle. The two Pd/CZO redox aged samples achieved about the same level of apparent Pd dispersion in dry air at 700°C with just 0.1 hours as was achieved over two hours, which may be simply removal of Ce from the Pd surface. The Pd/CZO sample #1 with two hour lean treatment had an increase to the exposed Pd surface as measured by H_2 chemisorption yet no increase in bulk average Pd particle size as measured by XRD. If any PdO particles migrated and ruptured over those two hours, the new fragments were below the XRD detection limit and did not affect the bulk measurement. The following air treatment of 700°C/0.1h showed a dramatic increase in Pd dispersion to 12%, demonstrating that significant Pd redispersion was possible after the reducible Ce oxide covering was removed. Subsequent 700°C/0.1h air treatments showed no further improvements to Pd dispersion on Pd/CZO sample #1, but minor

improvements to Pd dispersion were observed with Pd/CZO sample #2 to a cumulative total of 30 minutes with the Pd dispersion improved to 7.8% as measured by H_2 chemisorption. The improvements to Pd dispersion were confirmed with Pd size measurements by XRD then converted to dispersion; starting at a Pd crystallite size of 20 nm or 5.5% dispersion, the Pd on sample #1 shrank to 13 nm for 8.2% dispersion and the Pd on sample #2 shrank to 14 nm for 7.8% dispersion. Since both Pd/CZO samples ended with similar Pd size and dispersion by XRD, yet had different Pd dispersion by H_2 chemisorption, the discrepancy suggests that Pd/CZO sample #2 still had some reducible Ce oxide coverage on the Pd surface, causing only gradual improvement in Pd dispersion with each lean treatment. The 700°C dry air treatment likely worked to reintegrate the decomposed reducible Ce oxide from the Pd surface into the phase segregated CZO, to a larger extent over two hours than in just 0.1 hour. The surface of sample #2 was likely in a reversible state that allowed limited Ce creep over the Pd during each subsequent reduction in H_2 at 350°C.

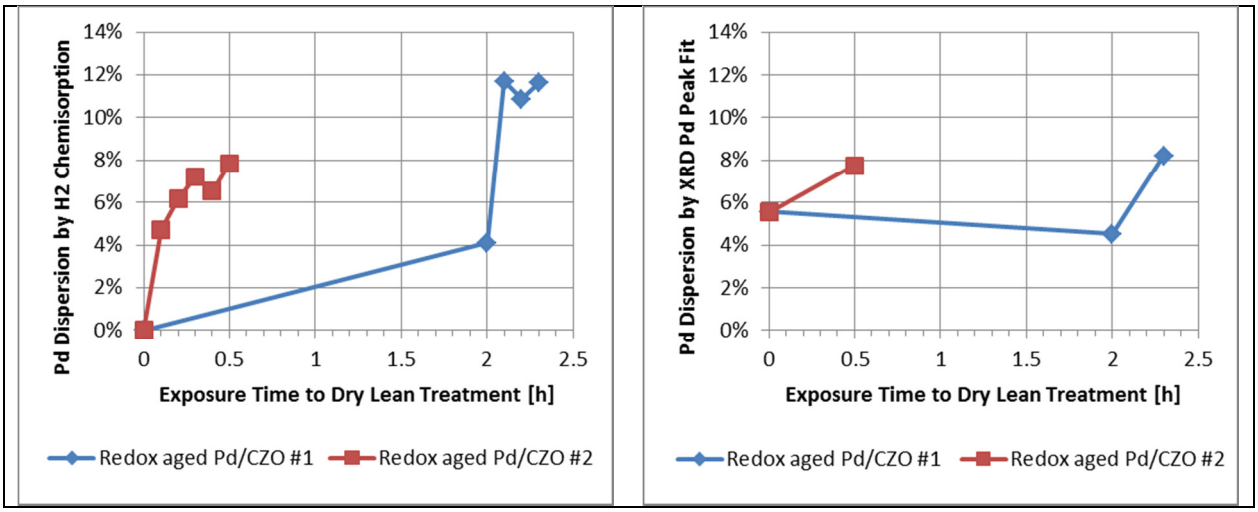

Figure 3-15: Characterization of Pd/CZO after separate dry lean treatment schemes

3.3.8 Comparision of Lean Pd Redispersion to Vehicle Exhaust Conditions

So far we have looked at model catalysts under laboratory conditions. We now consider if these redispersion effects are consistent with conditions on a vehicle. A 2009MY 2.0L Ford Focus on gasoline fuel was driven at speeds from 0-80 mph while the catalytic converter bed temperature and exhaust gas equivalence lambda were

acquired as shown in Figure 3-16. The catalytic converter bed temperature reached temperatures in excess of 700°C on multiple occasions when the vehicle speed was over 50 miles per hour. On a few of these occasions, the fuel was also shut off to the engine while the vehicle slowed down as shown when the engine exhaust lambda was in excess of 1. These events extended up to several seconds on the supplementary federal drive cycle US06. This confluence of air flowing through the engine for several seconds combined with a hot catalyst in excess of 700°C should be similar to the dry lean Pd redispersion environments used in this study, although at a much shorter duration.

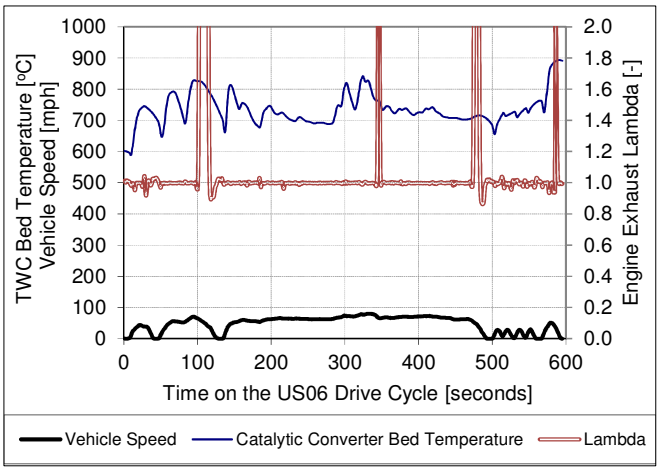

Figure 3-16: Environment of a catalytic converter on the US06 drive cycle

The model powder catalysts showed dynamic changes to Pd dispersion in the laboratory depending on oxygen concentration in the 700°C aging environment for 16 hours. The rich-only and redox environments caused much more severe loss of Pd dispersion than the fixed lean-only exhaust gas compositions, for both Pd/Al and Pd/CZO samples, producing samples with the lowest activity for the WGS and OSC tests. Exposure to dry air at 700°C caused Pd particles to increase dispersion on alumina and CZO supports. Based on these observations made on the model catalysts and the environment shown in Figure 3-16, one should operate the engine so that the exhaust gas composition falls along a trajectory that avoids the fuel-rich environment or includes periodic dry air events to reoxidize Pd into PdO to redisperse the Pd and restore lost activity. Automotive fuel-rich environments include fuel enrichment events

commonly used to cool engine-out exhaust temperature and protect exhaust system components from thermal damage (i.e., catalyst protection). To maximize Pd dispersion on automotive catalysts either a lean exhaust environment or fuel cut event would be required prior to 16 hours of 700°C redox exhaust exposure or right after fuel enrichment events so that most of the Pd particles would be small enough to redisperse under moderate driving conditions. These conditions are achievable on a production vehicle and the fuel-cut frequency could be further enhanced through additional engine control features or parameter calibration refinement. Since this study evaluated a 16 hour aging duration and lean Pd redispersion treatment at 2 hours in length, further work will need to be done on measuring the time scales of Pd oxidation, redispersion and sintering. This appears to be a good strategy for maintaining adequate Pd dispersion on a catalytic converter under real-world driving conditions.

3.4 Discussion

3.4.1 Oxidation of the system, collapse of SMSI effect

Figure 3-17a shows a proposed mechanism for the fresh Pd/Al redox aging, reoxidation and redispersion based on surface area, H_2 chemisorption, XPS, XRD and STEM results. The 16 hour redox (and rich-only) aging environment sintered Al_2O_3 and increased La_2O_3 at the surface as measured by XPS, which caused the Pd/Al samples to have much larger Pd particle size measured by H_2 chemisorption than by XRD or STEM. To examine the SMSI effects caused by the La_2O_3 dopant, two alumina supports were used in this work, Pd/A was undoped while Pd/Al contained La_2O_3 and both had similar initial Pd dispersions. Comparing the redox aged Pd/Al and Pd/A samples showed a 7 fold difference in Pd diameter by H_2 chemisorption, yet the XRD method showed Pd particle diameters just 1 nm different from each other. This suggests that the reducing environment initiated an interaction between Pd and La_2O_3 in the Pd/Al sample that caused H_2 chemisorption to not accurately detect the exposed metal surface to provide a good estimation of Pd diameter. Comparing the redox aged Pd/Al samples before and after the 550°C/2h lean treatment, the H_2 chemisorption

results showed the Pd particle shrank by over 5 fold, while the XRD and STEM methods showed the Pd particle size underwent a modest reduction. The oxidation of the system reversed the SMSI effects on Pd in the Pd/Al samples to enable improved gas phase adsorption onto Pd and a more accurate estimate of Pd size from H_2 chemisorption.

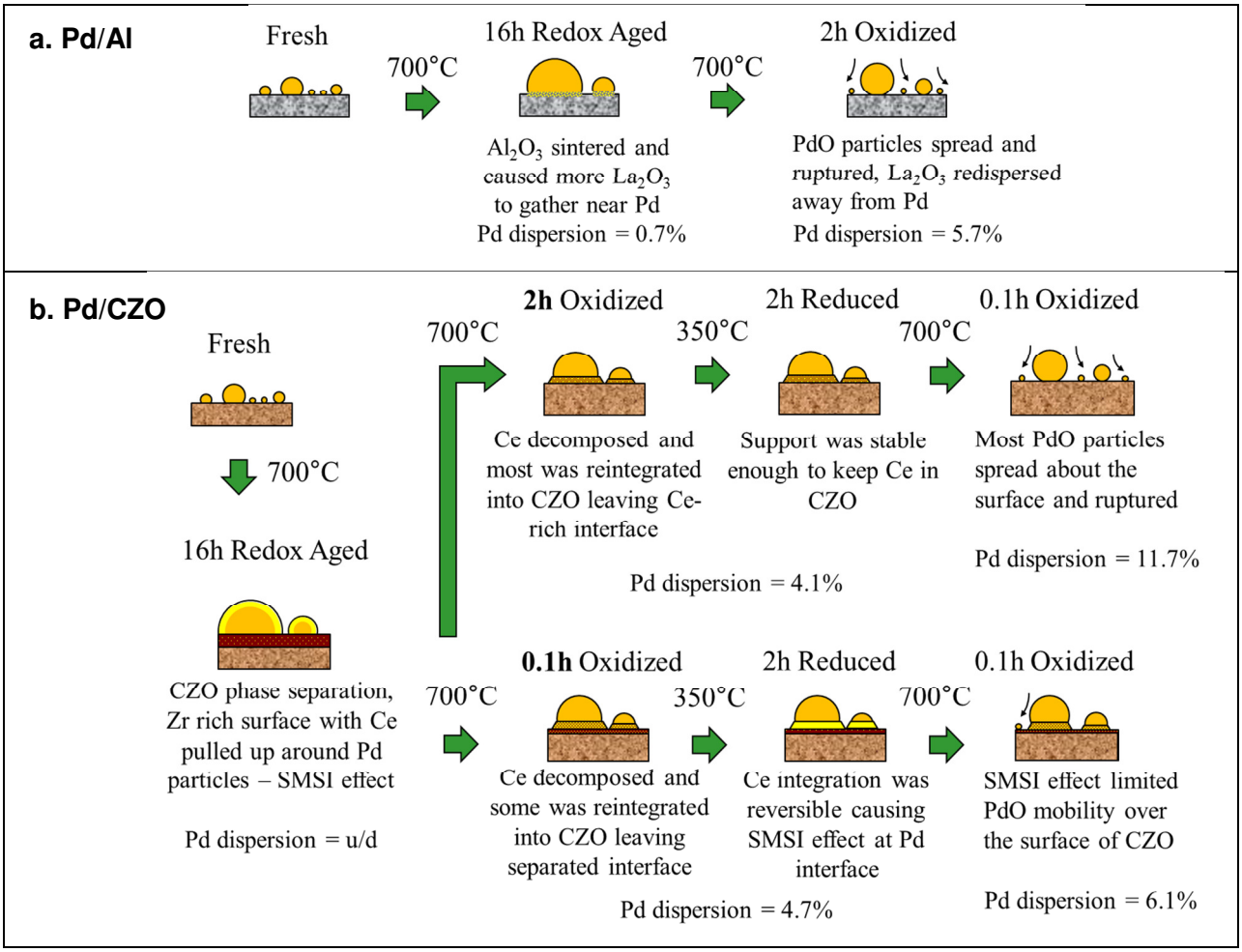

Figure 3-17: Proposed Pd redispersion mechanism on Al and CZO supports

There is some debate in the literature as to how La_2O_3 affects Pd when exposed to high temperature reducing conditions. Rieck and Bell showed H_2 saturation coverage results on Pd/SiO_2 catalysts with an H atom coverage that diminished by half after it was promoted with 4wt% La_2O_3, which they attributed to decoration of Pd particles by partially reduced LaO_x [19]. Ahn *et al.* used a H_2 temperature programmed reduction experiment with similar Pd catalysts to show a Pd reduction peak near 120°C for all samples, plus an extra reduction peak near 320°C with Pd/La_2O_3 and Pd/La_2O_3-SiO_2

catalysts, which they attributed to La_2O_3 reduction made possible by interaction with Pd [36]. However, others have concluded that the discrepancies with chemisorption on Pd-La_2O_3 catalysts stem from an electronegative shift of Pd shown by XPS [18], while others showed no change in the La^{+3} valence state after H_2 reduction at 600°C [49]. Recently, Kim *et al*. furthered the work of Ahn *et al*. with Pd/SiO_2 and Pd/La_2O_3-SiO_2 catalysts, and concluded that the observed difference in the H_2 uptake from H_2 chemisorption coupled with an observed shift in Pd 3d electronic binding energy from XPS were both due to a change in the properties of Pd as influenced by the partially reduced La oxide, which lowered the adsorption strength of gas phase molecules onto the Pd surface [37]. Although La_2O_3 is claimed to be unreducible [18], in our work La_2O_3 caused the H_2 chemisorption measurement to underestimate the Pd/Al sample's Pd dispersion, relative to the Pd/A sample. The XPS results on the Pd/Al sample did not show decreased surface Pd coincident with the increased surface La after redox aging, so any coverage of Pd by La_2O_3 was ruled out in our case.

Figure 3-17b shows a proposed mechanism for the fresh Pd/CZO redox aging, reoxidation and redispersion based on H_2 chemisorption, XPS, XRD, and normalized WGS and OSC results. The redox aging environment caused several changes: severe support sintering shown by dramatic BET surface area loss, no exposed Pd by H_2 chemisorption results, no Pd-support oxygen transfer by WGS activity tests and significantly increased surface Ce and Zr coupled with lowered surface Pd in our XPS results. Kępiński *et al.* used Pd supported on CeO_2 and claimed that thin films of reducible Ce oxide formed over Pd particles when reduced in hydrogen at 700°C [20, 34]. The Pd/CZO support used in this work contained 50% CeO_2, that once reduced is known to atomically migrate and decorate the surface of Pd particles [34], and creep up around the sides of Pd particles from the metal-support interface and cause partial encapsulation [33]. Taking all of these observations into contextual consideration, the best explanation is reducible ceria pulled from the Pd-CZO interface, decorated the Pd surface as a film. While these observations suggest a strong metal support interaction between ceria in CZO and the Pd interface during reducing conditions [20, 33, 34, 38], we were unable to confirm this explanation with STEM images. We also could not confirm a CZO phase separation with the acquired XRD patterns, but a monolayer of Ce

on the surface of Pd particles would not be detected by XRD. Because XRD involves constructive interference based on Bragg's Law, there have to be several layers of atoms for diffraction to occur. Even if the Ce was 3 or 4 atomic layers thick, the peak would be so broad and of low intensity (several degrees FWHM) that it would be lost in the background. In reality, a crystal needs to contain dozens or even hundreds of atom layers to be detected in powder XRD and even then significant peak broadening will be observed.

Post aging lean treatments appeared to reverse some of the reducible oxide effects, as evidenced by increased Pd dispersion and by increased CO_2 production during WGS and OSC activity measurements. There is precedent in the literature regarding why these Pd/CZO samples remained essentially unchanged after the 550°C/2h air treatment. Alexandrou and Nix deposited reducible Ce oxide films on a Pd [111] surface and heated it in N_2 under vacuum, then used XPS to show that Ce stayed on Pd relatively unchanged up to 500°C, but then the Ce 3d peak dramatically dropped at 600°C and completely vanished at 700°C [35]. Badri *et al*. used Diffuse Reflectance Infrared Fourier Transform Spectroscopy to show oxidation at 600°C was sufficient to remove reducible Ce oxide decoration from the Pd [111] surface while the Pd [100] surface remained unchanged [38]. Dry air at 700°C was a necessary first step to enable PdO mobility over the CZO support for redispersion, possibly by removal of a reducible ceria film decorated on the Pd surface or CZO from around the edges of the particle. The 700°C/2h air treatment enabled access for H_2 adsorption on the Pd surface, leading to better Pd dispersion agreement between H_2 chemisorption and XRD methods. The difference in Figure 3-17b in initial lean treatment duration (0.1 h vs. 2 h) led to different CZO surfaces and degrees of uncoupled metal/support interaction. The smaller increase in Pd dispersion with the shorter air treatment duration is consistent with a lesser degree of reintegration of the film of reducible ceria into the bulk CZO. Until this process of reintegration is complete, the mobility of PdO may be restricted. The ceria-rich interface on the lean treated sample may be the reason that the normalized WGS and OSC reaction rates were higher than for the fresh condition.

3.4.2 Redispersion of Pd

To understand why Pd can redisperse rather than sinter at elevated temperatures it is important to remember that the oxygen concentration essentially governs whether Pd forms oxide particles or remains in the metallic phase. Our lean aging conditions had just 0.5% O_2, which was above the Pd decomposition line shown in Figure 3-1. Gabasch *et al*. noted that PdO formation is kinetically limited near the decomposition temperature because the rate of PdO seeds formed at the onset of oxidation is comparable with the rate of PdO decomposition [61]. Therefore, in our lean-only aging condition, the Pd could not be sufficiently oxidized with 0.5% O_2 as the rate of PdO decomposition exceeded the rate of PdO seed formation. The Pd/Al catalysts sintered similarly in all three aging environments according to Pd size measurements by XRD, but the Pd/CZO catalysts were much less sintered in the lean-only environment than in the reducing aging environments suggesting enhanced PdO formation rates due to the support material. Our lean treatment conditions included 21% O_2 (air), which was well below the Pd decomposition line shown in Figure 3-1. Collussi *et al*. showed that as gas phase oxygen concentration was increased from 0.5% to 21%, the onset temperature for supported PdO decomposition increased and the amount of O_2 uptake increased suggesting a more complete Pd reoxidation [17]. The kinetically limited conditions in the lean-only aging environment of 0.5% O_2 were reversed upon increasing to 21% O_2. The improved sintering resistance of PdO versus Pd under oxidizing conditions also relates to the difference in thermodynamic and physical properties of the metal and oxide. Recent microscopy and density functional theory work by Johns *et al*. showed that bulk PdO in air at 800°C is very stable and does not emit atoms into the vapor phase (as by Ostwald ripening) [62]. Kang *et al*. aged Pd catalysts at 600°C in 3-21% O_2 or 3% CO and showed a lower extent of Pd particle sintering that scaled with higher oxygen concentration [32]. The literature review conducted by Johns and Kang enabled them to link properties such as the roughly three orders of magnitude lower vapor pressure and 50% lower surface tension of PdO versus Pd metal as the reason behind the stability of the oxide [62, 32]. Therefore, after the bulk oxide forms, the atomic Pd emission becomes more difficult, while PdO mobility and eventual fracture into smaller particles are enhanced.

The aftereffects of Pd redispersion was confirmed in this work through multiple

Pd particle size estimation techniques with Pd/Al powder samples, before and after 550°C or 700°C dry lean treatments, where 700°C showed more benefit than 550°C for Pd size reduction. The proposed mechanism for Pd redispersion is consistent with microscopy observations from Chen and Ruckenstein where PdO crystallites moved about the film at 500°C accompanied by rupturing and fracturing of the spreading PdO crystallites into smaller particles [11]. This mechanism is analogous to a reversed particle migration and coalescence sintering model requiring PdO mobility and sufficient time in the Pd redispersion zone shown in Figure 3-1 to rupture into new PdO particles.

In this work, Pd particles were measured *ex-situ* on supported catalyst powder after exposure to air at 700°C, holding for a fixed time and finally reducing in H_2 at 350°C. We do not consider that the mild reduction at 350°C in H_2 initiated a sloughing off of the oxide particle shell generating new Pd particles. Crozier *et al*. showed with high-resolution transmission electron microscopy on supported PdO exposed to H_2 from 200°C-550°C that the final Pd particle size was not smaller than expected given the oxide removal and formation of an inner void space [41]. While the role of the reduction was important to enable a following Pd-PdO transformation, the new Pd particles that we observed *ex-situ* arose from the process of Pd oxidation, the ensuing PdO mobility, or both. Datye *et al*. observed that the process of Pd transformation into PdO alone did not cause Pd to redisperse on undoped alumina, according to their XPS and microscopy results on quenched sample portions taken during heating in air to 1000°C then cooled in air to room temperature [63]. These results are consistent with recent work by Chen *et al*. who used a 550°C dry lean treatment to achieve only modest Pd dispersion on variants of the undoped Pd/A sample used in this work [10]. Yet Peterson *et al*. showed that supported Pd clusters treated in air at 700°C or with 1% O_2 achieved atomically dispersed Pd that was more stable on La-Al_2O_3 than on undoped alumina [64]. The observations of Peterson *et al*. also are consistent with our XPS results where Pd^{+2} was observed on the fresh Pd/Al and Pd/CZO samples, but not on the fresh Pd/A sample, which were all calcined then later reduced prior to analysis. The ability of Pd to form stable Pd^{+2} on the surface of La-Al_2O_3 or CZO may be vital to achieving significant Pd size reduction when inside the conditions of the Pd redispersion zone.

3.5 Conclusions

The three catalyst aging environments used in this study at 700°C for 16 hours produced Pd/CZO samples with distinct levels of residual surface area, Pd particle size and WGS/OSC activity. A ranking relative to the aging environment severity on these samples was as follows: redox > rich-only >> lean-only. The Pd particle size and WGS/OSC activity differences for the aged Pd/Al samples had similar trends, but were much smaller in magnitude, and even showed no significant difference in the residual surface area across the aging environments than the Pd/CZO samples. Therefore different aging protocols can to lead to very different catalyst structures and performance characteristics through a combination of metal oxidation state effects and support/additive interactions.

The fresh and lean-only aged Pd/CZO samples had exposed Pd particles measurable by H_2 chemisorption, while the rich-only and redox samples did not. The Pd/CZO samples with the highest dispersion had the highest CO oxidation in the OSC and WGS activity tests. Therefore, CO oxidation by support oxygen transfer appears to depend on the Pd dispersion, which correlates to the total number of metal-support interface sites. However, the lean treatments of 700°C after redox aging and 550°C after rich-only aging produced Pd/CZO samples that did not agree with this conclusion, demonstrating high catalyst activity with low Pd dispersion.

HAADF STEM images of Pd/Al redox aged samples confirmed the effects of dry air treatments on Pd particle size. The 550°C/2h lean treatment produced a 1.4 nm decrease in the mean Pd size with no increase in the fraction of particles at 10 nm and below, yet the large particles at 30 nm to 80 nm shrank down from 5% of the aged total to 1%. The 550°C in air treatment shrank the particles of 16 nm and higher, increasing the count of particles measuring 11-15 nm from 36% to 43% of the total. The 700°C/2h lean treatment produced a 4.4 nm decrease in the mean Pd size with a near doubling of the fraction of aged particles at 10 nm and below, confirming the significance of Pd redispersion under these conditions.

The 700°C lean treatment was confirmed to redisperse Pd on La-Al_2O_3, but on CZO the results were mixed. The reducing aging environment brought more La and Ce oxide to the surface from the support as measured by XPS, which showed no change in surface Pd on La-Al_2O_3, but caused a loss of half the surface Pd on CZO. The initial lean treatment on the redox aged Pd/CZO increased the exposed Pd surface as measured by H_2 chemisorption, perhaps by decomposition of decorated Ce from Pd, but the Pd crystal size was not diminished as measured by XRD. The next lean treatment showed a large improvement in Pd dispersion, as measured by both XRD and H_2 chemisorption, almost up to the lean-only aged sample. Since Pd redispersion appears to require PdO mobility, lean treatments via engine fuel cuts need to be applied before reducible oxides creep up and restrain the Pd metal or multiple lean treatments would be needed in close succession.

The insights gained from this study provide important guidance into the operation of a catalytic converter on a vehicle. The engine exhaust environment capable of redispersing palladium catalyst particles seems to be aligned with fuel cuts during a deceleration event from high vehicle speed. If the catalyst is properly positioned near the engine exhaust manifold, then the temperature may be above the threshold of 700°C when air would be pumped through the engine on a fuel cut. The automotive catalytic converter could then be periodically regenerated with active engine controls to prolong the performance throughout the life of the catalyst. The result of this work may enable lower initial amounts of noble metals in the catalytic converter if the dispersion can be maintained above 1% by full useful life.

3.6 Acknowledgements

The authors gratefully acknowledge the following sources of funding for this study: Ford University Research Program (URP), NSF GOALI grant # CBET-1159279 and NSF grant # DMR-9871177. The authors thank Dr. William Paxton at Ford Motor Company for valuable discussions regarding artifacts in XRD patterns of Pd/CZO.

3.7 References

[1] H.S. Gandhi, G.W. Graham, R.W. McCabe, "Automotive Exhaust Catalysis", *J. Catal.* 216 (2003) 433–442

[2] J. Kašpar, P. Fornasiero, N. Hickey, "Automotive catalytic converters: current status and some perspectives", *Catal. Today* 77 (2003) 419–449

[3] R.M. Heck, R.J. Farrauto, "Automobile exhaust catalysts", *Appl. Catal. A: Gen.* 221 (2001) 443–457

[4] C. Bartholomew, "Mechanisms of catalyst deactivation", *Appl. Catal. A: Gen.* 212 (2001) 17–60

[5] A. Datye, Q. Xu, K. Kharas, J. McCarty, "Particle size distributions in heterogeneous catalysts: What do they tell us about the sintering mechanism?", *Catal. Today* 111 (2006) 59–67

[6] R. Goeke, A. Datye, "Model oxide supports for studies of catalyst sintering at elevated temperatures", *Top. Catal.* 46 (2007) 3-9

[7] R. McCabe, R. Useman, "Characterization of Pd-based Automotive Catalysts", *Stud. Surf. Sci. Catal.* 101 (1996) 355–368

[8] Q. Xu, K. Kharas, B. Croley, A. Datye, "The Sintering of Supported Pd Automotive Catalysts", *ChemCatChem* 3 (2011) 1004–1014

[9] N. Hickey, P. Fornasiero, R. Di Monte, J. Kašpar, J. R. González-Velasco, M. A. Gutiérrez-Ortiz, M. P. González-Marcos, J. M. Gatica, S. Bernal, "Reactivation of aged model Pd/$Ce_{0.68}Zr_{0.32}O_2$ three-way catalyst by high temperature oxidising treatment", *Chem. Comm.* 1 (2004) 196-197

[10] X. Chen, Y. Cheng, C.Y. Seo, J.W. Schwank, R.W. McCabe, "Aging, re-dispersion, and catalytic oxidation characteristics of model Pd/Al_2O_3 automotive three-way catalysts", *Appl. Catal. B: Environ.* 163 (2015) 499–509

[11] J.J. Chen, E. Ruckenstein, "Role of Interfacial Phenomena in the Behavior of Alumina-Supported Palladium Crystallites in Oxygen", *J. Phys. Chem.* 85 (1981) 1606-1612

[12] N.M. Rodriguez, S.G. Oh, R.A. Dalla-Betta, R.T.K. Baker, "In-situ Electron Microscopy Studies of Palladium Supported on Al_2O_3, SiO_2, and ZrO_2 in Oxygen", *J. Catal.*, 157 (1995) 676-686

[13] E. Ruckenstein, J.J. Chen, "Wetting Phenomena during Alternating Heating in O_2 and H_2 of Supported Metal Crystallites", *J. Coll. Interface Sci.* 86 (1982) 1-11

[14] H. Lieske, J. Völter, "Pd Redispersion by Spreading of PdO in O_2 Treated Pd/Al_2O_3", *J. Phys. Chem.* 89 (1985) 1841-1842

[15] R.J. Farrauto, J.K. Lampert, M.C. Hobson, E.M. Waterman, "Thermal decomposition and reformation of PdO catalysts; support effects" *Appl. Catal. B: Environ.* 6 (1995) 263-270

[16] M. Peuckert, "XPS Study on Surface and Bulk Palladium Oxide, Its Thermal Stability, and a Comparison with Other Noble Metal Oxides", *J. Phys. Chem.* 89 (1985) 2481-2486

[17] S. Colussi, A. Trovarelli, E. Vesselli, A. Baraldi, G. Comelli, G. Groppi, J. Llorca, "Structure and morphology of Pd/Al_2O_3 and Pd/CeO_2/Al_2O_3 combustion catalysts in Pd–PdO transformation hysteresis", *Appl. Catal. A: Gen*. 390 (2010) 1–10

[18] R.F. Hicks, Q.-J. Yen, A.T. Bell, "Effects of Metal-Support Interactions on the Chemisorption of H_2 and CO on Pd/SiO_2 and Pd/La_2O_3", *J. Catal.* 89 (1984) 498-510

[19] J.S. Rieck, A.T. Bell, "Studies of the Interactions of H_2 and CO with Pd/SiO_2 Promoted with La_2O_3, CeO_2, Pr_6O_{11}, Nd_2O_3, and Sm_2O_3", *J. Catal.* 99 (1986) 278-292

[20] L. Kępiński, M. Wolcyrz, J. Okal, "Effect of Chlorine on Microstructure and Activity of Pd/CeO_2 Catalysts", *J. Chem. Soc., Farad. Trans.* 91 (1995) 507-515

[21] J.C. Jiang, X.Q. Pan, G.W. Graham, R.W. McCabe, J. Schwank, "Microstructure of a Pd/ceria–zirconia catalyst after high-temperature aging", *Catal. Lett*. 53 (1998) 37–42

[22] D. Briggs, M.P. Seah, Practical Surface Sci. Analysis by Auger and X-ray Photoelectron Spectroscopy, John Wiley & Sons, New York, 1984

[23] A.L. Patterson, "The Scherrer Formula for X-Ray Particle Size Determination", *Phys. Rev.* 56 (1939) 978-982

[24] J. E. Benson, H. S. Hwang, M. Boudart, "Hydrogen-Oxygen Titration Method for the Measurement of Supported Palladium Surface Areas", *J. Catal* 30 (1973) 146-153

[25] V. Ragaini, R. Giannantonio, P. Magni, L. Lucarelli, G. Leofanti, “Dispersion Measurement by the Single Introduction Method Coupled with the Back-Sorption Procedure: A Chemisorption and TPD Study of the Different Chemisorbed Hydrogen Species II. Pd on Alumina”, *J. Catal*. 146 (1994) 116-125
[26] T. Takeguchi, S. Manabe, R. Kikuchi, K. Eguchi, T. Kanazawa, S. Matsumoto, W. Ueda, “Determination of dispersion of precious metals on CeO_2-containing supports”, *Appl. Catal. A: Gen.* 293 (2005) 91–96
[27] D. Bresenham, J. Reisel, K. Neusen, “Spindt Air-Fuel Ratio Method Generalization for Oxygenated Fuels”, *Soc. Automot. Eng.,* SP-1381 (1998) 219-238
[28] A. Baylet, S. Royer, P. Marécot, J. Tatibouët, D. Duprez,” Effect of Pd precursor salt on the activity and stability of Pd-doped hexaaluminate catalysts for the CH_4 catalytic combustion”, *Appl. Catal. B: Environ.* 81 (2008) 88–96
[29] S. Meriani “Features of the Caeria-Zirconia System”, *Mat. Sci. Eng.,* A109 (1989) 121-130
[30] S. Suhonen, M. Valdin, M. Hietikko, R. Laitinen, A. Savimäki, M. Härkönen, “Effect of Ce–Zr mixed oxides on the chemical state of Rh in alumina supported automotive exhaust catalysts studied by XPS and XRD”, *Appl. Catal. A: Gen*., 218 (2001) 151-160
[31] I. Heo, J.W. Choung, P.S. Kim, I.S. Nam, Y.I. Song, C.B. In, G.K. Yeo” The alteration of the performance of field-aged Pd-based TWCs towards CO and C_3H_6 oxidation” *Appl. Catal. B: Environ*., 92 (2009) 114-125
[32] S.B. Kang, S.J. Han, S.B. Nam, I.S. Nam, B.K. Cho, C.H. Kim, S.H. Oh, “Effect of Aging Atmosphere on Thermal Sintering of Modern Commercial TWCs”, *Top. Catal*. 56 (2013) 298–305
[33] H.P. Sun, X.P. Pan, G.W. Graham, H.-W. Jen, R.W. McCabe, S. Thevuthasan, C.H.F. Peden, “Partial encapsulation of Pd particles by reduced ceria-zirconia”, *Appl. Phys. Letts.* 87 (2005) 201915
[34] L. Kępiński, M. Wolcyrz, “Microstructure of Pd/CeO_2 catalyst: Effect of high temperature reduction in hydrogen”, *Appl. Catal. A: Gen.* 150 (1997) 197-220
[35] M. Alexandrou, R.M. Nix, “The growth, structure and stability of ceria overlayers on Pd(111)”, *Surf. Sci.* 321 (1994) 47-57
[36] I.Y. Ahn, W.J. Kim, S.H. Moon, “Performance of La_2O_3- or Nb_2O_5- added Pd/SiO_2 Catal. in acetylene hydrogenation”, *Appl. Catal. A: Gen.* 308 (2006) 75–81
[37] E. Kim, E.W. Shin, C.W. Bark, I. Chang, W.J. Yoon, W.-J. Kim, “Pd catalyst promoted by two metal oxides with different reducibilities: Properties and performance in the selective hydrogenation of acetylene”, *Appl. Catal. A: Gen.* 471 (2014) 80– 83
[38] A. Badri, C. Binet, J.-C. Lavalley, “Metal-support interaction in Pd/CeO_2 catalysis Part 2. – Ceria textural effects”, *J. Chem. Soc. Farad. Trans.* 92(9) (1996) 1603-1608
[39] L.F. Allard, E. Voelkl, D.S. Kalakkad, A.K. Datye, “Electron holography reveals the internal structure of palladium nano-particles”, *J. Mat. Sci.* 29 (1994) 5612-5614
[40] F.J. Cadete Santos Aires, R. Darji, J.F. Trillat, A. Howie, A. Renoprez, “Hollow metallic particles obtained by oxidation/reduction treatment of organometallic precursors”, *Stud. Surf. Sci. Catal.* 130 (2000) 1109-1114
[41] P.A. Crozier, A.K. Datye, “Direct observation of reduction of PdO to Pd metal by in situ electron Microscopy”, *Stud. Surf. Sci. Catal.* 130 (2000) 3119-3124
[42] J. Railsback, A. Johnston-Peck, J. Wang, J. Tracy, “Size-Dependent Nanoscale Kirkendall Effect During the Oxidation of Nickel Nanoparticles”, *ACS Nano* 4 (2010) 1913-1920
[43] Y. Yin, R. Rioux, C. Erdonmez, S. Hughes, G. Somorjai, P. Alivisatos, “Formation of Hollow Nanocrystals Through the Nanoscale Kirkendall Effect”, *Sci.* 304 (2004) 711-714
[44] A.J. Hayter, Probability and Statistics for Engineers and Scientists, PWS Publishing Co., Boston, MA, 1996
[45] C.R. Adams, H.A. Benesi, R.M. Curtis, R.G. Meisenheimer, “Particle Size Determination of Supported Catalytic Metals: Platinum on Silica Gel”, *J. Catal.* 1 (1962) 336-344
[46] T.H., Fleisch, R.F. Hicks, A.T. Bell, “An XPS Study of Metal-Support Interactions on Pd/SiO_2 and Pd/La_2O_3”, *J. Catal.* 87 (1984) 398-413
[47] J.S. Rieck, A.T. Bell, “Studies on the Interactions of H_2 and CO with Silica- and Lanthana-Supported Palladium”, *J. Catal.* 96 (1985) 88-105

[48] M. Zhao, X. Li, L. Zhang, C. Zhang, M. Gong, Y. Chen, “Catalytic decomposition of methanol to carbon monoxide and hydrogen over palladium supported on $Ce_{0.65}Zr_{0.30}La_{0.05}O_2$ and La–Al_2O_3”, *Catal. Today* 175 (2011) 430-434
[49] M. Shelef, L.P. Haack, R.E. Soltis, J.E. deVries, E.M. Logothetis, “An XPS Study of Interactions in Thin Films Containing a Noble Metal with Valence-Invariant and Reducible Oxides”, *J. Catal.* 137 (1992) 114-126
[50] Z. Han, J. Wang, H. Yan, J. Fan, "Performance of dynamic oxygen storage capacity, water–gas shift and steam reforming reactions over Pd-only three-way catalysts", *Catal. Today* 158 (2010) 481–489
[51] C. Hori, A. Brenner, S. Ng, K. Rahmoeller, D. Belton, “Studies of the oxygen release reaction in the platinum-ceria-zirconia system”, *Catal. Today* 50 (1999) 299-308
[52] K. Hayek, R. Kramer, Z. Paál, “Metal-support boundary sites in catalysts”, *Appl. Catal. A: Gen.* 162 (1997) 1-15
[53] Y. Madier, C. Descorme, A. M. Le Govic, D. Duprez, “Oxygen Mobility in CeO_2 and $Ce_xZr_{(1-x)}O_2$ Compounds: Study by CO Transient Oxidation and $^{18}O/^{16}O$ Isotopic Exchange”, *J. Phys. Chem. B*, 103 (1999) 10999-11006
[54] A. Trovarelli, F. Zamar, J. Llorca, C. de Leitenburg, G. Dolcetti, J.T. Kiss, “Nanophase Fluorite-Structured CeO_2–ZrO_2 Catalysts Prepared by High-Energy Mechanical Milling: Analysis of Low-Temperature Redox Activity and Oxygen Storage Capacity”, *J. Catal.* 169 (1997) 490–502
[55] J.-P. Cuif, G. Blanchard, O. Touret, A. Seigneurin, M. Marczi, E. Quéméré, “(Ce, Zr)O_2 Solid Solutions for Three-Way Catalysts”, *Soc. Automot. Eng.,* SP-1288 (1997) 35-47
[56] M. Yang, M. Shen, J. Wang, J. Wen, M. Zhao, J. Wang, W. Wang., “Pd-Supported Interaction-Defined Selective Redox Activities in Pd-Ce0.7Zr0.3O2-Al2O3 Model Three-Way Catalysts”, *J. Phys. Chem. C* 113 (2009) 12778-12789
[57] A. Boisen, T.V.W. Janssens, N. Schumacher, I. Chorkendorff, S. Dahl, “Support effects and catalytic trends for water gas shift activity of transition metals”, *J. Mol. Catal. A: Chem*. 315 (2010) 163–170
[58] S. Zhao, R.J. Gorte, “The activity of Fe–Pd alloys for the water–gas shift reaction”, Catal. Letts. 92 (2004) 75-80
[59] L. Bollmann, J.L. Ratts, A.M. Joshi, W.D. Williams, J. Pazminoa, Y.V. Joshi, J.T. Miller, A.J. Kropf, W.N. Delgass F. H. Ribeiro, “Effect of Zn addition on the water–gas shift reaction over supported palladium catalysts”, *J. Catal*. 257 (2008) 43–54
[60] G. Graham, H. Jen, W. Chun, R. McCabe, "Encapsulation of Pd particles by ceria–zirconia mixed oxides", *Catal. Letts.* 44 (1997) 185-187
[61] H. Gabasch, W. Unterberger, K. Hayek, B. Klötzer, E. Kleimenov, D. Teschner, S. Zafeiratos, M. Hävecker, A. Knop-Gericke, R. Schlögl, J. Han, F.H. Ribeiro, B. Aszalos-Kiss, T. Curtin, D. Zemlyanov, “In situ XPS study of Pd(111) oxidation at elevated pressure, Part 2: Palladium oxidation in the 10^{-1} mbar range”, *Surf. Sci.* 600 (2006) 2980–2989
[62] T.R. Johns, R.S. Goeke, V. Ashbacher, P.C. Thüne, J.W. Niemantsverdriet, B. Kiefer, C.H. Kim, M.P. Balogh, A.K. Datye, “Relating adatom emission to improved durability of Pt–Pd diesel oxidation catalysts”, *J. Catal.* 328 (2015) 151-164
[63] A.K. Datye, J. Bravo, T.R. Nelson, P. Atanasova, M. Lyubovsky, L. Pfefferle, “Catalyst microstructure and methane oxidation reactivity during the Pd-PdO transformation on alumina supports”, *Appl. Catal. A: Gen.* 198 (2000) 179–196
[64] E.T. Peterson, A.T. DeLaRiva, S. Lin, R.S. Johnson, H. Guo, J.T. Miller, J.H. Kwak, C.H.F. Peden, B. Kiefer, L.F. Allard, F.H. Ribeiro, A.K. Datye, “Low-temperature carbon monoxide oxidation catalysed by regenerable atomically dispersed palladium on alumina”, *Nat. Comm.* 5 (2014) 4885

Chapter 4 - Pd Model Catalysts: Effect of Aging Duration on Lean Redispersion

Jason A. Lupescu[1,2,*], Johannes W. Schwank[1], Galen B. Fisher[1], Xiaoyin Chen[1], Sabrina L. Peczonczyk[2] and Andy R. Drews[2]

[1]University of Michigan, Ann Arbor, MI 48109 USA

[2]Ford Motor Company, Dearborn, MI 48124 USA

First published in: Applied Catalysis B: Environmental 185 (2016) 189–202

http://dx.doi.org/10.1016/j.apcatb.2015.12.012

Abstract

An automotive three-way catalyst (TWC) deteriorates as a function of temperature, time and aging environment. While much effort has gone into formulating durable exhaust catalysts, relatively little attention has been paid to controlling the aging environment on the vehicle with techniques currently in use to protect the catalyst and counteract the increasing demands for higher fuel economy (e.g., overfueling to reduce

exhaust temperatures). New engine control methods that are designed to minimize aging may be possible that can reduce the extent of catalyst deactivation and provide a lean environment capable of redispersing many of the precious metal particles. To develop improved engine control methods, detailed experimental information is needed to map the response of the catalyst to different aging conditions. In this report, we examine palladium-based model powder catalysts on ceria-zirconia, which were exposed to three different exhaust compositions, lean-only, rich-only and redox, each at 700°C for three different durations, 20 minutes, 2 hours and 16 hours. Residual catalyst activity and metal-support interaction were probed with Water Gas Shift (WGS) reaction and Oxygen Storage Capacity (OSC) measurements. The Pd metal particle size and dispersion were estimated by H_2 chemisorption and XRD line broadening. Lean catalyst treatments at 550°C and 700°C were applied to determine the effect on Pd size and catalyst activity. An infrared study of CO adsorption onto the catalysts was used to identify whether Pd crystallite facets were covered by the support after exposure to the redox aging environment then again after the lean treatments were applied. The aging temperature and reducing gas environment significantly deteriorated catalytic activity through a combination of metal oxidation state effects and support interactions, while the aging duration was linked to the extent of Pd sintering reversibility through lean treatments. These insights provide a basis to develop engine control and aftertreatment design strategies to avoid severe aging modes and determine how often to actively intervene to regenerate the catalyst.

4.1 Introduction

The automotive catalytic converter, or Three-Way Catalyst (TWC), works in unison with engine controls that manage exhaust gas oxygen (O_2) concentration to abate regulated fuel combustion products like carbon monoxide (CO). The TWC washcoat contains a noble metal catalyst (i.e., Pd) impregnated onto a high surface area support material composed of alumina (Al_2O_3), oxygen storage capacity (OSC) promoters including mixtures of ceria and zirconia (CZO), and durability stabilizers such as rare earth oxides lanthana (La_2O_3) and yttria (Y_2O_3) [1]. The on-board engine control computer is essential to enable brief, controlled cycling of fuel-rich (oxygen deficient) and fuel-lean (excess oxygen) combustion exhaust to perform simultaneous oxidation and reduction reactions [1, 2]. Over time, the TWC typically shows decreased efficiency of these reactions under the same exhaust environment, which is linked to deactivation. TWC deactivation modes include noble metal sintering [3, 4], poisoning by fuel and oil additives [5], loss of surface area and OSC component sintering [1, 2, 6]. Characterization studies of full useful-life aged automotive TWCs revealed that the dispersion of noble metals had fallen to only about 1-5% [7, 8], revealing that the vast initial amount of metal was buried inside large metal agglomerates and lost to involvement in gas-phase reactions. While in similar studies, OSC component sintering was explained by loss of contact between the noble metal and the OSC component [9, 10, 11, 12, 13, 14], and by partial migration of OSC component materials, covering the noble metal [15, 16, 17].

Although TWC deactivation is largely irreversible, prolonged exposure to an oxidative gas environment can cause changes to the metal that result in partial reactivation. An increase in the Pd metal dispersion was observed following dry oxygen treatment that resulted in a lower temperature required for 50% conversion of combustion pollutants [18, 19]. In another study, Pd particles on an Al_2O_3 support heated in a feed containing oxygen were observed to transform into PdO above 325°C, and upon further heating from 350°C to 800°C the particles wet and spread over the support [20, 21], ultimately shrinking to a size below the detection limit of the electron microscope used [22]. Pd redispersion is generally believed to begin at the temperature

when Pd particles oxidize to PdO, and this temperature depends upon the Pd particle size [20, 23]. PdO is stable up to 800°C in air and does not sinter or emit adatoms [24]. This enables PdO to wet and spread over the support. The onset temperature of redispersion was found to decrease with increasing Pd metal dispersion (decreasing Pd crystal size) [20, 23]. Pd redispersion is therefore thought to occur through the oxide form as it does not occur above the temperature of PdO decomposition [20, 21], which is both a function of the support material and gas phase oxygen concentration [21, 25, 26]. To be of automotive relevance, intentional Pd redispersion would ideally be performed within the time scale of an engine deceleration fuel cut, which was shown to expose the catalyst to air for about 2-10 seconds on the FTP-75 (federal drive cycle) [27]. Newton *et al.* performed redox cycling at 400°C with 2wt% Pd/Al_2O_3 and observed that the Pd particle size immediately dropped from an average of 600 atoms per particle to about 20 atoms per particle within 2 seconds of the lean cycle onset, coinciding with the Pd to PdO transition [28]. If the Pd oxidation rate can be measured, then the Pd redispersion rate can be estimated and used as part of an engine control strategy to optimize the redispersion process.

The goal of this investigation was to determine how characteristics of deactivated model Pd catalysts aged for different durations were affected by exposure to post-aging oxidizing gas environments. Active intervention into the TWC aging process using periodic oxidative engine exhaust events may be useful to restore the catalyst conversion efficiency. However, the limits to the effectiveness of this regeneration method are unknown. To be fully effective, a detailed understanding of the Pd particle size response is needed. There is no one technique that can derive the true Pd size on CZO supports, so a synthesis of multiple, yet limited techniques, were used so that a consistent interpretation could be made. This requires evaluation of a TWC to characterize the Pd particle size in concert with probe reactions to assess the metal-support interface and measure residual catalyst activity, support surface area changes and PdO formation rate. While these evaluations may suggest a strong metal support interaction (SMSI) with Ce migrating and decorating the Pd surface during reducing conditions [15, 29, 30, 31, 32], obtaining direct evidence with high resolution electron microscopy is extremely difficult due to poor contrast between Pd, Zr and Ce. However,

CO adsorption onto the surface of supported Pd catalysts during acquisition of infrared spectra has shown capability to identify the accessible Pd facets [33, 34] and provide evidence of coverage via SMSI [30]. Here, we characterize these changes and identify the most severe deactivation modes so that they can be avoided through engine control methods.

4.2. Experimental

4.2.1 Preparation of Model TWC Samples

A model powder catalyst of 1.5wt% Pd on ceria-zirconia (Pd/CZO) was prepared at a Ford OEM supplier laboratory by incipient-wetness impregnation of the ceria-zirconia ($Ce_{0.5}Zr_{0.5}O_2$) support with a palladium solution free from chlorides. After drying, this catalyst was calcined at 500°C for 4 hours in air to fix the Pd on the CZO material. Uncatalyzed ceria-zirconia ($Ce_{0.5}Zr_{0.5}O_2$) powder was also used as a standard to acquire baseline characterization data. The powders were then sieved to obtain particles between 40-60 mesh (250-420 microns).

4.2.2 TWC Aging Procedures

Catalyst aging environments were established in a continuous flow reactor at 700°C with a tight air-fuel modulation to represent operating conditions of an automotive close-coupled catalytic converter. Three aging gas compositions were used: lean-only (0.1% O_2, 10% H_2O and N_2), rich-only (0.15% CO, 0.05% H_2, 10% H_2O and N_2) and redox conditions where the lean and rich feeds were alternated in 10 minute step pulses. The CO gas stream was scrubbed of iron carbonyls. A round bottomed quartz boat measured 100 mm long, 17 mm wide and 5mm tall was loaded with 1.50 g of catalyst powder and placed inside a 19 mm ID quartz reaction tube in the heating zone of the surrounding oven with a 1/16 inch diameter thermocouple placed over the boat in the aging gas stream and a 1/32 inch diameter thermocouple bent into the boat with the tip buried in the powder. Sample sets were aged for 20 minutes, 2 hours and 16 hours, respectively.

4.2.3 TWC Preconditioning

Since gasoline engines operate close to stoichiometry, the catalyst OSC state is generally partly depleted. Therefore at the beginning of all characterization and activity measurements for this study, all samples were initially in a reduced state produced by exposure to 9% H_2 in argon at 300°C for 30 minutes flowing at 0.22 L/min to remove all surface oxygen. The samples were then cooled in argon to room temperature.

4.2.4 TWC Characterization Techniques

The phase identification of the Pd/CZO catalysts was confirmed by X-ray diffraction (XRD) pattern analysis. A Rigaku Miniflex II diffractometer was used with a Cu Kα X-Ray (λ = 1.5406Å) radiation source set at 30 kV and 15 mA. A catalyst sample mass of 0.1 g was wet-milled with a mortar and pestle in ethanol then dripped onto an off-axis cut silicon crystal sample substrate and dried. Scans were performed with a step size of 0.005°2θ at a scan speed of 1°2θ/min from 5°2θ to 90°2θ.

The surface characteristics of the catalysts were determined by N_2 physisorption, X-ray photoelectron spectroscopy (XPS) and Diffuse Reflectance Infrared Fourier Transform Spectroscopy (DRIFTS). The BET specific surface area and BJH pore volume (for pores between 17-300Å) were determined with a Micromeritics ASAP2420 instrument using N_2 adsorption at 77K. A 48-point adsorption and 33-point desorption isotherm plot was generated across a range of 0.1-0.9 P/P_0. Elemental composition and chemical state information were determined with a Kratos AXIS 165 Electron Spectrometer using a monochromatic Al Kα (1486.6 eV) X-ray excitation source operated at 12 kV, 20 mA (240 W). Each sample was pressed into a pellet and then mounted onto sticky double sided pressure sensitive adhesive tape. Data were collected using pass energies of 80 eV or 20 eV to obtain survey or high resolution spectra, respectively. All spectra were acquired using charge neutralization with an electron flood source. Elemental quantification of the high resolution spectra was accomplished using CASAXPS software Version 2.3.16, using routines based on Scofield photoionization cross-section values. A Shirley type background was used to fit all high resolution spectra. The Zr 3p fit was first determined from a CZO standard using

60% Gaussian and 40% Lorentzian line shapes with an area ratio of 0.5, a full width at half maximum (FWHM) constrained between 0.6-2.8, and a peak separation of 13.4 eV. The remaining area under the envelope was then fit by adding Pd 3d peaks. The Pd 3d species was fit with a doublet using 60% Gaussian and 40% Lorentzian line shapes with an area ratio of 0.667, a FWHM constrained within 0.6-2.8, and a peak separation of 5.2 eV. Binding energies were referenced to the aliphatic C 1s peak at 284.6 eV [35]. Infrared spectra were collected with a Nicolet 6700 FTIR spectrometer with Auxiliary Experiment Module including a praying mantis cell to facilitate gas exchange to and heating of the sample. Fine powder catalyst samples recovered from the XRD analysis were poured into the praying mantis sample cup onto a supporting screen. Clean samples were prepared as follows: 1) 25% H_2 in nitrogen fed to the sample for 16 hours at 400°C, 2) switched to 1% O_2 in nitrogen carrier gas to burn off saturated carbonate and formate surface species for an hour, 3) switched off O_2 and heated the sample cell to 600°C for one hour in nitrogen-only to decompose surface PdO, 4) sample was cooled to 22°C and stabilized over one hour. The IR spectra were collected with 64 scans at a resolution of 2 cm^{-1} in repeating loops every two minutes. A clean sample background was acquired first under flowing nitrogen then 1% CO was added to saturate the surface through two hours.

The mean Pd dispersion and particle size was determined with two methods. H_2 chemisorption was performed using a Micromeritics ASAP2020 instrument with a static volumetric adsorption/out-gas/re-adsorption method described by Chen *et al.* [19]. Prior to analysis, each sample was first degassed in N_2 at 500°C, then cooled under vacuum to 1 microtorr prior to evaluation. Each sample was then reduced at 350°C in pure H_2, (assumed to not sinter the Pd particles) then exposed to vacuum at 1 microtorr to remove Pd hydride prior to H_2 chemisorption measurements at 35°C. A hydrogen adsorption stoichiometry value of 1 was assumed, for one adsorbed H atom per every one surface Pd atom. This technique is an improvement upon the classic H_2–O_2 titration method and avoids problems of H_2 spill-over and Pd hydride formation from interfering with the irreversible adsorbed H_2 calculation [36, 37]. The differential results were used to report Pd dispersion and size to exclude physisorbed H_2 on the support. H_2 chemisorption was used for all samples since we found that CO chemisorption

significantly overestimated the Pd dispersion on the CZO supports, probably due in part to CO adsorption on CZO forming stable carbonate species [38]. Post-process curve fitting of the XRD pattern Pd [111] peak was performed with the Rigaku PDXL software program. The software calculations used for estimating mean Pd crystalline length from XRD pattern line broadening was based on the Scherrer equation [39]. The shape factor used was 0.89 for spherical crystallites and the peak integral method was used to determine peak breadth. The instrument broadening was corrected with a LaB_6 calibration standard.

4.2.5 High Temperature X-Ray Diffraction (HTXRD)

HTXRD was measured using a Bueler HDK furnace attachment mounted to a Scintag X1 diffractometer equipped with a low divergence (0.03°) beam of Cu-Kα radiation produced using an Osmic collimating optic. Data were collected using an Inel 120° position sensitive detector with a 250 mm radius. X-Ray source settings were 45 kV and 40 mA. Scans were performed with an interval of 0.015°2θ. Samples were prepared by wet-milling 20 mg of powder in ethanol and pipetting it onto a 1 mm thick, 10 mm square silicon carbide single crystal slide and allowing to dry. The slide was then placed onto the primary heating strip that includes a Pt thermocouple welded to its underside for feedback temperature control. Calibration of the sample temperature was verified to be within +/-5°C by comparing the observed melting transition in its HTXRD pattern to the known melting point of high purity aluminum. Gas flow into the furnace chamber was controlled with MKS mass-flow controllers at a total flow rate of 1 L/min. The internal volume of the furnace chamber was about 1.5 L. Oxidation experiments were conducted after an initial *in-situ* 1 hour reduction in 250 sccm of 5% H_2 in balance N_2 at 300°C. Prior to each experiment, the chamber was purged with pure N_2 for 5 minutes and the heating strip temperature was adjusted to the temperature of interest. HTXRD data were recorded with one scan during the purge to obtain the initial Pd [111] peak size and the feed gas was switched to dry air simultaneously with the beginning of an acquisition of repeated scans. The PdO phase fraction was calculated as one minus the quotient of the current integrated Pd peak area at time *t* divided by the initial Pd peak area at time zero. Temperatures used to collect HTXRD data were in the range of

200°C to 350°C.

4.2.6 Thermogravimetric Analysis (TGA)

Thermogravimetric analysis (TGA) of PdO decomposition and Pd reoxidation was carried out in a TA Q500 instrument. About 77 mg of Pd/CZO sample was placed on the sample pan. The sample was preconditioned by holding at 400°C in 10% O_2 environment and balance N_2 at 100 mL/min for 180-240 minutes for complete oxidation, then switching off O_2 and holding in N_2 for 60-120 minutes at 100 mL/min and heating to 700°C at a 5°C/min ramp rate to decompose PdO. The oven temperature was then adjusted to one of two desired measurement temperatures, 350°C or 700°C, and held for 30 minutes before switching on the 10% O_2 to begin Pd oxidation. A Curie point temperature calibration using nickel (placed in the sample pan) confirmed the actual oven temperature is within +/- 2°C of the set value.

4.2.7 TWC Activity Measurements

The ASAP2020 quartz j-tube that was fit onto a flow reactor measured 10.5 mm ID and was loaded with a catalyst sample mass of 0.30 g between 6 mm redistributing layers of quartz wool. The bed height for each Pd/CZO sample was 4 mm. Matheson dynablenders and flow controllers managed the gas flow through the system. A pyrex glass water bubbler was used to supply a stable stream of water vapor by saturation of the room temperature bulk gas stream. A solenoid set could be triggered to bypass the bulk gas around the water bubbler. The parts downstream of the water bubbler were stainless steel and wrapped in heat tape maintained at 150°C to prevent condensation. The CO gas stream was scrubbed of iron carbonyls. Two K-type 1/32-inch diameter thermocouples were placed 16 mm before and 13 mm after the sample bed. A Hiden HPR20 quadrupole electron ionization mass spectrometer, pressure sensor and Horiba lambda sensor were used to sample the gas downstream of the j-tube. The HPR20 SEM detector measured five mass values in torr with a 2 Hz sampling rate at an inlet sampling pressure of 1E-5 torr. Two corrections were required to normalize the signals from other species into individual concentrations. First, the double excitation argon mass 20 value was scanned, which is 11% of the total argon level, rather than the

typical mass 40 to get the measured argon value below the SEM detector limit of 1E-6 torr. Second, there was a CO and CO_2 mass overlap of 11.4%, so that amount of the CO_2 value was subtracted from the CO value during data processing.

Oxygen storage capacity (OSC) measurements were carried out by alternating one minute lean or rich exposures, each separated by a one minute purge. The purge pulse was just the constant bulk carrier gas of CO_2 and argon at 975 mL/min while microvalves added a square step pulse of CO or O_2 into the carrier gas at 25 mL/min. The bulk flow with lean pulse was 1% O_2, 2% CO_2 and balance Ar. The bulk flow with rich pulse was 2% CO, 2% CO_2 and balance Ar. The gas mixture was initially established at equilibrium over the catalyst sample at 50°C. At least five CO pulses were measured at a fixed oven temperature before increasing the heating set point to the next 50°C increment, to a maximum set point of 400°C.

Water gas shift (WGS) measurements were carried out with a constant feed of bulk carrier gas made up of 2% CO, 2% CO_2, 2.5% H_2O and argon at a total flow of 1 L/min. The bulk stream of argon and CO_2 were fed through the water bubbler at 22°C to saturate the bulk gas and later downstream the CO was injected at the microvalve. The gas mixture was initially established at equilibrium over the catalyst sample at room temperature before triggering the start of the heating ramp at 10°C/min to 400°C.

Multiple OSC and WGS tests were run to determine whether the results drifted with changes to the sample caused by exposure to the gas stream at 400°C. At least three OSC and WGS measurements were run on all samples. The last run was usually selected for comparison to the other sample aging conditions.

4.3 Results

4.3.1 Catalyst Aging and Pd Redispersion Zone

The catalyst aging and Pd redispersion conditions were compared to the results from Peuckert, which were used to develop an equation that predicts the bulk PdO

decomposition temperature as a function of O_2 concentration [26]. The results from this equation are plotted in Figure 4-1 for 1 atm total pressure. With just 0.1% O_2 in the lean-only and lean redox aging environments at 700°C, the catalyst was above the bulk PdO decomposition temperature of about 620°C. Lieske and Völter observed that Pd needed to be oxidized before redispersion would occur [23]. Incorporating the observations of Liekse and Völter, the area below the PdO decomposition line is shaded on Figure 4-1 and labeled as the "Pd Redispersion Zone". Entry into the lower Pd redispersion zone was tested with lean treatments at 550°C or 700°C with dry gas containing 21% O_2/He or zero air, an environment where the supported catalyst was well below the bulk PdO decomposition temperature of about 800°C. Farrauto *et al.* demonstrated that there was a hysteresis between the PdO formation and decomposition temperature in air that varied with support. For example, PdO on ceria decomposed during heating at 775°C and Pd reoxidized during cooling at 730°C [25]. At lower oxygen concentrations near 0.5% O_2, the support effects diminish and a supported PdO decomposition temperature is closer to the bulk PdO value in Figure 4-1 as demonstrated by Colussi *et al*. on both Pd/Al_2O_3 and $Pd/CeO_2/Al_2O_3$ catalysts [40]. Therefore, once the PdO had decomposed into metallic Pd around 620°C during heating under the redox or lean aging conditions at 700°C, reoxidation of Pd would not occur until the temperature had dropped below the hysteresis temperature. Consequently, the supported Pd would likely be in the metallic state for all three aging environments.

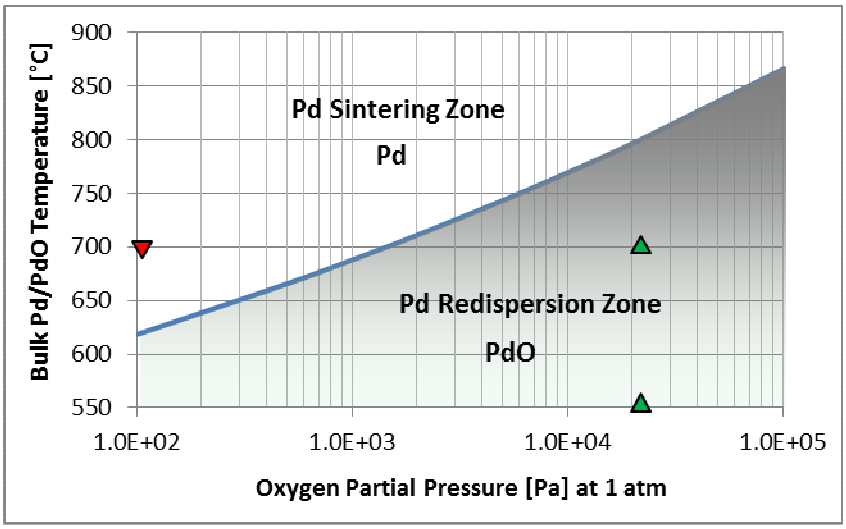

Figure 4-1: Bulk Palladium Oxide thermal stability using a published equation from reference [26]: log (pO_2/1 Pa) = 15.8 - 12300K/T. The red triangle represents the lean aging condition of 0.1% O_2 that is 80°C above the oxide decomposition temperature. The green triangles represent the lean treatment condition of 21% O_2 that are well below the oxide decomposition temperature.

4.3.2 Surface Area and Pore Volume Characterization

The BET surface area and BJH adsorption pore volume for each sample are listed in Table 4-1 below, both fresh and after exposure to various aging environments. The fresh Pd/CZO sample had a surface area of 91 m^2/g and a pore volume of 0.160 cm^3/g. The catalyst samples showed a loss in residual surface area after each aging duration interval, but in each case the lean-only aging environment was the least severe condition and the redox aging environment was the most severe aging condition after 2 hours. The 2 hour lean treatment caused some surface area loss when applied after 20 minutes of aging, while the 2 hour and 16 hour aged samples were more stable. All three 20 minute aged samples showed an increased pore volume over fresh, perhaps from the aging temperature exceeding the calcination temperature, but the aging conditions soon sintered the pores as evidenced by the 2 hour and 16 hour data. The redox aging showed the most pore volume loss after 2 and 16 hours. CZO is a reducible support under these conditions and the repeated redox cycling was more degrading to CZO than the other environments at 2 hours and beyond.

Table 4-1: Support surface area and Pd size characterization of Pd/CZO samples					
Environment	Duration	N_2 Physisorption		H_2 Chemisorption	
		Surface Area [m^2/g]	Pore Volume [cm^3/g]	Pd dispersion [%]	Pd particle size [nm]
Fresh	-	91	0.160	22%	5.1
Lean-only 700°C	20 min	66	0.162	19%	5.8
	2 hours	59	0.160	16%	6.7
	16 hours	49	0.159	13%	8.6
Rich-only 700°C	20 min	59	0.166	u/d†	u/d†
	+ 550°C/2h air	53	0.152	*3.6%†*	*30†*
	2 hours	52	0.159	u/d†	u/d†
	+ 550°C/2h air	48	0.154	*2.9%†*	*38†*
	16 hours	46	0.154	u/d†	u/d†
	+ 550°C/2h air	44	0.154	*2.0%†*	*55†*
Redox (10 min lean/10 min rich) 700°C	20 min	63	0.163	*7.9%†*	*14†*
	+ 550°C/2h air	60	0.156	*12%*	*9.1*
	+ 700°C/2h air	55	0.156	20%	5.4
	2 hours	51	0.156	u/d†	u/d†
	+ 550°C/2h air	47	0.151	*2.1%†*	*52†*
	+ 700°C/2h air	52	0.158	13%	8.8
	16 hours	41	0.150	u/d†	u/d†
	+ 550°C/2h air	40	0.152	*1.3%†*	*84†*
	+ 700°C/2h air	41	0.149	8.7%	13

† Pd particles suspected to be covered or partially encapsulated

4.3.3 XRD Pattern Phase Identification

The XRD patterns of the fresh, aged and post lean treated samples of Pd/CZO are shown in Figure 4-2 and are consistent with the expected peaks for a CZO support. The fresh sample Pd [111] peak was indistinguishable in the XRD pattern apart from the background. Figure 4-2a shows the XRD pattern after 20 minutes of aging. A slight appearance of a peak at 40°2θ emerged for the redox sample with a peak maximum of 40% above the average background measured at 42°2θ. The 700°C lean treatment applied to the redox aged sample caused the Pd[111] peak to vanish. A Pd [111] peak fit of the redox aged sample resulted in a bulk diameter of 20 nm, which was perhaps representing just the largest crystals. Pd particles less than 6 nm are often not distinguishable apart from the background XRD pattern. Therefore a significant number

of the Pd particles on the 20 minute redox aged sample were likely below the detectable threshold. Figures 4-2b and 4-2c shows the XRD pattern after 2 hours and 16 hours of aging, respectively. A significant Pd [111] peak was observed at 40°2θ only for the redox and rich-only aged Pd/CZO samples. The 700°C lean treatment decreased the area of the redox aged Pd [111] peak and shifted it slightly to a lower scattering angle of 39°2θ, indicating an expanded lattice that are similar to the shift observed with Figure 4-2d β-$PdH_{0.64}$ (reference card 04-002-0377).

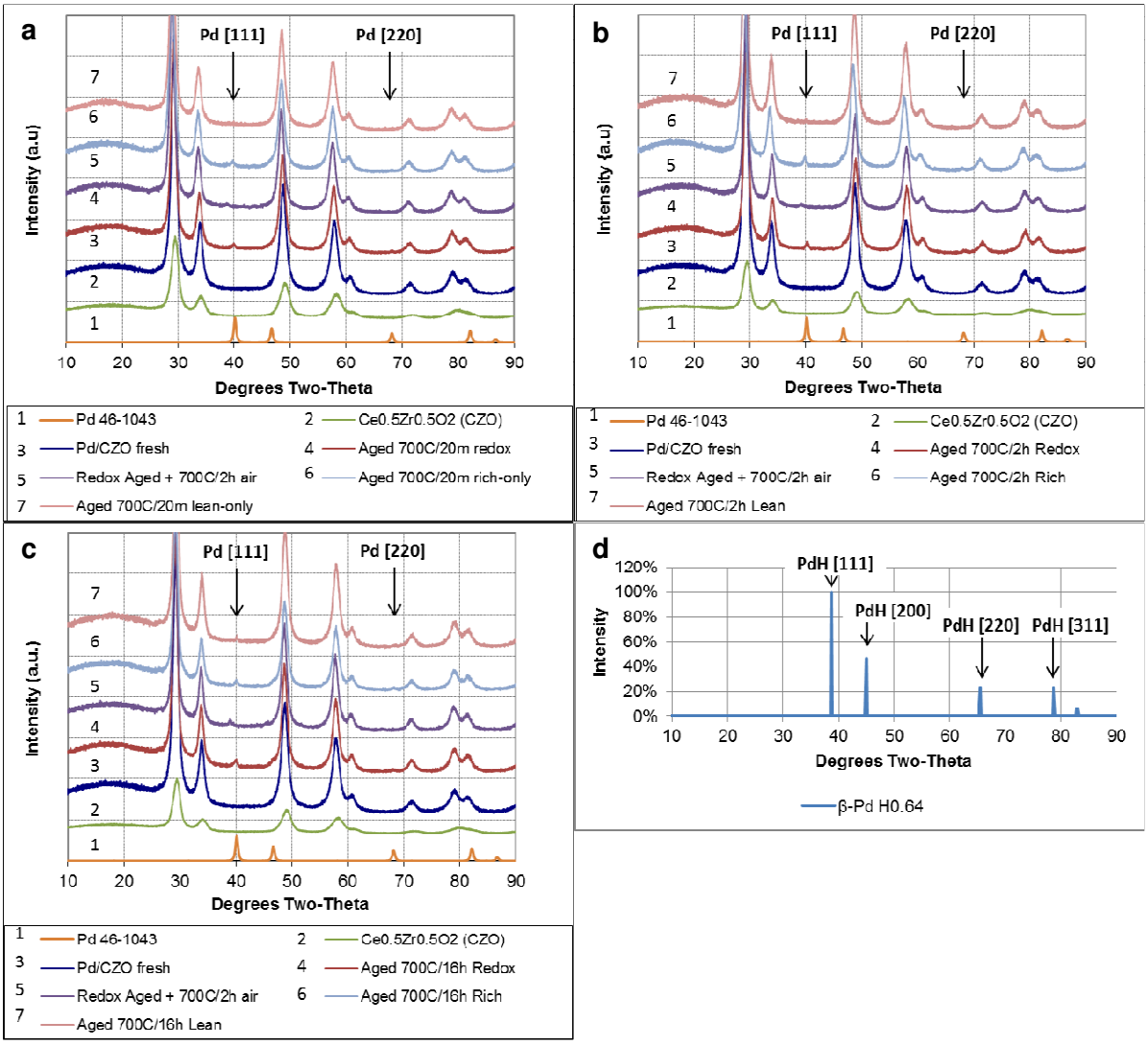

Figure 4-2: XRD pattern results. Plots for: a) 20 min aging, b) 2 hours aging, c) 16 hours aging, d) reference β-PdH0.64

4.3.4 Average Pd Size Comparison

The apparent Pd dispersion and Pd particle size for each sample are listed in Table 4-1. The Pd metal dispersion (D) was estimated as a function of the Pd particle size (d_P) using equation 1 below, which is described further by Baylet *et al.* assuming spherical shapes [41].

$$D\ [\%] = (6 \times 10^5) * (M_{Pd}) / (\rho_{Pd} * S_{Pd} * d_P\ [nm]) \quad \text{Equation 1}$$

With M_{Pd} as the Pd atomic weight of 106.4 g/mol, ρ_{Pd} as the Pd density of 12 g/cm^3, S_{Pd} as the molar surface area of Pd metal of 47,780 m^2/mol assuming an equidistribution of the low index faces.

The lean-only aging environment resulted in modest decreases in Pd dispersion with aging duration as measured by H_2 chemisorption. The redox and rich-only aging environments at 2 hours and 16 hours each had undetectable (u/d) Pd surface area as measured by H_2 chemisorption. H_2 chemisorption provides a quantitative measurement of the exposed metal surface. Strong metal support interaction (SMSI) with Pd under reducing conditions are known to confound the results of this technique, as any reducible oxide support material can decorate or otherwise chemically inhibit H_2 access to the metal surface [42, 43]. The undetectable Pd surface area results after exposure to the rich-only conditions at 700°C is consistent with SMSI effects, although perhaps surprising after just 20 minutes. At 20 minutes of aging the 550°C/2h lean treatment provided a modest increase in Pd dispersion, while the 700°C/2h lean treatment restored the Pd dispersion completely to the level of the lean-only aging. These lean treatment Pd redispersion benefits diminished as the sample was allowed to accumulate a longer aging duration prior to the lean treatment application.

The changes in Pd size determined by H_2 chemisorption was checked against the trends observed in XRD pattern Pd [111] peak fit estimates as shown in Table 4-2. The XRD Pd size estimate is a volumetric average technique and the result should be larger than the estimate from chemisorption, which is a surface average technique, while both techniques are weighted towards larger particles. The Pd particles in Table

4-2 were 21 nm or less and within the size range in the literature of 2-33 nm where crystallite length is synonymous with particle size, as those works used electron microscopy and chemisorption for confirmation [44, 45, 46, 47]. Note that crystallite length can be smaller than particle size if large particles are made of agglomerated crystals of if any poorly crystalline regions exist in the particle. The fresh and 20 minute aged samples were excluded from Table 4-2 as very small metal crystallites have excessively broad peaks that would not be completely detectable apart from the support diffraction pattern, since the width of the X-ray diffraction peak is inversely related to the crystallite length. The 2 hour and 16 hour rich-only and redox aged samples both showed Pd particles that were 17 nm and 20 nm, respectively by XRD, which would result in 5-6% dispersion if the Pd particles were not covered by support material through SMSI effects. No Pd size decrease was observed by XRD following the 550°C/2h lean treatment. However, the 700°C/2h lean treatment did show nearly a 33% reduction in Pd size on the 2 hour redox aged sample, yet a 10% reduction in Pd size on the 16 hour redox aged sample. After the 700°C/2h lean treatment, reasonable agreement in Pd size was shown for the two characterization techniques, since the SMSI effect was removed by oxidation and the sintered Pd particles were large enough to be detected apart from the background pattern. The XRD Pd size results confirm the diminishing benefit of the 700°C lean treatment the longer the sample is allowed to age.

Table 4-2: Comparison of Pd size characterization methods on Pd/CZO samples

Environment	Duration	H_2 Chemisorption		XRD Pd[111] peak fit	
		Pd dispersion [%]	Pd particle size [nm]	Pd dispersion [%]	Pd particle size [nm]
Redox (10 min lean/10 min rich) 700°C	2 hours	u/d†	u/d†	6.5%	17
	+ 550°C/2h air	*2.1%†*	*52†*	5.3%	21
	+ 700°C/2h air	13%	8.8	10%	11
	16 hours	u/d†	u/d†	5.4%	20
	+ 550°C/2h air	*1.3%†*	*84†*	5.4%	20
	+ 700°C/2h air	8.7%	13	6.3%	18

† Pd particles suspected to be covered or partially encapsulated

4.3.5 XPS Surface Characterization

The XPS spectra of the fresh and redox aged Pd/CZO samples are shown in Figure 4-3. The Pd 3d peaks were fit under the raw data between the shoulders of the Zr 3p peaks as is typically performed for analysis of Pd on CZO support [48, 49, 50, 51]. The fresh Pd/CZO sample had two Pd $3d_{5/2}$ peaks, at 334.7 eV for Pd metal and at 337.1 eV for Pd^{+2}. These results are consistent with those reported for Pd foil at 334.9 eV and PdO at 336.8 eV [52]. Pd peak shifting, due to redox aging or after a lean treatment, was not significant. However, redox aging suppressed the intensity of the Pd^0 peaks and eliminated the Pd^{+2} peaks. The 700°C/2h lean treatments restored the Pd^{+2} peaks, in spite of the reduction pre-treatment. Four more 700°C/30min lean treatments were needed with the 16h aged sample to achieve almost the same benefit observed with one lean treatment on the 2h aged sample.

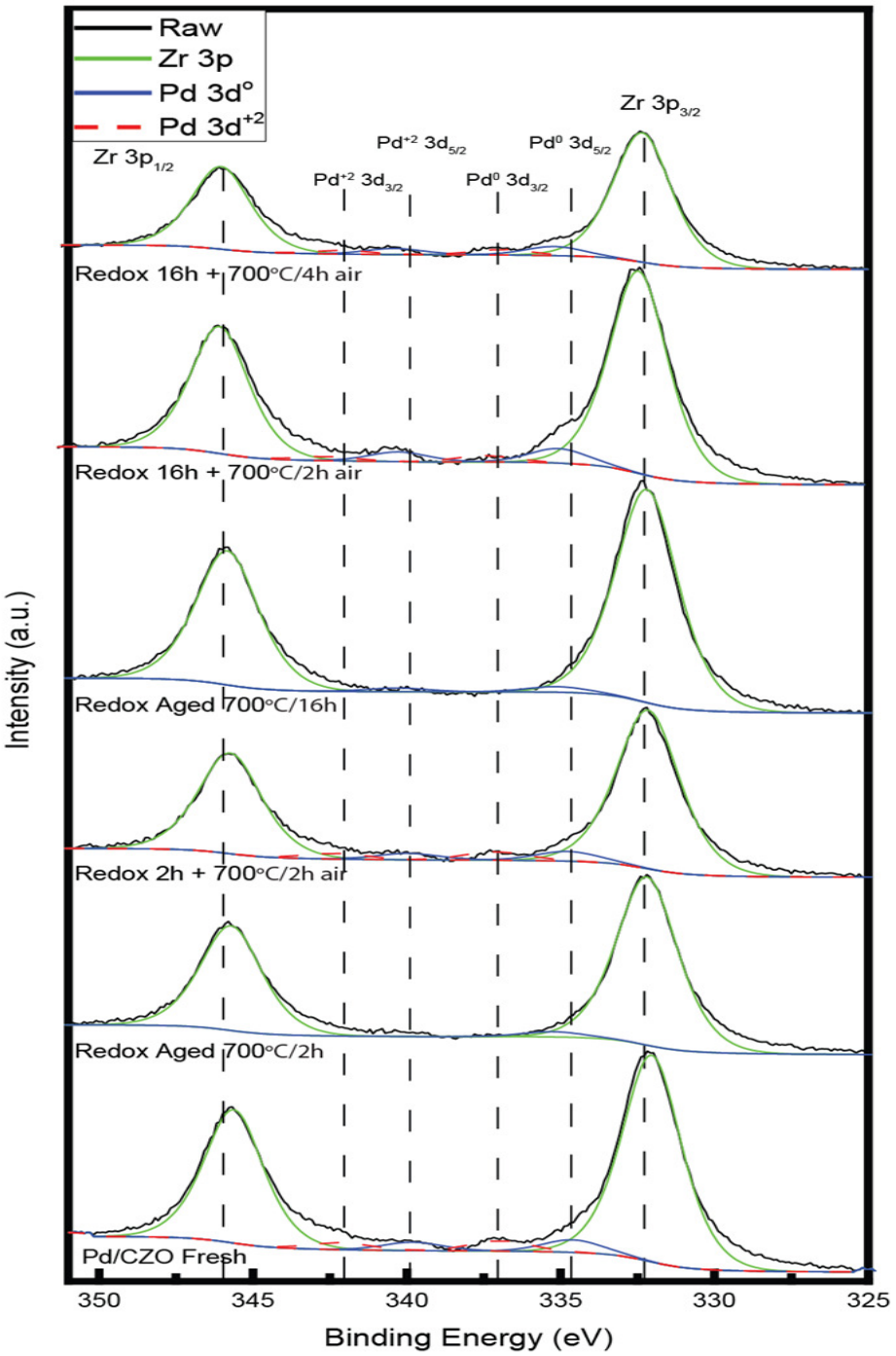

Figure 4-3: XPS Surface Analysis of Pd 3d. Solid blue lines are representative fits for Pd metal, dashed red lines are representative fits for Pd^{+2}. Spectra are offset for clarity.

The XPS spectra of the Ce 3d peaks are shown in Figure 4-4. Neither the Ce 3d $_{5/2}$ peak at 882.0 eV or the Ce 3d $_{3/2}$ peak at 900.4 eV showed a shift due to redox aging

or lean treatments. The other Ce 3d peaks shown are satellite peaks that arise from interactions with the Ce 4f valence electrons after the 3d core electron is emitted. Each core level (3d $_{5/2}$ and 3d $_{3/2}$) has 3 satellite peaks associated with it: the 3d $_{5/2}$ satellite peaks at v' = 884.0 eV, v'' = 889.1 eV and v''' = 897.8 eV; and the 3d $_{3/2}$ satellite peaks at u' = 903.2 eV, u'' = 908.1 eV and u''' = 916.3 eV. The u''' intensity varies linearly with the amount of Ce^{+4} and is fairly well separated from the rest of the peaks, enabling better estimation of the background. We can compare the signal from u''' to the intensity of the total envelope to get the percentage of Ce^{+4} on the surface. This technique is further described elsewhere [52].

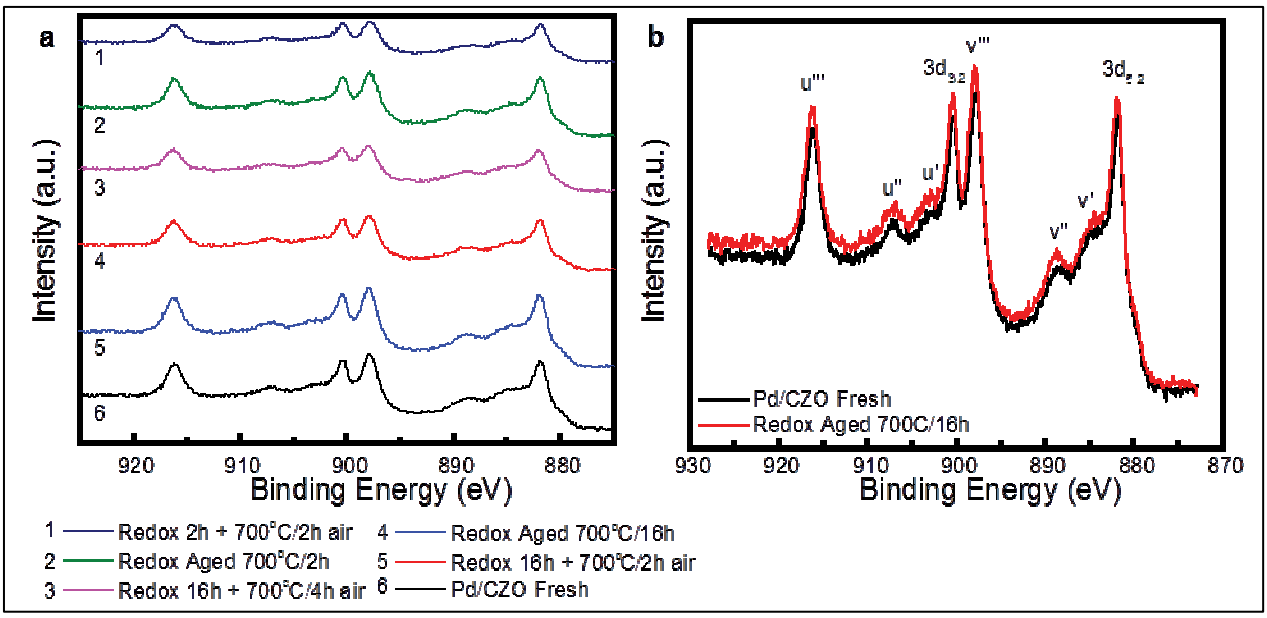

Figure 4-4: XPS Surface Analysis of Ce 3d. Spectra are offset for clarity. Plots: a) Fresh and Redox Aged Samples and b) identified satellite peaks

The atomic concentrations from the top surface layers are shown in Table 4-3 based on the peak intensities shown in Figures 4-3 and 4-4. Adventitious carbon formed from exposure to room temperature air during the sample transfer and pellet pressing. While all catalyst samples were initially reduced prior to XPS evaluation, about half of the fresh Pd was still Pd^{+2}, perhaps due to an abundance of interface sites with finely dispersed Pd and oxygen from CeO_2. After 2 hours of redox aging, the surface concentration of Pd^{+2} species vanished and the total Pd signal was decreased by 70% relative to fresh. The 700°C lean treatment applied to the 2 hour aged sample

restored Pd over the surface, reestablished the Pd^{+2} bonds with Ce up to the fresh level and lowered the surface concentration of Ce^{+3}. After 16 hours of redox aging, the surface concentration of total Pd was decreased by 70% coincident with a surface concentration increase in Ce by 15% and Zr by 10%, relative to fresh, without a significant increase in oxygen. This effect is consistent with Pd surface coverage by Ce [53]. The 700°C lean treatment applied to the 16 hour aged sample restored Pd over the surface, reestablished the Pd^{+2} bonds with Ce to near half of the fresh level and lowered the surface concentration of Ce^{+3}. Another four 700°C lean treatments in 30 minute durations increased the amount of Pd^{+2}, but again not to the level of the fresh catalyst. This improvement of exposed Pd surface from redox aged to 700°C/2h air regeneration agrees with the H_2 chemisorption measurements in Table 4-1. XRD does not detect surface coverage by support, but does confirm that the Pd particle size decreased following the lean treatment from 17 nm to 11 nm for the 2 hour redox aged sample and from 20 nm to 18 nm for the 16 hour redox aged sample. These Pd particle sizes are all within the detection depth of the XPS instrument so the dramatic loss in Pd surface concentration from fresh to redox aged was most likely due to CZO support coverage and not Pd sintering.

Table 4-3: Atomic surface concentrations of fresh and aged Pd/CZO samples by XPS

Duration	Sample	C	O	Ce^{+3}	Ce^{+4}	Zr	Pd^{0}	Pd^{+2}
0 min	Fresh	20.9	59.9	2.0	4.0	12.6	0.29	0.28
2 hours	Redox 700°C	24.9	58.6	1.4	4.0	10.8	0.16	-
	+ 700°C/2h air	25.2	58.8	1.2	4.6	9.4	0.40	0.29
16 hours	Redox 700°C	22.8	56.2	1.9	5.0	13.9	0.16	-
	+ 700°C/2h air	24.1	57.8	1.3	4.3	11.9	0.35	0.16
	+ 700°C/4h air	27.9	54.1	1.3	4.2	11.9	0.35	0.21

4.3.6 Infrared measurements

The wave numbers characteristic to CO adsorption onto ceria, single Pd crystals and supported Pd particles are well studied [54, 55, 56, 57] and summarized in Table 4-4. However, the IR band wave numbers are known to change with temperature, pressure and CO coverage [58, 59]. Therefore the corresponding species given in Table 4-4 are approximate.

Table 4-4: IR bands on CZO and Pd		
Species	**Wave number [cm^{-1}]**	**Reference**
Carbonates bidentate	1028, 1286, 1562	[54]
Carbonate unidentate	1062, 1454	[54]
CO-Ce^{+4} linear	1310-1330	[54]
Formates	1360, 1580	[54]
Hydrogen carbonate	1399-1408	[55]
Inorganic carboxylate	1510, 1560	[54]
Aromatic C=C bending	1500-1700	[56]
C=O stretch	1650	[56]
CO-Pd [111] bridge x3	1835-1890	[57]
CO-Pd [111] bridge x2	1948	[57]
CO-Pd [100] bridge x2	1895-1997	[57]
CO-Pd [111] linear	2050-2080	[57]

Figure 4-5 shows the IR spectra of uncatalyzed CZO and Pd/CZO samples during CO adsorption at 22°C. Spectra of the adsorbed species are the difference between the absorbance of the CO saturated sample and the clean sample background. As spectra for all samples were collected during flowing CO, gas phase CO appears as two similar bands starting at 2050 cm^{-1} through 2200 cm^{-1} with high frequency and low amplitude. The peaks for CO adsorbed on Pd linear and bridge sites from 1800-2000 cm^{-1} are shown for just the fresh and redox aged with 700°C/2h air treatment samples. The similarly sized CO-Pd linear adsorption IR peak at 2050-2080 cm^{-1} for these two samples suggests a comparable number of these sites, but the CO-Pd bridge sites appear more abundant for the fresh sample likely due to higher Pd dispersion results from Table 4-1. CO adsorption onto Pd is not observed for the Pd/CZO redox aged or Pd/CZO redox aged with 550°C/2h air treatment samples through two hours, which aligns with the undetectable chemisorption results from Table 4-1 for these samples, and provides evidence for coverage of Pd by SMSI with CeO_2 due to exposure to a high temperature reducing environment, in agreement with Badri *et al*. [30], since ZrO_2 is not reducible under these conditions.

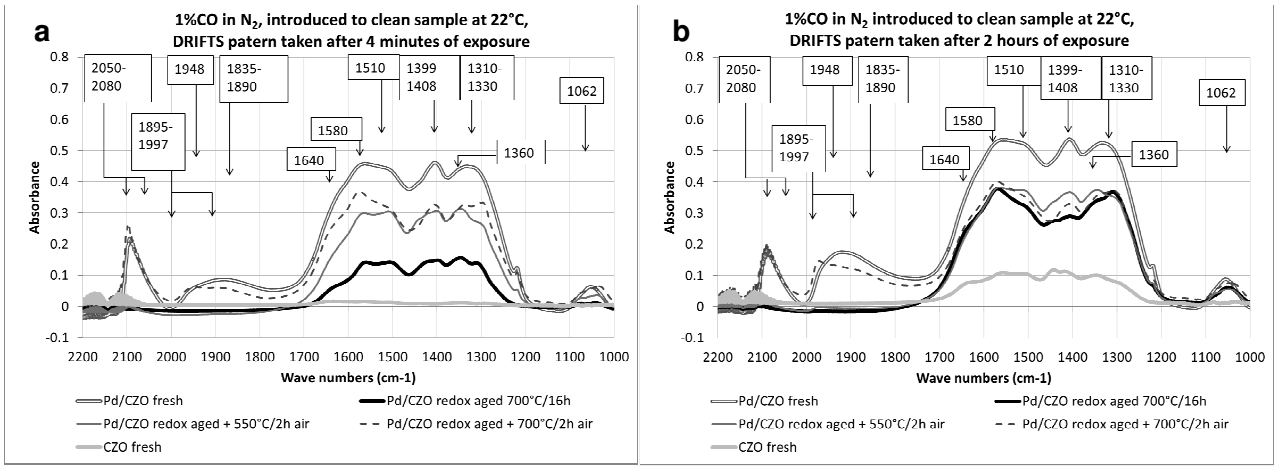

Figure 4-5: IR spectra during CO exposure to clean samples at 22°C. Plots: a) after 4 minutes, b) after 2 hours

The growth rate of carbonates and formates from 1000-1700 cm^{-1} in Figure 4-5 showed the following trend: fresh Pd/CZO > Pd/CZO redox aged with 700°C/2h air > Pd/CZO redox aged with 550°C/2h air > Pd/CZO redox aged >> CZO. This large difference between uncatalyzed CZO and the Pd/CZO samples implies that Pd enhances the formation of carbonates and formates at the Pd-CZO interface sites. For the Pd samples, the growth rate appears to be directly related to Pd dispersion results in Table 4-1. The difference in growth rate provides supporting evidence for the H_2 chemisorption results reported in Table 4-1.

4.3.7 Catalytic Activity

CO_2 production can be measured directly by the mass spectrometer in units of partial pressure (i.e, torr) and can be combined with the other measured gas species to determine the total pressure and thus enable a relative concentration calculation for each gas species. Micromoles of CO_2 per gram of catalyst can be calculated for the OSC experiment using equation 2 below where the average CO_2 20 seconds before and after the CO pulse is used as the background:

$$\text{OSC } CO_2 \text{ [µmoles/g]} = \frac{(\text{current } CO_2\ [\%] - \text{background } CO_2\ [\%]) * (\text{CO pulse length [m]}) * (\text{gas flow rate [L/m]})}{(22.414\ \text{L/mole}) * (\text{mass [g]})} \qquad \text{Equation 2}$$

Conversion of CO to CO_2 during the WGS experiment can be calculated using equation 3 below where the average CO_2 at room temperature is used as a background:

$$\text{WGS conversion of CO to } CO_2\ [\%] = \frac{100 * (\text{current } CO_2 - \text{background } CO_2)}{(\text{CO at room temperature})} \qquad \text{Equation 3}$$

The generation of CO_2 over the Pd/CZO samples at 300°C is shown in Figure 4-6 for the OSC test and in Figure 4-7 for the WGS test. In each case the lean-only aging environment was the least deteriorated. The rich-only aging environment was the harshest environment after 20 minutes, but after 2 hours the redox environment was the worst. The 550°C/2h lean treatment showed a modest improvement for the rich-only and redox aged samples, but the 700°C/2h lean treatment achieved restoration up to the lean-only aged sample. The OSC test of the most active catalysts at 350°C and 400°C showed complete consumption of CO so that the CO_2 conversion results were limited relative to the poorer catalysts. In all cases, the poorest performing catalysts were also the ones that had below 4% Pd dispersion measured by H_2 chemisorption as shown in Table 4-1.

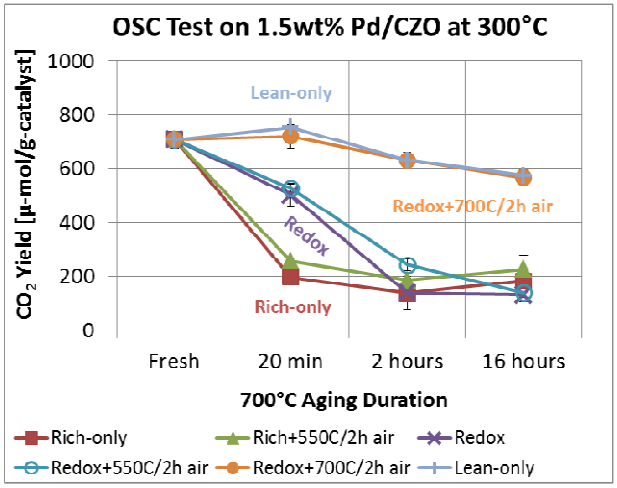

Figure 4-6: OSC test on Pd/CZO samples CO_2 yield as a function of age

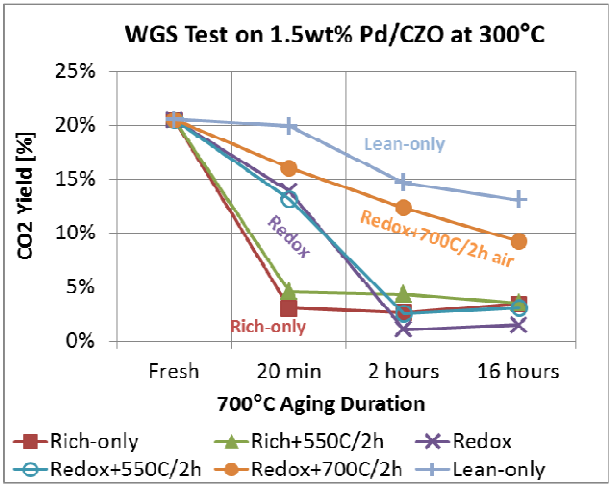

Figure 4-7: WGS test on Pd/CZO samples CO_2 yield as a function of age

4.3.8 PdO Formation Observed by HTXRD

PdO formation observed in air by XRD measurement of Pd [111] peak disappearance required samples that had well-defined Pd [111] peaks as shown in Figure 4-2. This study therefore excluded the 20 minute aged samples and the lean-only aged samples at all durations. In addition, we sought to avoid confounding of the Pd oxidation rate by SMSI effects such as partial encapsulation or decoration of Pd with Ce^{+3}. Therefore the 2h and 16h redox aged plus 700°C/2h lean treated samples were selected. The difference in bulk Pd size between these samples as shown in Table 4-2 was assumed significant enough to provide discrimination of PdO reoxidation rates.

Long sampling times were required for acceptable signal to noise diffraction patterns due to the large width of the beam (~ 1 mm) and the limited positional resolution of the detector (0.3 mm), causing relatively low instrumental resolution (~0.36°) compared to conventional focusing diffractometers. Figure 4-8 shows the results of scans acquired at various durations to observe the Pd[111] peak from the Pd/CZO redox aged sample. The signal to noise ratio is defined as the signal average divided by the standard deviation of the background, and a value of at least 5 is considered sufficient for distinguishing features from the background. The Pd[111] peak was well resolved apart from the background and not affected by the CZO support peaks as shown in Figures 4-2 and 4-8. Scans were spaced at 0.015°2θ intervals, providing 64 data points across each 1°2θ interval. The signal value was the average peak height at 38.8-39.8°2θ minus the average height of the background at 37-38°2θ and 41-42°2θ. The initial signal to noise ratio for the data in Figure 4-8 was 6 for the four minute scan, while it was 4 for the two minute scan. Therefore the four minute scan was considered an effective balance between fast data acquisition and low noise.

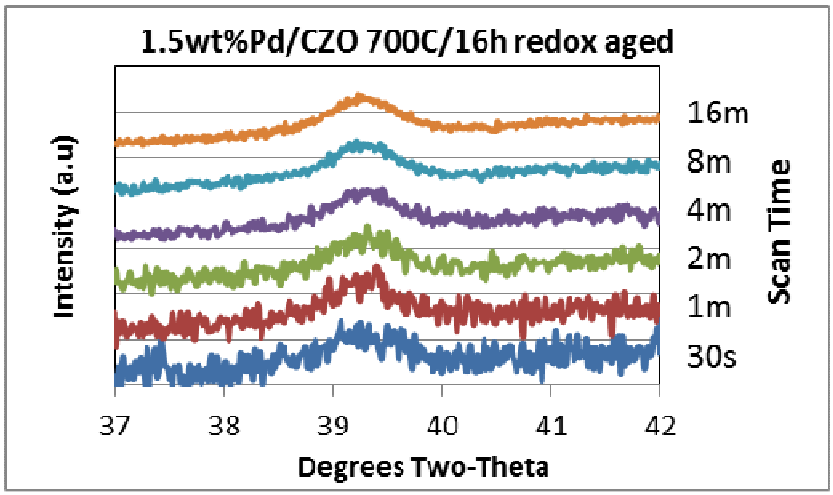

Figure 4-8: HTXRD data acquisition scans with Pd[111] on CZO

The long measurement times needed to monitor the Pd particle growth limited the accessible temperature range of the measurement. At sufficiently high temperatures, the growth of Pd particles becomes too fast for the HTXRD measurement acquisition time needed and an alternative method is needed to estimate the growth rate. To enable this approach, an accurate model of the time dependence of the growth is needed. The calculations used for the PdO phase fraction appearance during the HTXRD experiment are based on the Avrami-Erofe'ev model equation for the kinetics of phase transformations [60, 61]. The linearized Avrami-Erofe'ev model equation relates the growth of an emerging phase fraction α at time t, rate constant k, and growth exponent n as shown by equation 4 below.

$$\alpha = 1 - \exp(-kt)^n \qquad \text{Equation 4}$$

By plotting the phase fraction against time on a log-log scaling, k and n can be easily extracted assuming a linearized version as shown by equation 5 below.

$$\ln(\ln[1/(1-\alpha)]) = n * \ln(k) + n * \ln(t) \qquad \text{Equation 5}$$

The values of k were then plotted against inverse absolute temperature to determine the Arrhenius relationship and extract the activation energy E_a and frequency constant A by fitting the rate constants at the temperatures of each measurement by equation 6 below:

$$k = A * \exp(-E_a/RT) \qquad \text{Equation 6}$$

An XRD pattern with the initially reduced Pd[111] peak at a low temperature of interest was acquired under nitrogen and the area under the peak was integrated for the 100% Pd baseline at time zero (t_0). Once complete, air was introduced and acquisition began immediately of XRD patterns for the measurement of the Pd [111] peak at each time interval (t). At each scan time interval (t), Pd[111](t) was equal to the peak intensity integrated from 38.8-39.8°2θ minus the background intensity integrated from 37-38°2θ and 41-42°2θ. The PdO fraction at time *t* was determined by equation 7 below:

$$PdO(t) = 1 - (Pd[111](t) / Pd[111](t_0)) \qquad \text{Equation 7}$$

The PdO formation rate increased as a function of time and temperature as shown in Figure 4-9, plots a and b. The measured data was fit using the linearized Avrami model, yielding similar slopes with discrete intercepts at each measured temperature. Table 4-5 lists the average growth constant, n, and oxidation rate, k, determined from the fits in Figure 4-9 of the slope and intercept, respectively. The average value of the growth parameter n was 0.36 across the measured temperature range, corresponding to a $t^{0.36}$ relationship in the Avrami model, is similar to the $t^{1/3}$ growth relationship with fine Pd powder oxidation as studied by Matsui *et al*. [62].

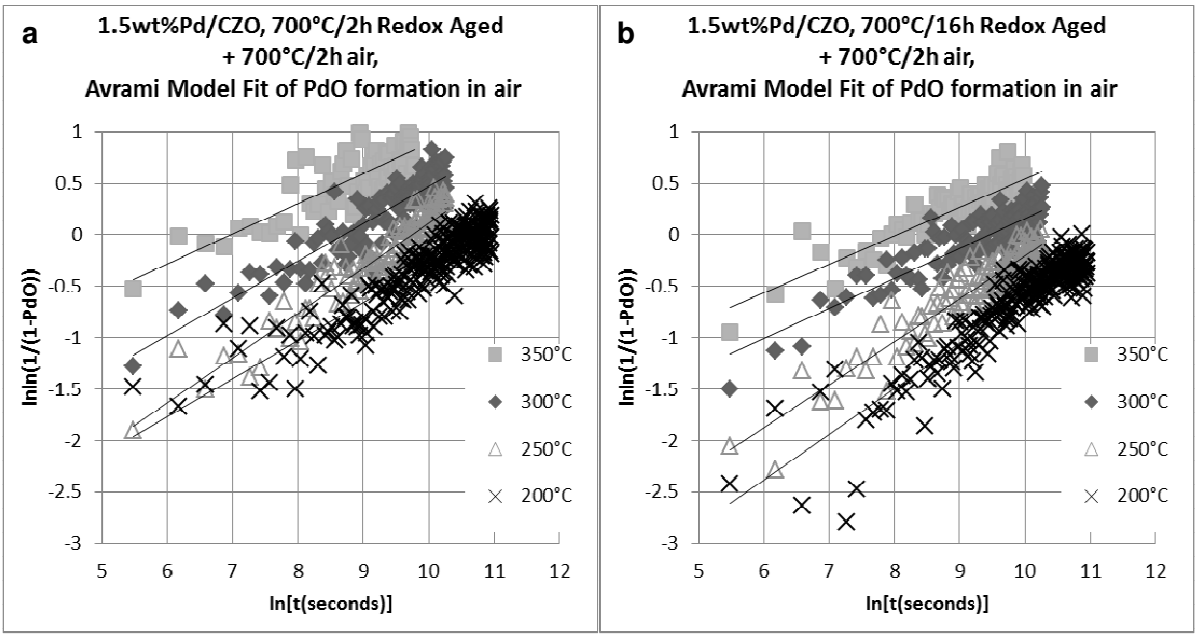

Figure 4-9: Measured and fit PdO formation rates in air at low temperature. Plots of redox aged-regenerated samples: a) 2h fit data, b) 16h fit data

Table 4-5: Avrami model rate constant and exponent for measured PdO formation				
Temperature	**Redox aged 700°C/2h + 700°C/2h air**		**Redox aged 700°C/16h + 700°C/2h air**	
T (°C)	***k (1/s)***	***n***	***k (1/s)***	***n***
200	2.06×10^{-5}	0.37	1.14×10^{-5}	0.44
250	5.75×10^{-5}	0.43	2.79×10^{-5}	0.42
300	1.64×10^{-4}	0.36	7.72×10^{-5}	0.29
350	9.45×10^{-4}	0.29	3.24×10^{-4}	0.28

Figure 4-10 shows a linear trend of the reaction rates plotted as an Arrhenius relationship with each measured temperature. Figure 4-10 lists the linear data fit equation, and activation energy, E_a, and constant, A, determined from the slope and intercept of the data fits. The rate parameter, k, for the 2h redox aged/regenerated sample was about twice that of the 16h redox aged/regenerated sample for each temperature. From Table 4-2, the Pd particle size of the 2 hours aged/regenerated sample was 8.8 nm by chemisorption or 11 nm by XRD while the 16 hour aged/regenerated sample was 13 nm by chemisorption or 18 nm by XRD. Therefore

the smaller Pd size (and higher Pd dispersion as per equation 1) led to faster oxidation. It is therefore important to keep Pd smaller than 8.8 nm to achieve rapid oxidation for possible redispersion during a brief vehicle fuel cut.

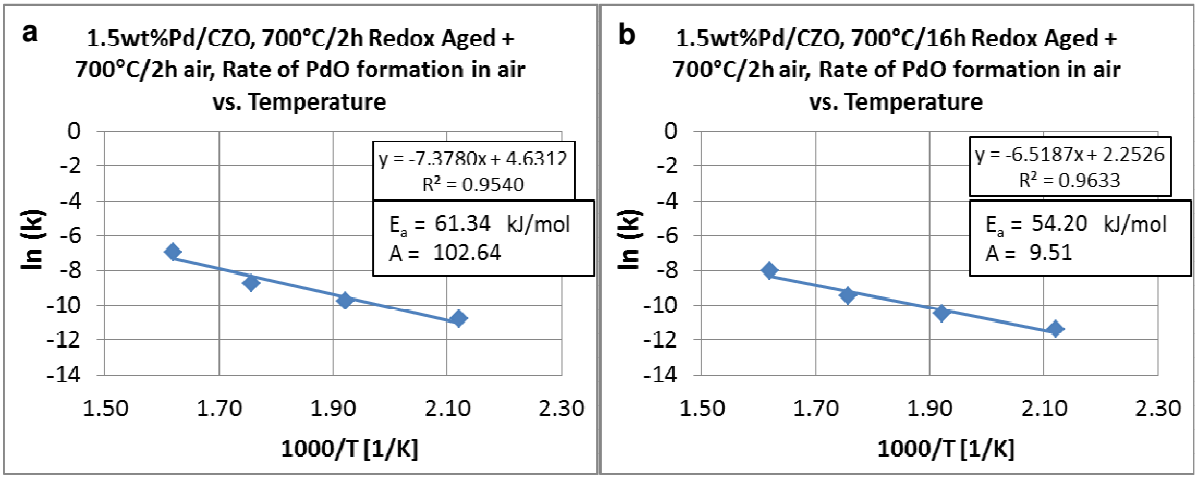

Figure 4-10: Arrhenius model fit of PdO formation rates in air at low temperature. Plots of redox aged-regenerated samples: a) 2h fit data, b) 16h fit data.

The above point can be further emphasized through a simplified extrapolation of the PdO formation rate at 700°C by working the above process in reverse. An extrapolated rate k at 700°C may be determined with equation 6, since E_a and A are known, then the PdO formation with time at 700°C may be determined with equation 4 with the average n value of 0.36 and the extrapolated rate k. Given a 10 second fuel cut at 700°C, such an extrapolation for each Pd/CZO sample would yield as follows: the 2 hour aged/regenerated sample would have 55% PdO while the 16 hour aged/regenerated sample would have 37% PdO, assuming no initial PdO, uncovered Pd surfaces and a dry air environment. So it is important to maintain Pd particles smaller than 8.8 nm as neither sample was predicted to be completely oxidized within 10 seconds. However, any high temperature extrapolation may not hold up to scrutiny given expected Pd sintering at 700°C (demonstrated by our aging results) or support coverage of Pd by SMSI in redox conditions in as little as 20 minutes. Sintering rates and SMSI of Pd are negligible under the measurement conditions at 350°C in nitrogen, or during the air pulse, and are not reflected in the measured parameters.

4.3.9 PdO Formation Observed by TGA

Figure 4-11 shows the result of TGA measurements for PdO decomposition in N_2, and confirmation of the HTXRD measurements of PdO formation rate at 350°C and the simplified extrapolation of the PdO formation rate at 700°C. The sample used for TGA analysis was the same 16h redox aged/regenerated sample from the HTXRD measurements. However, the initial condition of the sample had to be different for the two techniques. The TGA sample was oxidized to limit confounding weight gain by CZO oxygen uptake, while the HTXRD sample was reduced in order to view the Pd [111] peak. Figure 4-11a shows the PdO decomposition plot in N_2 to 700°C used to prepare the Pd metal for oxygen uptake. The derivative weight shows peak oxygen release near 600°C. The maximum theoretical weight gain for the complete Pd oxidation of 77 mg of 1.5wt% Pd/CZO sample was determined to be 0.174 mg. The actual weight loss of 0.146 mg reveals a reduction of 84% compared to the theoretical value, so the weight loss could be from just the PdO and not the CeO_2 in the support. The sample oven temperature was then adjusted to either 350°C or 700°C. In both Figure 4-11b and 11c, 10% O_2 was fed to the sample and a weight gain was observed. The calculated theoretical maximum weight gain of 0.174 mg was multiplied by the PdO formation fraction measured by HTXRD or extrapolated as a function of time by equation 4 above to obtain the weight gain by HTXRD in air. Weight gained was divided by the calculated theoretical maximum to obtain a fraction of PdO formation by TGA in 10% O_2. For Figure 4-11b and 11c, the results with TGA in 10% O_2 was similar in trend, yet just below that observed with HTXRD in air. The difference in Pd oxidation for the two techniques may be due to the higher amount of oxygen in the HTXRD feed stream or the lower extent of Pd reduction prior to the oxidation pulse with the TGA sample. The good consistency of the TGA and HTXRD measurements allows for estimation of the oxidation rates to temperatures beyond the range accessible by the HTXRD method. From the extrapolation, we are able to further estimate the effectiveness of the lean treatments to achieve redispersion and infer a recommendation for a practical engine control strategy.

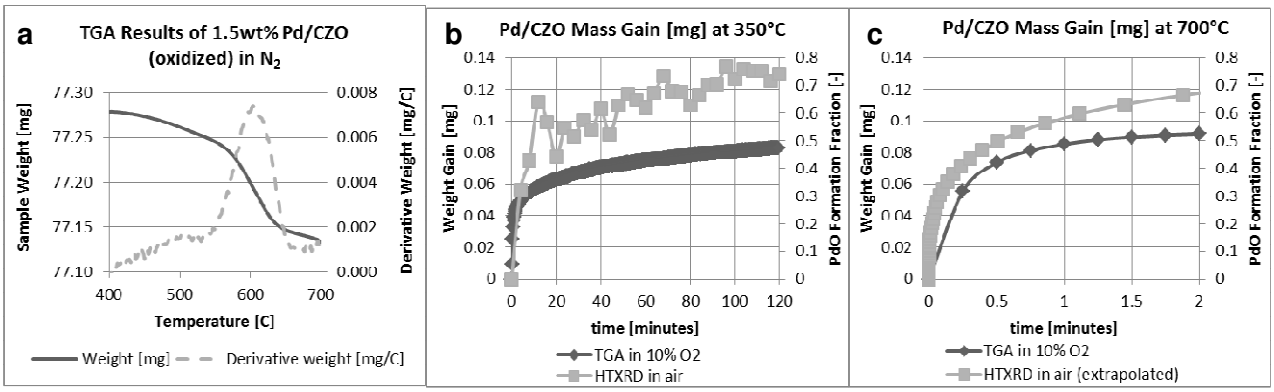

Figure 4-11: TGA results on Pd/CZO redox aged 700°C/16h + 700°C/2h air. Plots: a) PdO decomposition in N_2, b) comparison to HTXRD results at 350°C, c) comparison to HTXRD results extrapolated to 700°C.

4.3.10 Effect of Additional Brief Lean Treatments

Figure 4-12 shows the result of additional dry lean treatments on the Pd dispersion for the redox aged samples. With one 2 hour lean treatment, these redox aged-regenerated samples showed lower dispersion than the equivalent duration lean-only aged samples, except for the 20 minute redox aged-regenerated sample, which was just above the level of the lean-only 20 minute aged sample. The 20 minute redox aged sample may not have had the Pd covered by CZO after redox aging, but no confirmation of Pd redispersion by XRD was possible to confirm the improvement shown by H_2 chemisorption in Table 4-1. Additional 30 minute pulses of dry air at 700°C were applied to achieve essentially complete oxidation of Pd on both samples with each pulse. The 20 minute redox aged-regenerated sample showed slight increases in Pd dispersion with each 30 minute dry air pulse up to the fresh level. The 2 hour redox aged-regenerated sample showed a substantial increase in Pd dispersion with the first 30 minute dry air pulse to just above the level of the lean-only 2 hours aged sample, but the second 30 minute dry air pulse showed no further improvement. The 16 hour redox aged-regenerated sample also showed a substantial increase in Pd dispersion with the first 30 minute dry air pulse, but the result was just below the level of the lean-only 16 hours aged sample. A second 30 minute dry air pulse showed further improvement to above the level of the lean-only 16 hours aged sample, but the next two pulses did not bring further improvement. Multiple lean treatments were likely needed

due to the CZO support covering the Pd surface after redox aging, where the first pulse decomposed the CZO that prevented some PdO wetting and spreading. It appears that the lean treatment has limitations with improving Pd dispersion to the equivalent duration lean-only aged sample and this upper limit may be linked to residual catalyst surface area.

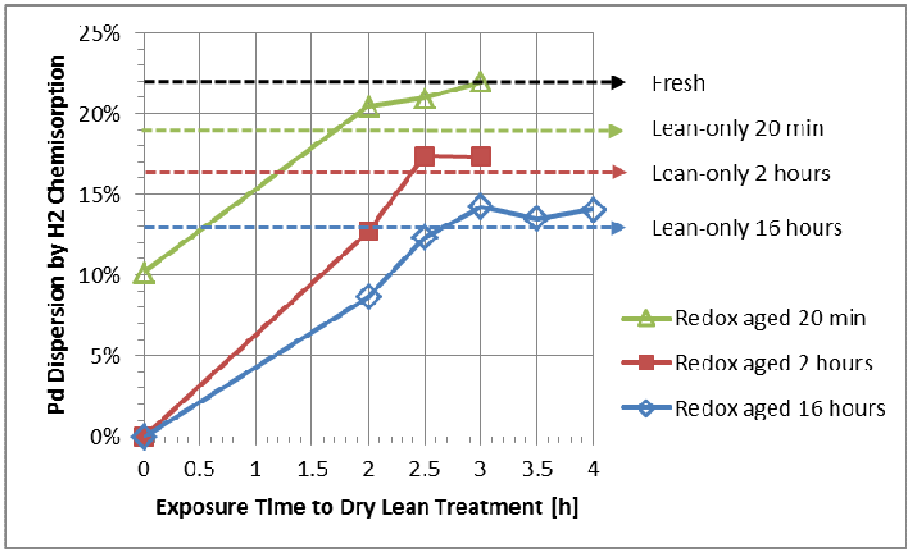

Figure 4-12: Effect of additional dry lean treatments

4.4 Discussion

4.4.1 Aging environment

Model powder catalysts showed dynamic changes to Pd dispersion depending on oxygen concentration in the 700°C aging environment. For the Pd/CZO samples, the rich-only and redox environments caused much more severe loss of Pd dispersion than the fixed lean-only exhaust gas compositions, producing samples with the lowest activity for the WGS and OSC tests. Exposure to dry air at 700°C caused the Pd dispersion to increase as measured by both H_2 chemisorption and XRD techniques. Based on these observations, one approach to maintain Pd dispersion on a catalytic converter is to manage engine operation so that the exhaust gas composition falls along a trajectory that avoids the fuel-rich environment or includes periodic fuel shut-off events during high speed driving conditions to reoxidize Pd into PdO to redisperse the Pd.

4.4.2 Aging duration

Studies on Pd sintering have shown the rapid particle agglomeration and loss of Pd dispersion as a function of aging duration [3, 8]. Recent studies of atomically dispersed Pd noted that subnanometer agglomerates of Pd atoms were easy to redisperse through a 700°C calcination, while larger PdO particles were found to be very stable in air and did not sinter up to 800°C [24, 63]. Peterson *et al.* speculated that the stability of bulk PdO may not allow it to be so easily redispersed as smaller Pd particles [63]. This agrees with earlier observations linking Pd particle size to the onset of PdO formation, wetting, spreading and rupture [20, 23]. Our focus here was to determine for how long operation at highway driving exhaust temperatures could be maintained while still allowing for effective regeneration of the activity lost due to Pd agglomeration. As the Pd/CZO catalyst is aged longer, the lean treatment becomes less effective and appeared to become limited to the dispersion achieved after lean-only aging as shown in Figure 4-12. Still, the 2 hour redox aged sample was able to achieve significant Pd redispersion comparable to that produced in the lean-only aged sample (13% vs. 16%). However, there is another important factor to consider: Pd redispersion first requires PdO formation and only Pd particles of a size just a few nanometers in diameter could achieve reoxidation and redisperse during the mere seconds of air that would be supplied by a typical fuel cut. Based on the measured Pd oxidation rate and the measurements of Pd size by chemisorption, the 8.8 nm Pd particles had twice the oxidation rate of the 13 nm Pd particles. In addition, the simplified extrapolation of PdO formation on the 8.8 nm Pd particles at 700°C suggests that even 10 seconds in air is not enough to achieve over 60% oxidation of Pd. Therefore a fuel cut should be performed before the Pd particles reach 8.8 nm in diameter to enable the lean treatment to be more efficient, which suggests a fuel cut just after 20 minutes of 700°C stoichiometric (i.e., redox) operation. Depending on the aging history of the catalyst, this fuel cut frequency can be adapted to continuously maintain proper catalyst performance through lean Pd redispersion.

Due to the limitations of XRD for discerning finely dispersed Pd particles apart from the background pattern, we were not able to measure the PdO formation rate on

the 20 minute redox aged-regenerated sample. Newton et al. acquired Pd oxidation data taken at the European Synchrotron Radiation Facility (ESRF) on Pd nanoparticles of 3 nm in diameter [28]. Further synchrotron work could be done to study Pd particles below an 8.8 nm diameter.

4.4.3 Support effects

The benefits of lean treatments on Pd were slightly confounded by the SMSI effect between Pd and CeO_2. In an electron microscopy study, Chen and Ruckenstein observed Pd on an alumina film with microscopy in a pure oxygen environment and observed that the smallest PdO crystallites (< 15 nm) wet and spread over the surface at 350°C while the larger PdO crystallites did not [20]. Then at 500°C, all PdO crystallites eventually moved about the surface, rupturing and fracturing of the spreading Pd crystallites was observed as a mechanism to form smaller particles. In our work, the 550°C regeneration on 16-20 nm Pd particles should have had an effect similar to that observed by Chen and Ruckenstein, but XRD did not confirm any significant bulk Pd crystal size decrease. Our XPS and DRIFTS results showed substantial coverage of the Pd by the CZO support that likely limited the mobility of Pd wetting and spreading over CZO. Other work has shown that ceria covering a Pd surface can be removed from just the Pd [111] surface when heated in air at 500°C [30], and completely decomposed when heated in air at 700°C [53]. These observations may explain the difference in Pd size reduction accomplished on the redox and rich-only aged Pd/CZO samples with the lean treatments at 550°C versus 700°C.

Pd was able to redisperse on the CZO support material as evidenced by the catalyst activity improvement and measured Pd size reduction of the 700°C lean treated redox aged samples versus the as-is redox aged samples. These results are consistent with Hickey *et al*. using Pd supported on $Ce_{0.68}Zr_{0.32}O_2$ and aged on a redox cycle, showing a lower temperature for conversion of CO after a high temperature lean treatment although no chemisorption results were reported to demonstrate a lower Pd size [18]. Peterson et al. showed supported Pd clusters treated in air at 700°C or with 1% O_2 achieved atomically dispersed Pd^{+2} species that were more stable on La_2O_3-

Al_2O_3 than on undoped alumina [63]. The observations of Peterson *et al*. also are consistent with our XPS results where Pd^{+2} was observed on the lean treated redox Pd/CZO samples, even though it was reduced prior to analysis. The ability of Pd to form stable Pd^{+2} on the support surface oxide may be vital to achieving significant Pd size reduction when inside the conditions of the Pd redispersion zone.

4.5 Conclusions

The trends in the aging severity at 700°C for different Pd/CZO sample aging methods for 2 hours and 16 hours were as follows: redox > rich-only >> lean-only. Reducing conditions produced a loss in exposed Pd surface area that was consistent with SMSI effects with support CeO_2. After each aging interval, the 700°C/2h lean treatment applied after redox aging always increased the Pd dispersion towards the level of the lean-only aged sample, but the magnitude of Pd dispersion recovery diminished with aging duration. These results show how quickly reducing conditions (i.e., engine fuel enrichment) and highway driving catalyst temperatures can deactivate Pd/CZO, and how frequent engine fuel-cut events must be delivered. We have shown the importance of maintaining Pd below 8.8 nm for efficient and rapid redispersion, and based on the increasing difficulty of achieving the same result for longer aging times, it is recommended that a fuel cut be performed just after 20 minutes of 700°C stoichiometric (redox) operation as a practical method to maintain activity.

The approach presented here combines several methods to elucidate the Pd particle size and dispersion at different temperatures, the fraction of reducible Pd, the coverage of particles by the CZO support and the effects of various aging treatments on the effectiveness of a lean redispersion method. The good consistency of the measurements with established models for particle growth kinetics allows for estimation of the growth rates to temperatures beyond the range accessible by these methods. From these extrapolations, we are able to further estimate the effectiveness of the lean treatments to achieve redispersion and infer a recommendation for a practical engine control strategy. This approach fills a critical gap in catalyst aging measurements and

allows for more confidence in applying engine control methods to preserve catalyst performance over the life of the vehicle.

4.6 Acknowledgements

The authors gratefully acknowledge the following sources of funding for this study: Ford University Research Program (URP), NSF GOALI grant # CBET-1159279 and NSF grant # DMR-9871177.

4.7 References

[1] J. Kašpar, P. Fornasiero, N. Hickey, "Automotive catalytic converters: current status and some perspectives", *Catal. Today* 77 (2003) 419–449
[2] M. Shelef, R. McCabe, "Twenty-five years after introduction of automotive catalysts: what next?", *Catal. Today* 62 (2000) 35–50
[3] A. Datye, Q. Xu, K. Kharas, J. McCarty, "Particle size distributions in heterogeneous catalysts: What do they tell us about the sintering mechanism?", *Catal. Today* 111 (2006) 59–67
[4] R. Goeke and A. Datye, "Model oxide supports for studies of catalyst sintering at elevated temperatures", *Top. Catal.* 46 (2007) 3-9
[5] L. Martín, J. Arranz, O. Prieto, R. Trujillano, M. Holgado, M. Galán, V. Rives, "Simulation three-way catalyst ageing Analysis of two conventional catalyst", *Appl. Catal. B: Environ.* 44 (2003) 41–52
[6] C. Bartholomew, "Mechanisms of catalyst deactivation", *Appl. Catal. A: Gen.* 212 (2001) 17–60
[7] R. McCabe, R. Useman, “Characterization of Pd-based Automotive Catalysts”, *Stud. Surf. Sci. Catal.* 101 (1996) 355–368
[8] Q. Xu, K.C. Kharas, B.J. Croley, A.K. Datye, “The Sintering of Supported Pd Automotive Catalysts”, *ChemCatChem* 3 (2011) 1004–1014
[9] Z. Han, J. Wang, H. Yan, J. Fan, "Performance of dynamic oxygen storage capacity, water–gas shift and steam reforming reactions over Pd-only three-way catalysts", *Catal. Today* 158 (2010) 481–489
[10] H. Vidal, J. Kašpar, M. Pijolat, G. Colon, S. Bernal, A. Cordón, V. Perrichon, F. Fally, "Redox behavior of CeO_2–ZrO_2 mixed oxides II. Influence of redox treatments on low surface area catalysts", *Appl. Catal. B: Environ.* 30 (2001) 75–85
[11] E. Mamontov, T. Egami, R. Brezny, M. Koranne, S. Tyagi, "Lattice Defects and Oxygen Storage Capacity of Nanocrystalline Ceria and Ceria-Zirconia", *J. Phys. Chem. B*, 104 (2000) 11110-11116
[12] T. Bunluesin, R. Gorte, G. Graham, "Studies of the water-gas-shift reaction on ceria-supported Pt, Pd, and Rh: implications for oxygen-storage properties", *Appl. Catal. B: Environ.* 15 (1998) 107-114
[13] R. J. Gorte, "Ceria in catalysis: from automotive applications to the water–gas shift reaction", *AIChE J.,* 56(5) (2010) 1126-1135
[14] M. Zhao, M. Shen, J. Wang, W. Wang, "Influence of Pd Morphology and Support Surface Area on Redox Ability of $Pd/Ce_{0.67}Zr_{0.33}O_2$ under CO-He Pulse and Transient CO-O_2 Measurements", *Ind. Eng. Chem. Res.* 46 (2007) 7883-7890
[15] L. Kępiński, M. Wolcyrz, J. Okal, “Effect of Chlorine on Microstructure and Activity of Pd/CeO_2 Catalysts”, *J. Chem. Soc. Farad. Trans.* 91 (1995) 507-515

[16] G. Graham, A. Shigapov, "Revised Model of Strain in Ceria-Zirconia Encapsulated Precious-Metal Particles", *Catal. Lett.*, 81 (2002) 253-258
[17] G. Graham, A. O'Neill, A. Chen, "Pd encapsulation in automotive exhaust-gas catalysts", *Appl. Catal. A: Gen.* 252 (2003) 437–445
[18] N. Hickey, P. Fornasiero, R. Di Monte, J. Kašpar, J. R. González-Velasco, M. A. Gutiérrez-Ortiz, M. P. González-Marcos, J. M. Gatica, S. Bernal, "Reactivation of aged model $Pd/Ce_{0.68}Zr_{0.32}O_2$ three-way catalyst by high temperature oxidising treatment", *Chem. Commun.* 1 (2004) 196-197
[19] X. Chen, Y. Cheng, C.Y. Seo, J.W. Schwank, R.W. McCabe, "Aging, re-dispersion, and catalytic oxidation characteristics of model Pd/Al_2O_3 automotive three-way catalysts", *Appl. Catal. B: Environ.* 163 (2015) 499–509
[20] J.J. Chen, E. Ruckenstein, "Role of Interfacial Phenomena in the Behavior of Alumina-Supported Palladium Crystallites in Oxygen", *J. Phys. Chem.* 85 (1981) 1606-1612
[21] N.M. Rodriguez, S.G. Oh, R.A. Dalla-Betta, R.T.K. Baker, "In-situ Electron Microscopy Studies of Palladium Supported on Al_2O_3, SiO_2, and ZrO_2 in Oxygen", *J. Catal.*, 157 (1995) 676-686
[22] E. Ruckenstein, J. J. Chen, "Wetting Phenomena during Alternating Heating in O_2 and H_2 of Supported Metal Crystallites", *J. Coll. Interf. Sci.* 86 (1982) 1-11
[23] H. Lieske, J. Völter, "Pd Redispersion by Spreading of PdO in O_2 Treated Pd/Al_2O_3", *J. Phys. Chem.* 89 (1985) 1841-1842
[24] T.R. Johns, R.S. Goeke, V. Ashbacher, P.C. Thüne, J.W. Niemantsverdriet, B. Kiefer, C.H. Kim, M.P. Balogh, A.K. Datye, "Relating adatom emission to improved durability of Pt–Pd diesel oxidation catalysts", *J. Catal.* 328 (2015) 151-164
[25] R. J. Farrauto, J. K. Lampert, M. C. Hobson, E. M. Waterman, "Thermal decomposition and reformation of PdO catalysts; support effects" *Appl. Catal. B: Environ.* 6 (1995) 263-270
[26] M. Peuckert, "XPS Study on Surface and Bulk Palladium Oxide, Its Thermal Stability, and a Comparison with Other Noble Metal Oxides", *J. Phys. Chem.* 89 (1985) 2481-2486
[27] J. Nunan, J. Lupescu, G. Denison, D. Ball, D. Moser. "HC Traps for Gasoline and Ethanol Applications", *SAE Int. J. Fuels and Lubrs.* 6(2) (2013) 430-449
[28] M.A. Newton, C. Belver-Coldeira, A. Martínez-Arias, M. Fernández-García, ""Oxidationless" Promotion of Rapid Palladium Redispersion by Oxygen during Redox $CO/(NO+O_2)$ Cycling", *Angew. Chem. Int. Ed.* 46 (2007) 8629-8631
[29] J.A. Lupescu, J.W. Schwank, K.A. Dahlberg, C.Y. Seo, G.B. Fisher, S.L. Peczonczyk, K. Rhodes, M.J. Jagner, L.P. Haack, "Pd Model Catalysts: Effect of Aging Environment and Lean Redispersion", *Appl. Catal. B: Environ. in press* (2015)
[30] A. Badri, C. Binet, J.-C. Lavalley, "Metal-support interaction in Pd/CeO2 catalysis Part 2. – Ceria textural effects", *J. Chem. Soc. Farad. Trans*. 92(9) (1996) 1603-1608
[31] H.P. Sun, X.P. Pan, G.W. Graham, H.-W. Jen, R.W. McCabe, S. Thevuthasan, C.H.F. Peden, "Partial encapsulation of Pd particles by reduced ceria-zirconia", *Appl. Phys. Lett.* 87 (2005) 201915
[32] L. Kępiński, M. Wolcyrz, "Microstructure of Pd/CeO_2 catalyst: Effect of high temperature reduction in hydrogen", *Appl. Catal. A: Gen.* 150 (1997) 197-220
[33] T.P. Bebee, J.T. Yeates, ""Spectroscopic Detection of (111) Facets on Supported Pd Crystallites: Site Blocking by Ethyldyne on Pd/Al_2O_3", *Surf. Sci. Lett.* 173 (1986) L606-L612
[34] R.F. Hicks, A.T. Bell, "Effects of Metal-Support Interactions on the Hydrogenation of CO over Pd/SiO_2 and Pd/La_2O_3", *J. Catal.* 90 (1984) 205-220
[35] D. Briggs, M.P. Seah, Practical Surface Sci. Analysis by Auger and X-ray Photoelectron Spectroscopy, John Wiley & Sons, New York, 1984
[36] J. E. Benson, H. S. Hwang, M. Boudart, "Hydrogen-Oxygen Titration Method for the Measurement of Supported Palladium Surface Areas", *J. Catal* 30 (1973) 146-153
[37] V. Ragaini, R. Giannantonio, P. Magni, L. Lucarelli, G. Leofanti, "Dispersion Measurement by the Single Introduction Method Coupled with the Back-Sorption Procedure: A Chemisorption and TPD Study of the Different Chemisorbed Hydrogen Species II. Pd on Alumina", *J. Catal.* 146 (1994) 116-125
[38] T. Takeguchi, S. Manabe, R. Kikuchi, K. Eguchi, T. Kanazawa, S. Matsumoto, W. Ueda, "Determination of dispersion of precious metals on CeO_2-containing supports", *Appl. Catal. A: Gen.* 293 (2005) 91–96
[39] A.L. Patterson, "The Scherrer Formula for X-Ray Particle Size Determination", *Phys. Rev.* 56 (1939) 978-982

[40] S. Colussi, A. Trovarelli, E. Vesselli, A. Baraldi, G. Comelli, G. Groppi, J. Llorca, “Structure and morphology of Pd/Al_2O_3 and $Pd/CeO_2/Al_2O_3$ combustion catalysts in Pd–PdO transformation hysteresis”, *Appl. Catal. A: Gen.* 390 (2010) 1–10
[41] A. Baylet, S. Royer, P. Marécot, J. Tatibouët, D. Duprez,” Effect of Pd precursor salt on the activity and stability of Pd-doped hexaaluminate catalysts for the CH_4 catalytic combustion”, *Appl. Catal. B: Environ.* 81 (2008) 88–96
[42] R.F. Hicks, Q.-J. Yen, A.T. Bell, “Effects of Metal-Support Interactions on the Chemisorption of H_2 and CO on Pd/SiO_2 and Pd/La_2O_3”, *J. Catal.* 89 (1984) 498-510
[43] J.S. Rieck, A.T. Bell, “Studies of the Interactions of H_2 and CO with Pd/SiO_2 Promoted with La_2O_3, CeO_2, Pr_6O_{11}, Nd_2O_3, and Sm_2O_3”, *J. Catal.* 99 (1986) 278-292
[44] C.R. Adams, H.A. Benesi, R. M. Curtis, R. G. Meisenheimer, “Particle Size Determination of Supported Catalytic Metals: Platinum on Silica Gel”, *J. Catal.* 1, (1962) 336-344
[45] J.K. Plischke, M.A. Vannice, “Effect of Pretreatment on the Adsorption Properties of Silver Crystallites”, *Appl. Catal*. 42 (1988) 255-283
[46] R.T.K Baker, E.B. Prestridge, G.B. McVicker, “The Interaction of Palladium with Alumina and Titanium Oxide Supports” *J. Catal*. 89 (1984) 422-432
[47] F.M. Dautzenberg, H.B.M. Wolters, “State of Dispersion of Platinum in Alumina-Supported Catalysts” *J. Catal.* 51 (1978) 26-39
[48] L. Yang, X. Yang, S. Lin, R. Zhou, “Insights into the role of a structural promoter (Ba) in three-way catalyst Pd/CeO2–ZrO2 using in situ DRIFTS”, *Catal. Sci. Technol.,* 5 (2015) 2688-2695
[49] K. Tanikawa, C. Egawa, “Effect of barium addition on CO oxidation activity of palladium catalysts”, *Appl. Catal. A: Gen.* 403 (2011) 12–17
[50] M. Zhao, X. Li, L. Zhang, C. Zhang, M. Gong, Y. Chen, “Catalytic decomposition of methanol to carbon monoxide and hydrogen over palladium supported on $Ce_{0.65}Zr_{0.30}La_{0.05}O_2$ and $La–Al_2O_3$”, *Catal. Today* 175 (2011) 430–434
[51] M.Y. Smirnov, G.W. Graham, “Pd oxidation under UHV in a model Pd/ceria–zirconia catalyst” *Catal. Lett*. 72 (2001) 39-44
[52] J.Z. Shyu, K. Otto, W.L.H. Watkins, G.W. Graham, R.K. Belitz, H.S.Gandhi, “Characterization of Pd γ-Alumina Catalysts Containing Ceria”, *J. Catal.* 114 (1988) 23-33
[53] M. Alexandrou, R.M. Nix, “The growth, structure and stability of ceria overlayers on Pd(111)”, *Surf. Sci.* 321 (1994) 47-57
[54] A. Holmgren, B. Anderson, D. Duprez, “Interactions of CO with Pt/ceria catalysts”, *Appl. Catal. B: Environ*. 22 (1999) 215–230
[55] G.N. Vayssilov, M. Mihaylov, P. St. Petkov, K.I. Hadjiivanov, K.M. Neyman, “Reassignment of the Vibrational Spectra of Carbonates, Formates, and Related Surface Species on Ceria: A Combined Density Functional and Infrared Spectroscopy Investigation”, *J. Phys. Chem. C* 115 (2011) 23435–23454
[56] N.B. Colthup, “Spectra-Structure Correlations in the Infra-Red Region”, *J. Optic. Soc. Amer.* 40 (1950) 397- 400
[57] F.M. Hoffmann, “Infrared Reflection-Absorption Spectroscopy of Adsorbed Molecules”, *Surf. Sci. Rep.* 3 (1983) 107-192
[58] J. Szanyi, W.K. Kuhn, D.W. Goodman, “CO adsorption on Pd(111) and Pd(100): Low and high pressure correlations”, *J. Vac. Sci. Tech. A* 11 (1993) 1969-1974
[59] S. Bertarione, D. Scarano, A. Zecchina, V. Johánek, J. Hoffmann, S. Schauermann, M.M. Frank, J. Libuda, G. Rupprechter, H.-J. Freund, “Surface Reactivity of Pd Nanoparticles Supported on Polycrystalline Substrates As Compared to Thin Film Model Catalysts: Infrared Study of CO Adsorption”, *J. Phys. Chem. B*, 108 (2004) 3603-3613
[60] M. Avrami, “Kinetics of Phase Change. I General Theory”, *J. Chem. Phys.* 7 (1939) 1103-1112
[61] M. Avrami, “Kinetics of Phase Change. II Transformation-Time Relations for Random Distribution of Nuclei”, *J. Chem. Phys.* 8 (1940) 212-224
[62] T. Matsui, T. Hoshikawa, K. Naito, “Oxidation of Simulated Fission-Produced Noble Metals and Alloy”, *Sol. Stat. Ion.* 40/41 (1990) 996-999
[63] E.T. Peterson, A.T. DeLaRiva, S. Lin, R.S. Johnson, H. Guo, J.T. Miller, J.H. Kwak, C.H.F. Peden, B. Kiefer, L.F. Allard, F.H. Ribeiro, A.K. Datye, “Low-temperature carbon monoxide oxidation catalysed by regenerable atomically dispersed palladium on alumina”, *Nat. Commun.* 5 (2014) 4885

Chapter 5 - Pd Model Catalysts: Effect of Air Pulse Length during Redox Aging on Pd Redispersion

Jason A. Lupescu[1,2,*], Johannes W. Schwank[1], Galen B. Fisher[1] and Sabrina L. Peczonczyk[2]

[1]University of Michigan, Ann Arbor, MI 48109 USA

[2]Ford Motor Company, Dearborn, MI 48124 USA

Abstract

The noble metal particles of automotive catalytic converters that are initially on a nanoscale agglomerate into larger particles during customer in-use operation with temperature, time and aging environment, decreasing the performance of the catalytic converter. Engine control methods are needed to provide an environment capable of partially redispersing noble metal catalyst particles while the particle size is still small. In this study, Pd-based model powder catalysts supported on ceria-zirconia (Pd/CZO) or 4wt% La_2O_3 stabilized γ-Al_2O_3 (Pd/Al) were exposed to simulated customer in-use operation engine exhaust of redox cycling at 700°C for 16 hours either continuously or interrupted with brief air pulses. The keys to this research are 1) determine the air pulse length required so that any Pd redispersion gains achieved by air treatment in each 20

minute cycle will be retained by the end of the redox aging cycle, and 2) determine if these supports are capable of rapid Pd redispersion. Catalyst activity was determined by CO oxidation with the Water Gas Shift (WGS) reaction and Oxygen Storage Capacity (OSC) measurements to probe the contact between the noble metal and support at a given state of catalyst deterioration, plus CO light-off to confirm trends observed with Pd metal dispersion. We found that air pulses applied to interrupt short redox aging spans enabled Pd redispersion on the time scale of a common engine ~10 second fuel cut on Pd/Al catalysts, but not for Pd/CZO catalysts. Strong metal support interaction by decoration of the Pd surface by Ce_2O_3 was suspected to slow Pd redispersion by limiting metal mobility. The insight gained from this work could be used to develop engine control and aftertreatment systems to actively intervene and regenerate a catalyst capable of rapid Pd redispersion.

5.1 Introduction

Automotive catalytic converters are irreversibly deactivated by exposure to combustion exhaust under in-use operating temperatures (500°C-900°C) or by more severe rapid aging protocols (>1000°C) used to simulate 150,000 miles of in-use operation in just hours. The catalytic converter or Three-Way Catalyst (TWC) washcoat technology contains noble metals (Pt, Pd and/or Rh) impregnated onto a complex support material that includes alumina to provide high surface area and mixed oxides of ceria and zirconia (CZO) for oxygen storage capacity (OSC) promotion [1, 2, 3]. Precious metals are known to undergo sintering causing loss of catalytic activity. Previous attempts to counteract the sintering induced loss of Pd dispersion relied upon feeding excess oxygen to deactivated TWC samples aged under in-use operating temperatures [4, 5, 6, 7] or under more mild conditions [8, 9]. These works achieved modest gains in Pd dispersion and partial regeneration of activity.

Observations of PdO migration during heating of Pd/Al_2O_3 catalysts in oxygen and filming them under an electron microscope revealed that Pd changed to PdO above 325°C then wet and spread over the support between 350°C to 800°C, and finally mobile particles ruptured over the support surface and redispersed [10, 11, 12]. While PdO is the prerequisite for redispersion [6], support collapse and metal-support interaction may limit PdO mobility and particle rupture. Other deactivation modes linked to strong metal support interaction (SMSI) include geometric effects where reducible oxide species partially block the active metal surface and weaken the interaction of adsorbates onto the Pd metal surface [13, 14, 15, 16, 17, 18] and electronic effects where a negative binding energy shift indicates increased Pd electronegativity [19, 20]. In our initial study with redox aged Pd based model catalysts, a post-aging treatment in dry air at 700°C for 2h on the 1.5wt% Pd supported on 4wt% La_2O_3 stabilized γ-Al_2O_3 (Pd/Al) demonstrated: 1) reversal of strong metal support interaction (SMSI) effects, and 2) reduced Pd particle sizes [21]. However, the 1.5wt% Pd supported on CeO_2-ZrO_2 mixed oxide (CZO) achieved just the first effect as the Ce decoration on Pd seemed to prevent Pd redispersion until the reduced Ce oxide species was removed from the Pd surface. Our follow up study demonstrated that a two hour oxidizing gas treatment was

more effective for Pd redispersion when performed after a short 20 minute redox aging when Pd particles were still relatively small (8.8 nm) rather than after a long 16 hour redox aging when the Pd particles were larger (20+ nm) and more difficult to fully oxidize [22]. Small metal particles are thermodynamically less stable than larger particles since atoms on the particle surface are energetically less stable than the interior atoms already well ordered and packed. While it would be beneficial to conduct an in-situ regeneration of a catalytic converter, a two hour dry air treatment at 700°C is not a realistic automotive operating exhaust condition. However, an operating condition of spaced short intervals of air at 700°C would be analogous to a common engine fuel cut during a slowing down from high speed and would last about 2-10 seconds [21]. Newton *et al*. showed that 2-10 seconds is enough time to redisperse very small Pd particles on a fresh CZO-Al_2O_3 support during CO/NO cycling at 400°C [8]. However, it is unclear if air exposure for such a short time is also sufficient to first reverse aging induced SMSI effects and then redisperse sintered Pd.

The goal of this investigation was to determine the length of interrupting air treatments during simulated automotive operating conditions that can limit or reverse Pd-based TWC deactivation on La_2O_3-Al_2O_3 and CZO supports. Pd particle size and dispersion measurements were performed with complimentary techniques of H_2 chemisorption and XRD pattern Pd [111] peak width since H_2 chemisorption is vulnerable to errors from SMSI effects and XRD is insensitive to very small Pd particles (< 6 nm). Carbon Monoxide (CO) adsorption infrared spectra were collected on the Pd catalyst samples to determine the surface characteristics based on the types of carbonaceous species formed and to identify the accessible Pd facets as performed in other works [13, 23, 24]. The oxygen storage capacity (OSC), CO light-off and water-gas shift (WGS) tests were included since the oxidation of CO gives insight into activity of the exposed Pd particle surface and contact between the Pd particle and support at a given state of catalyst condition.

5.2 Experimental

5.2.1 Preparation of Model TWC Samples

Two model powder catalysts of 1.5wt% Pd were prepared by a Ford OEM supplier using incipient-wetness impregnation with a palladium solution free from chlorides. The first catalyst was on a ceria-zirconia ($Ce_{0.5}Zr_{0.5}O_2$) support (Pd/CZO) and the other catalyst was on a 4wt% La_2O_3 stabilized γ-Al_2O_3 support (Pd/Al). After drying, this catalyst was calcined at 500°C for 4 hours in air to fix the metals on the support material. Uncatalyzed ceria-zirconia ($Ce_{0.5}Zr_{0.5}O_2$) powder was also used as a standard to acquire baseline characterization data. All powders were sieved to obtain particles between 40-60 mesh (250-420 microns).

5.2.2 Model TWC Sample Aging and Air Treatment Procedures

Catalyst aging environments were established in a continuous flow reactor at a total flow rate of 3 L/m and heated at 700°C for 16 hours to simulate in-use drive cycle conditions at the engine-out location. The continuous redox aging gas composition contained 10% H_2O in N_2 plus alternating 10 minute step pulses of lean (0.1% O_2) then rich (0.15% CO and 0.05% H_2) as shown in Figure 5-1a. This environment should keep Pd in the metallic state during the entire 16 hours as with just 0.1% O_2 in the lean step, the aging temperature of 700°C was well above the PdO decomposition temperature [22]. Our previous works used 2 hour dry air post-aging treatments to restore lost Pd dispersion [21, 22]. However in this plan, brief air treatments will be inserted during the lean step pulse of the redox cycle to interrupt the deterioration caused by the rich step pulse. Compressed dry air at 700°C was applied to the catalyst by replacing the redox aging gas feed for a portion *x* minutes of the 10 minute lean pulse as shown in Figure 5-1b. A 1/6 minute air pulse is similar in length to an actual engine fuel cut when a vehicle slows down from highway speed [21]. A 2 minute air pulse during each 20 minute redox cycle accumulated over 16 hours nearly equals 2 hours of total air exposure. The 2 minute air pulse will be used to investigate whether dry air is more effective when applied to interrupt redox aging over 16h compared to when applied as a 2h post treatment after the 16h continuous redox aging cycle. The 10 minute air pulse replaces

the entire lean pulse and equals the length of the rich pulse, which will compare against other redox cycles with lean steps containing excess O_2 to completely oxidize Pd [7].

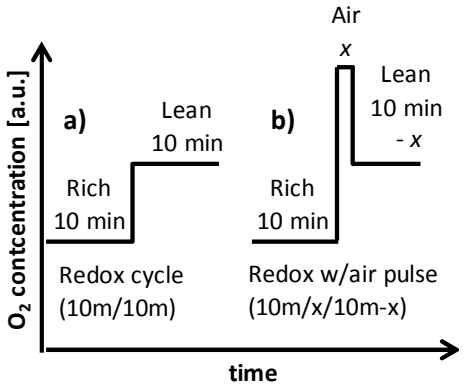

Figure 5-1: Redox aging cycle and air pulse length

A 1.50 g portion of catalyst powder was loaded in a quartz boat and placed inside a 19 mm ID quartz reaction tube in the heating zone of the surrounding oven. A thermocouple was placed over the boat in the aging gas stream and a second thermocouple was bent into the boat with the tip buried in the powder. The CO gas stream was scrubbed of iron carbonyls before introduction to the reactor. Gasoline engines typically operate about the fuel/air stoichiometric ratio so the automotive catalyst OSC state is partly depleted. All catalyst samples in this work were characterized and evaluated in the reduced state by exposing them to a flow of 9% H_2 in Ar at 300°C for 30 minutes prior to cooling in Ar to room temperature.

5.2.3 Catalyst Characterization Techniques

Support phase identification was performed with X-ray diffraction (XRD) pattern analysis. The instrument used for pattern acquisition was a Rigaku Miniflex II diffractometer with Cu Kα X-Ray (λ = 1.5406Å) radiation source set at 30 kV and 15 mA. A catalyst sample mass of 0.1 g was wet-milled with a mortar and pestle in ethanol then dripped onto a quartz slide and dried. Scans were collected from 20°2θ to 90°2θ at a resolution of 0.005°2θ at 1°2θ/min.

The surface characteristics of the catalysts were determined by N_2 physisorption, Diffuse Reflectance Infrared Fourier Transform Spectroscopy (DRIFTS) and X-ray

photoelectron spectroscopy (XPS). The BET specific surface area and BJH pore volume (for pores between 17-300Å) were determined with a Micromeritics ASAP2420 instrument using N_2 adsorption at 77K. A 48-point adsorption and 33-point desorption isotherm plot was generated across a range of 0.1-0.9 P/P_0. Infrared spectra were collected with a Nicolet 6700 FTIR spectrometer with Auxiliary Experiment Module including a praying mantis cell to facilitate gas exchange to and heating of the sample. Fine powder catalyst samples recovered from the XRD analysis slide were poured into the praying mantis sample cup onto a supporting screen. The IR spectra were collected with 64 scans at a resolution of 2 cm^{-1} repeating every two minutes. Spectra on the "as-is" samples were first obtained in N_2-only feed gas at the end of a 1 hour stabilization at fixed temperatures in the range of 22°C-400°C, then again during a 2 hour soak in 1% O_2 balance N_2 at the same temperatures for comparison. Clean sample surfaces were prepared as follows: 1) 25% H_2 in nitrogen fed at 0.2 L/min for 16 hours at 400°C, 2) added 0.8 L/min N_2, switched off H_2 and waited for 10 minutes to purge 3) added 1% O_2 to the nitrogen carrier gas to burn off saturated carbonates and formates for an hour, 4) switched off O_2 and waited for 10 minutes to purge, 5) heated the sample cell to 600°C for one hour in nitrogen-only to decompose surface PdO. A clean sample background was acquired first under flowing nitrogen in stabilized temperature intervals from 400°C to 22°C. After the clean spectra at 22°C were collected, 1% CO was added for two hours to saturate the surface while spectra were collected. Elemental composition and chemical state information were determined with a Kratos AXIS 165 Electron Spectrometer using a monochromatic Al Kα (1486.6 eV) X-ray excitation source operated at 12 kV, 20 mA (240 W). Each sample was pressed into a pellet and then mounted onto sticky double sided pressure sensitive adhesive tape. Data was collected using pass energies of 80 eV or 20 eV to collect survey or high resolution spectra, respectively. All spectra were acquired using charge neutralization with an electron flood source. Elemental quantification of the high resolution spectra was accomplished using CASAXPS software, using routines based on Scofield photoionization cross-section values. A Shirley type background was used to fit all high resolution spectra. For Pd on alumina support the high resolution Pd 3d spectra was fit with a doublet using 60% Gaussian and 40% Lorentzian line shapes with an area ratio of 0.667, a full width

at half-maximum (FWHM) constrained within 0.6-2.8, and a peak separation of 5.2 eV. For Pd on CZO support, the Zr 3p fit was first determined from a CZO standard using 60% Gaussian and 40% Lorentzian line shapes with an area ratio of 0.5, a FWHM constrained between 0.6-2.8, and a peak separation of 13.4 eV. The remaining area under the envelope was then fit by adding Pd 3d peaks using the fitting parameters described above for Pd on alumina. Binding energies were referenced to the aliphatic C 1s peak at 284.6 eV [25].

Pd particle size estimates were performed using complimentary techniques of XRD peak fitting and H_2 chemisorption. Post-process curve fitting of the XRD pattern Pd peak for mean Pd crystalline length was performed with the Rigaku PDXL software program. The software calculations used for estimating mean Pd crystalline length from XRD pattern line broadening was based on the Scherrer equation [26]. The shape factor used was 0.89 for spherical crystallites and the peak integral method was used to determine peak breadth. The instrument broadening was corrected with a LaB_6 calibration standard. XRD peak analysis provides a bulk average estimate of the Pd crystallite length, which may be analogous to the Pd particle size as has been demonstrated for metal particles in the size range of 2-33 nm when electron microscopy and chemisorption were also used for confirmation [27, 28, 29, 30]. Note that crystallite length can be smaller than particle size if large particles are made of agglomerated crystals of if any poorly crystalline regions exist in the particle. H_2 chemisorption was performed using a Micromeritics ASAP2020 instrument with a static volumetric adsorption/out-gas/re-adsorption method described by Chen *et al.* [5]. Prior to analysis, each sample was first degassed in N_2 at 500°C, reduced at 350°C in pure H_2, exposed to vacuum at 1 microtorr and finally dosed with H_2 at 35°C for chemisorption measurements using a 5-point isotherm extrapolated to zero pressure. This technique is an improvement upon the classic H_2–O_2 titration method and avoids problems of H_2 spill-over and Pd hydride formation from interfering with the irreversible adsorbed H_2 calculation [31, 32]. The differential results were used to report Pd dispersion and size to exclude physisorbed H_2 on the support. H_2 chemisorption was used for all samples since CO chemisorption tests significantly overestimated the Pd dispersion on the CZO supports, likely due to CO adsorption on CZO forming stable carbonate species [33].

The XRD Pd size estimate is a volumetric average technique that detects crystallite length regardless if the particles are covered by support, while chemisorption is a surface average technique that will not detect support-covered metal particles, with both techniques average size calculations weighted towards larger particles.

The Pd metal dispersion (D) was estimated as a function of the Pd particle size (d_p) using equation 1 below, which is described further by Baylet *et al.* assuming spherical shapes [34]. With M_{Pd} as the Pd atomic weight of 106.4 g/mol, ρ_{Pd} as the Pd density of 12 g/cm^3, S_{Pd} as the molar surface area of Pd metal of 47,780 m^2/mol assuming an equidistribution of the low index faces.

$$D\ [\%] = (6 \times 10^5) * (M_{Pd}) / (\rho_{Pd} * S_{Pd} * d_p\ [nm]) \quad \text{Equation 1}$$

5.2.4 Catalyst Activity Measurements

A flow reactor was used to enable measurement of CO_2 formed by probe reaction tests on a characterized catalyst sample. The ASAP2020 quartz j-tube and sample used in the H_2 chemisorption test was fit onto the flow reactor. The j-tube measured 10.5 mm ID and a catalyst sample mass of 0.30 g was loaded between 6 mm redistributing layers of quartz wool. The bed height was 4 mm for the Pd/CZO samples. Matheson dynablenders and flow controllers managed the gas flow through the system. The gas stream could be triggered to route through a water bubbler and lines were maintained at 150°C to limit condensation. The CO gas stream was scrubbed of iron carbonyls. Two K-type 1/32-inch diameter thermocouples were placed 16 mm before and 13 mm after the sample bed. A Hiden HPR20 quadrupole electron ionization mass spectrometer with Secondary Electron Multiplier (SEM) detector measured five configurable mass values in the outlet gas stream. It had a 2 Hz sampling rate at an inlet sampling pressure of $1x10^{-5}$ torr and required two post-processing data corrections. First, the double excitation argon (Ar) mass 20 value was scanned, which is 11% of the total Ar level, rather than the typical mass 40 to get the measured Ar value below the SEM detector limit of $1x10^{-6}$ torr. Second, there was a CO and CO_2 mass overlap of 11.4%, so that amount of the CO_2 value was subtracted from the CO value. OSC measurements were run by alternating one minute lean or rich square step pulses, each

separated by a one minute purge. The bulk carrier gas was 2% CO_2 in Ar at 975 mL/min. The lean pulse was 1% O_2, 2% CO_2 in Ar at 1 L/min and the rich pulse was 2% CO, 2% CO_2 in Ar at 1 L/min. At least five CO pulses were measured in each 50°C increment, starting at 50°C and ending at 400°C. The WGS and CO light-off measurements were run with a constant feed at 1 L/min. The WGS feed was 2% CO, 2% CO_2, 2.5% H_2O and balance Ar. The CO light-off feed was 2% CO, 2% CO_2, 1% O_2 and balance Ar. The WGS and light-off gas mixtures were initially established at equilibrium over the catalyst sample at 30°C, then the oven heating ramp was triggered at 10°C/min to 400°C. A special step was required for Pd/CZO samples to prevent light-off at a 30°C inlet temperature driven primarily by support reoxidation with gas phase oxygen since the catalysts were initially reduced; CO was not introduced until the temperature rise from reoxidized CZO was cooled back down to room temperature.

5.3 Results

5.3.1 Support Phase Identification

The XRD patterns of the fresh, redox aged and air treated Pd model catalyst samples are shown in Figure 5-2. The XRD patters are consistent with the expected peaks for CZO in Figure 5-2a and alumina support in Figure 5-2b. In Figure 5-2a, the fresh CZO sample Pd [111] peak was indistinguishable in the XRD pattern apart from the background. No CZO phase separation was evident after 16 hours of exposure to the redox aging environment. A significant Pd [111] peak was observed at 40°2θ for all redox aged Pd/CZO samples, while the redox aged samples with air pulse length of 0-1 minutes also had a small Pd [200] peak at 46°2θ and small Pd [220] peak at 68°2θ. The air pulse length of 2-10 minutes decreased the area of the Pd peaks, indicating Pd particle redispersion, and the Pd peaks were shifted to lower scattering angles, indicating an expanded Pd crystal lattice. In Figure 5-2b, the Al support peaks obscured all the Pd peaks, except the Pd [311] peak. The fresh Pd peak was distinguishable in the XRD pattern, above the Al support peaks, while after redox aging the peaks increased in area and became sharper. The 1/6 minute and longer air pulses all

showed decreased Pd peak intensities and Pd peaks shifted to lower scattering angles, relative to the continuous redox aged sample, indicating that Pd redispersion occurred. These results suggest that Pd redispersion was more restricted on the CZO support compared to the Al support.

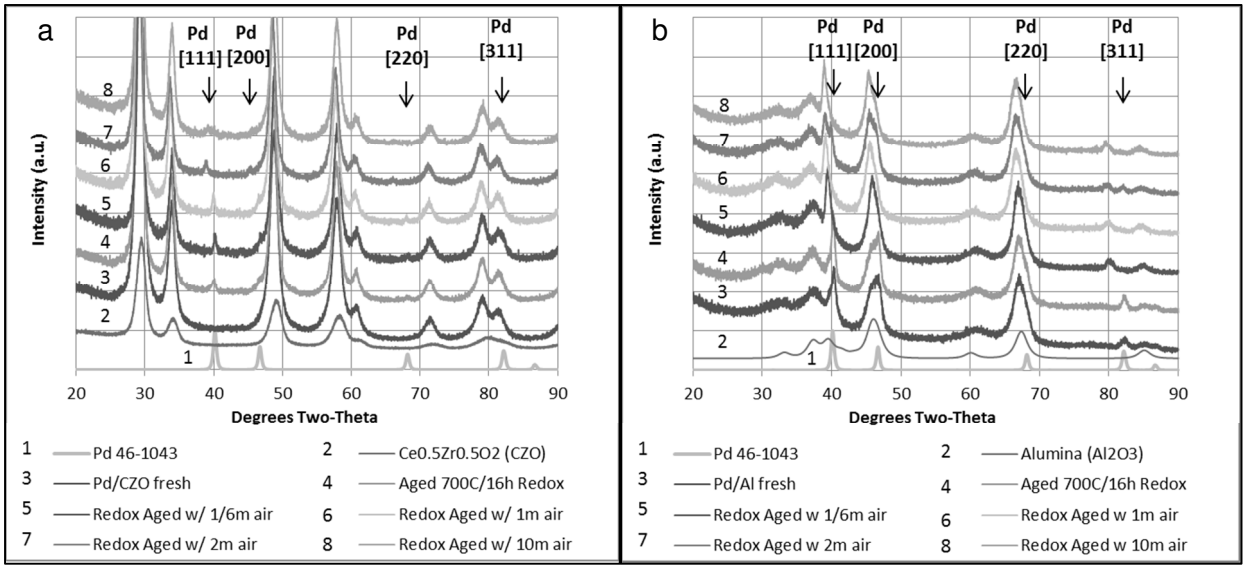

Figure 5-2: XRD Patterns of Pd model catalyst samples. Plots: a) Pd/CZO, b) Pd/Al

3.2 Catalyst Characterization

The BET surface areas for each sample are listed in Table 5-1. The fresh Pd/CZO catalyst had a surface area of 91 m^2/g and redox aging with or without simulated air pulses sintered the surface area by 53-58%. The fresh Pd/Al catalyst (Pd on 4wt% La_2O_3 stabilized γ-Al_2O_3) had a surface area of 209 m^2/g and redox aging with or without simulated air pulses sintered the surface area by 23-26%. Therefore replacement of lean pulse portions with air did not show much of an effect on the surface area of either support.

Table 5-1: Catalyst Samples and Characterization Results							
Samples		**Length of air pulse x [min]**	**Surface area [m^2/g]**	**H_2 Chemisorption**		**XRD Pd peak fit**	
ID#	**Condition**			**d_p [nm]**	**D [%]**	**d_p [nm]**	**D [%]**
1	Pd/CZO fresh	-	91	5.1 nm	21%	u/d *	u/d *
2	Pd/CZO redox aged (10 min rich / *x* min air / 10 min lean – *x* min)	0	41	u/d †	u/d †	21 nm	5.4%
3		1/6	38	u/d †	u/d †	28 nm	3.9%
4		1	38	u/d †	u/d †	25 nm	4.4%
5	"	2	40	90 nm †	1.2% †	17 nm	6.4%
6	"	10	43	35 nm †	3.2% †	8 nm	14%
7	#2 + 700°C/2h air	-	41	13 nm	8.7%	18 nm	6.3%
8	Pd/Al fresh	-	209	12 nm	9.1%	14 nm	7.9%
9	Pd/Al redox aged (10 min rich / *x* min air / 10 min lean – *x* min)	0	154	433 nm †	0.3% †	18 nm	6.3%
10		1/6	161	43 nm †	2.6% †	10 nm	11%
11	"	1	157	37 nm †	3.0% †	10 nm	11%
12	"	2	156	41 nm †	2.8% †	10 nm	11%
13		10	157	23 nm †	4.9% †	11 nm	10%
14	#9 + 700°C/2h air	-	152	20 nm	5.4%	19 nm	5.8%

u/d = undetectable, * No XRD pattern Pd peak, † Pd particles suspected to be affected by SMSI

The apparent Pd dispersion and Pd particle size for each sample are listed in Table 5-1. The fresh Pd/CZO sample #1 had Pd particles that were too small to be observed with an XRD pattern fit, but these particles were detected by H_2 chemisorption to have a bulk size of 5.1 nm in diameter for a dispersion of 21%. The fresh Pd/Al sample #8 (Pd on 4wt% La_2O_3 stabilized γ-Al_2O_3) had Pd particles that were detected by H_2 chemisorption to have a bulk size of 12 nm in diameter for a dispersion of 9.1%, in reasonable agreement with the XRD measurement of 14 nm for a dispersion of 7.9%. The continuous redox aged Pd/CZO sample #2 and Pd/Al sample #9 showed large disagreements between H_2 chemisorption and XRD results. SMSI can cause inaccuracies in the H_2 chemisorption results, due to the support La_2O_3 electronically coupling with the Pd metal [19, 20] or Ce_2O_3 covering the Pd surface [13, 14, 15], which cause lower adsorbate gas coverage of the Pd metal. These effects are reversed by sufficient reoxidation [13, 21, 22] and Ce_2O_3 decomposition from the surface [13, 35]. Samples #2 and #9 were given a post aging treatment of 700°C/2h with dry air to arrive at samples #7 and #14, respectively, and only then did the H_2 chemisorption and XRD results show good agreement. The Pd size after the continuous redox aging may have been too large to achieve more than a modest reduction in size with the dry air post

aging treatment. While these two hour air post aging treatments were studied in our previous works [21, 22], the remaining focus of this study will be on using shorter air pulses to interrupt the redox aging deterioration to achieve Pd size reductions on smaller Pd particles.

Pd/CZO samples #3 and #4 with aging interrupted by 1/6 minute and 1 minute air pulses, respectively, did not show a Pd size reduction relative to the continuous redox aged sample #2 in Table 5-1. The air pulses of 1/6 minute and 1 minute lacked sufficient time to achieve the Pd oxidation needed to reverse SMSI support coverage that enables Pd redispersion into smaller particles [21, 22]. Therefore brief isolated fuel cuts even up to 1 minute during vehicle operation may not be effective for maintaining small Pd size on this support. The redox aged sample #5 interrupted by 2 minute air pulses had a bulk Pd size 4 nm below sample #2 and a exhibited some SMSI reversal as the Pd surface was detected by H_2 chemisorption, although a 1.2% dispersion result is well below the XRD value and believed to be artificially low due to suspected residual ceria coverage of Pd. The redox aged sample #6 interrupted by 10 minute air pulses had a Pd size of 8.0 nm by XRD measurement, which was near the fresh 5.1 nm Pd size as measured by H_2 chemisorption, although a 3.2% dispersion result by H_2 chemisorption for sample #6 is well below the 14% dispersion result by XRD likely due to some residual ceria coverage of Pd.

Pd/Al sample #10 with aging interrupted by 1/6 minute air pulses had a bulk Pd size 9 nm less than the continuous redox aged sample #8 in Table 5-1. The remaining samples with aging interrupted by 1 minute air pulses or longer showed diminishing benefits over the 1/6 minute air pulse. The 1/6 minute air pulse was much more effective at redispersing the Pd on the Al support than on CZO, and achieved about the same Pd size on Pd/Al as with the 10 minute air pulse on redox aged Pd/CZO. These results suggest that SMSI electronic effects between Pd-La_2O_3 on Al_2O_3 were much faster to reverse upon reoxidation than SMSI decoration effects of Ce_2O_3 on the Pd surface.

5.3.3 XPS Surface Characterization

The XPS spectra of the Pd/Al and Pd/CZO catalyst samples are shown in Figure 5-3. Figure 5-3a showed the Pd $3d_{5/2}$ peak at 334.8 eV +/- 0.1 eV for both fresh and aged Pd/Al samples that corresponds to Pd^0 [36]. The fresh Pd/Al sample had a shoulder in the Pd $3d_{5/2}$ peak at about 336.5 eV, which was likely Pd^{2+} interface sites with the support La_2O_3 [21, 37], but these sites were lost after aging and not restored with air pulses. The La 3d and Zr 3p peaks did not show a change in peak height or location from the fresh to aged state as shown in Figure 5-3b and Figure 5-3c, respectively. Figure 5-3c showed Pd $3d_{5/2}$ peaks fit inside the shoulders of the Zr 3p peaks as is typically performed for analysis of Pd on CZO support [37, 38, 39, 40]. Figure 5-3c showed that the fresh Pd/CZO sample had two similarly sized Pd $3d_{5/2}$ peaks at 334.7 eV and 337.1 eV that corresponds to Pd^0 and Pd^{2+}, respectively [36]. The fresh Pd/CZO had an abundance of interface sites with finely dispersed Pd^{2+} and oxygen from CeO_2, but these sites were lost after aging and not restored with air pulses. No significant Pd peak shifting was observed due to redox aging with or without air pulses. Figure 5-3d did not show a binding energy shift due to redox aging or lean treatments for the Ce $3d_{5/2}$ peak at 882.0 eV or the Ce $3d_{3/2}$ peak at 900.4 eV. The other Ce 3d peaks shown are satellite peaks that arise from interactions with the Ce 4f valence electrons after the 3d core electron is emitted.

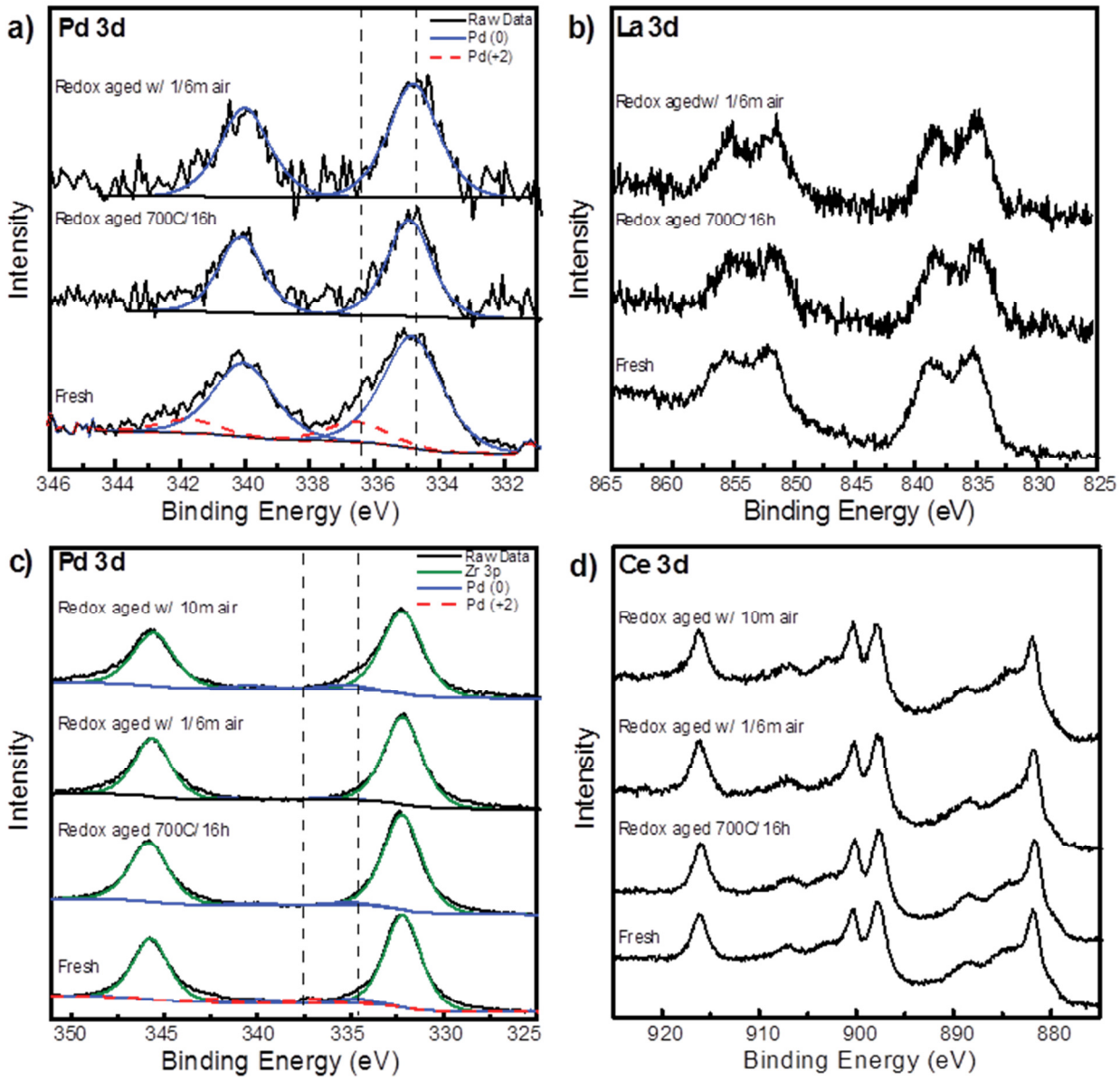

Figure 5-3: XPS Patterns of Pd model catalyst samples. Vertical dashed black lines indicate Pd peak centers. Solid blue lines are representative fits for Pd metal, dashed red lines are representative fits for Pd^{+2}. Spectra are offset for clarity. Plots: a) Pd 3d on Pd/Al, b) La 3d on Pd/Al, c) Pd 3d on Pd/CZO, d) Ce 3d on Pd/CZO

The atomic concentrations from the top surface layers are shown in Table 5-2 based on the peak intensities shown in Figure 5-3. The reported values are an average of two pressed pellet samples. Adventitious carbon formed from exposure to room temperature air during the sample transfer and pellet pressing. The observed range in concentration for the two pellets of each sample was +/- 0.2at% for Ce, +/- 0.04at% for La and +/- 0.02at% for Pd. The fresh surface Pd concentration on CZO support was

diminished by about 72% after redox aging, indicating Pd sintering plus a geometric SMSI effect of Ce_2O_3 coverage on Pd. The increased air pulse length significantly decreased the surface concentration of Ce and the Ce/Pd ratio, indicating a gradual removal of Ce_2O_3 from Pd with longer air pulses. The fresh Pd surface concentration on Al support was reduced nearly by about 50% after redox aging, consistent with Pd sintering from Table 5-1 yet did not diminish as severe as the Pd surface on CZO, since La_2O_3-Al_2O_3 is not reducible under these conditions [41]. The fresh La surface concentration on Al support did not yield a significant change with aging or with air pulses. The added 1/6 minute air pulse showed essentially no change in the surface La/Pd concentration ratio or Pd concentration.

Table 5-2: Atomic surface concentrations of fresh and aged samples by XPS [at%]

Sample		C	O	Ce	Zr	La	Pd	Ce/Pd	La/Pd
Pd/CZO	Fresh	20.9	59.9	6.0	12.6	-	0.57	10.5	-
	Redox aged 700°C/16h	22.8	56.2	6.9	13.9	-	0.16	43.1	-
	Redox aged w/ 1/6m air	34.3	48.7	5.5	11.3	-	0.21	26.2	-
	Redox aged w/ 2m air	34.0	50.1	4.9	11.0	-	0.22	22.6	-
	Redox aged w/ 10m air	36.0	47.4	5.2	11.2	-	0.31	16.8	-
Pd/Al	Fresh	14.5	50.7	-	-	0.24	0.20	-	1.2
	Redox aged 700°C/16h	16.4	52.7	-	-	0.30	0.12	-	2.5
	Redox aged w/ 1/6m air	16.0	52.5	-	-	0.26	0.12	-	2.2

5.3.4 Infra-red measurements

The wave numbers characteristic to CO adsorption on ceria and Pd according to earlier work is shown in Table 5-3 [23, 24, 42, 43, 44, 45]. The IR band wave numbers can change with temperature, pressure and CO coverage [46, 47]. Therefore the wave numbers given in Table 5-3 are approximate.

Table 5-3: Probable locations of IR bands from literature		
Species	**Wave number [cm^{-1}]**	**References**
Carbonates bidentate	1028, 1286, 1562	[42]
Carbonate unidentate	1062, 1454	[42]
C-O stretch	900 – 1300	[44]
CO-Ce^{+4} linear	1310 – 1330	[42]
OH bend	1200 – 1450	[44]
C-H bend	1300 – 1475	[44]
Formates	1360, 1580	[42]
Hydrogen carbonate	1399 – 1408	[43]
Inorganic carboxylate	1510, 1560	[42]
N-H bend	1500 – 1650	[44]
C=C stretch	1575 – 1700	[44]
C=O stretch	1640 – 1850	[44]
CO-Pd [111] bridge x3	1826 – 1890	[23, 45]
CO-Pd [111] bridge x2	1920 – 1948	[23, 24, 45]
CO-Pd [100] bridge x2	1874 – 1997	[23, 24, 45]
CO-Pd [111] on top	2050 – 2080	[23, 24, 45]

Figure 5-4 shows Pd catalyst samples after evaluation on the catalyst activity tests, which will be referred to as an “as-is” condition with carbonaceous species formed from a combination of air and CO exposure. Spectra of the adsorbed species are the difference between the absorbance of the “as-is” samples and the clean sample background. Residual carbonaceous species decorated each support surface as no CO-Pd peaks were observed in the characteristic range of 1800-2100 cm^{-1}. In Figure 5-4a for Pd/CZO, the peaks from 1000-1700 cm^{-1} are consistent with carboxylates, carbonates and formates. Most carbonaceous species were present through at least 400°C even under oxidizing conditions, which demonstrates their role as spectator species on the CZO support. The oxidation feed at 400°C enhanced formation of peaks at 1230 cm^{-1} (OH bend) and 1524 cm^{-1} (N-H bend) over the N_2-only feed gas. In Figures 5-4b for Pd/Al, the only major peaks were at 1464 cm^{-1} (C-H bend) and 1576 cm^{-1} (N-H bend or C=C stretch) are present after 2 hours in 1% O_2, which demonstrates their role as spectator species on the Al support.

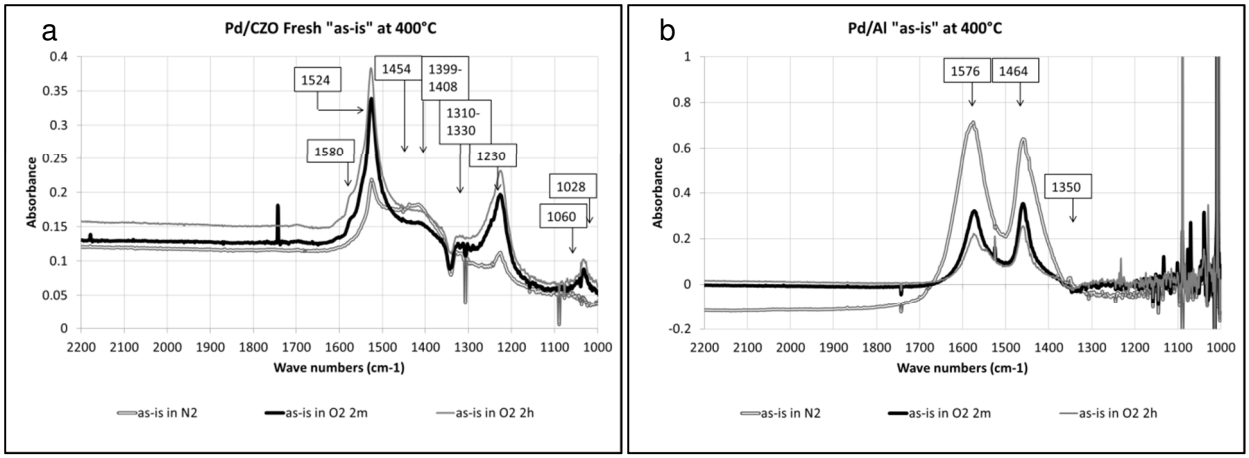

Figure 5-4: IR spectra of "as-is" fresh samples in N_2-only or with 1%O_2. Plots: a) Pd/CZO at 400°C, b) Pd/Al at 400°C

Figure 5-5 shows Pd catalyst samples that were preconditioned to clean the surfaces of carbonaceous species, and then exposed to gas phase CO while spectra was acquired every 2 minutes over 2 hours. Spectra of the adsorbed species are the difference between the absorbance of the CO saturated samples and the clean sample background. For all samples, gas phase CO appears as two similar bands starting at 2050 cm^{-1} through 2200 cm^{-1} with high frequency and low amplitude of approximately 0.04 absorbance, which partially obscures peaks of linearly adsorbed CO on Pd[111]. In Figure 5-5a, the peaks from 1000-1700 cm^{-1} are carbonaceous species consistent with carboxylates, carbonates and formates, and similar with the peaks observed for "as-is" surface condition in Figure 5-4a. The growth rate of carbonaceous species showed the following trend: fresh Pd/CZO > Pd/CZO redox aged with 10m air > Pd/CZO redox aged with 1/6m air > Pd/CZO continuous redox aged >> CZO. This large difference between uncatalyzed CZO and the Pd/CZO samples implies that Pd enhances the formation of carbonaceous species at the Pd-CZO interface or adlineation sites. In Figure 5-5b, the carbonaceous species formed on Pd/Al showed peaks at 1340 cm^{-1} and 1611 cm^{-1} on just the aged Pd/Al samples that are suspected to have an SMSI effect with the H_2 chemisorption results in Table 5-1. There were also weak peaks at 1544 cm^{-1} for N-H bending and 1611 cm^{-1} for C=C stretching. Bands observed at 1464 cm^{-1} and 1576 cm^{-1} for the Pd/Al "as-is" samples in Figure 5-4b were not clearly shown in Figure 5-5b. Carbonaceous species formed much slower and at lower intensity on Pd/Al than for Pd/CZO after 4 minutes, with absorbance on Pd/Al lower by

an order of magnitude.

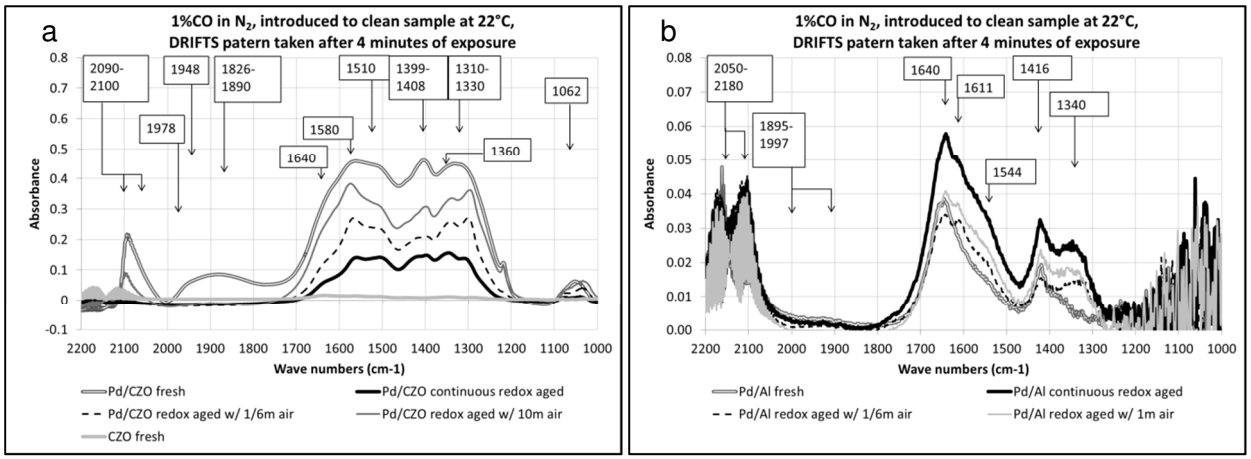

Figure 5-5: IR spectra during CO exposure onto clean samples at 22°C. Plots: a) Pd/CZO after 4 minutes, b) Pd/Al after 4 minutes

Figure 5-6 shows the IR spectra range just for CO adsorbed on Pd after two hours of CO saturation. The spectra were acquired with CO turned off to avoid gas phase interference bands. In Figure 5-6a, fresh Pd/CZO showed multiple IR bands: a strong linear CO-Pd[111] band near 2080 cm^{-1}, a strong two-fold bridged CO-Pd[100] near 1980 cm^{-1}, a weak two-fold bridged CO-Pd[111] near 1920 cm^{-1}, and a strong three-fold bridge CO-Pd[111] band near 1850 cm^{-1}. Redox aging of Pd/CZO caused changes to the metal and support that resulted in prevention of CO adsorption onto Pd facets. Therefore on CZO support, the SMSI effect was consistent with Pd covered by Ce_2O_3, since ZrO_2 is not reducible under these conditions. These results are consistent with Badri *et al*. for 1.2wt% Pd on CeO_2 [13]. The continuous redox aging along with redox aging interrupted by 1/6 minute and 1 minute air pulses all showed equivalent spectra, as these air pulses were not long enough to reverse this SMSI effect on CZO support. The redox aging interrupted by 2 minute and 10 minute air pulses showed much more intense CO-Pd linear and bridge peaks, but were still significantly below the fresh Pd/CZO spectra. These results confirm the suspicions in Table 5-1 that all aged Pd/CZO samples were affected by SMSI, only to a lesser degree with longer air pulses. In Figure 5-6b, Pd/Al fresh showed similar CO adsorption onto Pd as with the redox aged samples exhibiting a relatively strong linear CO-Pd[111] band near 2100 cm^{-1}, weaker two-fold bridged CO-Pd[100] and CO-Pd[111] bands near 1948 cm^{-1} and 1970

cm^{-1}, respectively, and a faint three-fold bridge CO-Pd[111] band near 1838 cm^{-1}. These IR results are consistent with the work by Lear *et al*. for CO saturation of Pd/Al_2O_3 catalysts that were with different Pd precursors and matches the IR pattern profile of their 1wt% $Pd(acac)_2$ sample [48]. Pd does not appear to be covered by La_2O_3 on the reduced samples, since Figure 5-6b shows all samples had similar peak intensities.

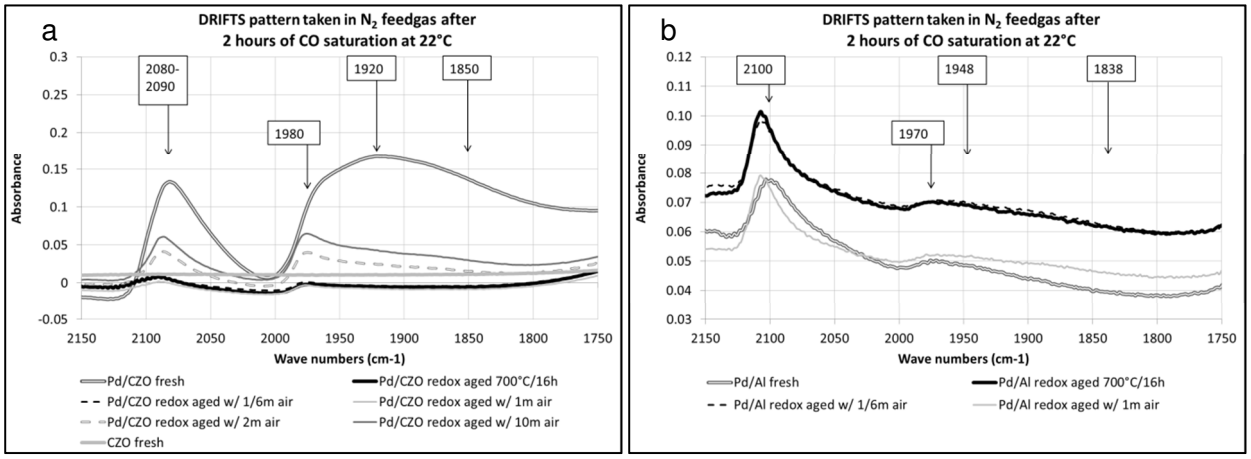

Figure 5-6: IR spectra in N_2 after 2h CO exposure at 22°C. Plots: a) Pd/CZO, b) Pd/Al

5.3.5 Catalyst Activity Tests

Figure 5-7a shows the OSC results for the Pd/CZO samples. The aged samples showed a severe loss in CO_2 yield from fresh at 200°C and 300°C. At 350°C and 400°C, the fresh Pd/CZO sample consumed the entire inlet CO pulse for the first several seconds, showing diminishing CO_2 yield with increasing temperature. The 1/6 minute and 1 minute air pulses showed slightly increased CO_2 yield over the redox aged sample at 300°C. These three samples had no exposed Pd as measured by H_2 chemisorption as shown in Table 5-1. The 2 minute and 10 minute air pulses showed increased CO_2 yield over the other aged samples at 300°C. These two air pulse samples had exposed Pd as measured by H_2 chemisorption as shown in Table 5-1. Figure 5-7b shows the OSC results for the Pd/Al samples. La_2O_3-Al_2O_3 has negligible oxygen mobility under these conditions and the OSC CO_2 yield measured during the CO step was based upon PdO formed on the O_2 step. Fresh uncatalyzed CZO had similar OSC CO_2 yield to the Pd/Al samples.

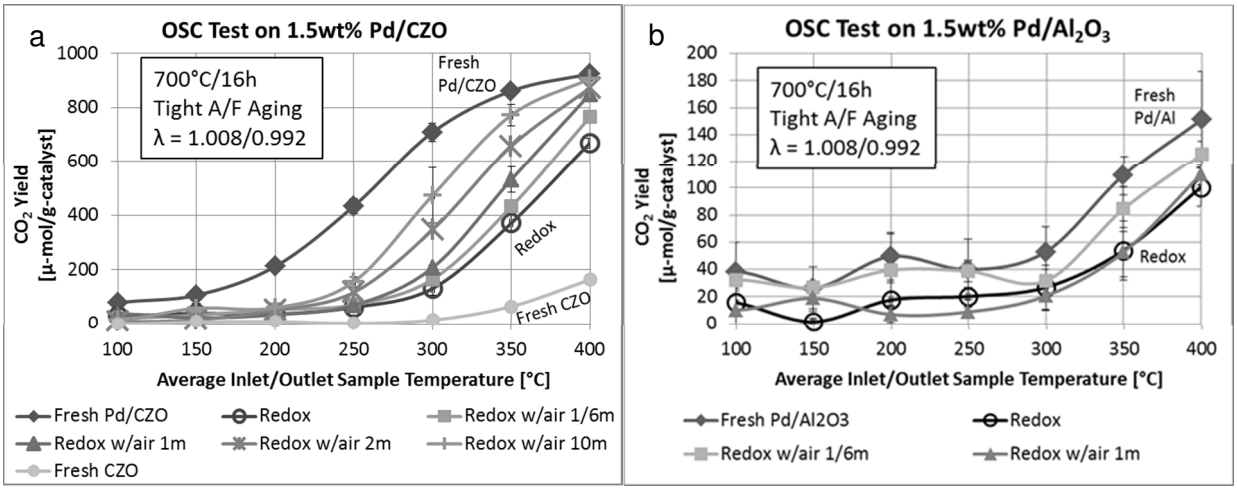

Figure 5-7: OSC catalyst activity tests. Plots: a) Pd/CZO, b) Pd/Al

Figure 5-8a shows the WGS results for the Pd/CZO samples. The redox aged sample showed a severe loss in CO_2 yield, at 300°C and above, compared to fresh. The 1/6 minute and 1 minute air pulses had only a slight increase in CO_2 yield over the redox aged sample. Even though the redox aging prevented access to the Pd particles by H_2 chemisorption according to Table 5-1, these catalysts were still more active than uncatalyzed fresh CZO on both OSC and WGS tests. The 2 minute and 10 minute air pulses showed a large CO_2 yield increase over the redox aged sample at 400°C, since air pulses on these two samples exposed Pd by H_2 chemisorption as in Table 5-1. Figure 5-8b shows the WGS results for the Pd/Al samples. The fresh Pd/Al sample had the highest CO_2 yield at 350°C-400°C while the other samples were similar to each other. The redox aged Pd/CZO sample had similar performance to the aged Pd/Al samples, indicating that both samples had a lack of oxygen mobility at the metal-support adlineation sites. These adlineation sites were restored with air pulses to increase WGS activity on Pd/CZO samples, but not to a measurable degree on the Pd/Al samples.

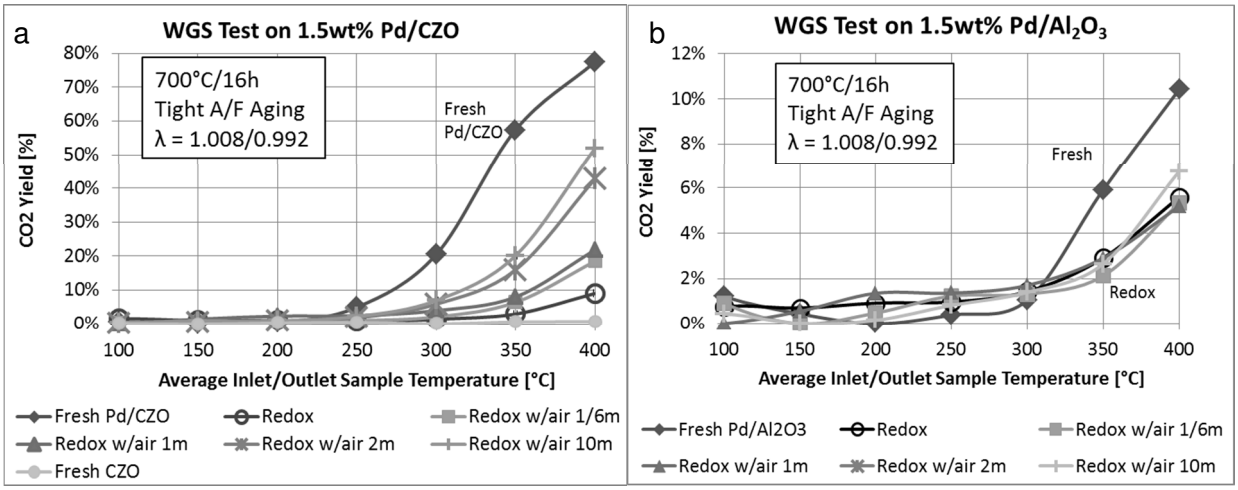

Figure 5-8: WGS catalyst activity tests. Plots: a) Pd/CZO, b) Pd/Al

Figure 5-9 shows the CO light-off test results, as the CO_2 yield, on the Pd/CZO and Pd/Al samples with the 50% CO conversion temperature (T_{50}) noted in the legend. In Figure 5-9a, the T50 over Pd/CZO samples was shown to follow the following trend: fresh < air 10 min = air 2 min < redox < air 1/6 min. Generally, the Pd/CZO T_{50} scaled with Pd size by XRD from Table 5-1 and confirms those results. In Figure 5-9b, the T_{50} over Pd/Al samples was shown to be the lowest on the fresh sample and highest on the aged samples. However, the catalytic activity of all aged Pd/Al samples was much poorer than the aged Pd/CZO samples due to the difference in support oxygen mobility. Generally, the Pd/Al T_{50} scaled inversely with Pd dispersion by H_2 chemisorption from Table 5-1, except for the redox and air pulse samples, which had a similar T_{50} of 203°C +/- 6°C. The Pd-La_2O_3 electronic SMSI effect may hinder catalytic activity as evidenced by the 1/6 and 1 minute air pulses not restoring performance relative to continuous redox aging, yet the Pd dispersion was higher by both XRD and H_2 chemisorption.

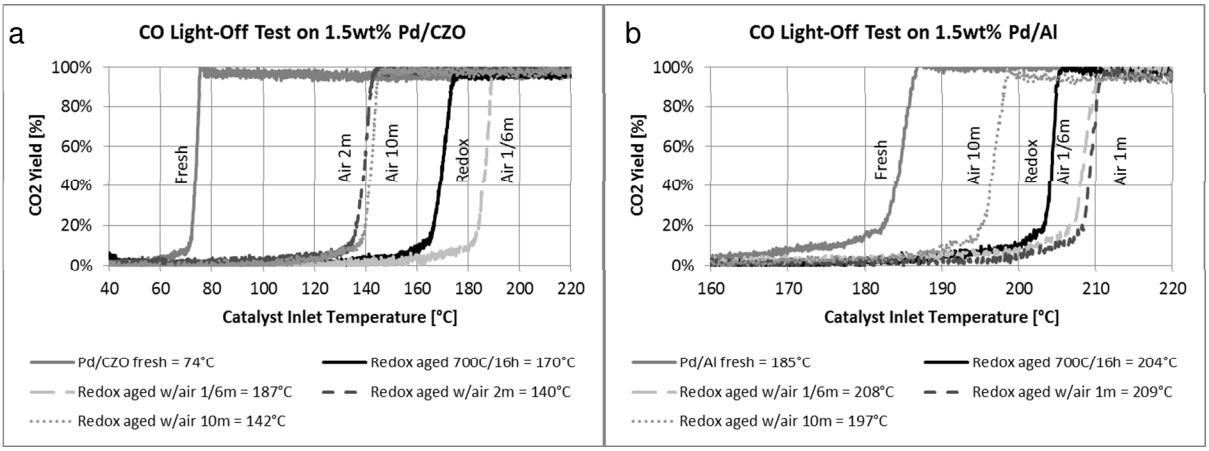

Figure 5-9: CO light-off catalyst activity tests. Plots: a) Pd/CZO, b) Pd/Al

5.4 Discussion

The Pd/CZO samples showed gradual improvement in Pd surface recovery with increasing length of air pulses. After 1 minute into a longer air pulse, some Pd facets become exposed as ceria overlayers are retracting similar to the mechanism observed by Alexandrou and Nix [35]. Once exposed, the Pd can now oxidize, migrate, redisperse and shrink according to microscopy work by Rodriguez, and Chen and Ruckenstein [10, 11, 12]. We also observed a characteristic Pd lattice expansion accompanied by the redispersion of Pd as shown in Figure 5-2 for both supports. Even though the redox aging with 2 minute and 10 minute air pulses achieved a Pd size reduction, the Pd-CeO_2 SMSI effects were not completely reversed as with sample #7, indicating the long time required to reintegrate reduced ceria decomposed from the Pd surface back into the bulk support. The technique of repeated transformation of Pd to PdO with 10 minute air pulses is better at keeping Pd near the fresh size than the 700°C/2h air post aging treatment and perhaps a constant lean aging with 0.1% O_2 in our prior work where Pd was 8.6 nm by H_2 chemisorption [22]. These results appear consistent with work by Kang *et al*. with Pd-TWC samples aged with a redox-type aging at 600°C for 16 h while cycling 3% CO to form Pd metal or 3% O_2 to form PdO, although the final Pd dispersion was not stated, a lower CO light-off temperature was shown for their redox cycling sample than for aging in constant 3% O_2 [7]. For DRIFTS patterns

on the Pd/CZO samples, the growth rate of carbonaceous species appeared to be directly related to the increasing air pulse length corresponding to the decreasing Ce/Pd ratio in the XPS results in Table 5-2. The longer air pulses likely restored or preserved adlineation sites that facilitate rapid growth of carbonaceous species, which were lost in the continuous redox aging.

The decorated Pd-Ce_2O_3 sites on redox aged Pd/CZO enabled some CO oxidation on both OSC and WGS tests that exceeded the performance of uncatalyzed fresh CZO. From Table 5-4 below, the OSC conversion for redox aged Pd/CZO at 400°C was 669 µ-mol/g-catalyst and fresh Pd/Al was 151 µ-mol/g-catalyst. Figure 5-7a showed that the OSC conversion for fresh CZO was near 180 µ-mol/g-catalyst at 400°C, so there was some support participation that would only be boosted if Pd were added. The results at least appear additive as Pd/CZO had twice the OSC of the sum of Pd/Al and uncatalyzed CZO. These results also suggest that the decorated Pd-Ce_2O_3 sites acted like Pd-Al_2O_3 adlineation sites, with weak O_2 adsorption for reaction with gas phase CO since O_2 adsorption likely does not reoxidize the site Pd-Ce_2O_3 given the poor relative performance to other Pd/CZO aged samples. From Table 5-4, the WGS conversion at 400°C for redox aged Pd/CZO was 9.1% and fresh Pd/Al was 10%. Figure 5-8a shows the WGS conversion for fresh CZO was near 0% at 400°C as this reaction requires a metal-support interface. These results suggest that the decorated Pd-Ce_2O_3 sites act like Pd-Al_2O_3 adlineation sites, inert to oxidization (by water).

Table 5-4: Summarized catalyst activity tests				
Sample		**OSC CO_2 yield at 400°C [µ-mol/g-catalyst]**	**WGS CO_2 yield at 400°C [%]**	**CO T_{50} light-off [°C]**
Pd/CZO	Fresh	924	77%	74
	Redox aged 700°C/16h	669	9.1%	170
	Redox aged w/ 1/6m air	765	19%	187
	Redox aged w/ 2m air	872	43%	140
	Redox aged w/ 10m air	906	52%	142
Pd/Al	Fresh	151	10%	185
	Redox aged 700°C/16h	100	5.6%	204
	Redox aged w/ 1/6m air	125	5.3%	208
	Redox aged w/ 1m air	110	5.2%	209
	Redox aged w/ 10m air	104	6.7%	197

In the literature, Pd-La_2O_3 geometric SMSI effects were proposed when 1) the Pd dispersion results by H_2 chemisorption or H_2-O_2 titration methods were much lower for Pd supported on La_2O_3 than on SiO_2 [17, 18, 19, 24], or 2) the Pd dispersion on Pd-La_2O_3-SiO_2 samples measured by the H_2 chemisorption method were much lower than when measured by a different method [49], or 3) the CO-Pd IR peak intensity for Pd-La_2O_3-SiO_2 samples were reduced compared to Pd-SiO_2 [49, 50]. This geometric SMSI effect, as proposed by Fleisch *et al.*, begins when reduced La_2O_3 species migrate onto Pd-H sites and form adducts of $LaPd_xO$ in patches on the Pd surface [19]. In our work, redox aging of fresh Pd/Al showed a large drop in Pd dispersion by both H_2 chemisorption and XRD methods in Table 5-1 coupled with the H_2 chemisorption result being far below that the XRD result. These trends may also be explained by the literature Pd-La_2O_3 geometric effect or simply by Pd and Al_2O_3 sintering coupled with La_2O_3 surface richening near Pd causing the Pd to behave as if supported on La_2O_3 and exhibit just electronic SMSI effects. Interrupting redox aging with air pulses revealed a large increase in Pd dispersion by H_2 chemisorption in Table 5-1, which may indicate a reversal of the La_2O_3 migration off of Pd as with Ce_2O_3, but since XRD also showed a Pd dispersion increase, a better explanation that aligns the results of both methods is that Pd redispersion occurred. In addition, no significant change in surface Pd or La was shown by XPS in Table 5-2 that would be required if La was removed from on top

of Pd due to the air pulses. Our CO saturation DRIFTS results also did not support claims of geometric SMSI effects as fresh and aged Pd/Al samples had CO-Pd peaks that were similar in height corresponding to similar access to all Pd facets. In addition, other works cast doubt upon formation of reduced La_2O_3 species: 1) XPS work with a thin film of Pd-La_2O_3 exposed to H_2 at 600°C was shown to lack reduced surface La_2O_3 [51], 2) H_2 reduction work through 700°C on Pd-La_2O_3-Al_2O_3 showed no added consumption beyond that of Pd-Al_2O_3 [41], and 3) repeated H_2 reduction work through 700°C separated by a 500°C reoxidation step in air on Pd-La_2O_3-SiO_2 showed no added H_2 consumption beyond that of Pd-SiO_2 [49]. Recent room temperature CO saturation DRIFTS results by Gaudet *et al*. showed similar IR peak locations for 2.5wt%Pd on both 3wt%La_2O_3 stabilized γ-Al_2O_3 and γ-Al_2O_3 supports, while their La_2O_3 containing catalyst showed reduced linear CO-Pd peak height, they explained it as the result of stable Pd-O sites that diminished the number of Pd sites for room temperature CO adsorption [52]. Our XPS results with fresh Pd/Al also showed a significant stable PdO concentration that resisted a mild ex-situ reduction treatment prior to analysis, which was not present in our earlier XPS spectra work for 1.5wt%Pd on γ-Al_2O_3 support [21]. Therefore, apparent literature Pd-La_2O_3 geometric SMSI effects may be better explained by electronic effects or stable Pd-O sites.

In the literature, Pd-La_2O_3 electronic SMSI effects were claimed when the Pd $3d_{5/2}$ binding energy on La_2O_3 was more electronegative than Pd on SiO_2 or Pd^0 foil [19, 20] or 2) the reaction product selectivity increased for Pd-La_2O_3-SiO_2 versus Pd-SiO_2 [53, 54]. Pd $3d_{5/2}$ binding energies reported in the literature for supported catalysts with similar Pd loading as our Pd/Al samples depend upon the support material as follows:

1.9wt% Pd on La_2O_3 support: Pd^0 at 334.7 eV [19]

1.2wt% Pd on Al_2O_3 support: Pd^0 at 334.9 eV [36]

2.0wt% Pd on SiO_2 support: Pd^0 at 335.3 eV [19]

Figure 5-3 showed the Pd $3d_{5/2}$ peak at 334.8 eV +/- 0.1 eV for Pd^0 for Pd/Al, which was approximately that of 334.9 eV reported in the literature for Pd foil [36, 55]

and the literature values of Pd/La_2O_3 and Pd/Al_2O_3 above, yet showed a binding energy shift of about -0.5 eV relative to the literature value of Pd/SiO_2. We did not verify any significant differences in the aged Pd/Al catalyst activity tests, even with different measured Pd dispersion results as the support material had essentially no oxygen mobility. In addition, all catalysts used in this study had about the same Pd^0 binding energy and the reactions used did not facilitate observations of variable product selectivity, making confirmation of electronic SMSI effects by this route difficult.

Another reason to suspect $Pd\text{-}La_2O_3$ electronic SMSI effects versus geometric SMSI effects is regarding the time required for reversal through reoxidation. The Pd/Al samples demonstrated rapid Pd surface recovery to near the fresh state with just 1/6 minute air pulses, compared to the 10 minute air pulses required for Pd/CZO. Longer air pulses on aged Pd/Al samples showed small diminishing gains in Pd dispersion by H_2 chemisorption, but did not demonstrate gains in Pd dispersion by XRD, or gains in Pd surface by DRIFTS. These results suggest that SMSI electronic effects between $Pd\text{-}La_2O_3$ were much faster to reverse upon reoxidation than SMSI decoration effects of Ce_2O_3 on the Pd surface.

While the aged Pd/Al catalyst was capable of redispersing Pd in the time frame of a 10 second engine fuel cut due to a lack of geometric SMSI effects, it was not nearly as active for CO oxidation as the Pd/CZO catalyst. An automotive catalytic converter washcoat designed to facilitate rapid Pd redispersion with high automotive emissions conversion activity warrants further study. A $\gamma\text{-}Al_2O_3$ support stabilized with both CeO_2 and La_2O_3 may limit the amount of Ce_2O_3 migration onto Pd from a bulk CZO support yet enable enhanced oxygen mobility for low temperature CO oxidation. XPS work by Shelef et al. with thin films of these mixed oxides and Pd showed that the presence of La_2O_3 provided a synergistic effect that during reduction in H_2 at 600°C inhibited complete CeO_2 reduction [51]. Catalyst formulation work by Yang *et al*. showed a synergy between CeO_2 and La_2O_3 for methanol decomposition and did not show a loss in as-prepared Pd dispersion with increasing La_2O_3 content from 0-20wt% as with their $Pd\text{-}La_2O_3\text{-}Al_2O_3$ catalyst [56]. Catalyst formulation work by Mokhnachuk *et al*. showed improvements to thermal stability of $\gamma\text{-}Al_2O_3$ through 1000°C annealing by adding CeO_2

and La_2O_3 [57].

5.5 Conclusions

We determined the air pulse length required so that any Pd redispersion gains achieved by air treatment during the lean step will not be quickly undone on the following rich step in each 20 minute redox aging cycle. Air pulses applied to interrupt short redox aging spans enabled Pd redispersion in the time scale of a common engine fuel cut on Pd/Al catalysts, but not for Pd/CZO catalysts. The 1/6 minute air pulses restored the fresh-like Pd size on the redox aged Pd/Al samples, while the 10 minute air pulse restored the fresh-like Pd size on the redox aged Pd/CZO samples. These results suggest that SMSI electronic effects between Pd-La_2O_3 were much faster to reverse upon reoxidation than SMSI decoration effects of Ce_2O_3 on the Pd surface.

5.6 Acknowledgements

The authors gratefully acknowledge the following sources of funding for this study: Ford University Research Program (URP), NSF GOALI grant # CBET-1159279 and NSF grant # DMR-9871177.

5.7 References

[1] H.S. Gandhi, G.W. Graham, R.W. McCabe, "Automotive Exhaust Catalysis", *J. Catal.* 216 (2003) 433–442
[2] J. Kašpar, P. Fornasiero, N. Hickey, "Automotive catalytic converters: current status and some perspectives", *Catal. Today* 77 (2003) 419–449
[3] R.M. Heck, R.J. Farrauto, "Automobile exhaust catalysts", *Appl. Catal. A: Gen.* 221 (2001) 443–457
[4] N. Hickey, P. Fornasiero, R. Di Monte, J. Kašpar, J. R. González-Velasco, M. A. Gutiérrez-Ortiz, M. P. González-Marcos, J. M. Gatica, S. Bernal, "Reactivation of aged model Pd/$Ce_{0.68}Zr_{0.32}O_2$ three-way catalyst by high temperature oxidising treatment", *Chem. Comm.* 1 (2004) 196-197
[5] X. Chen, Y. Cheng, C.Y. Seo, J.W. Schwank, R.W. McCabe, "Aging, re-dispersion, and catalytic oxidation characteristics of model Pd/Al_2O_3 automotive three-way catalysts", *Appl. Catal. B: Environ.* 163 (2015) 499–509
[6] H. Lieske, J. Völter, "Pd Redispersion by Spreading of PdO in O_2 Treated Pd/Al_2O_3", *J. Phys. Chem.* 89 (1985) 1841-1842

[7] S.B. Kang, S.J. Han, S.B. Nam, I.S. Nam, B.K. Cho, C.H. Kim, S.H. Oh, "Effect of Aging Atmosphere on Thermal Sintering of Modern Commercial TWCs", *Top. Catal.* 56 (2013) 298–305
[8] M.A. Newton, C. Belver-Coldeira, A. Martínez-Arias, M. Fernández-García, ""Oxidationless" Promotion of Rapid Palladium Redispersion by Oxygen during Redox CO/(NO+O2) Cycling", *Angew. Chem. Int. Ed.* 46 (2007) 8629-8631
[9] E.T. Peterson, A.T. DeLaRiva, S. Lin, R.S. Johnson, H. Guo, J.T. Miller, J.H. Kwak, C.H.F. Peden, B. Kiefer, L.F. Allard, F.H. Ribeiro, A.K. Datye, "Low-temperature carbon monoxide oxidation catalysed by regenerable atomically dispersed palladium on alumina", *Nat. Comm.* 5 (2014) 4885
[10] J.J. Chen, E. Ruckenstein, "Role of Interfacial Phenomena in the Behavior of Alumina-Supported Palladium Crystallites in Oxygen", *J. Phys. Chem.* 85 (1981) 1606-1612
[11] N.M. Rodriguez, S.G. Oh, R.A. Dalla-Betta, R.T.K. Baker, "In-situ Electron Microscopy Studies of Palladium Supported on Al_2O_3, SiO_2, and ZrO_2 in Oxygen", *J. Catal.*, 157 (1995) 676-686
[12] E. Ruckenstein, J.J. Chen, "Wetting Phenomena during Alternating Heating in O_2 and H_2 of Supported Metal Crystallites", *J. Coll. Interface Sci.* 86 (1982) 1-11
[13] A. Badri, C. Binet, J.-C. Lavalley, "Metal-support interaction in Pd/CeO2 catalysis Part 2. – Ceria textural effects", *J. Chem. Soc. Farad. Trans*. 92(9) (1996) 1603-1608
[14] L. Kępiński, M. Wolcyrz, J. Okal, "Effect of Chlorine on Microstructure and Activity of Pd/CeO_2 Catalysts", *J. Chem. Soc., Farad. Trans.* 91 (1995) 507-515
[15] H.P. Sun, X.P. Pan, G.W. Graham, H.-W. Jen, R.W. McCabe, S. Thevuthasan, C.H.F. Peden, "Partial encapsulation of Pd particles by reduced ceria-zirconia", *Appl. Phys. Letts.* 87 (2005) 201915
[16] L. Kępiński, M. Wolcyrz, "Microstructure of Pd/CeO_2 catalyst: Effect of high temperature reduction in hydrogen", *Appl. Catal. A: Gen.* 150 (1997) 197-220
[17] J.S. Rieck, A.T. Bell, "Studies of the Interactions of H_2 and CO with Pd/SiO_2 Promoted with La_2O_3, CeO_2, Pr_6O_{11}, Nd_2O_3, and Sm_2O_3", *J. Catal*. 99 (1986) 278-292
[18] J.S. Rieck, A.T. Bell, "Studies on the Interactions of H_2 and CO with Silica- and Lanthana-Supported Palladium", *J. Catal*. 96 (1985) 88-105
[19] T.H., Fleisch, R.F. Hicks, A.T. Bell, "An XPS Study of Metal-Support Interactions on Pd/SiO_2 and Pd/La_2O_3", *J. Catal*. 87 (1984) 398-413
[20] R.F. Hicks, Q.J. Yen, A.T. Bell, "The Influence of Metal-Support Interactions on the Catalytic Properties of Pd/La_2O_3", *Appl. Surf. Sci*. 90 (1984) 315-329
[21] J.A. Lupescu, J.W. Schwank, K.A. Dahlberg, C. Seo, G.B. Fisher, S.L. Peczonczyk, K. Rhodes, M.J. Jagner, L.P. Haack, "Pd Model Catalysts: Effect of Aging Environment and Lean Redispersion", *Appl. Catal. B: Environ.* 183 (2016) 343–360
[22] J.A. Lupescu, J.W. Schwank, G.B. Fisher, X. Chen, S.L. Peczonczyk, A.R. Drews, "Pd Model Catalysts: Effect of Aging Duration and Lean Redispersion", *Appl. Catal. B: Environ.* 185 (2016) 189–202
[23] T.P. Bebee, J.T. Yeates, ""Spectroscopic Detection of (111) Facets on Supported Pd Crystallites: Site Blocking by Ethyldyne on Pd/Al2O3", *Surf. Sci. Lett*. 173 (1986) L606-L612
[24] R.F. Hicks, A.T. Bell, "Effects of Metal-Support Interactions on the Hydrogenation of CO over Pd/SiO_2 and Pd/La_2O_3", *J. Catal*. 90 (1984) 205-220
[25] D. Briggs, M.P. Seah, Practical Surface Sci. Analysis by Auger and X-ray Photoelectron Spectroscopy, John Wiley & Sons, New York, 1984
[26] A.L. Patterson, "The Scherrer Formula for X-Ray Particle Size Determination", *Phys. Rev.* 56 (1939) 978-982
[27] C.R. Adams, H.A. Benesi, R. M. Curtis, R. G. Meisenheimer, "Particle Size Determination of Supported Catalytic Metals: Platinum on Silica Gel", *J. Catal.* 1, (1962) 336-344
[28] J.K. Plischke, M.A. Vannice, "Effect of Pretreatment on the Adsorption Properties of Silver Crystallites", *Appl. Catal*. 42 (1988) 255-283
[29] R.T.K Baker, E.B. Prestridge, G.B. McVicker, "The Interaction of Palladium with Alumina and Titanium Oxide Supports" *J. Catal*. 89 (1984) 422-432
[30] F.M. Dautzenberg, H.B.M. Wolters, "State of Dispersion of Platinum in Alumina-Supported Catalysts" *J. Catal*. 51 (1978) 26-39
[31] J. E. Benson, H. S. Hwang, M. Boudart, "Hydrogen-Oxygen Titration Method for the Measurement of Supported Palladium Surface Areas", *J. Catal* 30 (1973) 146-153
[32] V. Ragaini, R. Giannantonio, P. Magni, L. Lucarelli, G. Leofanti, "Dispersion Measurement by the Single Introduction Method Coupled with the Back-Sorption Procedure: A Chemisorption and TPD Study of the Different Chemisorbed Hydrogen Species II. Pd on Alumina", *J. Catal*. 146 (1994) 116-125
[33] T. Takeguchi, S. Manabe, R. Kikuchi, K. Eguchi, T. Kanazawa, S. Matsumoto, W. Ueda, "Determination of dispersion of precious metals on CeO_2-containing supports", *Appl. Catal. A: Gen.* 293 (2005) 91–96
[34] A. Baylet, S. Royer, P. Marécot, J. Tatibouët, D. Duprez," Effect of Pd precursor salt on the activity and stability of Pd-doped hexaaluminate catalysts for the CH_4 catalytic combustion", *Appl. Catal. B: Environ.* 81 (2008) 88–96
[35] M. Alexandrou, R.M. Nix, "The growth, structure and stability of ceria overlayers on Pd(111)", Surf. Sci. 321 (1994) 47-57

[36] J.Z. Shyu, K. Otto, W.L.H. Watkins, G.W. Graham, R.K. Belitz, H.S.Gandhi, “Characterization of Pd γ-Alumina Catalysts Containing Ceria”, *J. Catal.* 114 (1988) 23-33
[37] M. Zhao, X. Li, L. Zhang, C. Zhang, M. Gong, Y. Chen, “Catalytic decomposition of methanol to carbon monoxide and hydrogen over palladium supported on $Ce_{0.65}Zr_{0.30}La_{0.05}O_2$ and La–Al_2O_3”, Catalysis Today 175 (2011) 430–434
[38] L. Yang, X. Yang, S. Lin, R. Zhou, “Insights into the role of a structural promoter (Ba) in three-way catalyst Pd/CeO2–ZrO2 using in situ DRIFTS”, *Catal. Sci. Technol.,* 5 (2015) 2688-2695
[39] K. Tanikawa, C. Egawa, “Effect of barium addition on CO oxidation activity of palladium catalysts”, *Appl. Catal. A: Gen.* 403 (2011) 12–17
[40] M.Y. Smirnov, G.W. Graham, “Pd oxidation under UHV in a model Pd/ceria–zirconia catalyst” *Catal. Lett*. 72 (2001) 39-44
[41] C. Yang, J. Ren, Y. Sun, “Role of La_2O_3 in Pd-supported catalysts for methanol decomposition”, *Catal. Lett*., 84 (2002) 123-129
[42] A. Holmgren, B. Anderson, D. Duprez, “Interactions of CO with Pt/ceria catalysts”, *Appl. Catal. B: Environ*. 22 (1999) 215–230
[43] G.N. Vayssilov, M. Mihaylov, P. St. Petkov, K.I. Hadjiivanov, K.M. Neyman, “Reassignment of the Vibrational Spectra of Carbonates, Formates, and Related Surface Species on Ceria: A Combined Density Functional and Infrared Spectroscopy Investigation”, *J. Phys. Chem. C* 115 (2011) 23435–23454
[44] N.B. Colthup, “Spectra-Structure Correlations in the Infra-Red Region”, *J. Optic. Soc. Amer.* 40 (1950) 397- 400
[45] F.M. Hoffmann, “Infrared Reflection-Absorption Spectroscopy of Adsorbed Molecules”, *Surf. Sci. Rep.* 3 (1983) 107-192
[46] J. Szanyi, W.K. Kuhn, D.W. Goodman, “CO adsorption on Pd(111) and Pd(100): Low and high pressure correlations”, *J. Vac. Sci. Tech. A* 11 (1993) 1969-1974
[47] S. Bertarione, D. Scarano, A. Zecchina, V. Johánek, J. Hoffmann, S. Schauermann, M.M. Frank, J. Libuda, G. Rupprechter, H.-J. Freund, “Surface Reactivity of Pd Nanoparticles Supported on Polycrystalline Substrates As Compared to Thin Film Model Catalysts: Infrared Study of CO Adsorption”, *J. Phys. Chem. B*, 108 (2004) 3603-3613
[48] T. Lear, R. Marshell, J.A. Lopez-Sanchez, S.D. Jackson, T.M. Klapötke, M. Bäumer, G. Rupprechter, H.-J. Freund, D. Lennon, “The application of infrared spectroscopy to probe the surface morphology of alumina supported palladium catalysts”, *J. Chem. Phys.* 123 (2005) 174706
[49] X.L. Seoane, N.S. Figoli, P.C. L'Argentiere, J.A. González, A. Arcoya, “Palladium-lanthanum interaction phenomena in Pd-$LaCl_3$/SiO_2 and Pd-La_2O_3/SiO_2 catalysts”, *Catal. Lett*. 47 (1997) 213-220
[50] W.H. Cassinelli, L.S.F. Feio, J.C.S. Araújo, C.E. Hori, F.B. Noronha, C.M.P. Marques, J.M.C. Bueno, “Effect of CeO_2 and La_2O_3 on the Activity of CeO_2–La_2O_3/Al_2O_3-Supported Pd Catalysts for Steam Reforming of Methane”, *Catal. Lett*. 120 (2008) 86–94
[51] M. Shelef, L.P. Haack, R.E. Soltis, J.E. deVries, E.M. Logothetis, “An XPS Study of Interactions in Thin Films Containing a Noble Metal with Valence-Invariant and Reducible Oxides”, J. Catal. 137 (1992) 114-126
[52] J.R. Gaudet, A. de la Riva, E.J. Peterson, T. Bolin, A.K. Datye, “Improved Low-Temperature CO Oxidation Performance of Pd Supported on La-Stabilized Alumina”, *ACS Catal*., 3 (2013) 846–855
[53] I.Y. Ahn, W.J. Kim, S.H. Moon, “Performance of La_2O_3- or Nb_2O_5- added Pd/SiO_2 catalysts in acetylene hydrogenation”, *Appl. Catal. A: Gen*. 308 (2006) 75–81
[54] E. Kim, E.W. Shin, C.W. Bark, I. Chang, W.J. Yoon, W.J. Kim, “Pd catalyst promoted by two metal oxides with different reducibilities: Properties and performance in the selective hydrogenation of acetylene”, *Appl. Catal. A: Gen*. 471 (2014) 80– 83
[55] E.H. Voogt, A.J.M. Mens, O.L.J. Gijzeman, J.W. Geus, “Adsorption of oxygen and surface oxide formation on Pd(111) and Pd foil studied with ellipsometry, LEED, AES and XPS”, *Surf. Sci*. 373 (1997) 210-220
[56] C. Yang, J. Ren, Y. Sun, “Role of La_2O_3 in Pd-supported catalysts for methanol decomposition”, *Catal. Lett*. 84 (2002) 123-129
[57] O.V. Mokhnachuk, S.O. Soloviev, A.Y. Kapran, “Effect of rare-earth element oxides (La_2O_3, Ce_2O_3) on the structural and physico-chemical characteristics of Pd/Al_2O_3 monolithic catalysts of nitrogen oxide reduction by methane”, *Catal. Today* 119 (2007) 145–151

Chapter 6 – Conclusions and Future Work

6.1 Concluding Remarks

In this research work, we examined the effects of aging environment and aging duration on Pd size and dispersion, and the extent that a post aging treatment of hot dry air can redisperse Pd and improve catalytic performance. All results were primarily derived from model powder catalysts of 1.5wt% Pd impregnated upon oxide materials of 4wt% La_2O_3 stabilized Al_2O_3 (Pd/Al) or $Ce_{0.5}Zr_{0.5}O_2$ (Pd/CZO). This approach attempted to observe changes in the bulk average Pd size and dispersion primarily with H_2 chemisorption and XRD pattern peak fitting, while measuring CO_2 yield during oxygen storage capacity and water-gas shift activity tests to estimate structure-activity relationships. Strong metal support interaction (SMSI) effects were also observed, which required more characterization tests to help resolve the discrepancies in the chemisorption and XRD techniques. We followed these works by incorporating the minimum redox aging duration that yielded effective Pd redispersion to find the minimum air pulse duration necessary to realize gains in Pd dispersion while interrupting a 16 hour redox aging cycle. The insight gained from this work could be used to develop engine control and aftertreatment design strategies to track (or infer) the aging process on the vehicle, avoid severe aging modes and actively intervene at various points to regenerate the catalyst.

The three aging environments used in the aging environment and duration studies at 700°C produced Pd/CZO samples with distinct levels of residual surface area, Pd particle size and WGS/OSC activity. A ranking relative to aging severity at 700°C for different Pd/CZO sample aging methods after 2 hours and 16 hours were as follows:

redox > rich-only >> lean-only. Reducing conditions produced a loss in exposed Pd surface area that was consistent with SMSI effects with support CeO_2. After each aging interval, the 700°C/2h lean treatment applied after redox aging always increased the Pd dispersion towards the level of the lean-only aged sample, but the magnitude of Pd dispersion recovery diminished with aging duration. These results show how quickly reducing conditions (i.e., engine fuel enrichment) and highway driving catalyst temperatures can deactivate Pd/CZO, and how frequent engine fuel-cut events must be delivered. The Pd particle size and WGS/OSC activity differences for the aged Pd/Al samples had similar trends, but were much smaller in magnitude, and even showed no significant difference in the residual surface area across the aging environments than the Pd/CZO samples. Therefore different aging protocols can to lead to very different catalyst structures and performance characteristics through a combination of metal oxidation state effects and support/additive interactions.

The fresh and lean-only aging environments used in the aging environment and duration studies at 700°C produced Pd/CZO samples with exposed Pd particles measurable by H_2 chemisorption, but not by XRD pattern peak fitting. The SMSI effects caused by reducing environments had undetectable Pd surfaces, which prevented examination of structure-activity relationships on these samples. The Pd/CZO samples with the highest measured dispersion had the highest CO oxidation in the OSC and WGS activity tests. Therefore, CO oxidation by support oxygen transfer appears to depend on the Pd dispersion, which correlates to the total number of metal-support interface sites. However, redox aged samples were given a 700°C lean treatment and resulted in samples with Pd particles in good agreement with chemisorption and XRD techniques, which had even higher TOF rates than fresh and demonstrated high catalyst activity with low Pd dispersion.

While chemisorption and XRD provide indirect evidence for estimates of bulk Pd size, electron microscopy is the most established technique to gather direct evidence. HAADF STEM images of Pd/Al redox aged samples confirmed the effects of post-aging treatments of hot dry air on Pd particle size and dispersion. The 550°C/2h lean treatment produced a 1.4 nm decrease in the mean Pd size with no increase in the

fraction of particles at 10 nm and below, yet the large particles at 30 nm to 80 nm shrank down from 5% of the aged total to 1%. The 550°C in air treatment shrank the particles of 16 nm and higher, increasing the count of particles measuring 11-15 nm from 36% to 43% of the total. The 700°C/2h lean treatment produced a 4.4 nm decrease in the mean Pd size with a near doubling of the fraction of aged particles at 10 nm and below, confirming the significance of Pd redispersion under these conditions. HAADF STEM images of Pd/CZO samples had very poor contrast and no data on Pd size could be gathered for confirmation. The 700°C lean treatment was confirmed to redisperse Pd on Pd/Al samples, but on Pd/CZO samples the results were mixed.

Surface analysis by XPS was performed for both aging environment and duration studies. The reducing aging environment brought more La and Ce oxide to the surface from the support relative to the fresh Pd/Al and Pd/CZO samples. However, from fresh to aged there was no change in surface Pd on Pd/Al to confirm that Pd was not covered by La_2O_3, yet half the surface Pd was lost on CZO to confirm that Pd was covered by Ce_2O_3 as ZrO_2 is not reducible under these conditions. After 2 hours and 16 hours of redox aging on Pd/CZO, the surface concentration of Pd^{+2} species vanished and the total Pd signal was decreased by 70% relative to fresh. The 700°C lean treatment applied to both aged samples restored Pd over the surface, lowered the surface concentration of Ce^{+3}, and reestablished the Pd^{+2} bonds with Ce up to the fresh level for the 2 hour aged sample and near half of the fresh level for the 16 hour aged sample.

Since Pd redispersion appears to require PdO mobility, lean treatments via engine fuel cuts need to be applied before reducible oxides creep up and restrain the Pd metal or multiple lean treatments would be needed in close succession. The approach we used combined several methods to elucidate the Pd particle size and dispersion, the coverage of particles by the CZO support and the effects of various aging treatments on the effectiveness of a lean redispersion method. The good consistency of the PdO phase formation measurements with established models allows for estimation of the Pd oxidation rates to temperatures beyond the range accessible by these methods. From these extrapolations, we are able to further estimate the effectiveness of the lean treatments to achieve Pd oxidation and redispersion with

temperature and time, and infer a recommendation for a practical engine control strategy. Bulk average Pd particle size below 8.8 nm was required for efficient reoxidation and rapid redispersion, and based on the increasing difficulty of achieving the same result for longer aging times, it was recommended that a fuel cut be performed just after 20 minutes of 700°C stoichiometric (redox) operation as a practical method to maintain activity.

We determined the air pulse length required so that any Pd redispersion gains achieved by air treatment during the lean step will not be quickly undone on the following rich step in each 20 minute redox aging cycle. Air pulses applied to interrupt short redox aging spans enabled lean Pd redispersion in the time scale of a common engine fuel cut on Pd/Al catalysts, but not for Pd/CZO catalysts. The 1/6 minute air pulses restored the fresh-like Pd size on the redox aged Pd/Al samples and were as effective at redispersing the Pd as the 10 minute air pulse was at redispersing the Pd on the redox aged Pd/CZO samples. These results suggest that SMSI electronic effects between Pd-La_2O_3 were much faster to reverse upon reoxidation than SMSI decoration effects of Ce_2O_3 on the Pd surface.

The insights gained from the studies on aging environment and duration provided important guidance into the operation of a catalytic converter on a vehicle. The engine exhaust environment capable of redispersing Pd catalyst particles seems to be aligned with fuel cuts during a deceleration event from high vehicle speed. If the catalyst is properly positioned near the engine exhaust manifold, then the temperature may be above the threshold of 700°C when air would be pumped through the engine on a fuel cut. The automotive catalytic converter could then be periodically regenerated with active engine controls to prolong the performance throughout the life of the catalyst. The result of this work may enable lower initial amounts of noble metals in the catalytic converter if the dispersion can be maintained above 1% by full useful life.

6.2 Potential Future Work

6.2.1 Higher Catalyst Aging Temperature

The temperature used for all catalyst aging in this work was 700°C, which was a typical customer in-use temperature for the catalytic converter. However, it is common for catalyst research in the literature to investigate 1000°C+ aging temperature typical of rapid aging conditions on a dynamometer to produce simulated 150,000 miles of deterioration in mere hours as higher temperatures are used to compress the catalyst deterioration time scale along an Arrhenius relationship. Graham *et al*. observed that 1050°C/12h redox aging on 2.25wt%Pd on CZO support (same Ce/Zr ratio as ours) exhibited just 3 m^2/g surface area and Pd particle encapsulation by the support material so that near 25% of the Pd metal could not be reoxidized during a 700°C/2h air treatment [1]. Therefore the results of this study cannot be successfully incorporated into an aging environment near 1000°C, but could influence operation under real-world in-use conditions at highway speeds where 700°C is well within the range of operating temperatures.

Similar to the catalysts and conditions described in chapter 4, a small sample set of Pd/CZO model catalysts were aged for 2 hours, but at a temperature of 900°C. The XRD pattern for reduced Pd/CZO redox aged 900°C/2h sample set are below in Figure 6-1 and are consistent with the expected peaks for CZO support. No new support phases were observed during the 900°C/2h aging for either model catalyst. All aged patterns appear similar and Pd peaks are now visible at 40°2θ, 46.7°2θ and 68°2θ, which was not true for the 700°C/2h lean-only and redox aged samples in chapter 4.

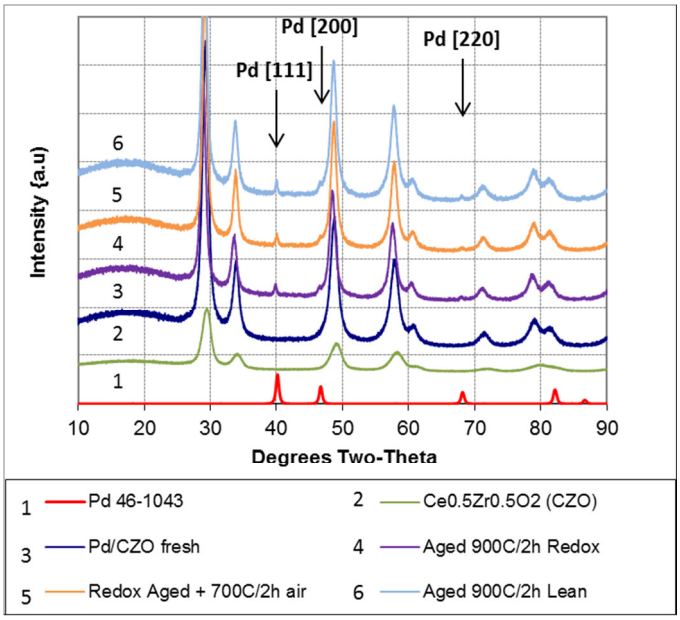

Figure 6-1: XRD Patterns of Pd/CZO catalysts

Table 6-1 has the characterization data for the Pd/CZO redox aged 900°C/2h sample set compared to reference data from chapter 4 for the Pd/CZO redox aged 700°C/2h. The BET surface area of the 700°C aged catalysts was just over 1/2 of the fresh value while the value for the 900°C aged catalysts was just 1/3 of the fresh value. These samples still had a significant portion of their initial surface area after aging, but given the work by Graham cited above, an XRD pattern should be collected for both oxidized and reduced powder samples to detect for encapsulated particles (a Pd [111] peak at 40°2θ even after 700°C/2h oxidation [1]). The BJH pore volume of the 700°C aged catalyst was essentially unchanged from the fresh value while the 900°C aged catalyst was over 80% of the fresh value. The higher aging temperature diminished the Pd size and dispersion differences between lean-only and redox aging environments as observed at the lower aging temperature, perhaps due encapsulation or decoration of Pd particles by Ce_2O_3. The lower redox aging temperature caused Pd to sinter to 17 nm and the 700°C/2h air post aging treatment was effective at shrinking Pd down by 6 nm to 11 nm. The higher aging redox temperature caused Pd to sinter to 26 nm and the same post aging treatment showed just a 3 nm size reduction due to either the initially higher Pd size or lower support surface area limiting PdO particle mobility.

Table 6-1: Support surface area and Pd size characterization of Pd/CZO samples							
Duration	**Condition**	**Surface Area [m^2/g]**	**Pore Volume [cm^3/g]**	**Pd dispersion [%]**		**Pd particle size [nm]**	
				by H_2[a]	**by XRD[b]**	**by H_2[a]**	**by XRD[b]**
0 min	Fresh	91	0.160	22%	u/d*	5.1	u/d*
700°C 2 hours	Lean-only 700°C	59	0.160	16%	u/d*	6.7	u/d*
	Redox (10/10) 700°C	51	0.156	u/d†	6.5%	u/d†	17
	+ 700°C/2h air	52	0.158	13%	10%	8.8	11
900°C 2 hours	Lean-only 700°C	30	0.130	0.7%†	3.1%	157†	35
	Redox (10/10) 700°C	31	0.131	u/d†	4.2%	u/d†	26
	+ 700°C/2h air	30	0.130	1.2%†	4.7%	92†	23

u/d = undetectable, * No XRD pattern peak, † Pd particles suspected to be affected by SMSI

Similar to the activity test conditions described in chapter 4, the 900°C/2h redox aged Pd/CZO model catalysts were evaluated with OSC and WGS tests and the results are shown in Figure 6-2. In Figure 6-2a, the 700°C aging temperature showed close OSC performance between fresh and lean only aged and a large gap down to redox aged, which was bridged by the 700°C/2h air treatment up to the lean-only sample. In Figure 6-2b, the 900°C aging temperature showed a large gap in OSC performance between fresh and lean only aged and a further large gap down to redox aged. The 700°C/2h air treatment on the 900°C redox aged sample brought the OSC performance up near the lean-only aged sample. For both aging temperatures, the upper limit of benefits realized through post aging lean treatments appears to be at the lean-only aged performance, consistent with the Pd dispersion results reported in Table 6-1.

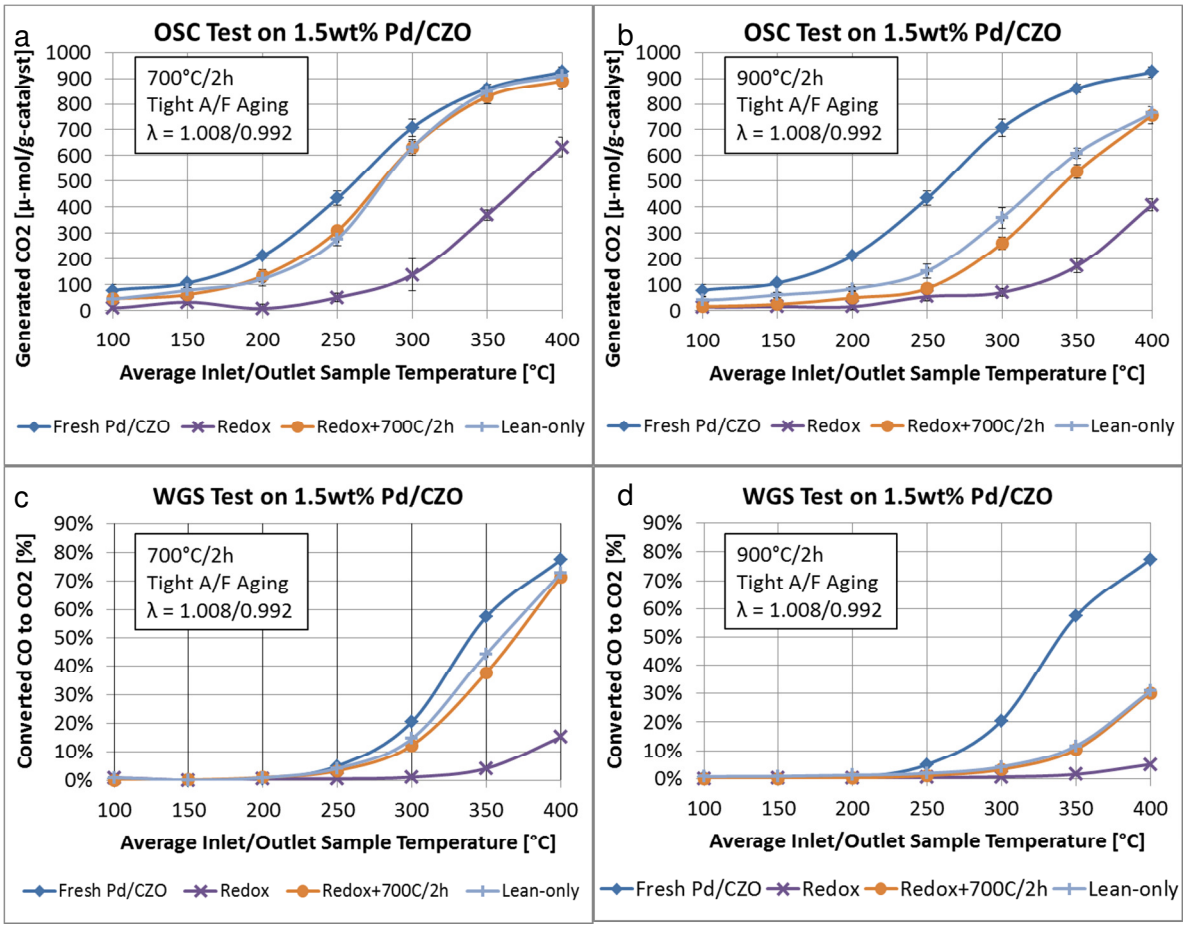

Figure 6-2: Catalyst activity tests on Pd/CZO samples. Plots: a) OSC 700°C/2h aged, b) OSC 900°C/2h aged, c) WGS 700°C/2h aged, b) WGS 900°C/2h aged

Questions for future students regarding 900°C redox operation are as follows:

- What is the optimal CZO ratio for 900°C redox operation for low temperature catalyst activity and minimizing SMSI effects?
- Will Pd on γ-Al_2O_3 stabilized with CeO_2 and La_2O_3 provide any benefit at 900°C compared to the Pd model catalysts used in chapter 3?
- What is the optimal support selection for low temperature catalyst activity while enabling rapid Pd redispersion with interrupting air pulses during redox aging as in chapter 5?
- Are the mechanisms that seem to limit the extent of Pd redispersion (restricted Pd mobility by SMSI effects or surface area collapse) different than

at 700°C? Are these mechanisms still reversible with interrupting air pulses during 900°C redox aging as in chapter 5?

6.2.2 Post Aging Lean Treatment Effects

Chapter 3 showed several effects on the redox aged Pd catalyst samples after post aging lean treatments by 700°C/2h air exposure. The regenerated Pd/Al samples showed smaller Pd particles by multiple techniques, hollow Pd particles by STEM and Pd lattice expansions by XRD. The regenerated Pd/CZO samples showed increased catalyst activity up to the lean-only aged samples, smaller Pd particles and Pd lattice expansions by XRD, and increased turnover frequency for CO oxidation by OSC and WGS reactions over fresh Pd/CZO.

Recall that the turnover frequency (TOF) is the number of molecules of CO reacted per second divided by the number of exposed Pd surface atoms (N_S^{Pd}) as determined by H_2 chemisorption. The TOF from the catalyst activity tests can be plotted in terms of the Arrhenius equation to determine the activation energy (E_a) and coefficient (A) as: $\ln(TOF) = (-E_a/R)*(1/T) + \ln(A)$. Chapter 3 showed TOF plots versus temperature for Pd/CZO samples. Figure 6-3a-b shows the regenerated redox aged versions of those chapter 3 samples (after the 700°C air treatment). The regenerated redox aged samples had elevated TOF results (higher intercept A) versus the fresh or lean-only aged samples yet similar slope (E_a) to the redox aged and lean only aged samples. Figure 6-3c-d shows a higher E_a with redox aging duration for OSC, but not WGS. This increased Arrhenius equation A value may indicate a change to the catalyst surface geometry as the composition of the metal-support interface sites were likely altered by the redox aging environment followed by reducible Ce oxide decomposition from the Pd surface, enriching the local Pd interface sites with more CeO_2 than the original $Ce_{0.5}Zr_{0.5}O_2$ support of the fresh and lean aged samples. The TOF equation contains an exposed Pd surface atoms term (N_S^{Pd}) that does not account for adlineation site participation from reducible oxides in the support. Other work with CZO solid solutions has shown available OSC was increased by over 20% when CeO_2 compositions were adjusted from 50% to 65% [2, 3, 4].

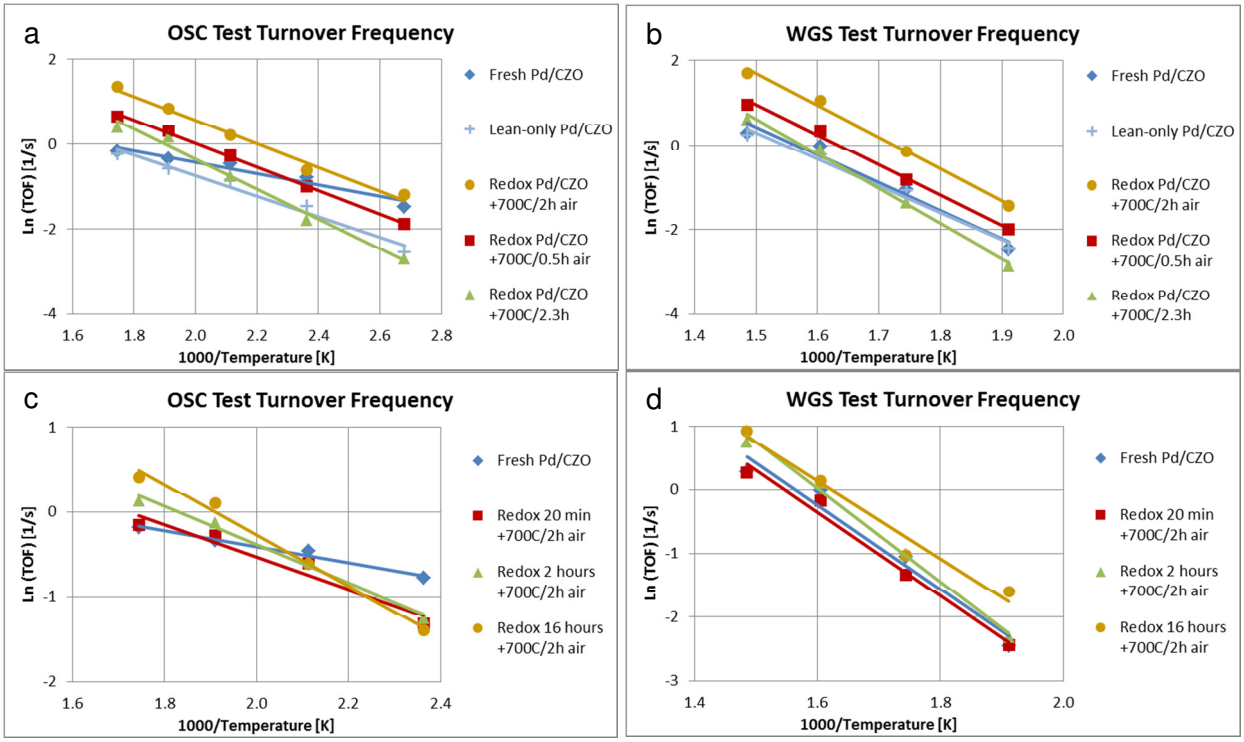

Figure 6-3: Catalytic activity test TOF on Pd/CZO samples. Aging environment for 16h sample plots: a) OSC, b) WGS. Aging duration results for redox aged samples: c) OSC, d) WGS

The changes in OSC and WGS kinetics as shown in Figure 6-3, and the associated Arrhenius parameters E_a and A, may give clues to the changes on the catalyst surface. Work by Wang et al. on 1wt%Pd on CeO_2 samples that were fresh and redox aged at 500°C or 800°C acquired similar CO/O_2 OSC data to our work and also made TOF plots that demonstrated similar slopes (E_a values) for all samples over the first few seconds of the CO pulse and lower TOF plot intercept (A values) with more severe aging and lower surface area [5]. This is consistent with our work in chapter 3, and in Figure 6-3a and 6-3c where lower A values were linked to aging, unless a lean treatment was applied afterwards. As Wang tracked the Ce^{+3}/Ce reduction levels progressed beyond the first few seconds, the TOF slopes sharply increased towards zero, in addition E_a values were plotted as a function of Ce^{+3}/Ce reduction levels where

E_a increased with higher aging temperature [5]. If increasing E_a means less labile oxygen at the catalyst surface, then that may explain the trends shown in Figure 6-3c as increased redox aging duration had a more negative slope. Wang suggested that the rate limiting step for CO oxidation varied with the participating oxygen species originating from different parts of the CeO_2 particles as the processes were different at the onset of reduction, eventually the E_a of the samples became similar at higher reduction levels [5]. If so, then the intercepts A from the initial reductions used to make Figure 6-3 would be differentiated if the samples had more oxygen provided by the Ce^{+4} at the Pd adlineation sites as was suggested earlier, but if we continued to calculate the TOF beyond the first few seconds of the OSC CO pulse, then perhaps the TOF intercepts would converge and the lean treatments would not exhibit a difference from fresh or lean-only aged.

Questions for future students regarding regeneration effects are as follows:

- Can the reasons behind the differences in the Arrhenius equation A value be more directly explored with new catalysts more easily characterized by specific surface differences, perhaps through microscopy?
- How can adlineation sites be probed more effectively to explain the TOF differences?

Another possibility for the higher TOF is that the measured Pd dispersion by H_2 chemisorption was incorrect and below the actual value. However the dispersion for the lean-only sample was 15% (7.3 nm) and the redox-regenerated sample was 4.1% (27 nm), a 20 nm difference in Pd size is well beyond the 15% error of the method as described in chapter 2. Chapter 4 showed the regeneration conditions restored Pd^{+2} sites as by XPS detection that were not reduced by the pretreatment conditions of 1% CO/H_2 at 300°C-350°C for up to 1 hour. Perhaps robust Pd^{+2} sites formed during the post aging lean treatment were not reduced in pure H_2 at 350°C, which affected the H_2 chemisorption measurement at 35°C. Chapter 3 showed that the H_2 chemisorption results for the Pd/CZO samples had the following trends for Pd dispersion: fresh > 700C/2.3h air > 700C/0.5h air > 700C/2h air >> redox. The DRIFTS results with CO

saturation acquired on the samples from chapter 3 are shown below in Figure 6-4. The Pd [111] and [100] surface sites allowed more CO adsorption with increasing duration of 700°C air exposure, which should scale with Pd dispersion, but is not in line with the trend in H_2 chemisorption results. The multiple brief 0.1 hour treatments used to obtain the 700C/0.5h air sample may have created a more unstable surface structure than the 2h continuous air exposure did for the redox aged sample so that different results would be achieved for H_2 and CO adsorption. This may mean that the surface characteristics of the sample dominated the TOF and characterization trends, rather than errors in the H_2 chemisorption method.

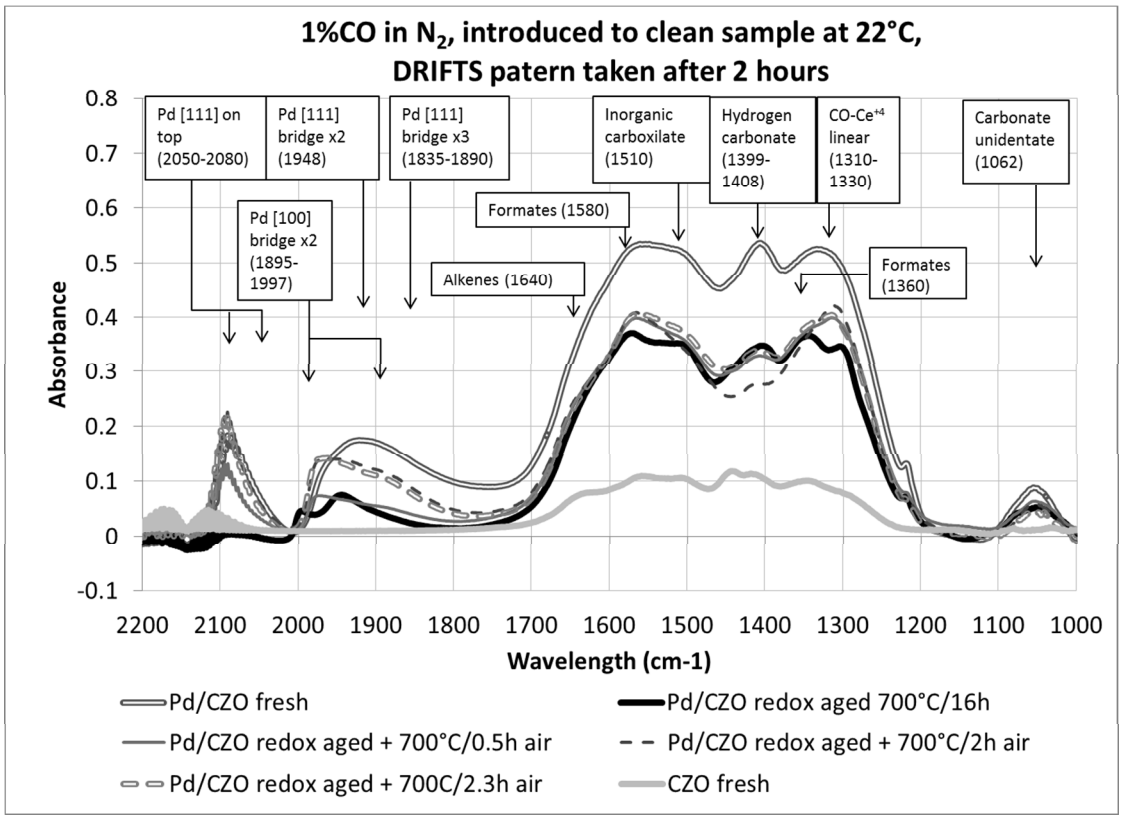

Figure 6-4: DRIFTS pattern of CO adsorption onto cleaned samples for 2 hours at 22°C

6.2.3 Redox Aging Environment Length

The 10 minute long redox pulses used for our quartz boat powder aging are unrealistic for modern stoichiometric operation that is typically switched at 1Hz or faster. A more realistic step length for catalyst powder redox aging is not known. Our intention was to produce deteriorated catalysts and we succeeded in deteriorating the catalysts

systematically based on aging environment and conditions. With a quicker step pulse transient operation, there would always be doubt that the full extreme of each redox pulse was sufficiently inflicted upon the entire depth of powder in the quartz boat. Our conditions were adopted from prior work with quartz boat powder aging in a flow reactor [6]. At 10 minutes in pulse length, we assumed that the powder bed depth was sufficiently exposed to rich and lean environments on each step, rather than an average gas composition due to fast switching.

Questions for future students regarding redox aging methods are as follows:

- Chapter 5 showed with a 2 minute air pulse during redox aging of Pd/CZO, the SMSI effects from 10 minutes of rich step length were sufficiently reversed to expose Pd. Was the air pulse length correlated to the rich step length or the rate of Ce_2O_3 decomposition off from the Pd surface and then reintegration into the bulk CZO material? Would Pd/CZO show full recovery with 1/6 minute air pulses if the redox rich/lean step lengths were shortened to 2 minutes each?
- Work by Hepburn *et al*. developed a realistic aging system with a flow-through combustion reactor, coated monolithic samples, liquid gasoline-type fuel and oxygen sensor feedback [7]. Their overall exhaust conditions approximated the rich/lean environment extremes of real-world stoichiometric operation (λ = 0.97/1.03). Do our aging environment severity trends hold with monoliths aged at 1Hz redox cycling?

6.2.4 Redox Aging Environment Lambda

The samples in chapters 4 and 5 were aged with a tight air/fuel aging environment (λ = 0.992/1.008, 0.2%CO/H_2 or 0.1%O_2) to try and avoid the SMSI effects first observed with the samples that were aged with the initial air/fuel conditions (λ = 0.97/1.03, 1%CO/H_2 or 0.5%O_2) in chapter 3. Table 6-2 compares the redox aged samples to show that in spite of the air/fuel amplitude difference, the effect on Pd size was comparable, SMSI effects were similarly observed by H_2 chemisorption and Pd dispersion was restored with 700°C/2h air treatments. Note that both redox

environments sintered the Pd size to the same 20 nm size by XRD. Figure 6-5 shows that both air/fuel aging environments for fixed 700°C operation were in the Pd metallic state while the regeneration treatments in air were in the PdO state.

Table 6-2: Characterization of redox aged and regenerated catalyst samples

Sample	Condition	Redox aging environment	Surface Area [m^2/g]	Pd dispersion [%]		Pd particle size [nm]	
				by H_2[a]	by XRD[b]	by H_2[a]	by XRD[b]
Pd/Al	Redox 700°C/16h	0.5%O_2 or 1%CO/H_2	164	0.7%	6.8%	159	16
	+ 700°C/2h air		157	5.7%	7.6%	19	14
	Redox 700°C/16h	0.1%O_2 or 0.2%CO/H_2	154	0.3%	6.3%	433	18
	+ 700°C/2h air		152	5.4%	5.1%	20	22
Pd/CZO	Redox 700°C/16h	0.5%O_2 or 1%CO/H_2	35	u/d	5.6%	u/d	20
	+ 700°C/2h air		35	4.1%	4.5%	27	24
	Redox 700°C/16h	0.1%O_2 or 0.2%CO/H_2	41	u/d	5.4%	u/d	20
	+ 700°C/2h air		41	8.7%	6.3%	13	18

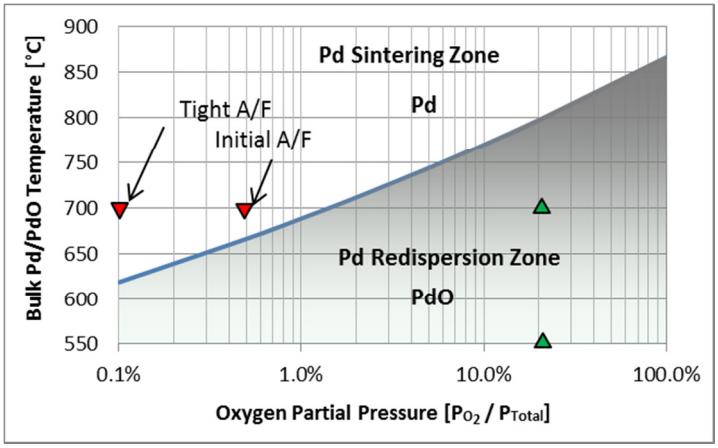

Figure 6-5: Illustration of O_2 concentrations used for both aging environments relative to bulk PdO decomposition line

Questions for future students regarding redox environments are as follows:

- Why was the redox aging environment a more severe mode than lean-only or rich-only environments as shown in chapters 3 and 4?
- What is the dependence of CeO_2 oxidation state in the Pd/CZO catalyst with oxygen concentration and temperature? Experimental development of a

decomposition map for CeO_2 would help correlate these observed SMSI effects as Figure 6-5 is useful to determine when Pd is metallic or an oxide.

Chapter 5 investigated adding air pulses after the 10 minute rich step in the redox aging cycle at 700°C. Air pulses are effective at oxidizing Pd and redispersing PdO up to 800°C operation according to Figure 6-5. Vehicle operation at 650°C may accomplish Pd redispersion on each lean redox step if O_2 achieves above 0.3%. Kang *et al*. aged Pd-TWC monolith samples in a flow through reactor with a periodic redox environment at 600°C for 16 h while cycling for 5s with 3% CO to form Pd metal then for 5s with 3% O_2 to form PdO, although the final Pd dispersion was not quantified, a 30°C lower CO light-off temperature was disclosed for their periodic redox cycling sample than for aging in constant 3% O_2 [8]. However, later in that same work they aged their catalysts at 900°C and observed a 44°C lower light-off temperature after a periodic redox environment than the lean-only conditions, even though both conditions preserve Pd in the metallic state. A comparison of our work to Kang's work poses new questions and could generate new avenues of research

Questions for future students regarding PdO/Pd redox operation are as follows:

- At 650°C and the initial A/F conditions, the lean-only and lean steps are below the PdO decomposition line. Will our conclusions about aging environment severity hold when samples are aged at a fixed 650°C temperature? Will lean steps about the PdO decomposition line show differences in SMSI effects or Pd size?
- Kang *et al*. seems to conflict with our work in chapter 3 as the Pd/TWC lean-only aged sample performed better than the Pd/TWC redox aged sample on our OSC and WGS tests. Why would the 3% O_2 that Kang *et al*. used in their aging environments make such a difference?

6.2.5 Adlineation site length

From chapter 1, the second hypothesis was that oxygen transfer depends on the contact line between the support and the perimeter precious metal particles (so-called

adlineation sites). This hypothesis could not be fully investigated with these types of catalyst supports. The problems with acquiring convincing results were: 1) a wide initial Pd particle size distribution on the prepared samples preventing associated structure-activity links, 2) SMSI effects limiting the H_2 chemisorption measurement to determine accurate Pd size and dispersion on redox and rich-only aged samples preventing reaction rate turn-over frequency calculations for comparison.

6.3 References

[1] G. Graham, H. Jen, W. Chun, R. McCabe, "Encapsulation of Pd particles by ceria–zirconia mixed oxides", *Catal. Letts*. 44 (1997) 185-187

[2] Y. Madier, C. Descorme, A. M. Le Govic, D. Duprez, "Oxygen Mobility in CeO_2 and $Ce_xZr(1-x)O_2$ Compounds: Study by CO Transient Oxidation and $^{18}O/^{16}O$ Isotopic Exchange", *J. Phys. Chem. B*, 103 (1999) 10999-11006

[3] A. Trovarelli, F. Zamar, J. Llorca, C. de Leitenburg, G. Dolcetti, J.T. Kiss, "Nanophase Fluorite-Structured CeO2–ZrO2 Catalysts Prepared by High-Energy Mechanical Milling: Analysis of Low-Temperature Redox Activity and Oxygen Storage Capacity", *J. Catal.* 169 (1997) 490–502

[4] J.-P. Cuif, G. Blanchard, O. Touret, A. Seigneurin, M. Marczi, E. Quéméré, "(Ce, Zr)O2 Solid Solutions for Three-Way Catalysts", *Soc. Automot. Eng., SP-1288* (1997) 35-47

[5] B. Wang, D. Weng, X. Wu, J. Fan, "Influence of H_2/O_2 redox treatments at different temperatures on Pd-CeO_2 catalyst: Structure and oxygen storage capacity", *Catal. Today* 153 (2010) 111–117

[6] J.C. Jiang, X.Q. Pan, G.W. Graham, R.W. McCabe, J. Schwank, "Microstructure of a Pd/ceria–zirconia catalyst after high-temperature aging", *Catal. Lett*. 53 (1998) 37–42

[7] J.S. Hepburn, D.A. Dobson, C.P. Hubbard K. Otto, "The Pulse Flame Combustor Revisited", *SAE technical paper 962118* (1996) doi:10.4271/962118

[8] S.B. Kang, S.J. Han, S.B. Nam, I.S. Nam, B.K. Cho, C.H. Kim, S.H. Oh, "Effect of Aging Atmosphere on Thermal Sintering of Modern Commercial TWCs", *Top. Catal.* 56 (2013) 298–305